The Weak Charge of the Proton: A Search For Physics Beyond the Standard Model

by

Scott J MacEwan

A Thesis submitted to the Faculty of Graduate Studies of

The University of Manitoba

in partial fulfillment of the requirements of the degree of

DOCTOR OF PHILOSOPHY

Department of Physics and Astronomy

University of Manitoba

Winnipeg, Manitoba, Canada

This dissertation is dedicated to my family.

Abstract

The Q_{weak} experiment will provide the most precise determination of the proton's weak charge Q_W^p by measuring the parity-violating asymmetry in elastic electron-proton scattering at low momentum transfer $Q^2 \sim 0.0250\,(\mathrm{GeV/c})^2$. Q_W^p is related to the weak mixing angle $\sin^2\theta_W$, a fundamental parameter of the standard model. A final measurement of the weak charge at the proposed 4% relative uncertainty is sensitive to certain types of new parity-violating physics beyond the standard model at the TeV mass-scale.

Data were taken over a two year period beginning in 2010, using a custom apparatus installed in Hall-C at the Thomas Jefferson National Accelerator Facility in Newport News, Virginia. A 180 μA beam of longitudinally polarized electrons was accelerated to 1.165 GeV and then scattered from unpolarized protons in a liquid hydrogen target. The scattered electrons were then collimated and steered using a magnetic spectrometer onto a set of azimuthally symmetric quartz bar Čerenkov detectors. The performance of this main detector subsystem will be described in detail in this dissertation.

A blinded analysis of Run-II, roughly 2/3 of the entire Q_{weak} data set, resulted in an elastic $\vec{e}p$ asymmetry of -235.6 ± 8.7 (Stat) $\pm$ 9.3 (Syst.) $\pm$ 39.3 (Blind) ppb. Using this value, the proton's weak charge was calculated to be $Q_W^p = 0.0714 \pm 0.0093$. This constitutes a 17% relative measurement, that will reduce to < 9% upon unblinding of the asymmetry. This dissertation will provide the details that went into extracting both the parity-violating asymmetry and the weak charge of the proton.

Acknowledgements

I would first like to thank my advisor, Dr. Michael Gericke, for providing the guidance and motivation that I needed in order to complete this research. I owe him and Dr. Shelley Page a great deal of gratitude for their understanding of the difficulties associated with raising a family so far from home.

I would also like to take this opportunity to extend special thanks to those senior collaborators at JLab who offered me help along this journey: Dave Mack for helping me with countless hardware and analysis-related questions, and Greg Smith for always keeping his door open when I needed help during the final weeks of my analysis. Q_{weak} was fortunate to have so many brilliant collaborators who were always willing to provide help and guidance to the students. I owe thanks to all of these people, especially Roger Carlini, David Armstrong, Mark Pitt, and Kent Paschke. Special thanks go to Paul King who guided the software and analysis as they progressed over time. I'd also like to recognize Ross Young who supported my attempts to provide on-site support for his Mathematica routines.

A number of postdoctoral fellows made hugely significant contributions to Q_{weak} . I am indebted to Rob Mahurin for taking me under his wing and providing a consistent source of feedback and knowledge. Thanks to Jeong Han Lee for all of his work with the data acquisition systems and software development, and Mark Dalton for stimulating physics discussions during lunch. Thank you to Wouter Deconinck for his guidance in both physics and software topics.

I am thankful to all of my fellow Q_{weak} students, including those who have moved on to the next chapters in their careers: Peiqing Wang, John Leacock, John Leckey, Adesh Subedi, Katherine Myers, and Nurruzaman. Great thanks are warranted to Rakitha Beminiwatha and Buddhini Waidyawansa who were great office-mates as well as friends to my family. Thank you to those students who are still working hard to bring Q_{weak} to a conclusion: Wade Duvall, Anna Lee, Josh Magee, Juan Carlos Cornejo, Jim Dowd, Josh Hoskins, Emanouil Kargiantoulakis, Don Jones, and anyone who I've regretfully forgotten.

Finally, I want to thank my family. I'm very grateful to my parents for always being there when we've needed them. Most importantly however, I want to thank my wife, Dana. Thank you for your patience and understanding as I attempted to juggle a degree and a family. I could not have done any of this without your support.

Table of Contents

List of Figures

List of Tables

Acronyms

ADC Analog to Digital Converter.

APV Atomic Parity Violation.

BB Beamline Backgrounds.

BCM Beam Current Monitor.

BPM Beam Position Monitor.

CEBAF Continuous Electron Beam Accelerator Facility.

CFD Computational Fluid Dynamics.

CL Confidence Level.

CODA CEBAF Online Data Acquisition.

DAC Digital to Analog Converter.

DAQ Data Acquisition.

DS Downstream.

HDC Horizontal Drift Chamber.

HV High Voltage.

IHWP Insertable Half Wave Plate.

LED Light-Emitting Diode.

LH2 Liquid Hydrogen.

LINAC Linear Accelerator.

MD Main Detector.

MPS Macropulse.

NC Neutral Current.

PMT Photomultiplier Tube.

PPM (PPB) Parts per million (billion).

PV Parity Violating.

PVES Parity Violating Electron Scattering.

QE Quantum Efficiency.

QED Quantum Electrodynamics.

QTOR Qweak Toroidal Magnet.

RC Radiative Corrections.

SM Standard Model.

SRF Superconducting Radio Frequency.

SUSY Supersymmetry.

TDC Time to Digital Converter.

US Upstream.

VDC Vertical Drift Chamber.

Chapter 1

Introduction

In the natural sciences we develop models in an effort to provide a theoretical understanding of observed phenomena. Testing a model in the form of rigorous experimentation can result in its revision, rejection, or its acceptance as a well-established theory. In the field of nuclear and particle physics the *standard model* (SM) is one such model, in which three of the four fundamental forces of nature are described in the framework of quantum field theories. Gravitation is not yet included in the standard model while strong nuclear, weak nuclear, and electromagnetic interactions are accounted for in such a way that the theory largely agrees with experimental observations. This dissertation will provide details on $\mathrm{Q_{weak}}$, an experiment that used parity-violating electron-proton scattering to perform a high precision test of the standard model. More detail will accompany the discussions focused on those aspects of the experiment in which I played a key role. These will include the commissioning and maintenance of the main detector subsystem and analysis techniques used during linear regression as a means to correct for certain types of systematic effects. My efforts to understand Q_{weak}'s sensitivity to the electromagnetic form factors of the nucleon will also be presented in particular detail in Chapter 5.

1.1 The Standard Model

The standard model describes all interactions in terms of the exchange of particles called intermediate vector bosons which have spin $s = 1$. The photon (γ) and eight distinct gluons (g_i) are the mediators of the electromagnetic and strong nuclear forces respectively and are assumed to be massless in the model. The mediators of the weak nuclear force, the charged W^+, W^- and neutral Z^0 bosons, are massive with masses $m_{W^\pm} = 80.385 \pm 0.015\,\mathrm{GeV/c^2}$ and $m_{Z^0} = 91.1876 \pm 0.0023\,\mathrm{GeV/c^2}$[8]. To explain why particles have mass, the standard model also predicts the existence of a fundamental particle responsible for generating particle masses. The existence of the Higgs boson, with a mass of $m_H = 125.09 \pm 0.21 \pm 0.11\,\mathrm{GeV}$, was recently verified at the Large Hadron Collider (LHC)[9][10].

The remainder of the particles classified in the standard model are called fermions and have half-integer spin $s = 1/2$. The fermions, which make up all matter, are further split into two distinct groups called leptons and quarks. The leptons include the electron e^-, muon μ, and tau τ particles along with their respective neutrinos ν_e, ν_μ, ν_τ. Quarks are also separated into a hierarchy of three "generations," the first of which includes the up (u) and down (d) quarks. The up and down quarks possess nearly equal masses and are the lightest of all six; they are the primary constituents of all strongly interacting stable matter in the universe. The charm (c) and strange (s) quarks and top (t) and bottom (b) quarks make up the second and third generations respectively, and possess increasingly heavy masses. Quarks carry colour charge, which can take one of three possible values: red, green, or blue, and to date all observed particles have had zero net colour charge. This colour classification provides a convenient label for one possible set of basis states of the SU(3) symmetry group which describes the strong nuclear interactions in the standard model. Experimental status shows that quarks only exist in bound states of either a quark-antiquark pair (a meson) or of three quarks (a hadron)*.

*Additional exotic combinations of quarks paired with gluons are allowed in the theory of quantum

While quarks experience all four fundamental forces of nature, leptons do not interact via the strong interaction, and furthermore, neutrinos *only* interact via weak nuclear interactions. The standard model particle types and generations are summarized in Figure 1.1.

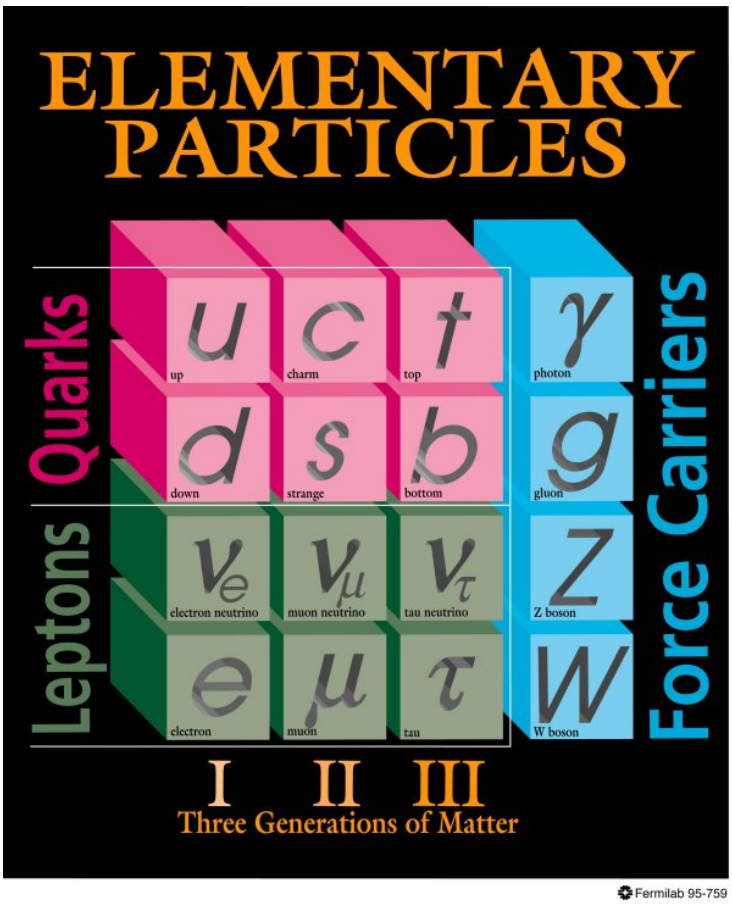

Figure 1.1: The elementary particles of the standard model, organized in their three generations based on particle masses[1].

Though the standard model has been very successful in predicting and explaining observed phenomena, evidence exists that it is not a fundamental theory of nature. The model itself provides no mechanism for providing numerical values for a number of parameters, including the relative coupling strengths of the electromagnetic, weak, and strong nuclear interactions. Similarly, although it provides a possible explanation for the

chromodynamics, but are beyond the scope of this dissertation

origin of mass, one cannot use the standard model to predict the masses of the quarks and leptons. Additionally, it provides no explanation of the "three generation" structure mentioned above. Candidates for standard model extensions can be tested either by direct searches for new particles/effects predicted by the theory, or by performing high precision measurements of quantities that may be sensitive to effects from standard model extensions; these two approaches are conducted in experimental regimes known as the *Energy* and *Precision Frontiers* respectively. The *Cosmological Frontier* represents another method of testing standard model extensions, where astronomical observations are performed in search of new effects predicted by theory.

1.1.1 Electroweak Theory

Mathematically, the standard model is classified as an SU(3)× SU(2)$_L$×U(1)$_Y$ gauge group[11], where the invariance under gauge transformations of each of these groups (from left to right) lead to the Lagrangians describing the quantum chromodynamics of the strong interaction, weak isospin symmetry of the isospinors in weak interactions, and a mixing of quantum electrodynamics (QED) and weak isospin symmetry of the isoscalar field components. The mixing between QED and the weak isoscalar field gives rise to the weak mixing angle, the fundamental parameter under investigation in this thesis. The subscript for the U(1)$_Y$ gauge group accounts for this latter mixing, and will be described in Section 1.4. This thesis is focused primarily on the electroweak theory of the SM, and so will concentrate on SU(2)$_L$×U(1)$_Y$ gauge invariance. The unification of the electromagnetic and weak interactions during the 1960's and 1970's was an enormously important event in the creation of the standard model as it predicted the existence of the $W^{\pm}$ and Z^0 bosons which would later be discovered experimentally. Sheldon Glashow, Abdus Salam, and Steven Weinberg were awarded the Nobel Prize in Physics in 1979 for their contributions to understanding electroweak unification.

The dynamics of a physical system can be described independent of any coordinate

system by a mathematical construct known as the *Lagrangian*. In the development of a Lagrangian which is invariant under SU(2)×U(1) gauge transformations one discovers a mixing of two neutral boson fields $A_{\mu 3}$ and B_μ. The former of these two is one of three fields resulting from satisfying the invariance of the Lagrangian under SU(2) gauge transformations, while the latter corresponds to the U(1) gauge invariance of the Lagrangian. It will be shown in Section 1.2 that this mixing is accomplished by means of a parameter known as the *weak mixing angle* or the *Weinberg angle* θ_W. The weak mixing angle is directly related to the relative coupling strengths of the electromagnetic and weak nuclear forces and as such constitutes a central parameter in the standard model. The standard model provides no theoretical prediction for the numerical value of θ_W, but does predict how it will vary with momentum transfer. Experiments conducted at the Z-pole (where the momentum transfer of the experimental probe is equal to the mass of the neutral weak Z^0 boson) determined the value of the weak mixing angle at that momentum transfer to be $\sin^2\theta_W = 0.23151 \pm 0.00016$ [9]. These measurements, along with the standard model-predicted running of $\sin^2\theta_W$ with energy scale, are shown in Figure 1.2

1.1.2 Parity Violation

The isolation of the weak parameter of interest for Q_{weak} requires the measurement of a parity-violating obserbable, and so a brief review of parity is warranted. The parity operator $\hat{P}$ is one that, when acting on the wave function describing a particle (or anti-particle), reverses the momentum but leaves the particle's spin intact:

$$\hat{P}\psi(\vec{p}) = \psi(-\vec{p}) \tag{1.1a}$$

$$\hat{P}\tilde{\psi}(\vec{p}) = -\tilde{\psi}(-\vec{p}), \tag{1.1b}$$

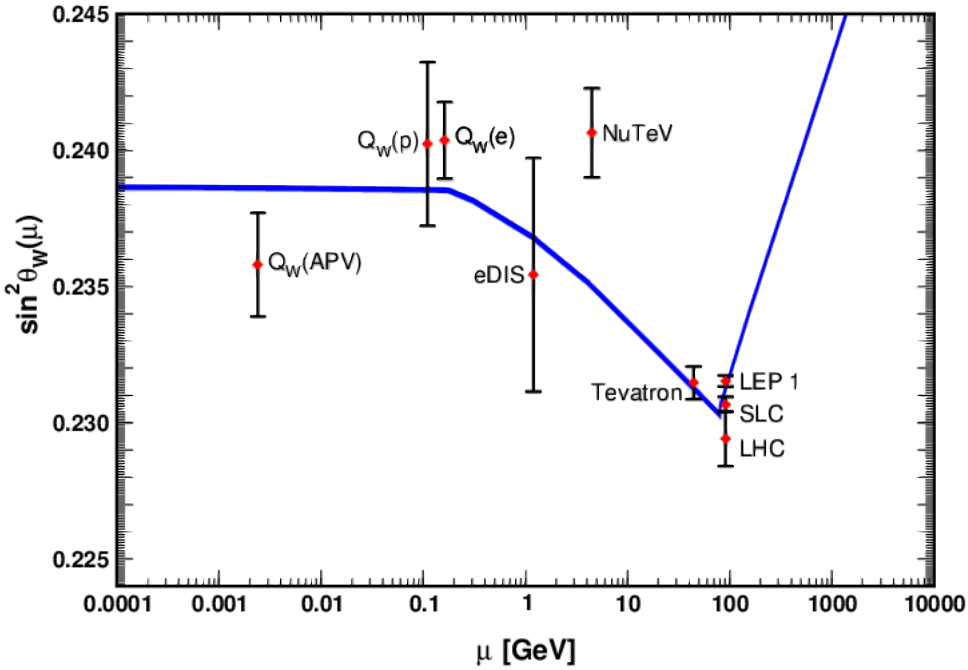

Figure 1.2: The "running" of the weak mixing angle with energy. Measurements at the Z-pole include the point labeled as Tevatron which has been artificially shifted along the horizontal axis to keep the plot uncluttered. The structure of the curve is predicted by the standard model but experimental measurements have been required to anchor the plot on the y-axis.[8] The $Q_w(p)$ point corresponds to an early result from the Q_{weak} experiment[12], using only 4% of the total data set.

where ψ and $\tilde{\psi}$ are the wave-functions for a particle and anti-particle with momentum $\vec{p}$ respectively. Equations 1.1 define particles to have positive parity and anti-particles to have negative parity. Parity-transformed fields are still solutions of the Dirac equation, the relativistic wave equation that describes massive spin-$1/2$ particles. The handedness of a system can be either "left-" or "right-handed," and is defined by the relative direction of the position, momentum, and angular momentum vectors that enter into the description of the system. The space of solutions to the Dirac equation can be decomposed into orthogonal states of this handedness using the projection operators, which will be discussed in detail in Section 1.4. Figure 1.3 illustrates how left- and right-handed fields transform under parity.

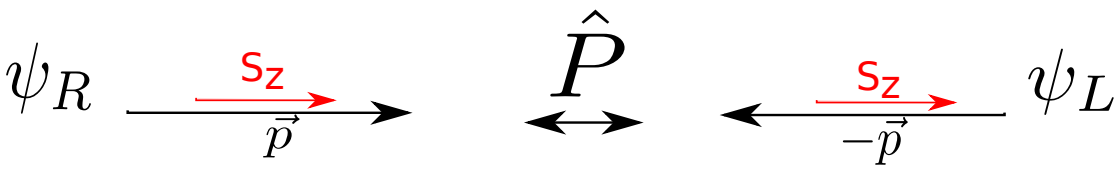

Figure 1.3: An illustration that shows how left-handed and right-handed fields transform under parity. For anti-particles, an additional negative sign on the transformed wave function is present.

If nature makes no distinction between the "handedness" of a process, that process is said to be *parity conserving*. In mathematics a tensor (including scalars and vectors) can be said to be either even or odd under a parity transformation. An even quantity remains unchanged while an odd quantity picks up a negative sign under a parity transformation. Parity odd quantities are called pseudo-scalars, pseudo-vectors (or axial vectors), and pseudo-tensors. The different behavior of left and right-handed fields in the electroweak theory of the standard model will be discussed in detail in Section 1.4.

1.2 Gauge Invariance

This section serves to review how the weak charge of the proton Q_W^p is defined within the standard model. This will be accomplished by a review of the formalism associated

with the electroweak theory and how it arises as a result of the unification of the weak and electromagnetic interactions by requiring invariance under general $SU(2)_L \times U(1)_Y$ gauge transformations. The section will provide a review of gauge transformations, followed by a formal discussion of electroweak unification and spontaneous symmetry breaking as a method for the generation of particle masses. A discussion in complete detail is beyond the scope of this thesis; exhaustive reviews are available in [11] and [13].

1.2.1 Gauge Transformations: U(1)

Consider, as a basic example of a gauge theory, the Lagrangian for a free Dirac fermion field ψ given by

$$\mathcal{L} = \overline{\psi}(i\gamma^\mu \partial_\mu - m)\psi, \tag{1.2}$$

where $\overline{\psi} = \psi^\dagger \gamma^0$ and $\partial_\mu = \partial/\partial x^\mu$[11]. Invariance under U(1) gauge transformations means that this Lagrangian is unchanged by transformations of the form

$$\psi \rightarrow \psi' = e^{i\alpha}\psi$$

and

$$\overline{\psi} \rightarrow \overline{\psi}' = e^{-i\alpha}\overline{\psi}$$

where α can be either a constant, in which case the transformation is called a *global gauge transformation*, or can vary $\alpha = \alpha(x^\mu)$ resulting in a *local gauge transformation.* In order to understand what this invariance means we calculate the variance of the Lagrangian:

$$\begin{aligned}\delta\mathcal{L} &= \frac{\delta\mathcal{L}}{\delta\psi}\delta\psi + \frac{\delta\mathcal{L}}{\delta\partial_\mu\psi}\delta\partial_\mu\psi \\ &= \partial_\mu\frac{\delta\mathcal{L}}{\delta\partial_\mu\psi}\delta\psi + \frac{\delta\mathcal{L}}{\delta\partial_\mu\psi}\partial_\mu\delta\psi\end{aligned} \tag{1.3}$$

where we have used Lagrange's Equation. For an infinitesimal transformation, we can write the following, where a negative sign will be picked up in the case of the complex conjugate $\delta\overline{\psi}$

$$\delta\psi = \psi' - \psi = i\alpha\psi. \tag{1.4}$$

Using Equation 1.4 along with the definition of a current density $J^\mu = -i\frac{\delta\mathcal{L}}{\delta\partial_\mu\psi}\psi$ we find that the Lagrangian variance can be further written as

$$\delta\mathcal{L} = -\left(\partial_\mu\alpha\right)J^\mu - \alpha\partial_\mu J^\mu. \tag{1.5}$$

In the case of a global gauge transformation we have $\partial_\mu\alpha = 0$ which shows that U(1) invariance implies conservation of current: $\delta\mathcal{L} = 0 \implies \alpha\partial_\mu J = 0$. This is an example of Noether's Theorem, which states that a symmetry in the Lagrangian of a system will correspond to a conserved quantity[14]. More care is required in the case of a local gauge transformation where α may vary with time and space. In this case we have

$$\delta\mathcal{L} = -(\partial_\mu\alpha)J^\mu. \tag{1.6}$$

In order to restore the invariance under all U(1) gauge transformations a new interaction term must be introduced into the Lagrangian of Equation 1.2: $\mathcal{L}_I = -eJ_\mu A^\mu$

where A^μ transforms as

$$A^\mu \to A'^\mu = A^\mu - \frac{1}{e}\partial^\mu \alpha, \tag{1.7}$$

resulting in

$$\begin{aligned} \mathcal{L}_I \to \mathcal{L}_I' &= -eJ_\mu A^\mu + J_\mu \partial^\mu \alpha \\ \implies \quad \delta\mathcal{L}_I &= J_\mu \partial^\mu \alpha \end{aligned} \tag{1.8}$$

This is precisely the factor required to cancel out the nonzero variance of the lagrangian present in Equation 1.6, and thus restores invariance under local U(1) gauge transformations.

This new vector gauge field A^μ corresponds to the particle which mediates the electromagnetic interaction, the photon (γ). Since a new field has been introduced into the Lagrangian, radiation terms must also be added. We define the covariant derivative now as a means of maintaining this invariance:

$$D_\mu \psi = (\partial_\mu + ieA_\mu)\psi \tag{1.9}$$

so that the full Lagrangian of quantum electrodynamics can be written as

$$\mathcal{L}_e = \frac{1}{2}\overline{\psi}\left(i\gamma^\mu D_\mu - m\right)\psi - \frac{1}{4}F_{\mu\nu}F^{\mu\nu} \tag{1.10}$$

where the last term corresponds to the previously mentioned radiation term with

$$F_{\mu\nu} = \partial_\mu A_\nu - \partial_\nu A_\mu. \tag{1.11}$$

To verify that this new radiation term does not affect the invariance under U(1) gauge transformations, we recall how A^μ transforms and perform the transformation on

Equation 1.11:

$$\begin{aligned} F'_{\mu\nu} &= \partial_\mu A_\nu - \partial_\nu A_\mu - \frac{1}{e}\left(\partial_\mu\partial_\nu\alpha - \partial_\nu\partial_\mu\alpha\right) \\ &= F_{\mu\nu}. \end{aligned} \tag{1.12}$$

This is the most basic form of a local gauge theory and is to be expanded on in Section 1.2.2 where the weak isospin symmetry imposed by invariance under SU(2) gauge transformations is unified with the above formalism. It is important to note however, that the property of invariance under these local group transformations *requires* the existence of a vector gauge boson and that we did not simply introduce the photon artificially.

1.2.2 SU(2)×U(1) Gauge Invariance

Following the same rationale as above, a new covariant derivative and Lagrangian can be developed which satisfies the weak isospin symmetry imposed by invariance under SU(2) gauge transformations. Since the research in this thesis is focused on the electroweak interaction, we will skip some of the formalism of SU(2) invariance itself and try to immediately tie in the results from the previous section to develop an SU(2)×U(1) invariant framework.

A general SU(2) transformation can be written as

$$\psi \rightarrow \psi' = e^{i\vec{\epsilon}\cdot\vec{t}}\psi \tag{1.13}$$

where $\vec{\epsilon}$ is a three-vector of real parameters that, similar to α above, can be either dependent or independent of space-time resulting in local or global transformations respectively. $\vec{t}$ is defined using the three Pauli spin matrices $t_i = \frac{1}{2}\tau_i$ with

$$\tau_1 = \begin{pmatrix} 0 & 1 \\ 1 & 0 \end{pmatrix}, \quad \tau_2 = \begin{pmatrix} 0 & -i \\ i & 0 \end{pmatrix}, \quad \tau_3 = \begin{pmatrix} 1 & 0 \\ 0 & -1 \end{pmatrix}. \tag{1.14}$$

The generators of SU(2) are the 2x2 Pauli matrices, operating on two component spinors of the form

$$\Phi(\vec{x}) = \begin{pmatrix} \Phi_a \\ \Phi_b \end{pmatrix}. \tag{1.15}$$

Combining the two group transformations we then have an SU(2)×U(1) transformation defined by

$$\Phi \rightarrow \Phi' = e^{i\vec{\epsilon}\cdot\vec{t}+i\alpha}\Phi$$

and

$$\Phi^\dagger \rightarrow \Phi'^\dagger = \Phi^\dagger e^{-i\vec{\epsilon}\cdot\vec{t}-i\alpha}.$$

Just as in the electromagnetic case discussed above, invariance under *local* transformations where $\epsilon_i = \epsilon_i(x)$ is not immediately satisfied in the simple Lagrangian for a Dirac fermion field. In order to restore invariance under combined SU(2)×U(1) transformations we must now introduce *four* gauge fields: one to satisfy the U(1) invariance (which we now denote as B_μ), and three corresponding to the weak isospin symmetry of SU(2) transformations $\vec{W}_\mu$. The introduction of these terms allows us to define the covariant derivative as

$$D_\mu = \partial_\mu + ig\vec{W}_\mu \cdot \vec{t} + \frac{1}{2}ig'B_\mu \tag{1.16}$$

where g and g' now represent two unique coupling constants.

Equation 1.7 already shows how the B_μ term will transform under a U(1) transformation; so we will continue on by determining how the $\vec{W}_\mu$ term will behave under an

SU(2) transformation. For an infinitesimal transformation we have

$$\begin{aligned}
\delta\left(D_\mu\Phi\right) &= \delta\left(\partial_\mu\Phi\right) + ig\delta\left(\vec{W}_\mu\cdot\vec{t}\right)\Phi + ig\vec{W}_\mu\cdot\vec{t}\delta\Phi \\
&= i\partial_\mu\left(\vec{\epsilon}\cdot\vec{t}\Phi\right) + ig\delta\left(\vec{W}_\mu\cdot\vec{t}\right)\Phi + ig\vec{W}_\mu\cdot\vec{t}\delta\Phi \\
&= i\left(\partial_\mu\vec{\epsilon}\right)\cdot\vec{t}\Phi + i\vec{\epsilon}\cdot\vec{t}\partial_\mu\Phi + ig\delta\left(\vec{W}_\mu\cdot\vec{t}\right)\Phi + ig\vec{W}_\mu\cdot\vec{t}\delta\Phi.
\end{aligned} \tag{1.17}$$

Recall at this point the definition of the covariant derivative: a derivative with a functional form that transforms covariantly under SU(2) transformations like ψ itself. In this case, we can equate Equation 1.17 to

$$\delta\left(D_\mu\Phi\right) = i\vec{\epsilon}\cdot\vec{t}D_\mu\Phi \tag{1.18}$$

which results in the following variance for the vector gauge field $\vec{W}_\mu$[11]:

$$\delta\vec{W}_\mu = -\frac{1}{g}\partial_\mu\vec{\epsilon} - \left(\vec{\epsilon}\times\vec{W}_\mu\right). \tag{1.19}$$

If Equation 1.16 is to maintain invariance under local SU(2) gauge transformations, then Equation 1.19 defines how $\vec{W}_\mu$ must transform. This transformation differs from the structure of the U(1) example (where $\delta B_\mu = -\frac{\partial_\mu}{e}\alpha$) in the presence of the cross term. This new term arises from the non-commuting nature of the 2×2 matrices $(\vec{W}_\mu\cdot\vec{t})$ and $(\vec{\epsilon}\cdot\vec{t})$ in Equation 1.17 and defines the invariance under SU(2) transformations as a "non-Abelian gauge theory."

Just as in Section 1.2.1, introducing a new vector gauge field requires the inclusion of radiation terms to the Lagrangian (the $F_{\mu\nu}F^{\mu\nu}$ term in Equation 1.10). For a Lagrangian that is invariant under SU(2) transformations this is accounted for by the *Yang Mills Field*[13]:

$$\mathcal{L}_{\mathrm{YM}} = -\frac{1}{4}\vec{E}_{\mu\nu}\cdot\vec{E}^{\mu\nu} \tag{1.20}$$

where

$$\vec{E}_{\mu\nu} = \partial_\mu \vec{W}_\nu - \partial_\nu \vec{W}_\mu - g\left(\vec{W}_\mu \times \vec{W}_\nu\right). \tag{1.21}$$

By using Equation 1.19 one can show that, as long as it is a massless vector field, this definition of the Yang-Mills Field is invariant under SU(2) gauge transformations.

By including the radiation terms associated with the U(1) and SU(2) formalism, the total Lagrangian is:

$$\mathcal{L} = \left(D_\mu \Phi\right)^\dagger \left(D^\mu \Phi\right) - \frac{1}{4} f_{\mu\nu} f^{\mu\nu} - \frac{1}{4} \vec{E}_{\mu\nu} \cdot \vec{E}^{\mu\nu} \tag{1.22}$$

where the U(1) term has been rewritten using

$$f_{\mu\nu} = \partial_\mu B_\nu - \partial_\nu B_\mu.$$

Upon inspection of our Lagrangian we see immediately that it cannot yet be complete because it has no mass terms corresponding to the massive $W^\pm$ and Z^0 bosons. In quantum electrodynamics this was not a problem: the photon is massless; however, we know that this is not the case for the weak mediators. We proceed in the electroweak formalism by introducing *spontaneous symmetry breaking* as a mechanism for generating particle masses. This will lead to the correct definitions of the $W^\pm$ and Z^0 bosons and will also provide a proper framework for deriving exactly how the electromagnetic and weak interactions become mixed.

1.3 Spontaneous Symmetry Breaking

The primary statement from which spontaneous symmetry breaking derives is as follows: a Lagrangian with degenerate energy states can maintain its invariance even if the states themselves are not invariant for a given transformation. Fields remain solutions

to the same Lagrangian even if they break a symmetry that the Lagrangian obeys[11]. Consider specifically a degenerate ground state of a system where there is no unique lowest energy state. The arbitrary selection of one such degenerate state around which to apply perturbation theory constitutes a breaking of the symmetry of the system. Consider how this would be applied to a field theory describing a real physical system where we already have a common definition of the lowest energy state: the vacuum. Spontaneous symmetry breaking would only be applicable if the vacuum state is one of a set of degenerate states. We then want to be able to choose one such "vacuum" state to serve as the ground state. The invariance of the vacuum under Lorentz translations and rotations requires that the vacuum must be a scalar field $\phi(x) = \phi_0$[11].

The simplest Lagrangian that exhibits the necessary gauge invariances and can illustrate the mechanism of spontaneous symmetry breaking has the form[†]

$$\mathcal{L} = \left(\partial^\mu \phi^*_\mu\right)\left(\partial_\mu \phi^\mu\right) - \mu^2|\phi^\mu|^2 - \lambda|\phi^\mu|^4. \tag{1.23}$$

Equation 1.23, known as the Goldstone model, is invariant under SU(2)×U(1) gauge transformations, has arbitrary real parameters μ and λ, and ϕ which is a complex scalar field that may be used to represent a symmetry-breaking ground state:

$$\phi_\mu(x) = \frac{1}{\sqrt{2}}\left(\phi_{\mu 1}(x) + i\phi_{\mu 2}(x)\right). \tag{1.24}$$

Recall that the definition of a vacuum state is one which corresponds to a field minimizing the energy of the system, given by the Hamiltonian

$$\mathcal{H} = \left(\partial^0 \phi^*_0(x)\right)\left(\partial_0 \phi^0(x)\right) + \vec{\nabla}\phi^*(x) \cdot \vec{\nabla}\phi(x) + V(\phi) \tag{1.25}$$

where the potential V has been defined as the following to adhere to the Hamiltonian structure of $\mathcal{H} = \mathcal{T} + V$:

[†]Note here that the μ-indices correspond to space-time indices and are distinct from the μ mass factor.

$$V = \mu^2|\phi(x)|^2 + \lambda|\phi(x)|^4. \tag{1.26}$$

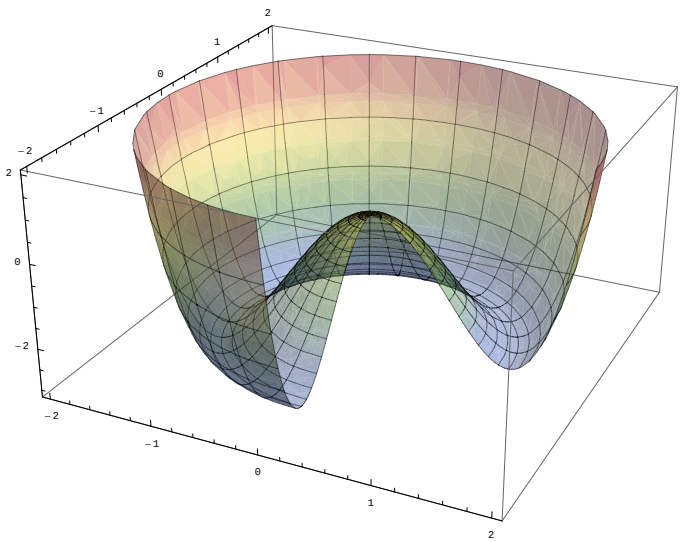

Figure 1.4: A simple visualization of a *Mexican Hat Potential* with $\mu^2 < 0$.

Solutions to this problem can be separated into two possibilities: those with $\mu^2 > 0$ and those with $\mu^2 < 0$ ($\lambda > 0$ is required to avoid the potential being unbounded negatively as opposed to positively). The case where $\mu^2 > 0$ corresponds to that with which we are already comfortable: a potential possessing a single minimum at $\phi(x) = 0$ resulting in a unique ground state incapable of spontaneous symmetry breaking. Figure 1.4 shows that the other case, with $\mu^2 < 0$, possesses a local maximum at $\phi(x) = 0$ and an infinite number of minima corresponding to solutions of the form

$$\phi(x) = \phi_0 = \left(-\frac{\mu^2}{2\lambda}\right)^{\frac{1}{2}} e^{i\theta}, \qquad 0 \leq \theta \leq 2\pi. \tag{1.27}$$

To reiterate, solutions with $\mu^2 < 0$ are degenerate in the value of θ, but since the Lagrangian in Equation 1.23 is independent of θ we are free to chose an arbitrary an-

gle without losing the invariance under U(1) gauge transformations. For the sake of simplicity, we choose $\theta = 0$ such that

$$\phi(x) = \phi_0 = \left(-\frac{\mu^2}{2\lambda}\right)^{\frac{1}{2}} \equiv \frac{1}{\sqrt{2}}v \tag{1.28}$$

with $v = \left(-\mu^2/\lambda\right)^{\frac{1}{2}}$. With this, we can define a unique ground state as

$$< 0|\phi(x)|0 > \frac{1}{\sqrt{2}}v \neq 0. \tag{1.29}$$

1.3.1 Symmetry Breaking in SU(2)×U(1) Unification

Recall the SU(2)×U(1) Lagrangian in Equation 1.22 and add to it the potential introduced above:

$$\mathcal{L} = \left(D_\mu\phi\right)^\dagger (D^\mu\phi) - \mu^2\phi^\dagger\phi - \lambda\left(\phi^\dagger\phi\right)^2 - \frac{1}{4}\vec{E}_{\mu\nu}\cdot\vec{E}^{\mu\nu} - \frac{1}{4}f_{\mu\nu}f^{\mu\nu} \tag{1.30}$$

where D^μ correspond to the definition in Equation 1.16. As was shown in Section 1.3, we find a minimum which corresponds to an isospin doublet of constant scalar fields:

$$\phi(x) = \begin{pmatrix} \phi_a \\ \phi_b \end{pmatrix} \tag{1.31}$$

with

$$\phi^\dagger\phi = |\phi_a|^2 + |\phi_b|^2 = -\frac{\mu^2}{2\lambda}. \tag{1.32}$$

We can, without loss of generality, choose a single direction in isospin space for the ground state to have, so we choose that which corresponds to Equation 1.28

$$\phi_0(x) = \begin{pmatrix} 0 \\ \frac{1}{\sqrt{2}}v \end{pmatrix}. \tag{1.33}$$

We proceed by applying the kinetic energy term $\left(D_\mu\phi\right)^\dagger (D^\mu\phi)$ of the Lagrangian in Equation 1.30 to this state. We use the following

$$D^\mu\phi_0 = \frac{1}{\sqrt{2}}\begin{pmatrix} \partial_\mu + \frac{1}{2}ig'B_\mu + igW_{\mu 3} & \frac{1}{2}ig\left(W_{\mu 1} - iW_{\mu 2}\right) \\ \frac{1}{2}ig\left(W_{\mu 1} + iW_{\mu 2}\right) & \partial_\mu + \frac{1}{2}ig'B_\mu - igW_{\mu 3} \end{pmatrix}\begin{pmatrix} 0 \\ v \end{pmatrix} \tag{1.34}$$

and find

$$\begin{aligned} \left(D_\mu\phi_0\right)^\dagger (D^\mu\phi_0) = \frac{1}{2}\Bigg[&\frac{1}{2}(-ig)v\left(W_{\mu 1} + iW_{\mu 2}\right) \times \frac{1}{2}(ig)v\left(W^{\mu 1} - iW^{\mu 2}\right) \\ &+ \left(\partial_\mu - \frac{1}{2}(ig')B_\mu + \frac{1}{2}(ig)W_{\mu 3}\right)v \times \left(\partial^\mu + \frac{1}{2}(ig')B^\mu - \frac{1}{2}(ig)W_3^\mu\right)v\Bigg] \\ = \frac{1}{8}v^2\left[g^2(W_{\mu 1}W_1^\mu + W_{\mu 2}W_2^\mu) + g^2(W_{\mu 3} - \frac{g'}{g}B_\mu)^2\right]. \end{aligned} \tag{1.35}$$

The first term inside the brackets of Equation 1.35 can be rewritten if we consider a change of basis reminiscent to the quantum mechanical ladder operators, but now using the linear combinations of $W_{\mu i}$. These operators have the form:

$$W_\mu^- = \frac{1}{\sqrt{2}}\left(W_{\mu 1} - iW_{\mu 2}\right) \tag{1.36a}$$

$$W_\mu^+ = \frac{1}{\sqrt{2}}\left(W_{\mu 1} + iW_{\mu 2}\right) \tag{1.36b}$$

such that

$$\frac{1}{2}\left(W_{\mu 1}W_1^\mu + W_{\mu 2}W_2^\mu\right) = W_\mu^+ W^{-\mu}. \tag{1.37}$$

As for the second term of Equation 1.35, we proceed by rewriting it in the following

matrix form:

$$\frac{1}{8}v^2(W_\mu^3, B_\mu)\begin{pmatrix} g^2 & -gg' \\ -gg' & g'^2 \end{pmatrix}\begin{pmatrix} W_\mu^3 \\ B_\mu \end{pmatrix}. \tag{1.38}$$

The 2×2 matrix above has eigenvalues of 0 and $(g + g')$, and the unitary matrix which transforms it into its diagonalized form is

$$S = \frac{1}{\sqrt{g^2 + g'^2}}\begin{pmatrix} g' & g \\ g & -g' \end{pmatrix}. \tag{1.39}$$

The diagonalized form, with the aforementioned eigenvalues on the diagonal, is commonly referred to as the *mass matrix*. By applying S to Equation 1.38, we find (ignoring the $\frac{1}{8}v$ for the moment):

$$\begin{aligned} &(W_{\mu 3}, B_\mu) S S^\dagger \begin{pmatrix} g^2 & -gg' \\ -gg' & g'^2 \end{pmatrix} S S^\dagger \begin{pmatrix} W_\mu^3 \\ B_\mu \end{pmatrix} \\ &= \frac{1}{\sqrt{g^2 + g'^2}}\left(g' W_\mu^3 + g B_\mu, g W_\mu^3 - g' B_\mu\right)\begin{pmatrix} 0 & 0 \\ 0 & g^2 + g'^2 \end{pmatrix}\frac{1}{\sqrt{g^2 + g'^2}}\begin{pmatrix} g' W_\mu^3 + g B_\mu \\ g W_\mu^3 - g' B_\mu \end{pmatrix}. \end{aligned} \tag{1.40}$$

The combinations of fields $W_{\mu 3}$ and B_μ in Equation 1.40 is a key result in this theory. The unification of electromagnetism (U(1)) and weak isospin symmetry (SU(2)) can now be parameterized in terms of the relative coupling strengths g and g' by defining a new parameter, the *weak mixing angle* θ_W as

$$\tan\theta_W = \frac{g'}{g} \tag{1.41}$$

so that the linear combinations of W_μ^3 and B_μ above can be recast into:

$$\frac{g' W_\mu^3 + g B_\mu}{\sqrt{g^2 + g'^2}} = W_\mu^3 \sin\theta_W + B_\mu \cos\theta_W \equiv A_\mu \tag{1.42a}$$

$$\frac{g W_\mu^3 - g' B_\mu}{\sqrt{g^2 + g'^2}} = W_\mu^3 \cos\theta_W - B_\mu \sin\theta_W \equiv Z_\mu. \tag{1.42b}$$

Using the above definitions and gathering the rewritten Equations 1.40 and 1.37 we can write the kinetic term of the electroweak Lagrangian in the following concise form, from which the mass terms of the vector gauge bosons can be read off easily:

$$\begin{aligned}
\left(D_\mu \phi_0\right)^\dagger (D^\mu \phi_0) &= \frac{1}{4} v^2 g^2 W_\mu^+ W^{-\mu} + \frac{1}{8} v^2 (g^2 + g'^2) Z_\mu Z^\mu \\
&= \frac{1}{4} v^2 g^2 W_\mu^+ W^{-\mu} + \frac{1}{8} v^2 \frac{g^2}{\cos^2\theta_W} Z_\mu Z^\mu \\
&= m_W W_\mu^+ W^{-\mu} + \frac{1}{2} m_Z Z_\mu Z^\mu
\end{aligned} \tag{1.43}$$

where the lack of any $m_A A_\mu A^\mu$ term is consistent with having a massless photon as the mediator of the electromagnetic interaction.

The definitions in Equation 1.42 can also be used to rewrite the radiation terms in the electroweak Lagrangian of Equation 1.30. This results in terms corresponding to the radiation energies of the three intermediate vector boson fields and the electromagnetic field, as well as a term corresponding to the self-interaction of the three vector fields $\vec{A}^\mu$:

$$\vec{E}_{\mu\nu} \cdot \vec{E}^{\mu\nu} + f_{\mu\nu} f^{\mu\nu} = F_{\mu\nu} F^{\mu\nu} - \left(W^{+\dagger}_{\mu\nu} W^{+\mu\nu} + W^{-\dagger}_{\mu\nu} W^{-\mu\nu} \right) + Z_{\mu\nu} Z^{\mu\nu}$$
$$+ g^2 \Big[(\vec{W}_\mu \times \vec{W}_\nu) \cdot (\partial^\mu \vec{W}^\nu - \partial^\nu \vec{W}^\mu) + (\partial_\mu \vec{W}_\nu - \partial_\nu \vec{W}_\mu) \cdot (\vec{W}^\mu \times \vec{W}^\nu) \tag{1.44}$$
$$- (\vec{W}_\mu \times \vec{W}_\nu) \cdot (\vec{W}^\mu \times \vec{W}^\nu) \Big] \tag{1.45}$$

where the Yang-Mills self-interaction term is a direct result of the definition of the SU(2) covariant radiation term Equation 1.21.

One could return to Equation 1.33 and insert a perturbative factor $\sigma(x)$ into the ground state such that $\phi_0^\dagger = \frac{1}{\sqrt{2}}(0, v + \sigma(x))$, perform the above derivation again, and the result would include additional terms corresponding to the mass, kinetic energy, and higher order couplings of an additional boson. This is called the *Higgs mechanism* and the new particle is called the Higgs boson: a rigorous treatment of which lies outside the scope of this review.

The Lagrangian formed from combining these last two equations describes the system only as far as the intermediate gauge bosons are concerned. We proceed by considering the matter fields, where invariant Lagrangians will be derived for a subset of the quarks and gluons introduced in Section 1.1. The coupling of these matter fields to the weak neutral gauge boson is defined by the weak mixing angle described in this section, making it the primary theoretical parameter for Q_{weak} .

1.4 Matter Fields

In the previous section we derived the form of the gauge fields for the electroweak interactions and found them to be Lorentz *vectors*. Maintaining Lorentz invariance strongly limits the types of currents which can be used to describe a system, since a

scalar amplitude can only result if the gauge vector fields couple with other vector-like currents. There are two such types of currents that satisfy this criterion: Lorentz vectors and axial-vectors (see Section 1.1.2). These currents take the form:

$$J_V^\alpha = \overline{\psi}\gamma^\alpha\psi \tag{1.46a}$$

$$J_A^\alpha = \overline{\psi}\gamma^\alpha\gamma_5\psi \tag{1.46b}$$

which produce the following possible currents:

$$J_\alpha = J_{\alpha V} \pm J_{\alpha A} = \overline{\psi_\ell}\gamma_\alpha(1 \pm \gamma_5)\psi_{\nu_\ell} \tag{1.47a}$$

$$J_\alpha^\dagger = \overline{\psi_{\nu_\ell}}\gamma_\alpha(1 \pm \gamma_5)\psi_\ell \tag{1.47b}$$

where ℓ and ν_ℓ correspond to the (ν_ℓ, ℓ) weak isospin pair and γ^α are the 4×4 Dirac matrices. The $\gamma^5 = i\gamma^0\gamma^1\gamma^2\gamma^3$ matrix is an useful identity that can be used to define a set of projection operators called *chiral projection operators*. These operators can be used to separate the solutions of the Dirac equation into components that transform under parity as either left- or right-handed fields as shown below:

$$\psi_L = \frac{1}{2}(1 - \gamma_5)\psi \tag{1.48a}$$

$$\psi_R = \frac{1}{2}(1 + \gamma_5)\psi. \tag{1.48b}$$

Experiments have repeatedly demonstrated that of the two general interactions possible, $\overline{\psi}\gamma^\mu(1 + \gamma_5)\psi$ and $\overline{\psi}\gamma^\mu(1 - \gamma_5)$, only the second occurs in charged weak interactions (those involving the charged weak bosons $W^\pm$). This phenomenon is referred to as $\mathcal{V} - \mathcal{A}$ (vector - axial vector) theory and is not a result of the standard model formalism. Since the $\mathcal{V} - \mathcal{A}$ structure matches that of the left-handed projection operator Equation 1.48a, we conclude that only the left-handed currents are observed as isospin

currents whereas right-handed currents must behave as isoscalars:

$$\Psi^L_\ell(x) = \begin{pmatrix} \psi^L_{\nu_\ell(x)} \\ \psi^L_\ell(x) \end{pmatrix}, \qquad \overline{\Psi^L_\ell}(x) = (\overline{\psi^L_{\nu_\ell}}, \overline{\psi^L_\ell}) \tag{1.49a}$$

$$\Psi^R_\ell(x) = \psi^R_\ell(x), \qquad \Psi^R_{\nu_\ell}(x) = \psi^R_\ell(x). \tag{1.49b}$$

The same structure is assumed to hold for weak interactions involving the quarks:

$$\Psi^L_q = \begin{pmatrix} \psi^L_u \\ \psi^L_{d_c} \end{pmatrix}, \begin{pmatrix} \psi^L_c \\ \psi^L_{s_c} \end{pmatrix}, \begin{pmatrix} \psi^L_t \\ \psi^L_{b_c} \end{pmatrix} \tag{1.50}$$

and similar to Equation 1.49b for the right-handed quark currents.

We could then proceed to write the matter field Lagrangian as[‡]

$$\mathcal{L}_e = i\left[\overline{\Psi^L}\partial\!\!\!/\Psi^L + \overline{\psi^R_1}\partial\!\!\!/\psi^R_1 + \overline{\psi^R_2}\partial\!\!\!/\psi^R_2\right] \tag{1.51}$$

where the notation implies that the derivatives act both left and right and the $(1, 2)$ subscripts correspond to the isospin states of the leptons (ν_ℓ, ℓ), or the quarks (u, d_c).

Since it is only the left-handed states which are invariant under SU(2) gauge transformations we write, in analogy to Equation 1.13,

$$\Psi^L(x) \to \Psi'^L(x) = e^{ig\vec{w}\cdot\vec{\tau}}\Psi^L(x) \tag{1.52}$$

where τ is the generator of this transformation, which right-handed states $\Psi^R(x) = \Psi'^R(x) = \psi^R(x)$ are unaffected by. All states, regardless of handedness, are invariant under U(1) gauge transformations:

$$\psi^{L,R}(x) \to \psi'^{L,R} = e^{ig'Yf(x)}\psi^{L,R}(x) \tag{1.53}$$

[‡]The Feynman slash notation is defined as $\partial\!\!\!/ = \gamma^\mu\partial_\mu$.

where Y is generator of the U(1) component of the combined SU(2)×U(1) gauge transformation and is called the *weak hypercharge*.

The covariant derivatives for the left-handed isospinors Ψ^L have a component corresponding to the SU(2) invariance, while both left- and right-handed fields $\psi^{L,R}$ will be invariant under U(1) transformations:

$$\partial^\mu \Psi^L \to D^\mu \Psi^L = \left(\partial^\mu + \frac{1}{2} i g \vec{\tau} \cdot \vec{W}^\mu - \frac{1}{2} i g' Y B^\mu\right) \Psi^L \tag{1.54a}$$

$$\partial^\mu \psi^{L,R} \to D^\mu \psi^{L,R} = \left(\partial^\mu + i g' Y B^\mu\right) \psi^{L,R}. \tag{1.54b}$$

1.4.1 Weak Hypercharge

In order to determine the form of the weak hypercharge we begin by forming an SU(2) gauge invariant current and looking closely at the form of the conserved quantities it implies; that is,

$$J_i^\alpha(x) = \Psi^L(x) \gamma^\alpha \tau_i \Psi^L(x) \tag{1.55}$$

implies the conservation of the *weak isospin charges* defined as [11]:

$$I_i^W = \int d^3x J_i^0(x) = \int d^3x \Psi^{L\dagger}(x) \tau_i \Psi^L(x). \tag{1.56}$$

Two of these three conserved charges correspond to those currents already mentioned in Equations 1.47, but the third current corresponds to the neutral current that couples like isospin states:

$$J_3^\alpha(x) = \frac{1}{2} \overline{\Psi^L}(x) \gamma^\alpha \tau_3 \Psi^L(x) = -\frac{1}{2} \left[\overline{\psi_1^L}(x) \gamma^\alpha \psi_1^L(x) - \overline{\psi_2^L}(x) \gamma^\alpha \psi_2^L(x)\right]. \tag{1.57}$$

Consider the leptonic case for this equation ($1 \to \nu_\ell$, $2 \to \ell$); the second half of

Equation 1.57 then possesses the same structure as the electromagnetic current $S^{\alpha}(x)$ minus the scaling factor $|e|$:

$$S^{\alpha}(x) = -e\overline{\psi}_{\ell}\gamma^{\alpha}\psi_{\ell}(x). \tag{1.58}$$

Finally, we can define the weak hypercharge current and the hypercharge itself as

$$J_Y^{\alpha}(x) = \frac{1}{e}S^{\alpha}(x) - J_3^{\alpha}(x) = -\frac{1}{2}\overline{\Psi^L}(x)\gamma^{\alpha}\Psi^L(x) - \overline{\psi^R}_2(x)\gamma^{\alpha}\psi_2^R(x) \tag{1.59a}$$

$$Y = \int d^3x J_Y^0(x) = \frac{Q}{|e|} - I_3^W, \tag{1.59b}$$

the results of which for the first generation quarks and leptons are tabulated in Table 1.1. The covariant derivatives of Equation 1.54 can now be determined explicitly.

	$Q(e)$	I_3^W	Y
e_L	-1	$-1/2$	$-1/2$
$\nu_{e,L}$	0	$1/2$	$-1/2$
e_R	-1	0	-1
$\nu_{e,R}$	0	0	0
u_L	$2/3$	$1/2$	$1/6$
d_L	$-1/3$	$-1/2$	$1/6$
u_R	$2/3$	0	$2/3$
d_R	$-1/3$	0	$-1/3$

Table 1.1: The electric charge, third component of weak isospin, and weak hypercharge of (first generation) left- and right-handed quarks and leptons.

1.4.2 Gauge-Matter Field Interactions

We are now in a position to derive the Lagrangian which describes interactions between the gauge fields of Sections 1.2 and 1.3 and the matter fields of Section 1.4. For the sake of simplicity and clarity, we will restrict the formalism to that associated with lepton fields and omit a rigorous treatment of quark interactions. This is appropriate in the context of Q_{weak} , where the kinematics (See Chapter 2) have been chosen to select

out those events with the axial coupling (the parity odd piece) at the electron vertex as opposed to the quark/proton vertex.

The Lagrangian in question can be written in a general form as[§]

$$\mathcal{L} = i\left[\overline{\Psi^L_\ell}\not{D}^\mu_{L,\ell}\Psi^L_\ell + \overline{\psi^R_{\nu_\ell}}\not{D}^\mu_{R,\nu_\ell}\psi^R_{\nu_\ell} + \overline{\psi^R_\ell}\not{D}^\mu_{R,\ell}\psi^R_\ell\right]. \tag{1.60}$$

where we recall that L, R subscripts correspond to left- and right-handed components, (ν_ℓ, ℓ) are the isospin pair that populate the left-handed isospinors, and μ are the standard Dirac indices.

Substituting values from Table 1.1 into Equation 1.54 leaves us with the following interaction terms:

$$\mathcal{L}^{\text{int}} = i\overline{\Psi^L_\ell}\gamma_\mu\left(\frac{1}{2}ig\vec{\tau}\cdot\vec{W}^\mu - \frac{1}{2}ig'B^\mu(x)\right)\Psi^L_\ell + i\overline{\psi^R_\ell}\gamma_\mu\left(-ig'B^\mu(x)\right)\psi^R_\ell. \tag{1.61}$$

Now recall the definitions of the vector gauge fields Z_μ, A_μ, W^+_μ, and W^-_μ from Section 1.3.1 and substitute them into Equation 1.61:

$$\begin{aligned}\mathcal{L}^{\text{int}} =& i(\overline{\psi^L_{\nu_\ell}}, \overline{\psi^R_\ell})\gamma_\mu\begin{pmatrix}\frac{1}{2}\left(igW_{\mu3} - ig'B_\mu\right)\psi^L_{\nu_\ell} + \frac{1}{2}ig\left(W_{\mu1} - iW_{\mu2}\right)\psi^L_\ell \\ \frac{1}{2}ig\left(W_{\mu1} + iW_{\mu2}\right)\psi^L_{\nu_\ell} + \frac{1}{2}\left(-igW_{\mu3} - ig'B_\mu\right)\psi^L_\ell\end{pmatrix} \\ &+ i\overline{\psi^R_\ell}\gamma^\mu(-i)B_\mu\psi^R_\ell\end{aligned} \tag{1.62}$$

[§]Recall that the gauge fields are buried in the definition of the covariant derivative $\not{D}^\mu$.

$$\mathcal{L}^{\text{int}} = -\overline{\psi^L_{\nu_\ell}}\gamma^\mu \frac{g}{2\cos\theta_W} Z_\mu \psi^L_{\nu_\ell} - \overline{\psi^L_{\nu_\ell}}\gamma^\mu \frac{g}{\sqrt{2}} W^-_\mu \psi^L_\ell \tag{1.63}$$

$$- \overline{\psi^L_\ell}\gamma^\mu \frac{g}{\sqrt{2}} W^+_\mu \psi^L_{\nu_\ell} + \overline{\psi^L_\ell}\gamma^\mu \frac{g}{2\cos\theta_W}\left(1 - 2\sin^2\theta_W\right) Z_\mu \psi^L_\ell \tag{1.64}$$

$$+ \overline{\psi^L_\ell}\gamma^\mu g \sin\theta_W A_\mu \psi^L_\ell + \overline{\psi^R_\ell}\gamma^\mu g \sin\theta_W A_\mu \psi^R_\ell \tag{1.65}$$

$$- \overline{\psi^R_\ell}\gamma^\mu \frac{g\sin^2\theta_W}{\cos\theta_W} Z_\mu \psi^R_\ell. \tag{1.66}$$

The next step is to use the definition of the projection operators from Section 1.4 to expand $\psi^{L,R}$, resulting in the following gauge-matter field interaction Lagrangian:

$$\begin{aligned}\mathcal{L}^{\text{int}} =& \frac{-g}{2\sqrt{2}}\overline{\psi_{\nu_\ell}}\gamma^\mu\left(1-\gamma_5\right)\psi_\ell W^-_\mu - \frac{g}{2\sqrt{2}}\overline{\psi^\ell}\gamma^\mu\left(1-\gamma_5\right)\psi_{\nu_\ell} W^+_\mu \\ &- \frac{g}{4\cos\theta_W}\left[\overline{\psi_{\nu_\ell}}\gamma^\mu\left(1-\gamma_5\right)\psi_{\nu_\ell} - \overline{\psi_\ell}\gamma^\mu\left(1-4\sin^2\theta_W-\gamma_5\right)\psi_\ell\right] Z_\mu \\ &- |e|\overline{\psi_\ell}\gamma^\mu\psi_\ell A_\mu\end{aligned} \tag{1.67}$$

where the first line corresponds to the charged weak currents, the second contains the neutral weak current terms, and the third line accounts for the electromagnetic current. By repeating the above derivation using the weak hypercharge of the quarks, a similar form can be derived for the electroweak gauge-matter field interaction Lagrangian for quarks.

Choosing now to focus on developing the formalism for parity violating elastic electron-proton scattering, we proceed by looking only at those Lagrangians corresponding to neutral current interactions with electrons and up, down, or strange quarks. The analogs for the last two lines of Equation 1.67 (labeled here as $\mathcal{L}^{\text{NC}}_j$ for particle j) for these specific particles can be determined by using Table 1.1 and Equation 1.54:

$$\mathcal{L}_e^{\mathrm{NC}} = -\frac{g}{4\cos\theta_W}\overline{\psi_e}\gamma^\mu\left(1 - 4\sin^2\theta_w - \gamma_5\right)\psi_e Z_\mu - g\sin\theta_W\overline{\psi_e}\gamma^\mu\psi_e A_\mu \tag{1.68a}$$

$$\mathcal{L}_u^{\mathrm{NC}} = -\frac{g}{4\cos\theta_W}\overline{\psi_u}\gamma^\mu\left(-1 + \frac{8}{3}\sin^2\theta_W + \gamma_5\right)\psi_u Z_\mu + g\frac{2}{3}\sin\theta_W\overline{\psi_u}\gamma^\mu\psi_e A_\mu \tag{1.68b}$$

$$\mathcal{L}_{d_c,s_c}^{\mathrm{NC}} = -\frac{g}{4\cos\theta_W}\overline{\psi_{d_c,s_c}}\gamma^\mu\left(1 - \frac{4}{3}\sin^2\theta_W - \gamma_5\right)\psi_{d_c,s_c} Z_\mu - g\frac{1}{3}\sin\theta_W\overline{\psi_{d_c,s_c}}\gamma^\mu\psi_{d_c,s_c} A_\mu. \tag{1.68c}$$

1.5 Neutral Current Form Factors and Weak Charges

In this section we introduce the neutral current form factors of the proton and neutron and show how they give the weak charges, in the limit of $Q^2 \to 0$.

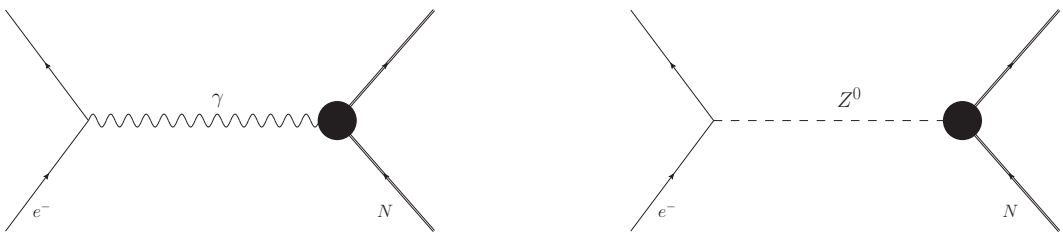

(a) Photon exchange. (b) Z boson exchange.

Figure 1.5: Tree-level diagrams illustrating the neutral current exchanges made possible due to the electromagnetic and weak interactions.

Begin by writing down the general neutral currents associated with the electron vertices in Figure 1.5 in which we introduce the vector and axial vector coupling constants g_V and g_A:

$$j_{\gamma,e}^\mu = \overline{\psi_e} e\gamma^\mu\psi_e \tag{1.69a}$$

$$j_{Z,e}^\mu = \overline{\psi_e}\gamma^\mu\left(g_{V,e} + g_{A,e}\gamma_5\right)\psi_e \tag{1.69b}$$

where e is the electric charge of the electron.

	g_V	g_A
e	$-1 + 4\sin^2\theta_W$	1
u	$1 - \frac{8}{3}\sin^2\theta_W$	-1
d,s	$-1 + \frac{4}{3}\sin^2\theta_W$	1

Table 1.2: The vector and axial vector weak couplings of the electron and up, down, and strange quarks.

We can now compare the forms of equations 1.68 and 1.69 to determine the values for the vector and axial vector coupling constants in terms of the weak mixing angle. The results are shown in Table 1.2, where we recall that these values are only accurate to tree level: where only those lowest level processes in Figure 1.5 are considered.

At lowest order, the weak charges of the standard model particles are written in terms of the *weak vector quark couplings*, C_{1i}, C_{2i} for quarks i, defined as[8]

$$C_{1i} = -\frac{1}{2}g_{V,i} \tag{1.70a}$$

$$C_{2i} = \frac{1}{2}g_{A,i}(1 - 4\sin^2\theta_W). \tag{1.70b}$$

The hadronic neutral current can also be written, but in this case the internal structure of the nucleon must be taken into consideration. This is accomplished by introducing the Dirac, Pauli, and Axial form factors F_1, F_2, and G_A respectively:

$$J^{\mu}_{\gamma,N} = \overline{\psi_N}\left[\gamma^{\mu}F_1^{\gamma N}(Q^2) + \frac{i\sigma^{\mu\nu}q_{\nu}}{2M}F_2^{\gamma N}(Q^2)\right]\psi_N \tag{1.71a}$$

$$J^{\mu}_{Z,N} = \overline{\psi_N}\left[\gamma^{\mu}F_1^{ZN}(Q^2) + \frac{i\sigma^{\mu\nu}q_{\nu}}{2M}F_2^{ZN}(Q^2) + \gamma^{\mu}\gamma_5 G^{ZN}(Q^2)\right]\psi_N \tag{1.71b}$$

The underlying physics represented by this formalism becomes more apparent when re-casting Equation 1.71 using the electric and magnetic Sachs form factors G_E, G_M which describe the charge and magnetization distributions of the nucleon respectively.

They are related to the Dirac and Pauli form factors by [15],[16].

$$G_E^{\gamma N}(Q^2) = F_1(Q^2) - \frac{Q^2}{2M}F_2(Q^2) \tag{1.72a}$$

$$G_M^{\gamma N}(Q^2) = F_1(Q^2) + F_2(Q^2). \tag{1.72b}$$

Alternatively to this redefinition, one could proceed from Equation 1.71 by decomposing the form factors into individual terms for each of the nucleon's constituent quarks. In doing this, we include the strange quark content that arises from $s\bar{s}$ pairs generated from the quark sea. We thus write:

$$F_{1,2}^{\gamma N} = \sum_j Q_j F_{1,2}^{\gamma j} \qquad F_{1,2}^{ZN} = \sum_j g_v^j F_{1,2}^{Zj} \qquad G_A^Z = \sum_j g_A^j G_A^{Zj} \tag{1.73}$$

where the j index runs over up, down, and strange quarks. Having done this, we can now write the electromagnetic and weak nucleon form factors in terms of the electromagnetic charges and weak vector and axial vector coupling constants of the quarks from Table 1.2. Adopting the Sachs notation for the result provides us with the following form factor expressions for the proton in terms of quark properties:

$$G_{E,M}^{\gamma p} = \frac{2}{3}G_{E,M}^u - \frac{1}{3}\left(G_{E,M}^d + G_{E,M}^s\right) \tag{1.74a}$$

$$G_{E,M}^{Zp} = \left(1 - \frac{8}{3}\sin^2\theta_W\right)G_{E,M}^u - \left(1 - \frac{4}{3}\sin^2\theta_W\right)\left(G_{E,M}^d + G_{E,M}^s\right) \tag{1.74b}$$

$$G_A^Z = -G_A^u + G_A^d + G_A^s. \tag{1.74c}$$

A number of different parameterizations for the electromagnetic form factors $G_{E,M}^{\gamma N}$ have been extracted by various groups over the last decade[7][17][18][19]. A review of these parameterizations and how they contribute to the extraction of Q_W^p alongside

other assumptions about proton form factors will be discussed in Chapter 5.

From Equation 1.74a it is clearly evident that electric form factors for the quarks $G^{j}_{E,M}$ correspond simply to the number of quarks with flavour j in the nucleon of question. For the proton (uud) and neutron (udd) we can then write Equation 1.74b as:

$$G_E^{Zp}(Q^2 = 0) = Q_W^p = 1 - 4\sin^2\theta_W \tag{1.75a}$$

$$G_E^{Zn}(Q^2 = 0) = Q_W^n = -1. \tag{1.75b}$$

Equation 1.75a defines the weak charge of the proton in terms of the weak mixing angle. Simply put, it is a measure of how strongly the proton couples to weak currents. This result can also be recast in the basis of the weak vector quark couplings in Equation 1.70:

$$Q_W^p = -2(2C_{1u} + C_{1d}) \tag{1.76a}$$

$$Q_W^n = -2(2C_{1d} + C_{1u}). \tag{1.76b}$$

1.6 Parity Violating $\vec{e}p$ Scattering Asymmetry

The electromagnetic and weak scattering amplitudes have tree-level expressions given by:

$$\begin{aligned} \mathcal{M}_\gamma &= -\frac{e^2}{Q^2} j^{\mu}_{\gamma,e} J^{\gamma,N}_{\mu} \\ \mathcal{M}_Z &= -\frac{G_F}{2\sqrt{2}} j^{\mu}_{Z,e} J^{Z,N}_{\mu} \end{aligned} \tag{1.77}$$

with currents defined in Equations 1.69 and 1.71. The tree level cross-section for elastic $\vec{e}p$ scattering is proportional to the quadrature sum of these amplitudes:

$$\sigma_{L,R} \propto |\mathcal{M}|^2 = |\mathcal{M}_\gamma + \mathcal{M}_Z|^2 = |\mathcal{M}_\gamma|^2 + |\mathcal{M}_Z|^2 + 2\Re\left(\mathcal{M}_\gamma^* \mathcal{M}_Z\right). \tag{1.78}$$

In this representation, the L, R subscripts correspond to left- and right-handed incident electrons and only the last term will change sign as the helicity changes. This is clear when considering how the currents in Equations 1.69 and 1.71 transform under parity: the γ_5 terms pick up a sign flip. We exploit the presence of this sign flip by calculating a helicity-correlated asymmetry. The fact that the electromagnetic interaction is a parity-conserving process results in the first term of Equation 1.78 vanishing in the difference below:

$$A_{\mathrm{PV}}^{\mathrm{ep}} = \frac{(d\sigma/d\Omega)_R - (d\sigma/d\Omega)_L}{(d\sigma/d\Omega)_R + (d\sigma/d\Omega)_L}. \tag{1.79}$$

The second term in Equation 1.78 also vanishes under parity, since the sign flip will occur twice. The final term provides an access point to the weak interaction that is magnified by its interference with the much larger amplitude electromagnetic interaction. As a result, the asymmetry can be written in terms of these amplitudes, where $\mathcal{M}_Z^{\mathrm{PV}}$ is the parity violating portion of the weak amplitude:

$$A_{\mathrm{PV}}^{\mathrm{ep}} = \frac{2\mathcal{M}_\gamma^* \mathcal{M}_Z^{\mathrm{PV}}}{|\mathcal{M}_\gamma|^2 + |\mathcal{M}_Z^{\mathrm{PV}}|^2 + 2\Re\left(\mathcal{M}_\gamma^* \mathcal{M}_Z^{\mathrm{PV}}\right)} \sim \frac{2\mathcal{M}_\gamma^* \mathcal{M}_Z^{\mathrm{PV}}}{|\mathcal{M}_\gamma|^2}. \tag{1.80}$$

Using the currents and form factor formalism introduced in Section 1.5 we can write[20]:

$$A_{\mathrm{PV}}^{\mathrm{ep}} = -\left(\frac{G_F Q^2}{4\pi\alpha\sqrt{2}}\right)\left[\frac{\epsilon G_E^{\gamma p} G_E^{Zp} + \tau G_M^{\gamma p} G_M^{Zp} - \left(1 - 4\sin^2\theta_W\right)\epsilon' G_M^{\gamma p} G_A^Z}{\epsilon\left(G_E^{\gamma p}\right)^2 + \tau\left(G_M^{\gamma p}\right)^2}\right] \tag{1.81}$$

with kinematic factors

$$\epsilon = \left(1 + 2\,(1+\tau)\tan^2\frac{\theta}{2}\right)^{-1}$$
$$\tau = \frac{Q^2}{4M^2}$$
$$\epsilon' = \sqrt{\tau\,(1+\tau)\,(1-\epsilon^2)}.$$

If one performs the experiment at low momentum transfer[¶] Q^2 and forward lab scattering angles θ, the expression can be simplified to the following expression, where $B(Q^2)$ is a hadronic form factor term that contains the Sachs form factors:

$$A_{\mathrm{PV}}^{\mathrm{ep}} = -\left(\frac{G_F Q^2}{4\pi\alpha\sqrt{2}}\right)\left(Q_W^p + Q^2 B(Q^2,\theta)\right). \tag{1.82}$$

The "B-term" here acts as a Q^2- and θ-dependent form factor that accounts for contributions from hadronic structure[2][16]. The weak charge of the proton can then be extracted by measuring the parity-violating asymmetry and momentum transfer, with the hadronic effects being determined by previous experiments[21][22][23][24][25].

1.7 Motivation for Q_{weak}

The primary goal of the Q_{weak} experiment is to perform the first high precision measurement of the proton's weak charge Q_W^p. The measurement is potentially sensitive to new parity violating physics beyond the standard model as a result of the suppressed nature of Q_W^p as shown in Table 1.3. Performing a precise measurement of a small coupling like Q_W^p is easier than attempting to make a part-per-billion measurement of a large coupling. Q_{weak} is a "semi-leptonic" experiment that provides complementary results

[¶]Throughout this thesis, Q^2 will be referred to as the momentum transfer as opposed to the momentum transfer squared. This language is commonly used within the experimental community.

	Q_{EM}	Q_W^p
u	$\frac{2}{3}$	$1 - \frac{8}{3}\sin^2\theta_W = 0.383$
d	$-\frac{1}{3}$	$-1 + \frac{4}{3}\sin^2\theta_W = -0.692$
p	1	$1 - 4\sin^2\theta_W = 0.075$
n	0	-1

Table 1.3: Comparing the relative sizes of the electric and weak charges of the first generation quarks and the nucleons. Weak charges are computed using $\sin^2\theta_W = 0.23126$[8].

to past (The SLAC E-158 experiment [26]) and future (the JLab MOLLER experiment [27]) purely leptonic measurements performed at low momentum transfer.

Q_W^p is not by itself a fundamental standard model quantity, but its measurement provides information about the weak mixing angle $\sin^2\theta_W$ and the weak vector quark couplings C_{1u}, C_{1d}. The energy-scale evolution of the weak mixing angle presented in Figure 1.2 shows a lack of high precision measurements at low Q^2; a 4% measurement of Q_W^p constitutes a 0.3% error on the extraction of $\sin^2\theta_W$ which would be the highest precision measurement of the weak mixing angle off the Z-pole.

Recall from Equation 1.76 that the proton's weak charge can be written as a linear combination of the weak vector quark couplings. A measurement of one combination, such as Q_W^p, is obviously insufficient to extract values for the couplings, but it can provide bounds on how the two couplings can be related to each other. Figure 1.6 displays the status of the isoscalar ($C_{1u} + C_{1d}$) and isovector ($C_{1u} - C_{1d}$) combinations allowed by the current world data set. Parity violating electron scattering (PVES) measurements provide complementary bounds to atomic parity non-conservation measurements and, because of this, $\mathrm{Q_{weak}}$ will provide data that can be used alongside other results in order to provide extractions for these couplings, as well as the neutron's weak charge Q_W^n.

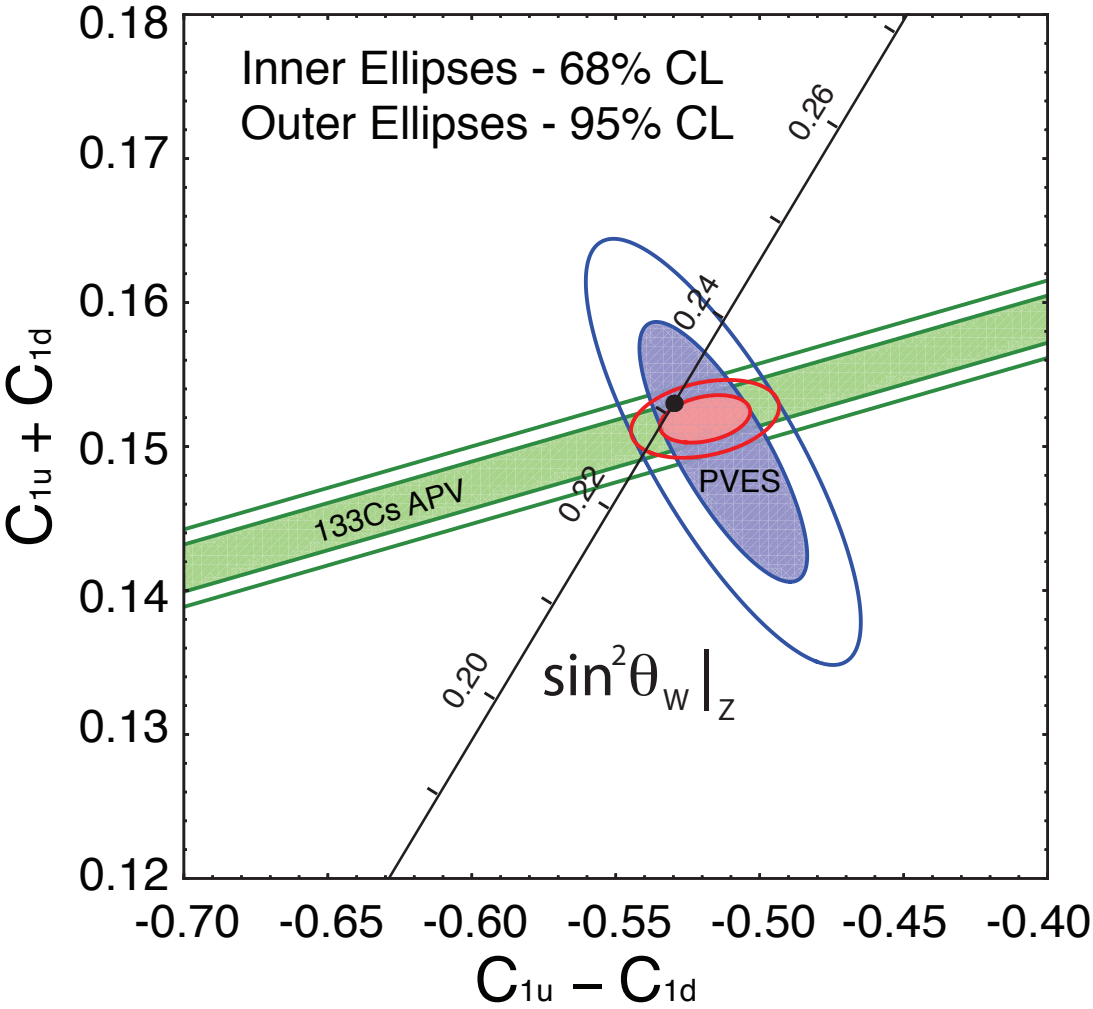

Figure 1.6: Constraints on the isoscalar and isovector combinations of the weak vector couplings using atomic parity violating and parity violating electron scattering experiments. An early Q_{weak} point[12] is included in the calculation of the blue band. Agreement is observed between the standard model prediction (black dot) and the combination of APV and PVES data (red ellipse). The diagonal axis corresponds to the value of the weak mixing angle at the Z-pole.

1.7.1 Physics Beyond the Standard Model

As a high precision test of the standard model, Q_{weak} is sensitive to certain types of new parity violating physics. In order to quantify the level of sensitivity to SM-extensions, we consider the model-independent analysis outlined in [2] by defining a new Lagrangian:

$$\mathcal{L} = \mathcal{L}_{\mathrm{SM}}^{\mathrm{PV}} + \mathcal{L}_{\mathrm{NEW}}^{\mathrm{PV}}. \tag{1.83}$$

In this formalism, we write $\mathcal{L}_{\mathrm{SM}}^{\mathrm{PV}}$ in terms of the C_{1q} couplings and propose constants to parameterize the new PV physics:

$$\mathcal{L}_{\mathrm{SM}}^{\mathrm{PV}} = -\frac{G_F}{\sqrt{2}}\overline{\psi_e}\gamma_\mu\gamma_5\psi_e \sum_q C_{1q}\overline{\psi_q}\gamma^\mu\psi_q \tag{1.84a}$$

$$\mathcal{L}_{\mathrm{NEW}}^{\mathrm{PV}} = \frac{g^2}{4\Lambda^2}\overline{\psi_e}\gamma_\mu\gamma_5\psi_e \sum_f h_V^q\overline{\psi_q}\gamma^\mu\psi_q. \tag{1.84b}$$

In Equation 1.84b we have introduced constants g, Λ, and h_V^q corresponding to the new physics coupling constant, appropriate mass scale, and coefficients respectively. In the absence of any new physics we have[‖]

$$Q_W^p(\mathrm{New}) = Q_W^p(\mathrm{SM}) - Q_W^p(\mathrm{Exp}) = 0 \tag{1.85a}$$

$$\delta Q_W^p(\mathrm{New}) = \delta Q_W^p(\mathrm{Exp}). \tag{1.85b}$$

and a lower limit mass reach can be quantified, assuming unity for both the h_V^q and g parameters, using

[‖]We assume here that there is no error in the standard model calculations. This is of course not true, but the experimental errors bars will dominate this expression.

$$\Lambda \sim \frac{1}{\sqrt{2\sqrt{2}G_F}} \cdot \frac{1}{\sqrt{\delta Q_W^p(\mathrm{Exp})}}. \tag{1.86}$$

For instance, a 4% measurement agreeing with the standard model value of ~ 0.0712 implies, at a 95% confidence level, a mass reach of ~ 2.3 TeV. There currently exists a controversy within the experimental community with regards to what value to choose for the coupling constant g and how to therefore quote mass limits; some groups[28] [29] have opted for a choice of $g = 4\pi$, claiming that it more appropriately accounts for possible types of new physics corresponding to an internal structure of quarks and leptons. In such a regime, the quoted mass scales correspond not to the mass of new particles, but to the binding energies of the involved quarks and leptons; Q_{weak} provides a lower limit for this compositeness scale of ~ 33 TeV in this model[28].

The specific standard model extensions discussed in [2] include the existence of a new neutral gauge boson (Z'), leptoquarks, and the extended gauge symmetry known as supersymmetry (SUSY). Figure 1.8 displays the relative sensitivities to these types of new physics based on early estimates for the experimental errors for Q_{weak} and the purely leptonic SLAC E-158[26] experiment. If one or both experiments measure quantities that disagree with the standard model, the extent to which their deviations are correlated could give insight into which of these possible models have merit.

Considering the possible effects of supersymmetry along with the known radiative corrections, one can write out an expression for Q_W^p in terms of these new physics effects[2]:

$$Q_W^p = [\rho_{\mathrm{NC}} + \Delta_e + \Delta\rho_{\mathrm{SUSY}}][1 - 4\sin^2\hat{\theta}_W(0) + \Delta_e'] + \Box_{WW} + \Box_{ZZ} + \Box_{\gamma Z} + \lambda_{\mathrm{SUSY}}, \tag{1.87}$$

where λ_{SUSY} ($\Delta\rho_{\mathrm{SUSY}}$) contains all flavour-independent (dependent) SUSY corrections, and $\sin^2\hat{\theta}_W(0)$ includes corrections to the weak mixing angle from supersymme-

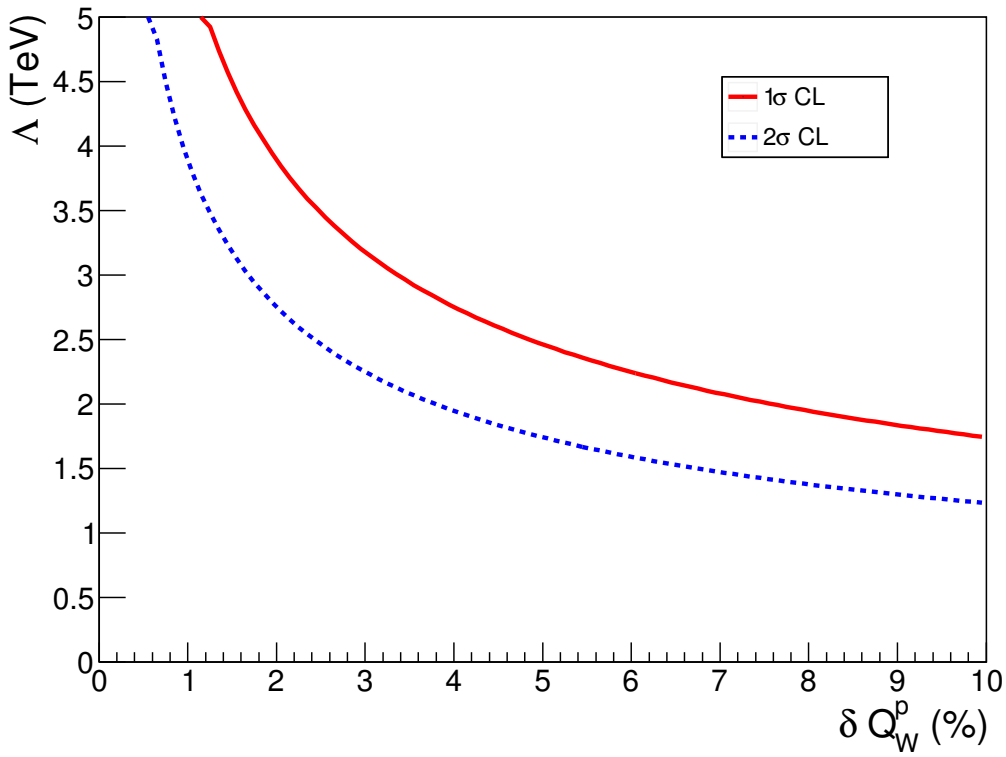

Figure 1.7: Lower bounds on the mass scale for new physics as a function of relative precision of the weak charge measurement. The solid (dashed) line corresponds to 1σ (2σ) confidence levels and assume that the weak charge measurement agrees with the standard model.

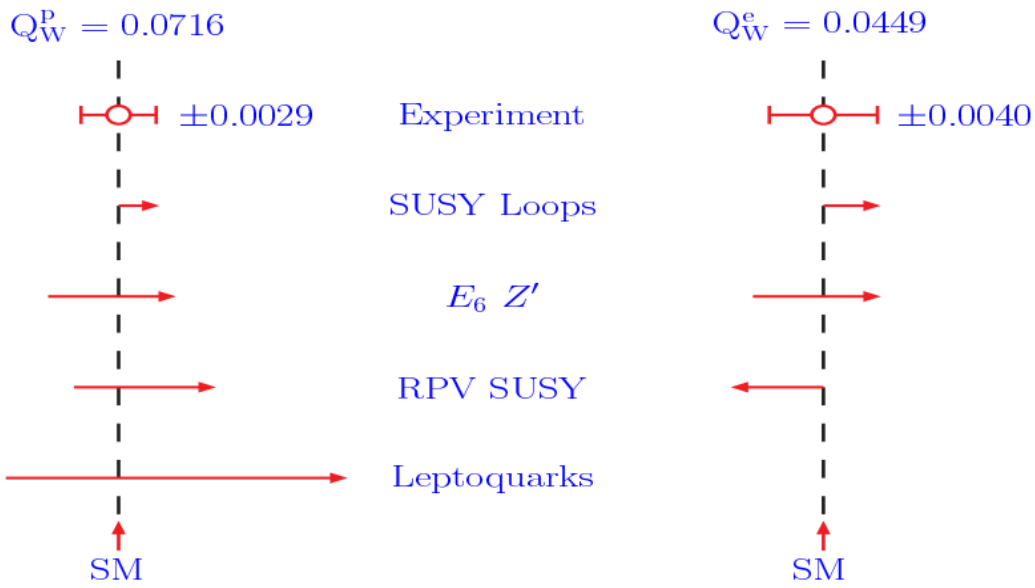

Figure 1.8: Comparing early expectations for experiment precisions with the size of deviations from the standard model that were allowed at 95% confidence level at the time of reference [2].

try. The other parts of the Equation 1.87 that do not correspond to new physics are equally important for the primary asymmetry measurement and correspond to radiative corrections: ρ_{NC} serves to renormalize the ratio of neutral to charged current interactions at low energies, Δ_e and Δ'_e provide corrections to the Zee and γee couplings respectively, and the $\square$ terms correct for the box diagrams in Figure 1.9.

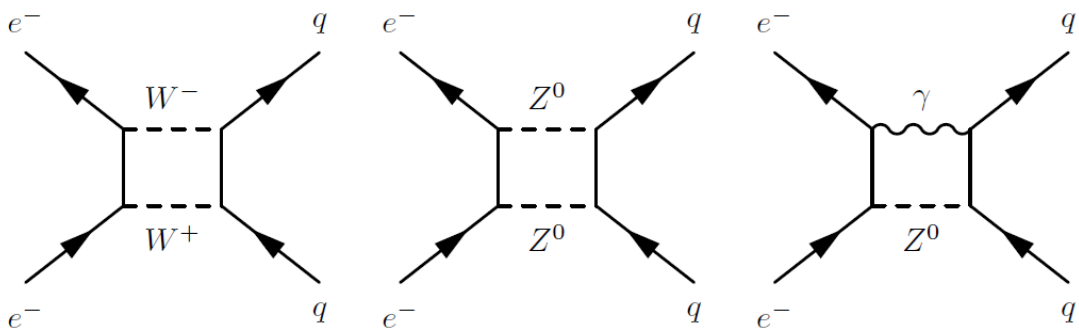

Figure 1.9: Purely weak ($\square_{WW}$ and $\square_{ZZ}$) and electroweak ($\square_{\gamma Z}$) box diagrams appropriate for PVES. The first two result in very small corrections to the weak charge[2] and the $\square_{\gamma Z}$ correction has been very well calculated[30][31].

1.8 Summary

The weak charge of the proton is related to the fundamental parameter $\sin^2\theta_W$ and is suppressed in the standard model. A high precision measurement of Q_W^p, when combined with measurements from purely leptonic and atomic sector measurements, can provide constraints on certain types of new parity violating physics.

Chapter 2

Experiment

2.1 Overview

The Q_{weak} experiment (E08-016)[6] ran from July 2010 through May 2012 in Experimental Hall-C at the Thomas Jefferson National Accelerator Facility (Jefferson Lab). The world's first dedicated measurement of the proton's weak charge Q_W^p was performed by measuring the parity-violating asymmetry associated with elastic electron-proton scattering. An entirely new experimental apparatus was installed at Jefferson Lab, where a history of successful parity experiments has resulted in the necessary infrastructure for such a measurement to be performed. The proposed uncertainty budget for the experiment, taken from the proposal document[6] is reproduced in Table 2.1. Typical running parameters, including beam current, energy, and the average acceptance kinematics of the apparatus are listed in Table 2.2. This chapter will serve to describe the Q_{weak} apparatus in detail, along with the general experimental methodology.

A rendering of the Q_{weak} apparatus from GEANT4 simulations is shown in Figure 2.2. The primary components of the Q_{weak} experiments included a highly polarized electron beam with rapidly reversing helicity, a target system, a collimation and magnetic spectrometer system, and a number of detector subsystems including the primary

Source of Error	Contribution to $\Delta A_{\text{phys}}/A_{\text{phys}}$	Contribution to $\Delta Q_W^p/Q_W^p$
Counting Statistics	2.1%	3.2%
Hadronic Structure	-	1.5%
Beam Polarimetry	1.0%	1.5%
Absolute Q^2	0.5%	1.0%
Backgrounds	0.5%	0.7%
Helicity-Correlated Beam Properties	0.5%	0.7%
Total	2.5%	4.1%

Table 2.1: Proposed experimental uncertainties for the Q_{weak} experiment[6].

Parameter	Value
Incident Beam Energy	1.165 GeV
Beam Polarization	85+%
Beam Current	180 μA
LH_2 Target Thickness	35 cm
Primary Events	$\sim$ 1.4 billion
Nominal Scattering Angle	7.9°
Scattering Angle Acceptance	±3°
ϕ-Acceptance	49% of 2π
Solid Angle	Ω = 37 msr
Acceptance-Averaged Q^2	$< Q^2 >= 0.026$ (GeV/c)^2
Integrated Rate (all octants)	6.5 GHz

Table 2.2: A summary of the basic parameters of the Q_{weak} experiment.

quartz bar Čerenkov detectors, luminosity monitors, and auxiliary background monitors. These systems will each be described in detail, with Chapter 3 dedicated to the main detector subsystem specifically. The coordinate system of the experiment is shown in Figure 2.3 where the detectors are numbered by octant, starting with octant one located beam left and increasing clockwise.

The main asymmetry measurement was carried out by scattering longitudinally polarized electrons from protons in an unpolarized liquid hydrogen target, and then steering them onto a set of 2 m long Čerenkov detectors. The electron helicity, defined by whether the spin and momentum vectors are parallel or anti-parallel, was changed at a rate of 960 Hz. The asymmetry was then measured by performing a time integration of the photomultiplier tube (PMT) signal over periods of constant beam helicity and computing the beam current-normalized difference of consecutive measurements with opposite helicity states. This is shown formally in Equation 2.1 where $Y^{L,R}$ correspond to the detector yield during periods with left- (anti-parallel) or right-handed (parallel) helicity:

$$A^{\text{raw}} = \frac{Y^R - Y^L}{Y^R + Y^L}. \tag{2.1}$$

For the Q_{weak} experiment, asymmetries were calculated based on pseudo-randomly chosen "quartets." The first helicity state in a pattern of four states was chosen in a pseudo-random fashion and the following sequence of events took the form *LRRL* or *RLLR* (See Figure 2.1). The fast helicity reversal and quartet structures were chosen in order to minimize the experiment's sensitivity to linear drifts and to reduce noise from boiling within the target. With this quartet structure we can more accurately define the Q_{weak} asymmetry as:

$$A^{\text{raw}} = \frac{(Y^{R1} + Y^{R2}) - (Y^{L1} + Y^{L2})}{Y^{R1} + Y^{R2} + Y^{L1} + Y^{L2}}. \tag{2.2}$$

where the 1,2 superscripts correspond to the first or second instance of a particular he-

licity state in the quartet. Details on how asymmetries were calculated from integrated signals will be discussed in Chapter 4.

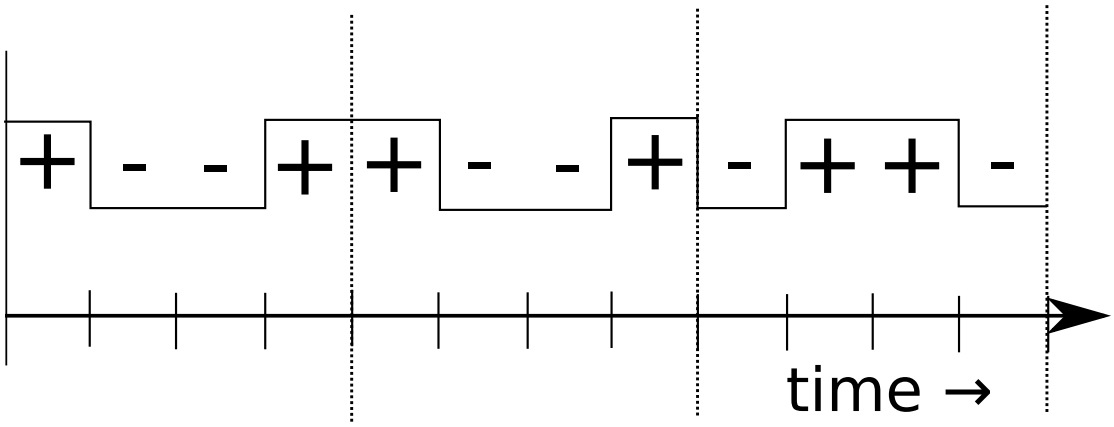

Figure 2.1: The helicity structure used by the Q_{weak} experiment. The initial helicity state of each quartet pattern is determined pseudo-randomly and the ABBA pattern structure is part of the design choice.

Since the extraction of Q_W^p requires a measurement of the momentum transfer, a *tracking* or *event* mode of running was also instrumented. In tracking mode, the experiment would operate at low beam current (100 pA to 1 nA) and would track individual scattered electrons through a set of drift chambers in order to reconstruct the kinematics of the system.

Q_{weak} took data during two separate periods*, between which certain configuration changes were made. These data sets are referred to as Run-I and Run-II and are defined further in Chapter 4.

2.2 Polarized Electron Beam

Before the recent 12 GeV upgrade, the Continuous Electron Beam Facility (CEBAF) accelerated electrons through two anti-parallel linear accelerators (LINACs) connected by magnetic recirculation arcs and could deliver polarized electrons to three end stations simultaneously (as shown in Figure 2.5). Nine recirculation beams allowed for five

*A third data set using commissioning data was also acquired and used for early analysis.

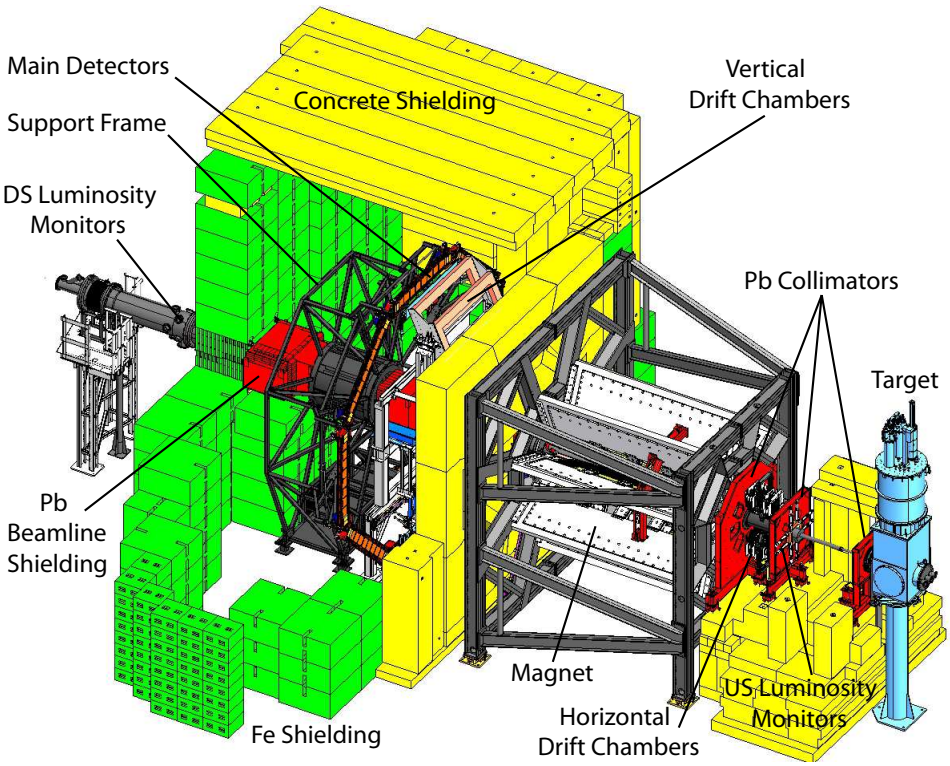

Figure 2.2: The Q_{weak} apparatus oriented with a leftward traveling electron beam. The experiment uses collimators and a spectrometer to select electrons that were elastically scattered from the protons in a liquid hydrogen cryotarget. Selected events are directed onto a set of quartz Čerenkov detectors (the main detectors).

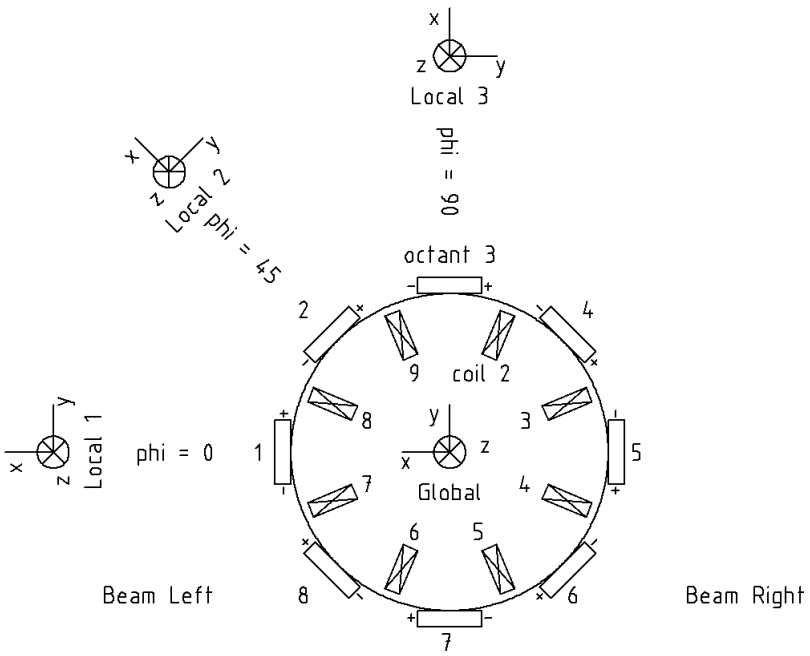

Figure 2.3: The Q_{weak} coordinate system. Main detector bars are numbered from 1 through 8 starting at the beam-left octant and increasing clockwise. The two PMT's on each bar are labeled as "+" and "-" according to the figure. Each bar possesses its own coordinate system when looking at data that varies across the face of the detector. In this local systems the *x* and *y* coordinates correspond to the short and long axes of the bar respectively.

passes through the LINACs resulting in a maximum beam energy of 6 GeV[32]. Each of the three experimental halls could receive a distinct electron beam with unique intensity, energy, and orientation of polarization. The three beams were generated by an equal number of independent circularly polarized lasers pulsing at 499 MHz on a common photocathode. The lasers were configured such that a 120° phase offset existed between them. The linearly polarized laser light was passed through a Pockels cell in order to produce either left- or right-handed circularly polarized light. The rapid switching of the orientation of circular polarization required for Q_{weak} was achieved using an optically isolated high voltage switch driven by the 960 Hz helicity signal. The left- or right-handed photons produced negative (spin $s = -1/2$) or positive ($s = 1/2$) electrons from the photocathode respectively.

The CEBAF photocathode used a gallium arsenide (GaAs) strained superlattice structure whose alternating GaAs/GaAsP configuration allowed for increased quantum efficiency (QE) when compared to a pure GaAs design. Longitudinally polarized electrons extracted from the photocathode routinely reached levels of $\sim$ 85% polarization[33] and were then accelerated by an applied electric field to be fed into the accelerator.

In addition to the fast helicity reversal, two independent types of "slow reversals" were instrumented in order to carefully study and perhaps minimize helicity-correlated false asymmetries. One such system was the Insertable Half Wave Plate (IHWP): an optical element which resulted in a flip of the direction of photon polarization, ultimately leading to a change in electron helicity that was independent of the fast helicity signal itself. The IHWP was inserted/removed approximately once every eight hours during normal running. The Q_{weak} data set was often split into IHWP-IN and IHWP-OUT subsets in order to study false asymmetries and the experiment's sensitivity to certain types of electronic noise. The other slow reversal system was the "Double Wien Flip" wherein the spin of the electrons themselves was flipped by use of a pair of Wien rota-

tors. These relative positions of these beam elements can be seen in Figure 2.4. This method of helicity reversal was only done approximately once per month and was used to extract optical effects that were not accessible using the IHWP method. Analysis of slow helicity reversals will be discussed in Section 4.3.

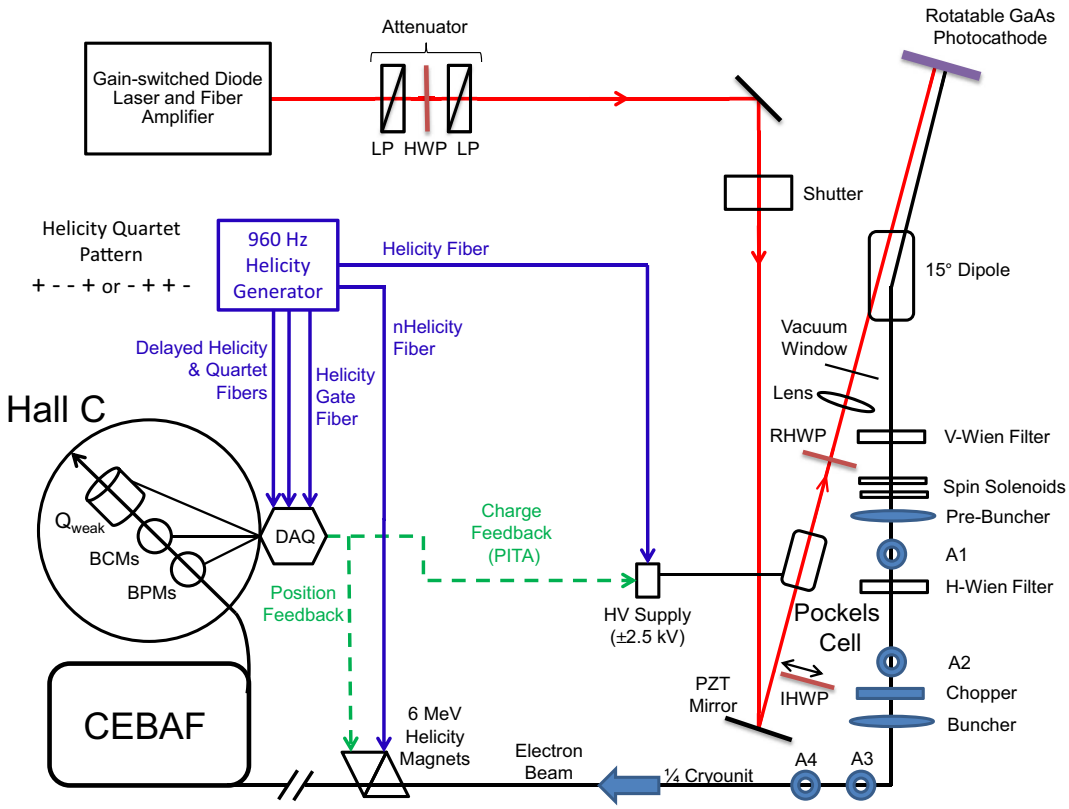

Figure 2.4: The layout of laser table during the Q_{weak} experiment. The beam begins at the laser in the top left of the diagram. The insertable half wave plate is labeled as IHWP and is located just before the Pockels Cell, there the fast helicity reversal is injected into the system. Slow helicity reversal of the electron polarization (as opposed to the direction of circular polarization of the laser) is achieved using the Wien flippers located downstream of the photocathode.

2.2.1 Beam Monitoring

The beam current, position, direction, and energy were monitored continuously throughout the experiment. A total of 47 beam position monitors (BPMs) were instrumented between the injector and the Q_{weak} target and were used to measure the absolute values

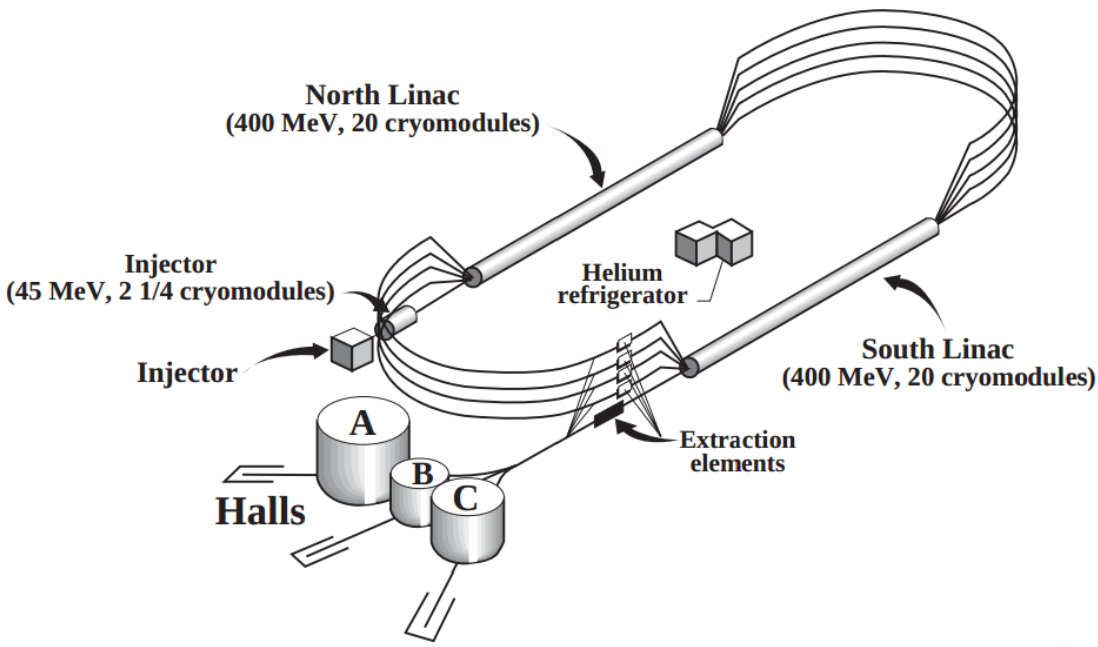

Figure 2.5: The layout of Jefferson Lab's Continuous Electron Beam Accelerator Facility (CEBAF) during the Q_{weak} experiment, prior to the facility's 12 GeV upgrade. Electrons are generated in the injector by shining a laser onto a photocathode and then accelerated out into the arc. Up to four recirculations through the two sets of superconducting linear accelerators can be performed before being delivered to one of three experimental halls.

and helicity-correlated differences for the beam's position (X and Y) along the beamline. Linear combinations of different BPMs could be used to construct angular information and thus an effective software BPM was created that used a combination of position monitors to determine the beam position and angle at the Q_{weak} target. Helicity correlated changes in the beam properties can lead to a false asymmetry leaking into the various detector systems used in parity analysis; we define the helicity-correlated position and angle differences as ΔX, $\Delta X'$, ΔY, and $\Delta Y'$, where primed variables correspond to angles. Corrections for these effects can be made if we know the magnitude of the variation between helicity states and the detector sensitivity to motion in the beam. This will be discussed in detail in Section 4.3.

The beam position monitors are composed of four thin quarter-wavelength antennae located inside the beam pipe and arranged parallel to and azimuthally symmetric around the beam direction[34]. The signal produced in the antenna is proportional to the proximity of the beam to the antenna, and so a combination of the four signals can be used to determine the beam position. The fast data acquisition associated with the BPM systems also allowed for the implementation of a *fast feedback* system capable of providing an order of magnitude of suppression of undesired beam motion[35]. This process worked by feeding the beam position information into a system that would adjust steering magnets to maintain a stable beam position.

In addition to the four beam properties introduced above, the beam energy E was also monitored. Absolute energy measurements were required in order to perform a number of corrections during post analysis, including radiative corrections described in Section 4.7. A measurement of the absolute beam energy was performed in Hall-C using the method outlined in [36]. By turning off all non-dipole magnetic elements such as focusing quadrupoles in the Hall-C transport arc and knowing the dipole field along with the beam position at the beginning and end of the arc, one can extract the beam energy from the following relationship:[37]

$$E = \frac{e}{\Theta} \int B d\ell. \tag{2.3}$$

where $\int B d\ell$ is the magnetic field integral over the path of the electron and Θ is the angle of deflection for the electron with charge e. This method has consistently provided measurements accurate at a level of 10^{-3}[36]. A full discussion of this method is beyond the scope of this thesis but is provided in [37]. Helicity correlated changes in beam energy can also give rise to false asymmetries in the same way as the position-like quantities explained above. Measurements of energy differences were performed by measuring position differences in the X direction at the point of highest dispersion in the beamline. Any residual position differences measured after accounting for actual position/angle variations could be attributed to helicity-correlated changes in energy. A linear combination of measurements using a BPM in the dispersive region and the aforementioned software variables provided a determination of energy differences at the target[38]. Residual energy dispersion at the target led to undesired coupling of energy and X-like position variables. The effect of this *strength sharing* of energy and X-like position quantities was that detector sensitivities determined by linear regression were also coupled. This will be discussed further in Section 4.3.1.

Helicity-correlated changes in beam current were removed to first order in the integrating mode detector signals by normalizing the photomultiplier tube (PMT) signal output to the beam current. A continuous, non-invasive measurement of the current was performed using a number of RF cavity type beam current monitors (BCMs). When tuned to the same frequency as the beam (3×499 MHz = 1497 MHz), the signal generated by the cavity was proportional to the beam current. Since the signal was not an absolute measurement of the beam current, calibrations against other systems such as the Hall-C Unser monitor (which provides a precise absolute measurement of the current but was too noisy for detector normalization[38]) and the accelerator's Faraday Cup

were made. During the first half of data taking Q_{weak} used two cavities with analog receivers (BCM1 and BCM2) and two with digital receivers (BCM5 and BCM6). For the last half of the experiment an additional two cavities (BCM7 and BCM8) were installed and all four digital systems were upgraded to use new readout electronics. These improved systems used higher-resolution digital to analog converters (DACs) and higher quality cabling in order to drastically reduce noise levels while maintaining the high dynamic range in current required for Q_{weak} [39].

The BCM performance was tracked by monitoring the *double differences*, a quantity defined as the difference in measured charge asymmetry between two monitors. A charge asymmetry is defined as the difference in beam current between different electron helicity states. Assuming that both monitors were properly calibrated, changes in the RMS width of this double difference could be attributed to noise in one or both of the monitors used in the calculation. Periods of time during which one or more monitors were unreliable were characterized by such an increase, and the aforementioned improvements to the digital receiver electronics are easily visible when comparing the appropriate double differences in Figure 2.6.

In the absence of a perfectly linear system, charge asymmetries and helicity-correlated changes in the beam's position will result in a false asymmetry contribution to the final measured asymmetry. An analytic method for minimizing this systematic will be discussed in Section 4.3, but efforts in the form of feedback systems were made in order to reduce the magnitude of helicity-correlated changes in the beam. Helicity-correlated beam position differences at the Q_{weak} target were minimized using a user-driven system when the beam was deemed to be of poor quality. A set of magnets located in the injector were used to modulate the beam in a helicity anti-correlated manner in such a way as to cancel out the previously existing helicity-correlated motion.

Minimization of the charge asymmetry A_Q was performed using an active feedback system which involved making repeated changes to the Pockels Cell high voltage in

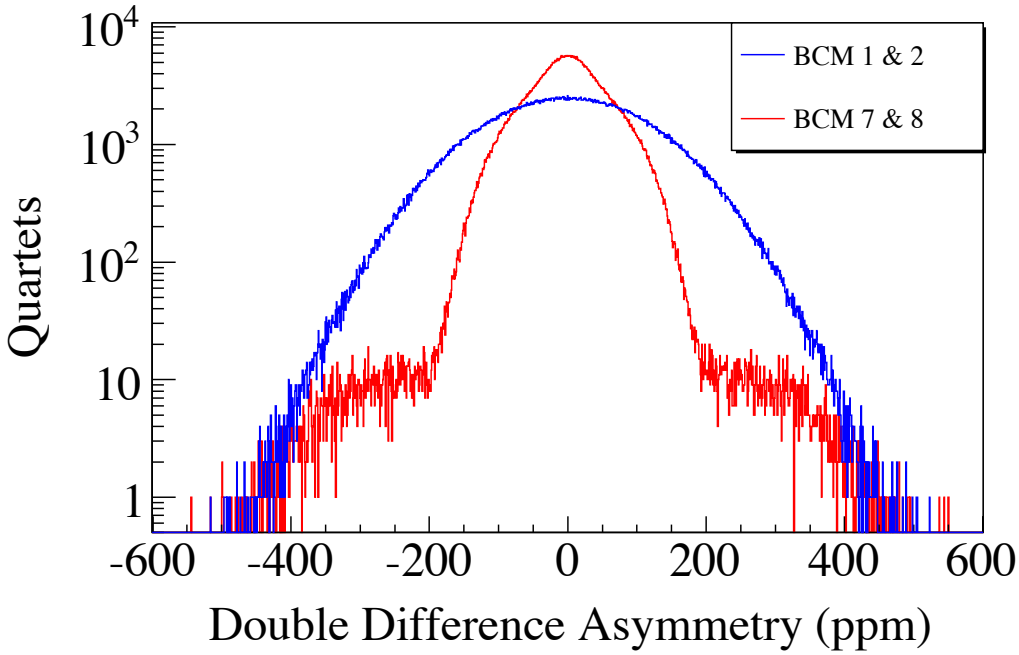

Figure 2.6: Charge monitor double differences from a typical one hour run. The RMS width of the `BCM1-BCM2` double difference is 115 ppm whereas the `BCM7-BCM8` width is only 57 ppm. The behaviour at large charge asymmetries is not important here, as a feedback system was in place that kept asymmetries at the $<$ 10 ppm level over 6 minute runs[40].

order to perform minor adjustments to the amount of charge corresponding to each helicity state of the beam. Extraction of the parameters relating Pockels Cell HV to charge asymmetry were performed approximately every 2-3 weeks[40] and the system ran continuously, performing adjustments approximately once per minute to keep the charge asymmetry within $\sim$ 10 ppm of zero over the course of a single 6 minute run segment.

2.2.2 Beam Modulation

Measuring a detector's response to changes in beam parameters could be done either by studying how its signals changed during natural beam jitter or by intentionally modulating (e.g. moving) the beam. Measurements of these sensitivities along with the

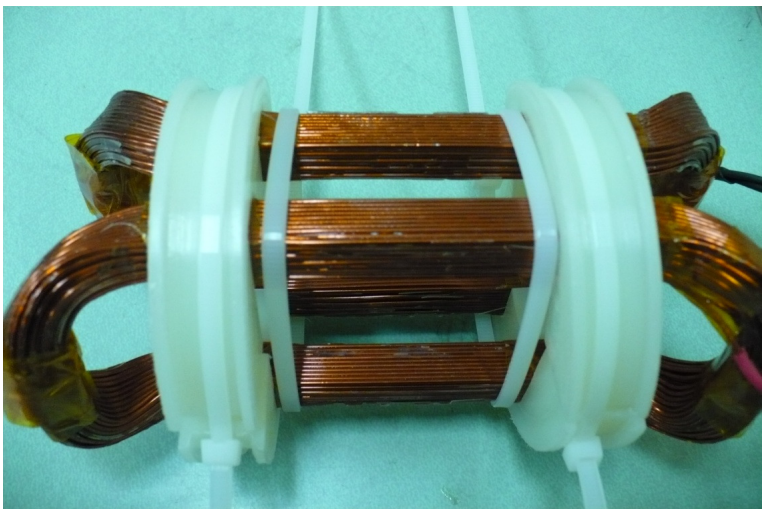

Figure 2.7: An air-core coil used in the intentional modulation of the beam.

magnitude of the beam's variations were all that was required to make a correction for any false asymmetry resulting from deviations in the beam's properties (beam corrections will be discussed in details in Section 4.3). During normal beam conditions, all parameters experience natural jitter and any single property of the beam is not guaranteed to be varying independently of others. Intentional and independent modulation of the various beam properties with amplitudes much larger than normal beam jitter allowed for a more accurate determination of detector sensitivities.

The modulation system hardware comprised four pairs of air-core inductive copper coils[41]: two for horizontal and two for vertical modulation. Moving the beam using these coils would result in a change in the beam's position/direction. Coils were driven by a 16 bit waveform generator with the drive signals also being digitized and written into the Q_{weak} data stream to be used for later analysis. For energy modulation, a similar drive signal was sent to a superconducting radio frequency cavity where variations in the input voltage would result in changes to the energy of the electron beam. This SRF cavity was located in the south LINAC of the accelerator. Figure 2.7 displays one of the air-core coils prior to installation.

2.3 Polarimetry

One of the first corrections that must be done to the experimental asymmetry is accounting for imperfect polarization of the electron beam. The design specifications for Q_{weak} called for a polarization of the electron beam $P_e \geq 85\%$ measured to an absolute uncertainty of 1%. The Q_{weak} experiment performed measurements of the beam polarization using two independent subsystems: the previously existing Hall-C Møller polarimeter and a new Compton polarimeter. The existing Møller system was invasive to normal running and would require an eight hour shift 2-3 times each week running at low ($\sim 10\,\mu$A) beam current. Each of these measurements would result in a $\leq 1\%$ polarization measurement. The Compton polarimeter was a new system designed and commissioned during Q_{weak} with the advantage of being non-invasive and capable of running during periods of high beam current.

2.3.1 Møller Polarimeter

A Møller polarimeter determines beam polarization by measuring the cross-section asymmetry in the scattering of longitudinally polarized electrons from electrons in a longitudinally polarized target where the spins are either aligned or anti-aligned. The asymmetry is derived from the cross-section determined using the lowest order diagrams for electron-electron scattering given by[42]

$$\frac{d\sigma}{d\Omega} = \frac{d\sigma_0}{d\Omega}\left[1 + P_t^{\parallel} P_b^{\parallel} A_{zz}(\theta)\right] \tag{2.4}$$

where $d\sigma_0/d\Omega$ is the unpolarized differential cross-section, $P_{t,b}^{\parallel}$ are the parallel components of target and beam polarizations, and $A_{zz}(\theta)$ is the analyzing power, which is dependent on the centre-of-mass scattering angle[42]:

$$A_{zz}(\theta) = -\sin^2\theta \frac{8 - \sin^2\theta}{(4 - \sin^2\theta)^2}. \tag{2.5}$$

Using Equations 2.4 and 2.5, the scattered electron asymmetry can then be written as

$$A^{ee}_{\uparrow\downarrow} = A_{zz}(\theta) P^{\parallel}_b P^{\parallel}_t. \tag{2.6}$$

The Hall-C Møller polarimeter uses a thin target of pure iron aligned perpendicular to the beam direction and magnetized by a 4 T field in the beam direction generated by a superconducting solenoid. Due to the saturation magnetization of pure iron being so well known, the polarization of the incident beam can be determined to better than 0.3%[43], though during Q_{weak} relative precisions of $\sim$ 0.4% were routinely achieved during each measurement[40].

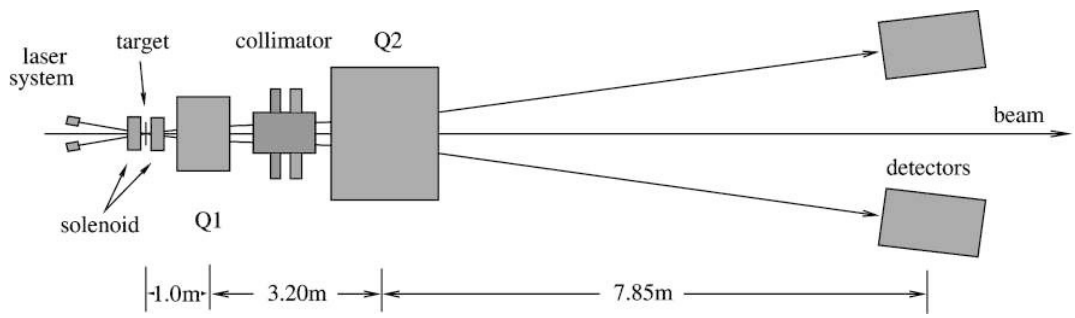

Figure 2.8: The Hall C Møller polarimeter. Scattered and recoil electrons are focused onto a detector plane using two quadrupole magnets (Q1 & Q2). Backgrounds are controlled through careful positioning of collimators between these magnets. The Q2 magnet was not used during this experiment.[40]

2.3.2 Compton Polarimeter

The goal of the newly commissioned Compton Polarimeter for Hall-C was to determine the incident beam polarization to the 1% level on the timescale of an hour[44] and to do so in a non-invasive way as compared to the already functioning Møller Polarimeter

of Section 2.3.1. In order to measure its polarization, the beam must first be steered by a magnetic chicane away from the primary beamline and into an interaction region. At this point the electrons interact with low-energy, circularly polarized photons from a 10 W green laser (532 nm) and both the scattered electron and back-scattered photon are detected. The scattered electrons are momentum-analyzed by a dipole magnet to steer them away from the primary beam and into the diamond strip electron detector described in [45]. The photons were detected by a calorimeter[†]. The relative positions of the interaction region and the photon and electron detectors are illustrated in Figure 2.9.

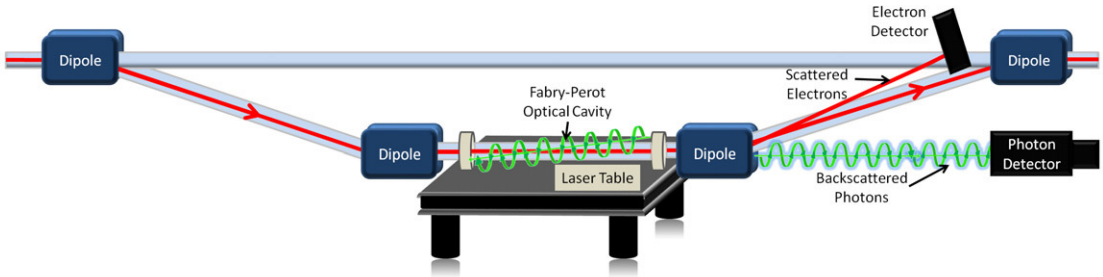

Figure 2.9: The newly commissioned Hall C Compton polarimeter. The primary CEBAF electron beam is steered through a chicane into a region where it interacts with a 10 W green laser. Compton scattering events are detected using both a photon and electron detectors. The unscattered primary beam exits the chicane and resumes its original course to the target.

2.4 Targets

2.4.1 Liquid Hydrogen Target

The primary target for Q_{weak} was liquid hydrogen. The cell was designed using computational fluid dynamics (CFD) to operate with 55 L of liquid hydrogen at 20 ± 0.02 K at a pressure of 207 – 241 kPa. The target cell had a conical geometry measuring

[†]Cesium iodide, germanium silicon oxide, and lead-tungstate were used as scintillating materials throughout the experiment.

34 cm (3.9% radiation lengths) in the beam direction with thin aluminum Al 7075-T6 windows. The energy loss of a 1.165 GeV electron beam through such a target is approximately 2.1 kW[46]; a high power heat exchanger was designed that was capable of dissipating this much power in addition to another ~ 700 W accounting other sources of heating (mechanical heating of the pump, radiative and convective heating of the target cell, etc.). A schematic of the hydrogen cell is provided in Figure 2.10.

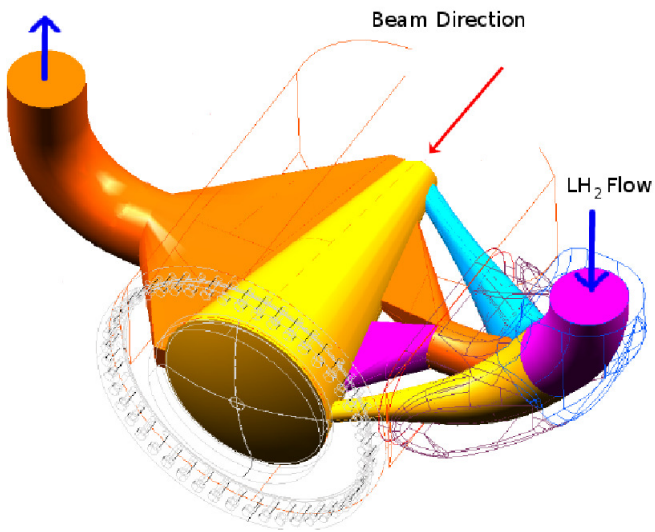

Figure 2.10: A schematic of the liquid hydrogen target cell. The primary cell is displayed as the yellow cone. A wire frame depiction of the cell housing is also shown. The cell was designed to maximize the rate of flow across the beam entrance and exit windows.

An important factor to consider when using a cryogenic target is that the instantaneous power deposited can often lead to density fluctuations throughout the length of the target cell. In addition to the target being designed to maximize the flow of liquid hydrogen across the entrance and exit windows of the cell, the beam was rastered in a uniformly distributed square of variable size in an effort to distribute the power evenly over a larger area. Without this distribution of power, the electron beam would burn a hole through the target windows. Density fluctuations would decrease as the raster area increased, and so varying the raster area in a systematic way from 9−25 mm^2, along with varying the beam intensity and target pump speed, proved to be an important instrumen-

tal technique in determining how much noise was introduced into the experiment from this source (See Figure 2.11). The noise introduced from this effect was determined by observing the root mean square width of the asymmetries measured using the main detector array (see Section 2.6.1) and accounting for contributions to the width from counting statistics as well as detector and BCM resolutions[‡]. It was determined using this method that for a nominal 16 mm^2 raster, an additional 46 ppm of noise was injected into the measured asymmetry, achieving the design goal of $\leq$ 50 ppm. This effect is negligible when compared to the main detector asymmetry width of $\sim$ 230 ppm.

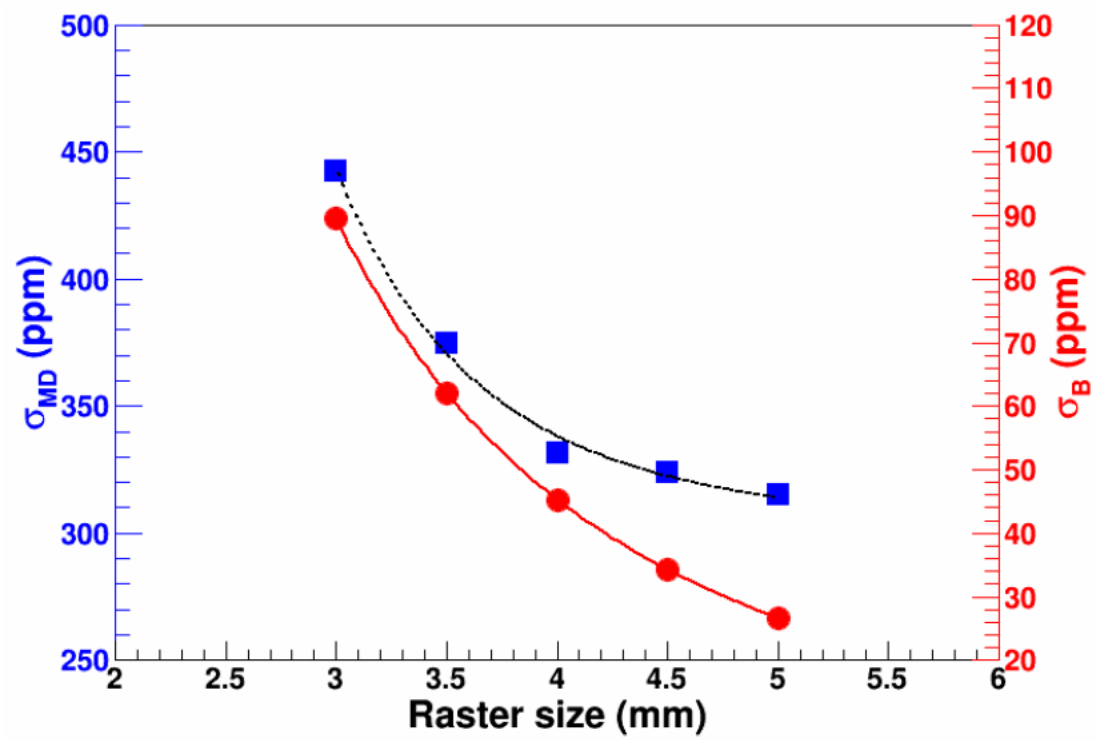

Figure 2.11: Blue: main detector asymmetry width as it differed with the size of a square raster. Data correspond to running at a beam current of 182 μA and a target pump frequency of 28.5 Hz. The red points quantify how much additional noise was injected into the main detectors as a result of density fluctuations in the liquid hydrogen.[47].

[‡]The BCM resolution enters into the width due to the normalization of the main detectors to the beam current.

2.4.2 Solid Targets

The asymmetry resulting from scattering polarized electrons from the aluminum windows of the target cell resulted in the largest correction to the measured asymmetry. In order to properly measure the aluminum asymmetry, a number of aluminum targets were installed on a ladder that could be moved into the beamline. In addition to aluminum dummy targets of varying thickness, other solid targets included those used to calibrate the target reference position in the tracking system, and other materials (carbon and beryllium oxide). The carbon target was used in studies that determined how much of the main detector signal resulted from scattering from the aluminum windows (see Chapter 4). Dedicated periods of data acquisition were assigned for running on the aluminum targets. A brief overview of the aluminum analysis will be provided in Chapter 4.

2.5 Collimation and Toroidal Spectrometer

2.5.1 Collimation and Shielding

The scattered electrons were collimated to select the kinematic region of interest, using a set of three lead antimony collimators, each with eight holes through which the scattered electrons traveled before being steered onto the detectors by a magnetic spectrometer (see Section 2.5.2). The design of the collimators was the result of extensive simulations to optimize the detector yields and the size of the asymmetry[48][3].

The first collimator was located directly downstream of the target scattering chamber and served as an initial method to clean up the scattered beam. Events with a very small scattering angle ($\theta \sim 0.75 - 4^\circ$) that would scatter in the beamline were stopped in a water cooled tungsten plug with a 14.7 mm inner radius located in the centre of this first collimator. The angular acceptance of the experiment was defined by a second

collimator positioned approximately 3 m downstream of the target[3]. The angular acceptance for this collimator for elastically scattered electrons from the LH_2 target was $\theta = 5.8° - 10.2°$ ($6.6° - 11.5°$) for events generated at the upstream (downstream) face of the target cell. This angle was measured relative to the unscattered beam. A final cleanup collimator was then placed on the upstream edge of the magnetic spectrometer.

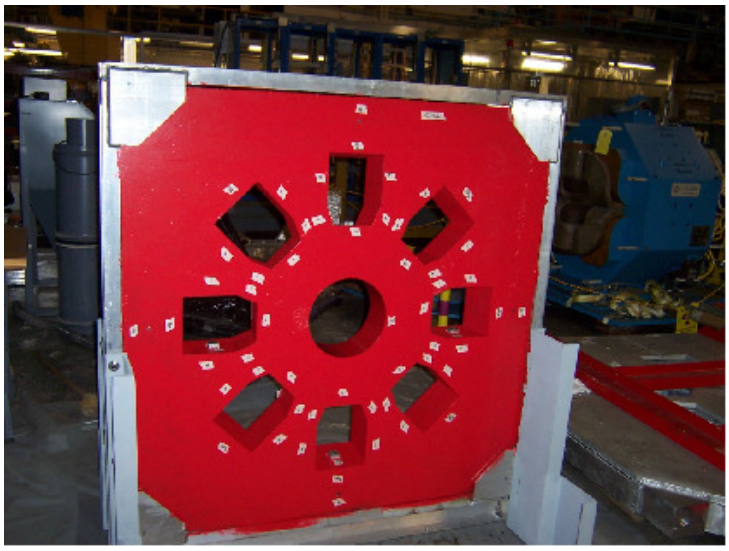

Figure 2.12: The primary collimator that defined the kinematic acceptance of the experiment. A 15 cm thick lead antimony (95.5% Pb, 4.5% Sb)[3] material was used.

2.5.2 The Q_{weak} Toroidal Spectrometer

The Q_{weak} Toroidal Magnet (QTOR) separated elastically scattered electrons from inelastic electrons and other backgrounds, and focused them onto the array of eight Čerenkov detectors (see Section 2.6 and Chapter 3). The magnet produced a field integral of approximately $\int B \cdot d\ell = 0.89$ T · m in order to bend 1.165 GeV/c electrons scattered an angle of 8° on average, over a small range of angles[6]. Events with lower momenta, such as inelastically scattered electrons, would spend more time within QTOR and were thus swept out to radii beyond the main detectors.

The QTOR magnet consisted of eight racetrack-shaped, water-cooled copper coils and was designed and optimized using GEANT4 Monte Carlo simulations. The iron-

free resistive magnet design was chosen for its simplicity, low-cost, and reliability when compared with modern superconducting techniques. A DC power supply with maximum current of $I_{\max} \sim 9\,\mathrm{kA}$ was used to power the magnet and was typically run at 8921 A during production running. Taking data at different QTOR currents provided opportunities to study parity violating physics in the $\mathrm{N} \rightarrow \Delta$ transition region as well as to perform systematic studies of the field-dependence of the main asymmetry.

Details on simulating and fabricating the coils can be found in [5].

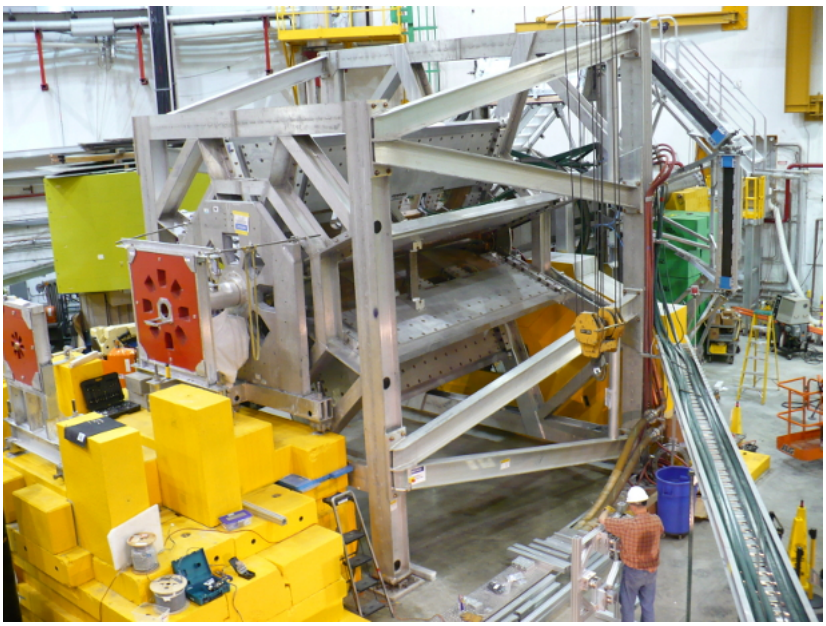

Figure 2.13: The eight-segment toroidal spectrometer QTOR shown in its final position between the collimators and the main detector array.

2.6 Detector Subsystems

The $\mathrm{Q_{weak}}$ experiment included three distinct asymmetry-measuring subsystems whose signals were integrated over periods of common beam helicity during high current running: the main detectors, background detectors, and luminosity monitors. Integrated signals had pedestals subtracted prior to any further manipulation (see Section 3.2.3 for details on pedestal extraction and stability). Signals were also normalized to beam

current so that the fully prepared basic detector yields for PMT i during helicity state $j = L, R$ can be written as:

$$Y_{i,j} = \frac{(Y_{i,j}^{\text{raw}} - Y_i^{\text{ped}})}{I_j} \tag{2.7}$$

where raw PMT yields are measured in units of Volts, and I_j is the beam current (in μA) measured during the same event window.

2.6.1 Main Detectors

The Q_{weak} main detector subsystem comprised eight, 2 meter long, quartz bar Čerenkov detectors arranged in an azimuthally symmetric array around the beamline as shown in Figure 2.3. Detectors were housed in aluminum exoskeletons and mounted onto a "Ferris wheel" structure located in a concrete-shielded hut. Shielding and material choices for the hut and detector housings were made in order to reduce shower backgrounds. The basic design of each main detector bar is given in Figure 2.14. A detailed review of the design, fabrication, and initial testing of the main detectors can be found in [5], and Chapter 3 will provide a complete report of the performance of this system during the Q_{weak} experiment.

2.6.2 Background Detectors

A number of dedicated background detectors were designed and implemented for the experiment, each with a distinct goal in mind. All of these detectors were designed to complement the main detector subsystem, and so their electronics chains exactly matched that of the main quartz bars: from the PMT all the way to digitization of the signal. Two of these background monitors consisted of a single photomultiplier tube placed in a light-tight box. These boxes were designed to be portable so that they could be placed in different locations as the experiment progressed, and included

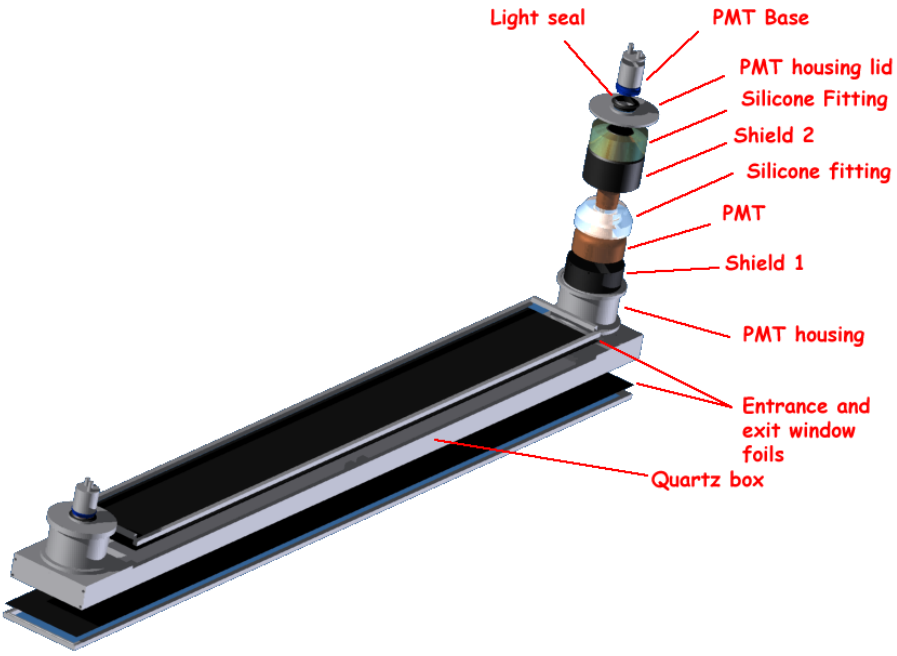

Figure 2.14: A rendering of a single unit of the main detector, including the quartz bar and PMT housings.

double layers of mu metal for magnetic shielding. These detectors, named `pmtonl` and `pmtltg`, included a bare PMT or a PMT+35 cm light-guide respectively. The monitors were used continuously throughout the experiment, with their locations changing in March 2011[§]. Initially, the boxes were located at the main detector focal plane, between octants 8 and 1, and 3 and 4 (see Figure 2.15). After the move, these boxes were located in octant 3, positioned at smaller radius when compared to the main detector bar (see Figure 2.15). Both locations were chosen in such a way that any signal generated would not correspond to elastically scattered electrons, but would still detect backgrounds in the vicinity of a main detector bar.

The aforementioned background detectors provided a way to study dispersive backgrounds in the room and how such a background interacted with the photomultiplier tube and its associated electronics. In order to more completely measure how these backgrounds interacted with the main detectors, a complete quartz bar detector (MD9) was instrumented with the same configuration as the primary detector subsystem. During Run-I this module was located downstream of the main detector support structure, laid horizontally above the beam pipe. In this position it measured dispersed backgrounds in the main detector hut. In Run-II it was relocated to stand vertically in octant 5 (beam-right), at a slightly lower height than the corresponding main detector module, where it was expected to measure background events that made it through the shield wall from upstream of the detector hut. Although MD9 was positioned at a larger radius from the beamline than the main detectors, the scattering kinematics was such that it saw events that would have passed the main detector at smaller radius. Figures 2.16 and 3.1 display these positions. Background detectors were ultimately used in correcting for a *beamline background* resulting from the beam scattering from the tungsten plug. The procedure used to correct for this background will be discussed in Chapter 4.

[§]Background detectors were moved during the running period labeled as Wien 2 in Run-I.

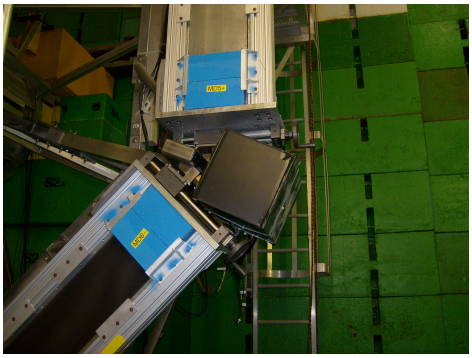

Initial position of the background detectors when looking downstream. Boxes were positioned in the main detector plane.

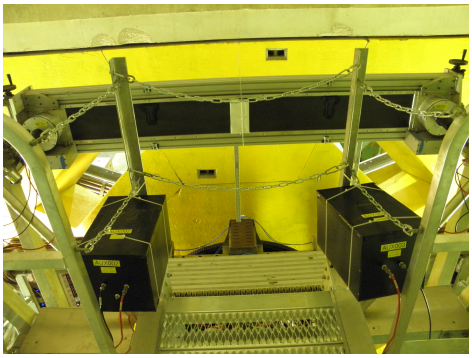

Final locations of the background detectors when looking upstream. Positioned in octant 3 but at smaller radius.

Figure 2.15: Background detector positions.

Figure 2.16: Initial position of the spare main detector bar MD9. It is located downstream of the main detectors, on top of the beamline shielding.

2.6.3 Luminosity Monitors

The Q_{weak} experiment used two separate sets of auxiliary detectors located outside of the main detector shield hut. These *luminosity monitors* (commonly abbreviated as lumis) were placed at very forward angles in regions where the parity violating asymmetry was expected to be very small. The scattered electron rate at these forward angles was also high compared to the main detector subsystem, leading to smaller statistical errors. These conditions made the luminosity monitors an ideal system for studying the effects of target density fluctuations as well as serving as a "null asymmetry monitor". With the physics asymmetry reduced at these angles, any measured asymmetry in the luminosity monitors would point to a possible systematic that must be addressed in the final parity violating asymmetry analysis. Both sets of detectors were designed and had their positions optimized with Monte Carlo techniques using GEANT3 and GEANT4[49].

One set of luminosity monitors was located on the upstream face of the defining collimator (see Section 2.5) and was designed to primarily detect Møller scattered electrons at angles $\leq 5^\circ$ and to serve as a target density monitor. Significant boiling in the liquid hydrogen would appear as a new source of noise in the detectors, whose statistical uncertainties were small enough for such effects to be studied in depth. The upstream lumi subsystem comprised four $4 \times 27 \times 2$ cm quartz bars, arranged symmetrically around the beam as seen in Figure 2.17. Light generated from the scattered electrons would travel through one of two 35 cm quartz light guides located on either end of the bar and into a Hamamatsu R375 photomultiplier. In practice, this set of detectors would serve to alert the collaboration to the existence of significant unexpected background asymmetries resulting from the beam interacting with the tungsten plug inside the first collimator. This unexpected background dominated the asymmetries measured in both the upstream luminosity monitors (lumis) and the background detectors[¶] described in

[¶]This observation is true for the final positions of the background detectors.

Section 2.6.2, and so these two systems could be used together to provide a correction for this background asymmetry to the main detector. A full analysis of this background is given in Chapter 4.

The other set of luminosity monitors, which used the same Hamamatsu R375 phototubes, was located downstream of the main detector shield hut at a scattering angle of 0.5° (Figure 2.17, right). This subsystem comprised eight $4\times3\times1.3$ cm pieces of quartz arranged in the same symmetric geometry as the main detectors. These pieces of quartz were connected to the PMTs through 34 cm air-core light guides[49] and were placed in cups that penetrated the beamline such that the detectors lay within 13 cm of the beam centre. Though they were primarily designed to act as a null asymmetry monitor, they were also much more sensitive to helicity-correlated changes in the beam, and so provided a set of azimuthally symmetric monitors independent from the main detectors on which our algorithms for addressing such effects could be studied.

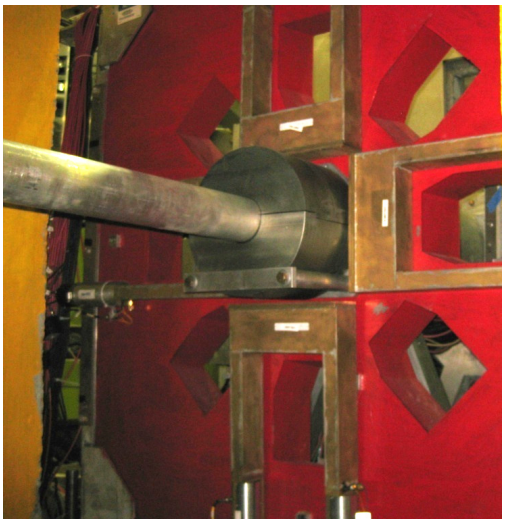

The upstream luminosity monitors.

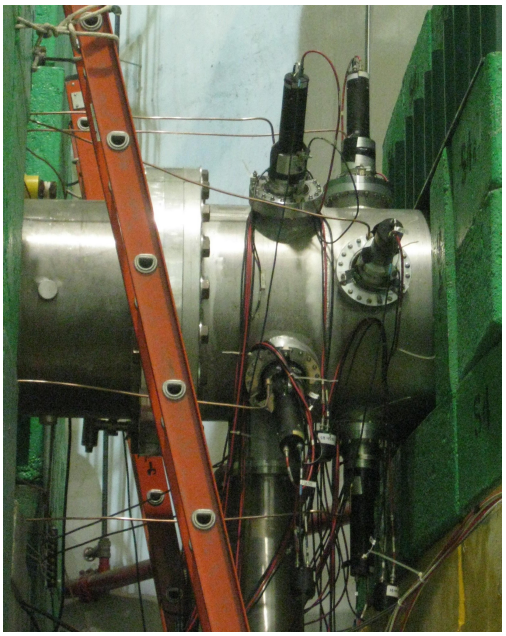

The downstream luminosity monitors.

Figure 2.17: The Luminosity monitors.

2.7 Tracking Systems

The primary goal of tracking measurements was to obtain data from which the kinematics of scattered events could be determined. The dependence of the parity violating physics asymmetry on momentum transfer in Equation 1.82 requires that the four momentum transfer Q^2 be accurately determined. In addition to this necessary extraction, the scattering vertex and angle can also be determined from tracking data, and important properties of the main detectors, such as position-dependent detector efficiency, can be systematically studied. Tracking mode data were also important in determining the relative contributions to detector signals resulting from background processes.

Particle track reconstruction was made possible by the use of drift chamber systems located both upstream and downstream of the QTOR spectrometer, timing and trigger information was provided by a *trigger scintillator* system, and a profile *scanner* was used in the mapping of detector response across the face of the main detectors. Full discussions of the tracking systems and their associated analysis are available in other dissertations[49][50], but an introduction will be provided here.

2.7.1 Horizontal Drift Chambers

The horizontal drift chambers (HDCs) were located upstream of QTOR and were designed to provide accurate measurements of scattering angle and vertex position within the target. Each drift chamber package comprised two chambers separated by 40 cm and each contained six planes of wires, all sandwiched between aluminum-coated Mylar foils. A gas mixture of 65-35 Argon-Ethane was flushed through each chamber. Charged particles passing through the chamber would ionize the gas and the resultant electrons would be attracted to those *sense wires* with a small potential, causing a signal to be generated in those wires. A complete package was installed on either side of a rotation system such that the chambers could be parked in any set of two opposite oc-

tants and the chambers could be moved radially so that they could be retracted from the scattered beam envelope during integrating mode, where the high beam current resulted in rates too large for the chambers to function[49]. Each chamber had an active area of 50×70 cm^2 and was located $\sim$ 70 cm from the beam centre. Figure 2.18 shows the horizontal drift chambers installed in their final position.

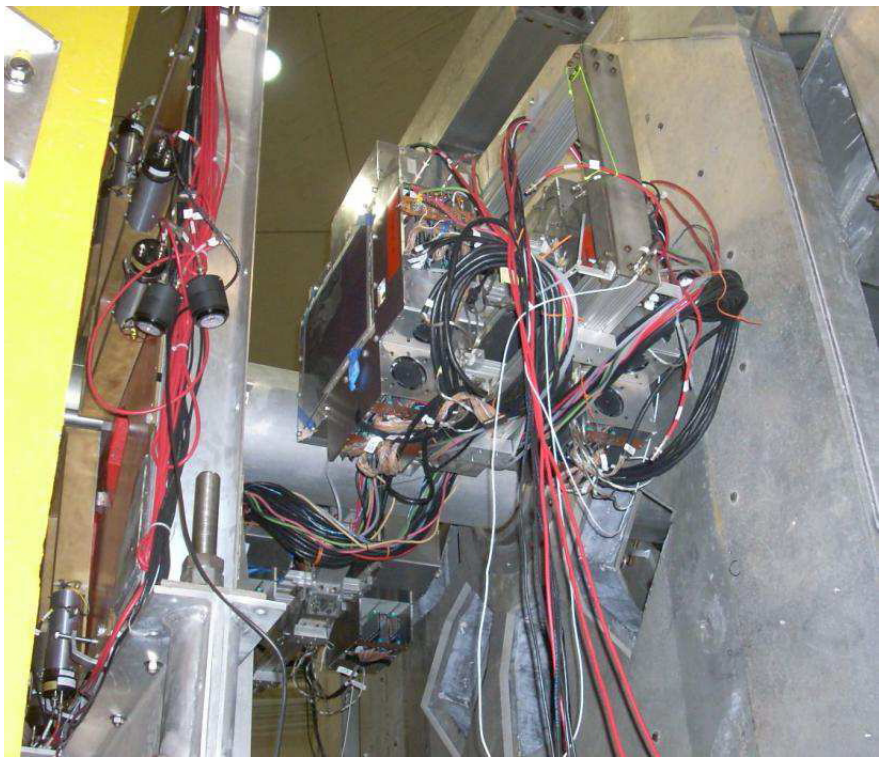

Figure 2.18: The horizontal drift chambers located upstream of the QTOR magnetic spectrometer.

2.7.2 Vertical Drift Chambers

The vertical drift chambers (VDCs) were another set of drift chambers which employed the same technology of using a readily ionizing gas (50-50 Argon-Ethane in this case) and a number of wire planes. The VDCs were located between QTOR and the main detectors, just downstream of the main shield hut wall as shown in Figure 2.19. In addition to being used for Q^2 reconstruction, the vertical drift chambers allowed for the

detection efficiency across the main detector quartz bars to be mapped out.

Similar to the HDCs, this subsystem contained two completed packages positioned in opposite octants on a rotator and could also be moved radially so that they could be safely extracted from the scattered envelope during high current running. Each package included two chambers separated by 30 cm and each chamber contained two planes of 279 sense wires[50]. The default position of the chambers was in octants 1 and 5, but rotation of ±90° was possible so that octants 3 and 7 could be occupied by either VDC package.

Timing and trigger information for the tracking measurements were provided by a set of *trigger scintillators* located on the downstream side of the VDC packages. These scintillators were made slightly larger than the main detector profiles to ensure that all events that could generate light in the quartz bars would pass through the scintillators. Details on the trigger scintillator are available in [3].

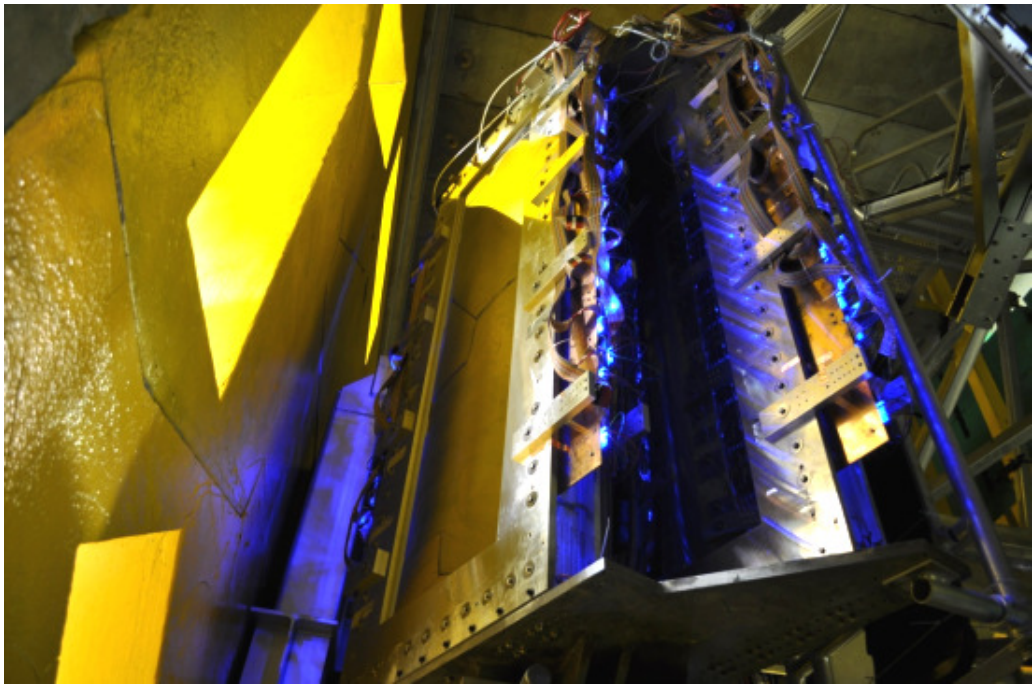

Figure 2.19: One of two vertical drift chamber (VDC) packages used in Q_{weak} . VDC's were located just downstream of the shield wall, with the scattered electron trajectory running from left to right in this photograph.

2.7.3 Focal Plane Scanner

Making measurements of the kinematics and detector response at low current in tracking mode is only useful if it can be confirmed that these quantities do not change as one goes to higher and higher beam currents. The focal plane scanner was designed to function in both tracking and current mode and thus provide a necessary link between the two running modes. The focal plane scanner consisted of two 1 cm^3 fused silica radiator cubes coupled to 2 inch PMTs through air-core light guides as is displayed in Figure 2.20. The small active area produced a rate of ~1 MHz during high current running: low enough to be operated in counting mode. Requiring a coincidence between the two PMTs allowed for a significant reduction in background so that only events from electros interacting in the quartz were used. The entire scanner system was attached to a two-dimensional motion system so that the small active area could be swept around an area of the octant 7 main detector face. The scanner could be placed on either the upstream or downstream side of the main quartz bar and could vary its position 0.35 m in the vertical direction and 2.5 m in the horizontal direction[51].

2.8 Data Acquisition System & Analysis Engine

In order to successfully operate as both an integrating and a counting experiment, two separate data acquisition (DAQ) systems needed to be implemented and maintained. Both systems used Jefferson Lab's *CEBAF Online Data Acquisition* (CODA) software to readout data from the various DAQ modules into raw data files to be stored on disks and backed up on tape drives for later replays. A simple block diagram that shows the flow of data from the main detector PMT to a data file is presented in Figure 2.21. The ~ 6 μA signal from a photomultiplier tube goes through a low noise trans-impedance pre-amplifier that provides a line driver that can maintain the signal amplitude over the distance from the detector to the electronics room. A digital integrator (TRIUMF

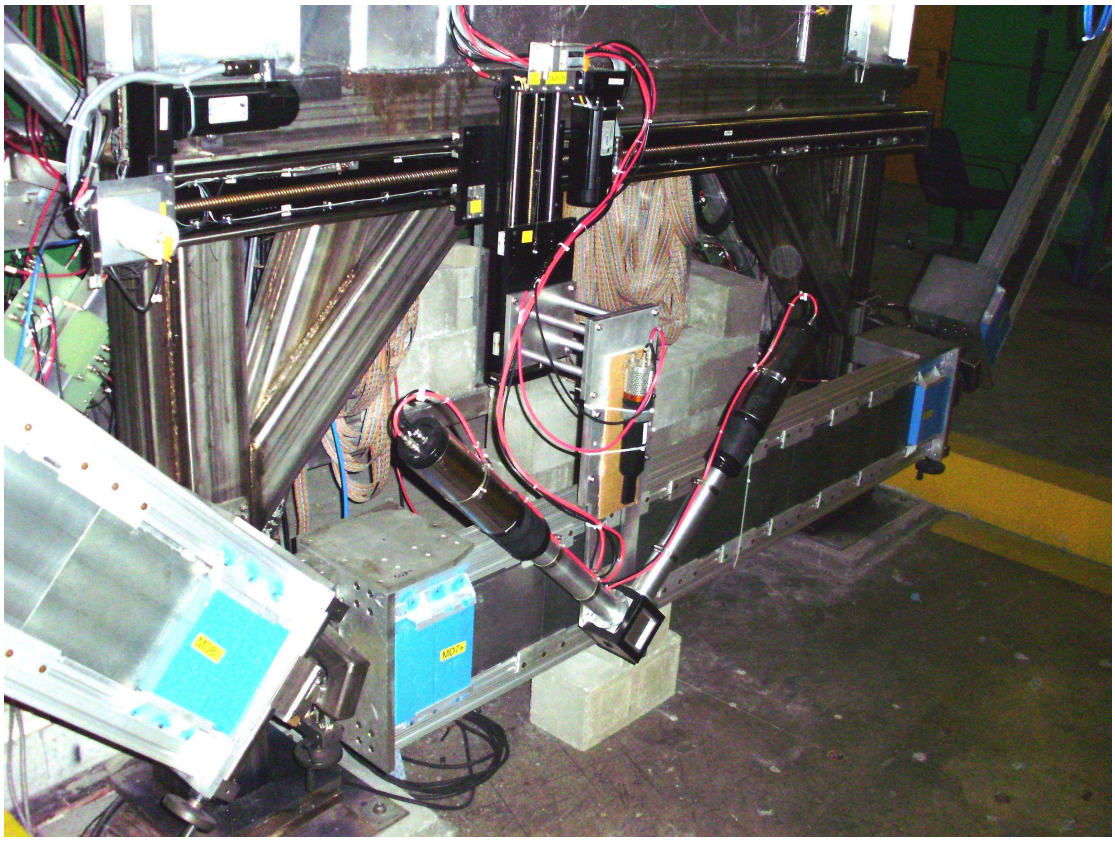

Figure 2.20: The focal plane scanner in its upstream configuration in octant 7. [The focal plane scanner in its upstream configuration in octant 7. A two dimensional motion system was used to scan a small quartz detector across the profile of a main detector bar.]

ADC's) digitizes the signal before the CODA system writes it into a data file to be read later.

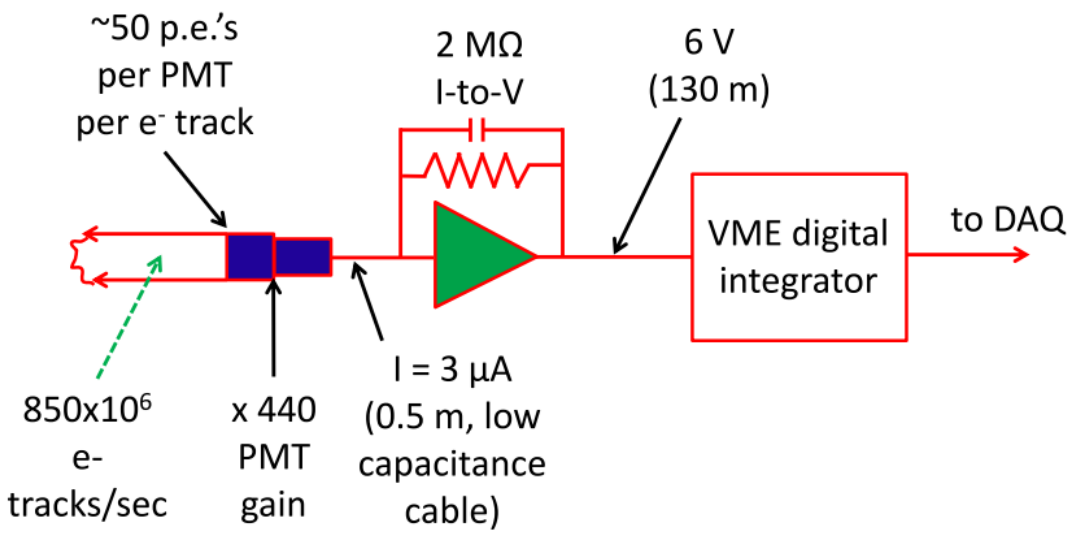

Figure 2.21: A simple schematic of the main detector signal chain. See the text for details. Figure taken from [4].

The primary modules used during integrating mode were TRIUMF ADCs, described in detail in [5]. Signals from the various Q_{weak} detectors, including beamline elements, were read out at a rate of four times the helicity flip rate of 960 Hz in order to provide a time interval smaller than the normal event rate (i.e. data shorter than the 4 events that make up an asymmetry quartet). A new *macropulse* (MPS) was defined by the flipping of the beam helicity, and this MPS signal was used as the DAQ trigger. In this configuration, an MPS represents the smallest unit of data, ignoring the four subblocks from oversampling used for systematic studies. Figure 2.22 shows the timing diagram for the integrating mode DAQ. The helicity gate signal sent to the DAQ was defined by a 70 μs period T_{settle} during which time the Pockels cell high voltage was flipped. The remaining time (1/960Hz - T_{settle} = 971.65 μs) was labeled T_{stable} and defines the period over which detector signals were integrated.

During tracking mode production the trigger could be defined according to what was being measured. For Q^2 measurements a coincidence of the two trigger scintillators was

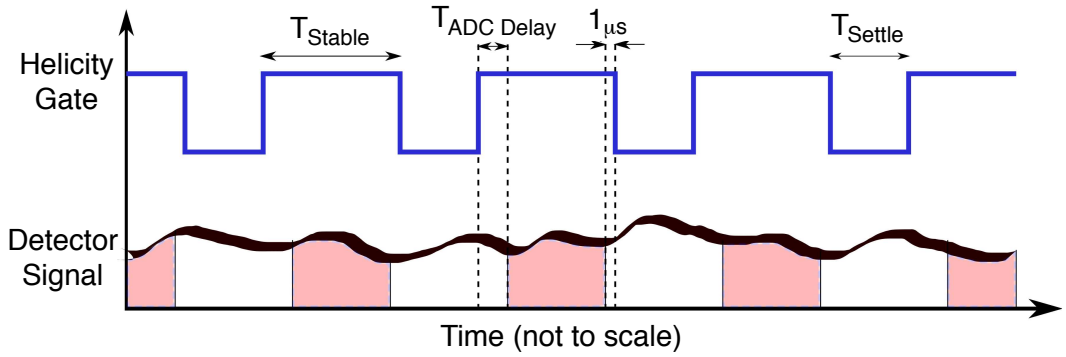

Figure 2.22: A timing diagram of the integrating mode DAQ. The shaded area in the detector signal indicates the signal region digitized by the ADCs. The horizontal axis scale is exaggerated to show details in the signal timing. Figure taken from [4].

used, but systematic studies of other subsystems could be performed by triggering on one-or-more main detector PMT's, the focal plane scanner, or a clock. At the time of Q_{weak} , the CODA system was only capable of operating at data rates up to 6 kHz, but rates of 1-2 kHz were typically used to avoid issues with computer deadtimes. Event rates higher than these limits were managed by prescaling the trigger a factor that would result in manageable rates. Upon receiving a trigger, the system would read out data from a number of front-end electronics, including CAEN V792 QDCs (charge to digital converters) for detector spectra, JLab F1TDC's for timing information, and SIS3801 scalers for event rates.

A C++ analysis engine was written using the ROOT packages developed at CERN. Separate analysis software was developed for integrating and tracking mode. The integrating mode analysis engine is capable of reading in the raw data files, along with a number of user-generated configuration files (including channel maps, calibration factors, etc), and builds asymmetries. Detector yields and quartet-level asymmetries (along with other diagnostic data, including non-helicity-correlated asymmetries, see Section 4) are then written to ROOTfiles: a convenient file format that is easily read/-manipulated within the ROOT framework. A number of post-processing tasks can then use these ROOTfiles as input. A single ROOTfile would typically correspond to ap-

proximately 6 minutes of data. These 6 minute bits were called *runlets* where a single *run* would often consist of 10-15 runlets. Runlet-level averages for most quantities were then uploaded to a MYSQL database for easy recollection in cases where quartet-level data was not required. A detailed explanation of DAQ system for each running configuration can be found in [38] and [40].

Chapter 3

The Q_{weak} Main Detectors

In this chapter I will discuss the basic design and functionality of the main quartz Čerenkov detector subsystem. I will focus primarily on a review of how the detectors performed during their use in the Q_{weak} experiment, including discussions of their use as both integrating and counting mode detectors. For a more complete review of the design process and specifications of the individual components please refer to [5].

3.1 Overview and Design

As previously described, in Section 2.5, the QTOR spectrometer steered scattered electrons into a set of eight azimuthally symmetric profiles in the focal plane as shown in Figure 3.1. The main detector subsystem comprised eight quartz bar Čerenkov detectors located at this focal plane with active volumes of 200 cm $\times$ 18 cm $\times$ 1.25 cm. Each bar was made out of two 100 cm pieces of fused silica Spectrosil® 2000 synthetic optical quartz and had deviations of thickness $\leq$ 250 μm and were polished smooth to a level of 25 Å. This material was chosen in part for its radiation hardness: an important factor when taking into account the considerable dose associated with $\sim$ 2500 hours of running with 180 μA of 1.1 GeV electrons*. Other advantages of using quartz included

*See [5] for details of a rough estimate that puts the accumulated dose at $\sim$ 100 kRad.

its low scintillation (making it relatively insensitive to neutral particles) and its uniform response (events at different positions across the bar should generate almost the same amount of light). Figure 3.2 shows a single quartz bar in its aluminum support structure.

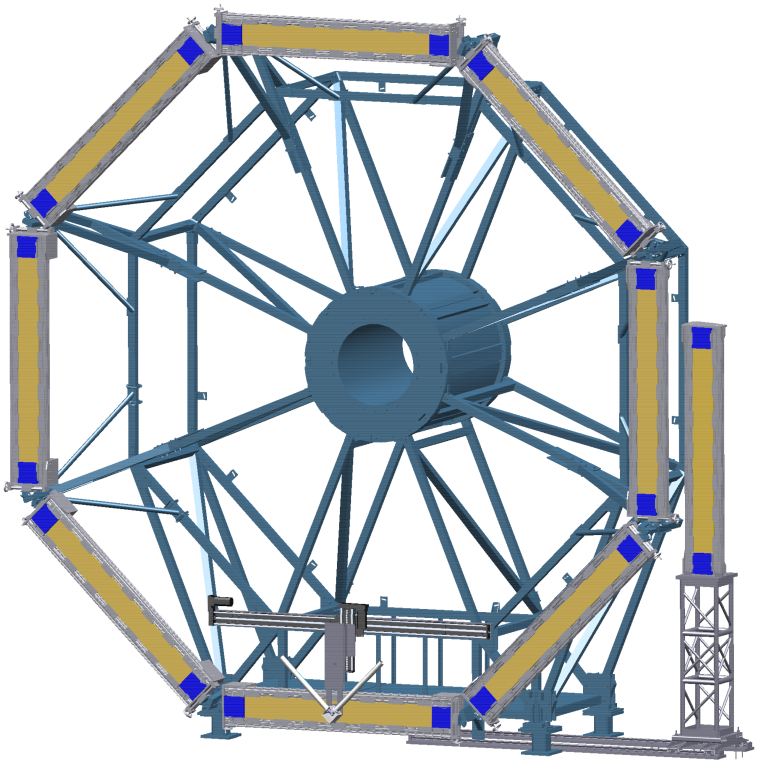

Figure 3.1: A CAD drawing of the full main detector array.

When a particle passes through a material with a velocity greater than the local phase velocity of light in that medium, a burst of light is emitted in a well-defined cone. This is called Čerenkov radiation, and the angle of the emission cone for the produced light is given by the following equation:

$$\cos\theta = \frac{1}{\beta n}. \tag{3.1}$$

where θ is relative to the electron angle of incidence, $\beta = v/c$ is the particle's velocity and n is the index of refraction for the material.

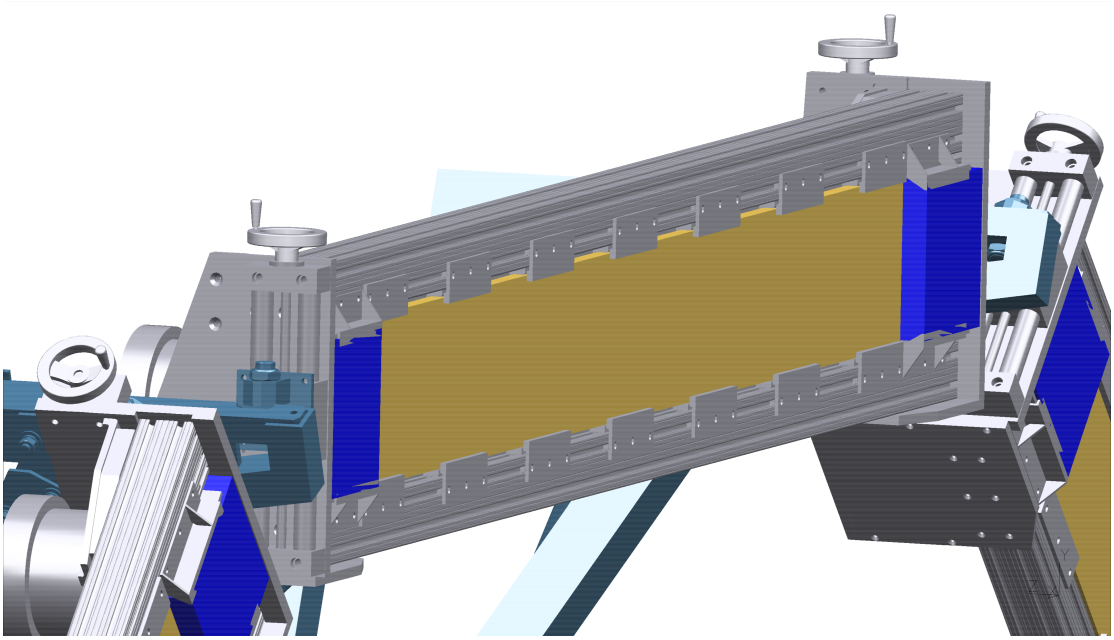

Figure 3.2: A CAD drawing of a single quartz bar detector in its housing. Blue blocks on either end represent lead shielding placed in front of the photomultiplier tubes.

The index of refraction for the synthetic quartz material used in Q_{weak} is $n = 1.482$ for 280 nm light. For 1.1 GeV electrons, this results in a Čerenkov angle of $\sim 48°$. Light produced at or above this angle was totally internally reflected and therefore transported to the two photomultiplier tubes (PMTs) on either side of the quartz bar. Each PMT (Electron Tubes 9312WKB) had a diameter of 13 cm (Figure 3.4) and was optically glued onto a light guide at either end of the bar; the light guide was a simple 20 cm extension of the main quartz bar. Placing the PMTs at these locations ensured that they were outside of the elastic envelope as shown in Figure 3.3.

Data taken during the Q_{weak} commissioning period showed that the component of the main detector signals corresponding to low energy neutral particles was larger than desired. One solution to this problem had already been studied extensively in Monte Carlo simulations: the addition of a thin pre-radiator material on the upstream face of the quartz bars. The advantages of such a system were twofold: to stop the low energy neutrals and to provide an initial multiplicative gain factor by means of electron showering in the material. For a 1 GeV electron, a maximum number of shower elec-

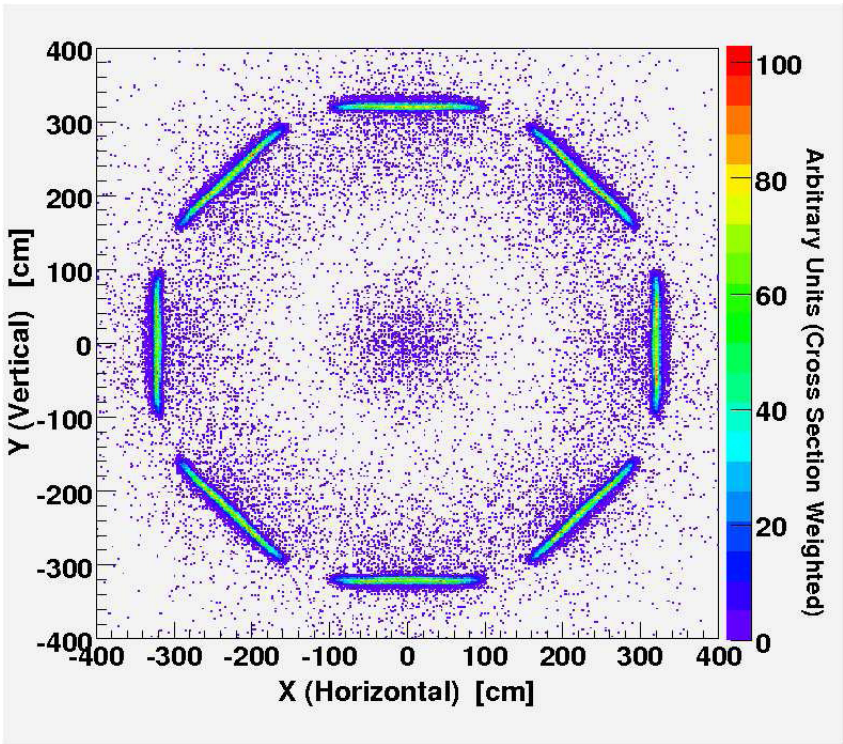

Figure 3.3: Simulated profile of the scattered electron flux at the main detector plane.

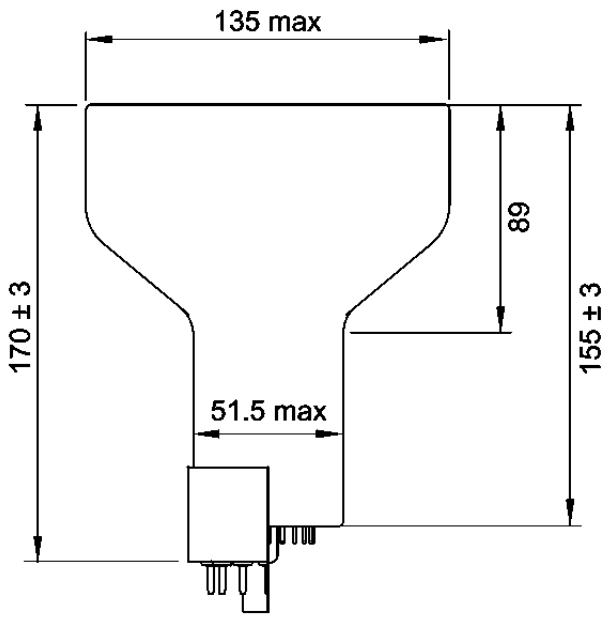

Figure 3.4: The 9312WKB photomultiplier tube by ET Enterprises, used for the main detector subsystem. Dimensions are in nm.

trons are generated when using a 2 cm thickness of lead as a pre-radiating material (See Figure 3.5). Lead tiles of that thickness were therefore added in front of the quartz prior to the start of production data acquisition. Simulations and early tests comparing bare and pre-radiated bars confirmed that the ~ 12% degradation of detector resolution resulting from the showering was small compared to the improvement in the signal-to-background ratio[5]. Each of the 16 main detector PMTs (2 PMTs per bar × 8 bars)

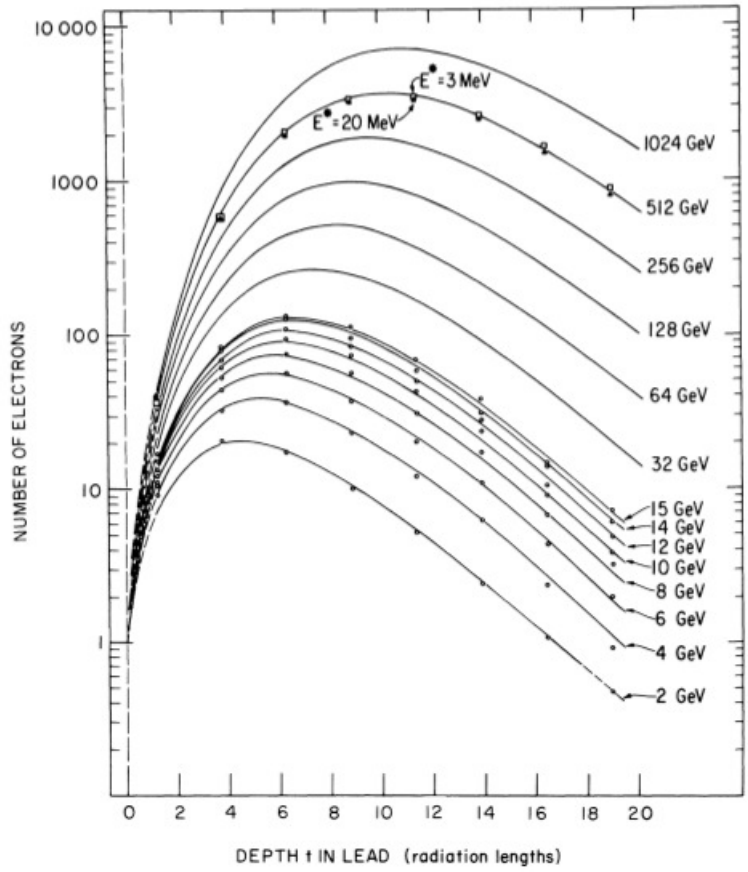

Figure 3.5: Electron scattering shower production for lead [52]. It can be estimated that the amount of showering is at a maximum at ~ 4 radiation lengths for 1 GeV electrons. Since the radiation length of lead is 0.5612 cm[8], the optimal thickness of lead for showering is ~ 2 cm.

could be read out in either integrating or event mode, where the only change in hardware was a swapping of the PMT base. Given the high beam current during periods of production data acquisition, the PMTs had to be operated at low gain to ensure stable,

long-term operation. Event mode data on the other hand, required a high single photoelectron resolution, necessitating high gain bases. Event mode spectra were required for use in detector calibration and efficiency tests. In order to be operated at the highest possible gain, high gain PMT bases were designed and constructed at Jefferson Lab. All 10 dynode stages of the high gain PMT bases were actively used, resulting in a net gain of approximately 2×10^6. The low gain bases were produced and tested at the University of Manitoba and are discussed in detail in the following section.

The main detectors were extensively simulated, using GEANT4. The simulation was designed to be as accurate as possible both in terms of detector design, component geometries, and physical processes. The simulated detectors included the quartz bars, glue joints between the two 100 cm segments, light guides, photomultiplier tubes, aluminum detector and PMT housings, lead shielding on the upstream face of the PMTs, and lead preradiators. Final positions, sizes, and orientations of the quartz bars were determined using these simulations[5]. In addition to being used during the design phase of the experiment, the simulation was also used to study the effects of certain physics processes (such as scattering from the aluminum target windows) and acceptance-based systematics.

Both simulations and early data indicated that events detected along the length of the bar vary in their momentum transfer (Figure 3.6). Simulations also showed that the light yield changed as a function of hit position on the bar (Figure 3.7). The size of this effect depends on the detector tilt angle with respect to the incoming electron. The minimization of this non-uniformity with a choice of zero tilt angle was confirmed using simulations. Since the physics asymmetry is dependent on Q^2, the coupling of these two phenomena can result in an experimental bias. The use of simulated data to correct for this effect will be discussed in Chapter 4.

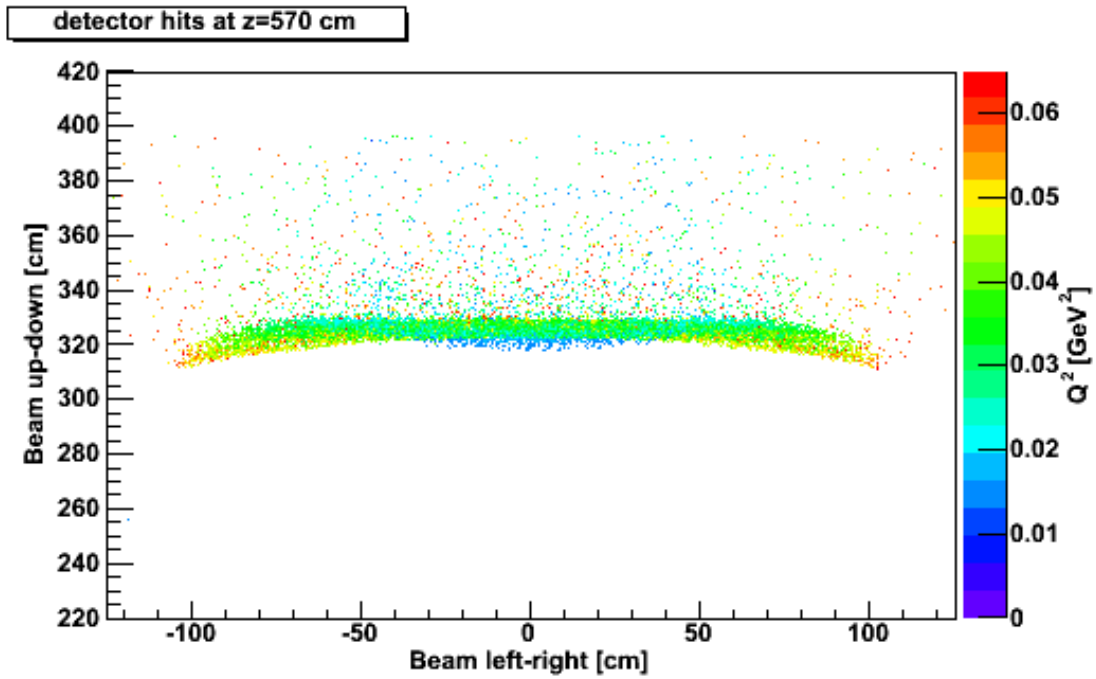

Figure 3.6: Simulated momentum transfer distribution for elastic events across the quartz bar. Taken from [5].

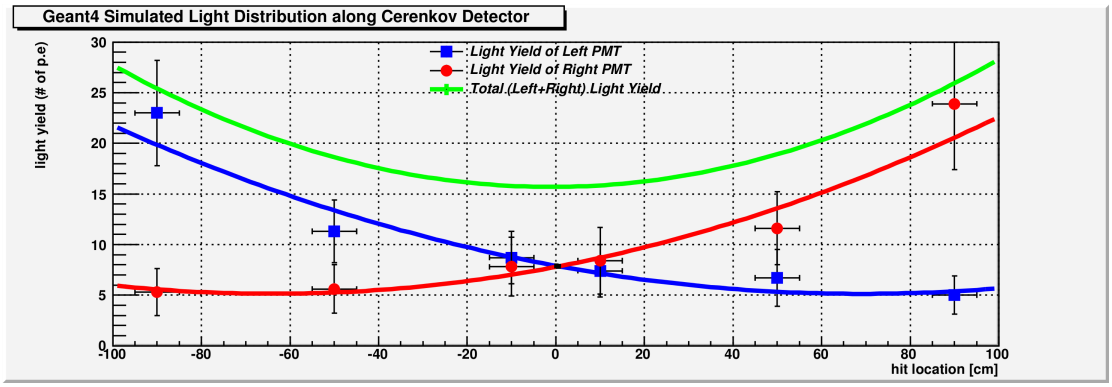

Figure 3.7: Simulated variation of the light yield measured in each photomultiplier as a function of event position along the face of the main detector. Events in this particular simulation hit the bar with a trajectory normal to the bar's surface. Taken from [5].

3.1.1 Low Gain Bases

The low gain PMT base was created with a design goal of < 0.1% nonlinearity at a gain of 1000 and 6 nA photocathode current[53]. The design evolved over a period of initial tests from using only the first four dynode stages to using seven[54][55]. The final design included a pair of zener diodes to fix the potential difference between the photocathode and the first dynode stage; this leads to an initial cascade that is independent of the bias voltage. Identical zener diodes located at the final stage of the PMT help to maintain stable anode currents, where the PMT's inherent non-linearity (no matter how small) would amplify the signal's instabilities. A bleeder resistor was added at the output, parallel to ground, to discharge the anode during periods when the base is disconnected and powered off.

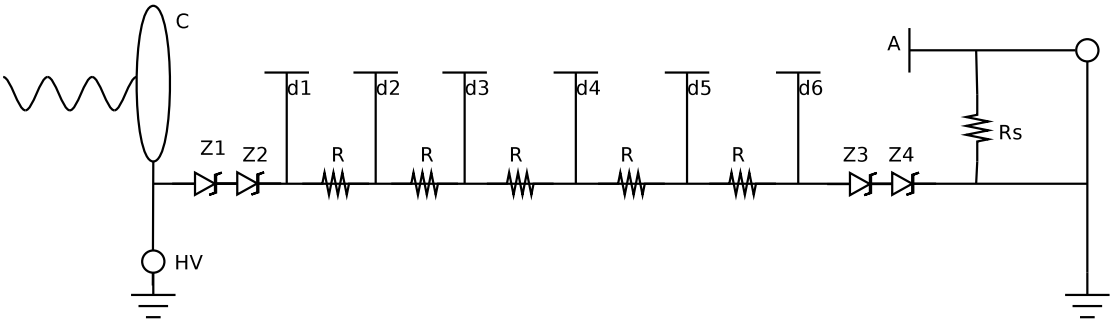

Figure 3.8: Schematic for the low gain current mode photomultiplier PMT base. Two 140 V, 5W rated zener diodes (Z1-4) maintained stable voltage drops at the first and last stages of the divider. Identical 1kΩ, 0.5 W resistors are labeled as R in the figure and R_s is a 10 kΩ, 0.5 W safety resistor.

In order to properly set the individual PMT gains for integrating mode, we needed to know how the gain changed with high voltage. A test stand was developed at the University of Manitoba to measure the current at the anode and cathode with and without a photoelectron signal in the PMT. The test signal light was generated by several UV diodes (250-350 nm) powered by a BK Precision 1670A power supply mounted in front of the PMT. The entire apparatus was placed inside a light-tight box, and anode current measurements were made using the actual Q_{weak} bases. Measurements of

the cathode current were acquired by altering an extra base so that all dynode stages were bypassed, resulting in a *diode mode* base with no signal gain[56]. Gain curves are reproduced in Appendix D which allowed for gains of all 16 main detector PMTs to be matched when configuration changes required changes in gain[†]. 21 low gain bases were required during production data acquisition (16 for the main detector bars, 5 for background detectors), and bases from the set of 4 extras were swapped in as needed when a base was damaged. One such swap occurred during the commissioning period after the high voltage lead within the base arced to the base housing.

3.2 Performance

3.2.1 Tracking Mode

During tracking mode, Q_{weak} ran at greatly reduced beam currents on the order of pA to nA. During these periods individual electron tracks could be determined and used to reconstruct the momentum and angle of the scattering event. High gain bases were installed onto the main detector PMTs during these times. This section will outline how the main detectors performed during tracking mode measurements.

During tracking mode data acquisition, the main detector signals were processed by three different DAQ modules: QADC's (charge ADC's, which measure how much charge is created in the PMT as a result of the light that is generated in the quartz and strikes the photocathode), F1TDC's (fast multi-hit TDC's, which provided timing information for each event), and simple scalers. Though these signals were not required for any direct asymmetry analysis, they provided data necessary for building particle track information alongside useful diagnostic data. Figure 3.9 displays a typical main detector photoelectron spectrum with x-axis units of photoelectrons, which were converted

[†]Gains were changed on a few occasions, including as a response to pre-radiator installation, and during studies where detector rates were lower than usual but high statistics asymmetry measurements were required.

from raw ADC channels by using carefully extracted conversion factors. These "adc channels per photoelectron" calibrations were determined during Q_{weak} tracking mode running using dimly lit pulsed LEDs[‡]. By triggering the data acquisition on the LED drive signal we obtained spectra that could then be fit to a basic Poisson distribution. The calibration factor as well as the average number of photoelectrons per event were then extracted as parameters of the fit. A complete set of calibration data is provided in Appendix C along with photoelectron spectra for all main detector PMTs.

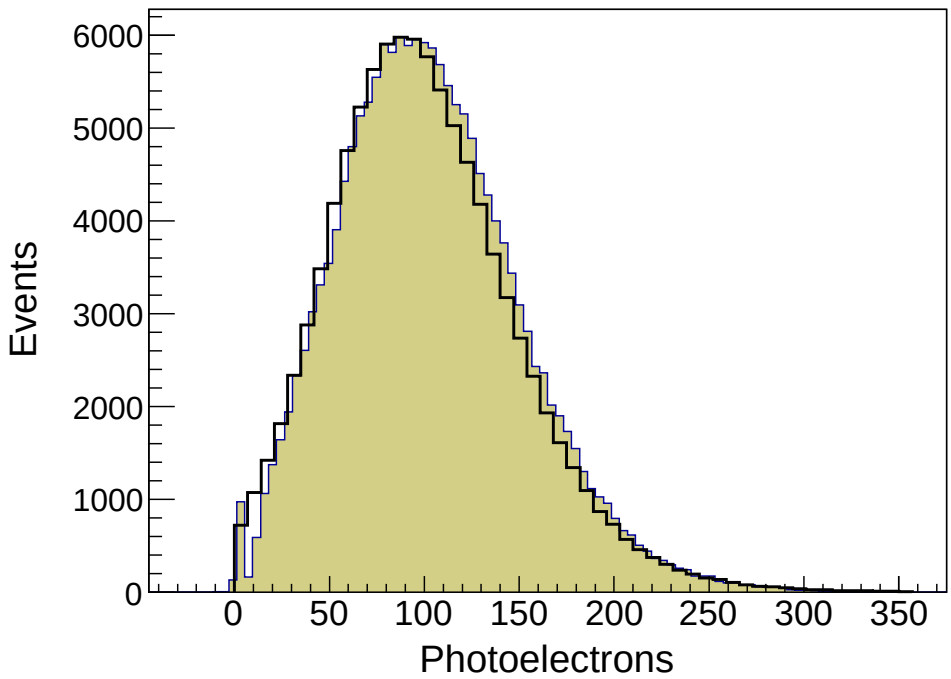

Figure 3.9: Simulated (curve) and measured (shaded) photoelectron spectrum for a typical main detector. The spectrum corresponds to the summation of events in both PMTs for a single quartz bar with a lead preradiator. Pedestals were removed from this spectrum, and were also removed during high current data acquisition.

Comparing the signal size measured in current mode (discussed in the following section) to that expected from event mode data was done by studying the main detector response to a varying magnetic field strength in the QTOR spectrometer. Varying the current supplied to the magnet had the effect of moving the envelope of elastically scat-

[‡]Details on these LED systems can be found in [5]

tered electrons radially, and focusing events corresponding to other physical processes (Møller, inelastic scattering) onto the quartz bars. The relevant equation to consider when doing this study is the voltage signal of the main detector, given by

$$V = \text{Rate}\left[\frac{Hz}{nA}\right] \times I_b[nA] \times e[C] \times R[\Omega] \times G_{\text{PMT}} \times < \text{N}_{\text{PE}} >, \tag{3.2}$$

where the rate is extracted from a TDC analysis done on real tracking mode ($\sim$ 10 nA) data as described in [40], I_b is the beam current, $e = 1.602 \times 10^{-19}$ C is the charge of the electron, $R = 2\,\text{M}\Omega$ is the effective impedance of the main detector signal chain with PMTs having gain G_{PMT} and $< \text{N}_{\text{PE}} >$ is the average number of photoelectrons generated in that PMT per event. Confirmation that tracking mode and integrating mode results are consistent with one another was achieved by calculating the expected signal for various QTOR currents using Equation 3.2 and comparing them to signals observed during a similar study performed at high current ($\sim$ 180 μA).

In order to perform this check, $< \text{N}_{\text{PE}} >$ would need to be measured at each QTOR current to account for the energy dependence introduced to the light yield of the detectors by showering in the pre-radiators. This information was extracted from tracking mode runs completed with a trigger scintillator trigger. Because no main detector-triggered data were available, the extraction of $< \text{N}_{\text{PE}} >$ is sensitive to timing cuts on the trigger scintillator. Performing these cuts and looking only at events triggered in the correct octant gave the best measurement of $< \text{N}_{\text{PE}} >$ as a function of QTOR current[57]. Figure 3.10 shows how the average number of photoelectrons generated per event varies with changing QTOR current. Comparing the expected signals calculated using these new photoelectron numbers with signals measured during a current mode QTOR scan could then be performed. Lowering the QTOR field results in the elastically scattered electrons deflecting less through the spectrometer, thus missing the main detectors and generating a smaller signal. The results of this study are shown in Figure 3.11 where

we see a $\sim$ 2% deviation between calculated and measured signals at QTOR currents near standard production levels (8921 A). Given the precision to which the photoelectron calibrations are known, this was deemed acceptable. Significant differences at the level of 30% at the lowest QTOR field settings are not fully understood, but could be attributed to poor extraction of $< N_{PE} >$ at low QTOR current. This discrepancy has no effect on the final asymmetry analysis.

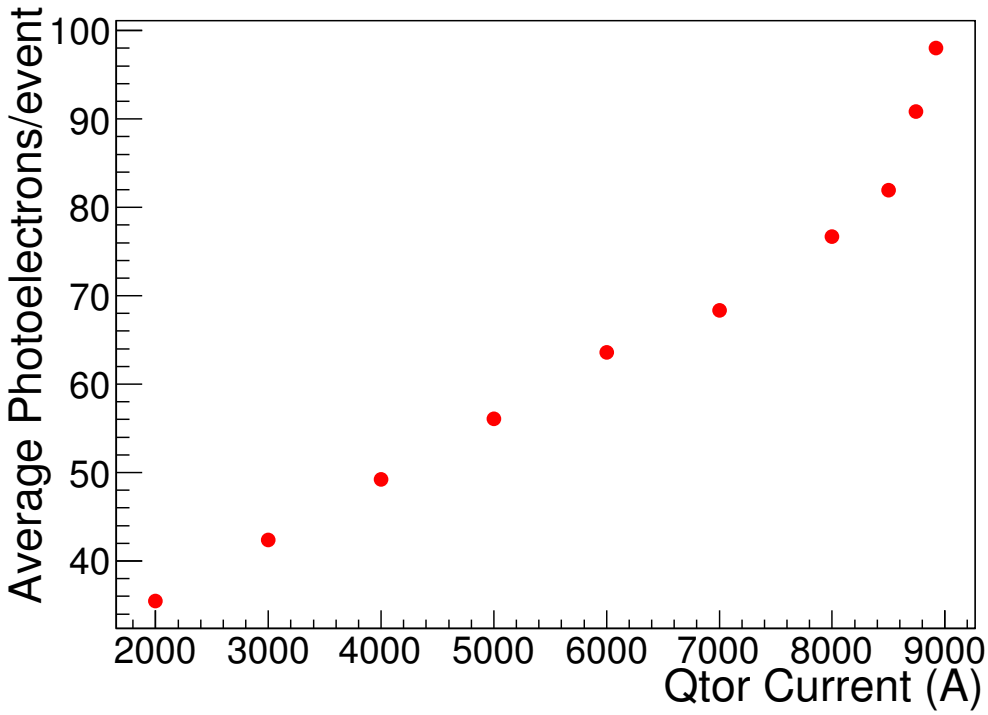

Figure 3.10: Variation of the average number of photoelectrons generated per event varies with QTOR current.

In addition to kinematic reconstruction and determining detector properties, tracking mode data were used to test the main detector PMT housings for possible light leaks. By looking at scaler rates from all main detector PMTs during runs with the detector hut lighting off or on, we were able to identify light leaks in octants 1 and 6 prior to Run-II. Periodic light leak testing was performed throughout the experiment with no additional instances of leaks detected beyond the joint inspection.

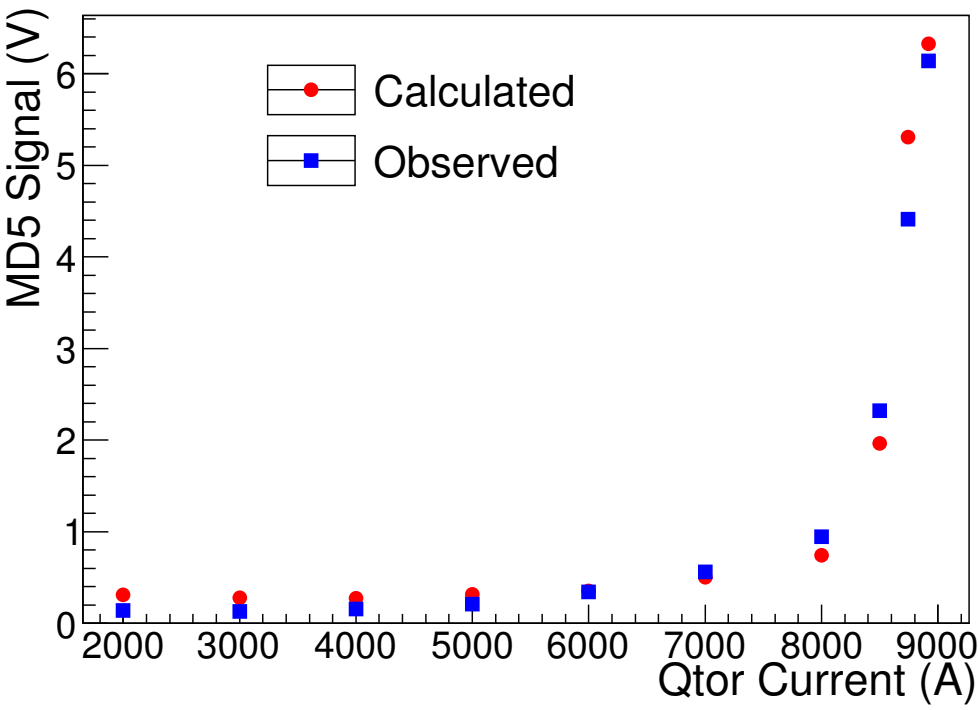

Figure 3.11: Main detector signals as a function of QTOR current. "Observed" data corresponds to detector signals measured during a high current QTOR scan. "Calculated" points represent the signal expected at that QTOR current based on rates and photoelectron yield numbers determined from tracking mode.

3.2.2 Integrating Mode

In integrating mode, a single data sample corresponded to the integrated detector signal over a single macropulse (MPS), during which the beam helicity was unchanged. The short integration windows (defined by the fast helicity flip rate) reduced noise coming from target density fluctuations and other longer timescale drifts in the signal (such as gain changes in the PMTs due to temperature drifts). Four consecutive helicity windows were used in the calculation of an asymmetry, as described in Section 2.1. In this mode of acquisition, the primary quantities of interest were the individual main detector PMT yield (the PMT voltage divided by the beam current) and asymmetry distributions. Hourly inspections of histograms allowed for rapid identification of problems in the signals, including 60 Hz noise. Figure 3.12 shows a typical PMT yield signal over two minutes of data, both before and after being normalized to the beam current. Target boiling would appear as sudden decreases in detector signal on this plot, when the beam passed through a bubble as opposed to a cell of uniformly distributed liquid hydrogen.

Monitoring changes in the RMS width of the main detector yield distributions allowed us to estimate how much noise was introduced into the system, keeping in mind that most noise sources for Q_{weak} were characterized by slow drifts that were not an issue for asymmetry measurements. The theoretical electronic shot noise floor at 960 Hz reversal frequency can be calculated using the following expression:

$$\sigma_{\text{shot}} = \sqrt{2 \times q \times I \times \frac{960\,\text{Hz}}{2}} \times R = 5.4\,\text{mV}, \tag{3.3}$$

where R is the effective impedance of the main detector signal chain, I is the PMT anode current, and q is the charge at the PMT's anode for each electron event. This noise is caused by the quantum mechanical nature of the conversion of photons into photoelectrons[58]. The calculation of a 5.4 mV shot noise floor is appropriate for running with a beam current of 180 μA. This represents a noise floor for a Gaussian

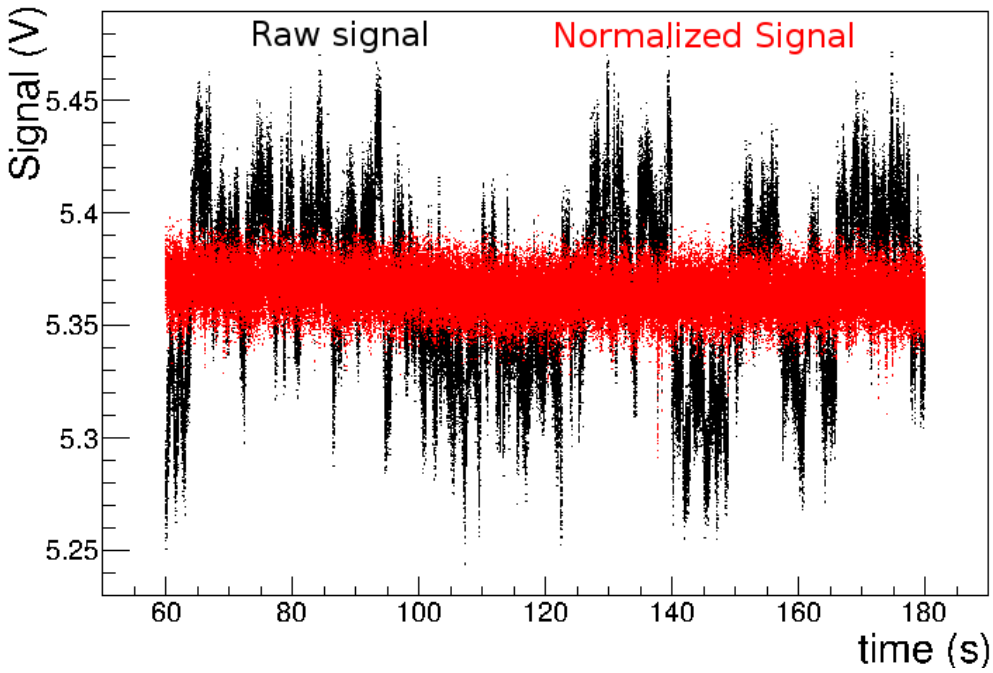

Figure 3.12: Two minutes of main detector data taken from a 180 μA run. The red points correspond to yield measurements that have been normalized to the beam current.

yield distribution. Comparing the observed yield widths to this noise floor then gives an estimate for how much additional noise is introduced into the main detector signal from sources such as target density fluctuation, standard electronic (Johnson-Nyquist) noise, and noise resulting from the electrons showering within the lead preradiator, which was not accounted for in Equation 3.3. Figure 3.13 compares the noise floor with raw and current-normalized main detector yield widths for a single PMT. Normalization of the detector signals by the beam current removes, to first order, the effects from variation in the beam intensity.

Monitoring of the main detector asymmetry widths was performed hourly throughout integrating mode data acquisition as a method for determining the general health of the experiment. A sudden increase in the RMS width of the quartet level asymmetry distribution could be attributed to the appearance of an unwanted background caused by poor beam conditions or damaged/misconfigured hardware. Typical main detector

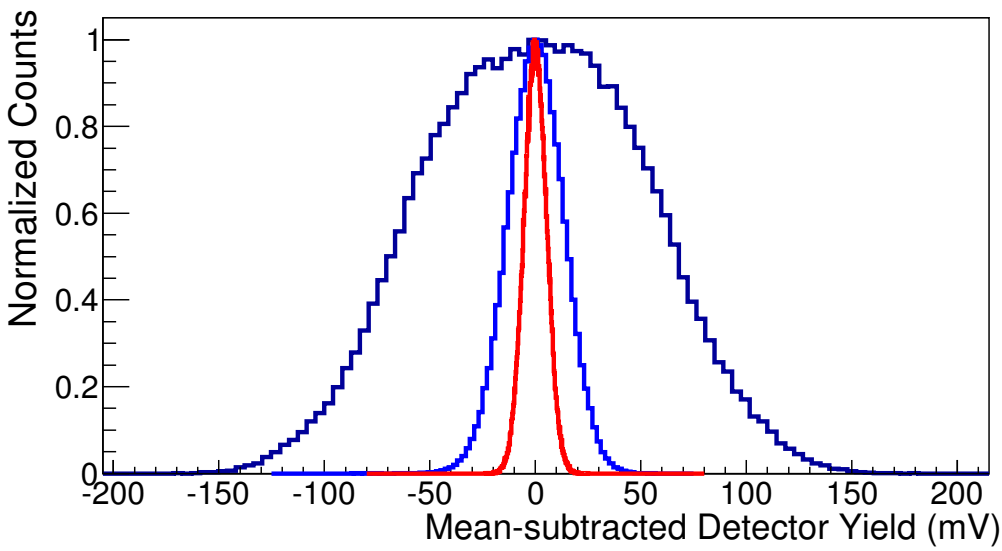

Figure 3.13: A typical 6 minute main detector PMT yield distribution. Means are subtracted to allow for comparison of the widths. The dark blue curve (σ = 50.4 mV) corresponds to the raw detector signal. The light blue distribution (σ = 13.4 mV) is the same data after having been normalized to the beam intensity. The red peak is a Gaussian distribution with a width corresponding to the 5.4 mV shot noise factor estimated in Equation 3.3. The difference between the red and light blue curves is discussed within the body of this section.

asymmetry distributions for a single PMT and the entire array are presented in Figure 3.14. In the absence of any correlations one would expect a decrease in asymmetry width of $\sqrt{16}$ between a single PMT and the full array. Because the two PMTs on a single bar are highly correlated we see a reduction that is closer to $\sqrt{8}$. Main detector width behaviour over the course of Run-II will be discussed further in the context of data quality in Section 4.2.

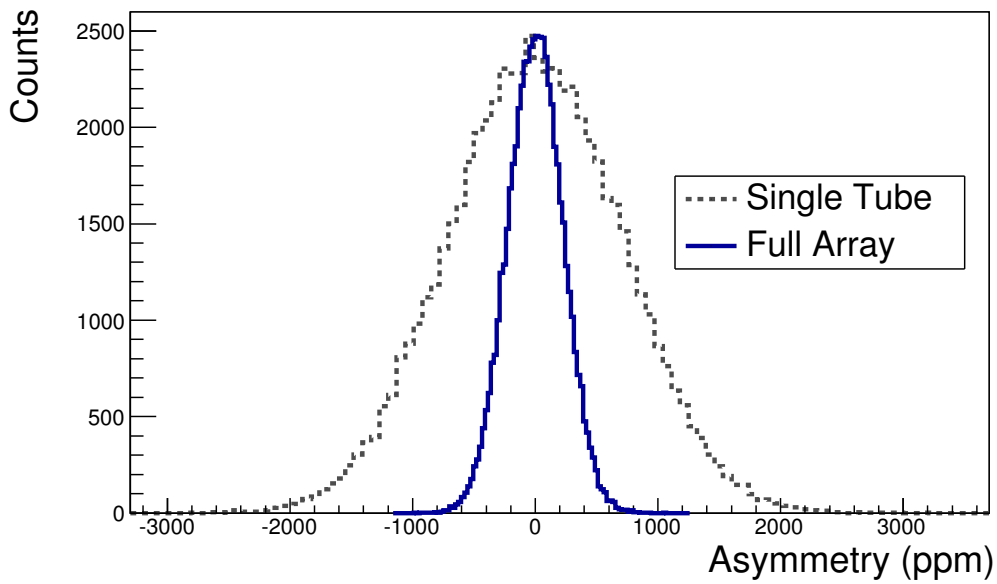

Figure 3.14: Typical asymmetry distributions for 6 minutes of data. A single-PMT RMS width of ~ 700 ppm for a 180 μA beam current is observed whereas the full 16 PMT combination has a typical asymmetry width of 225 ppm.

3.2.3 Stability and Pedestals

Any experiment that acquires data over an extended running period will have to study the effects of instabilities in any of the experimental parameters that enter into the asymmetry and attempt to quantify the impact they could have on the final result. Significant changes in detector response could be the result of a systematic issue that must be considered carefully in post analysis. For example, a sudden significant change in pho-

tomultiplier signal could be the result of PMT damage resulting in a change in gain; the products of studies relying on these yield measurements (for background dilution factors or transverse leakage, discussed in Chapter 4, for instance) could suffer as a result of not accounting for this change.

In order to properly remove any beam-off signal in the main detector, a dedicated *pedestal run* was taken approximately once every eight hours. Since the magnitude of the pedestal is determined by the electronics (the phototube dark current, preamplifier offset/gain, etc.) a significant change in pedestal would serve as an alert to a potential hardware failure. Figure 3.15 shows the pedestals for a single PMT over the full Q_{weak} running period. The sudden change near run 15000 corresponds to a period during which the temperature in the electronics room was not being regulated: this resulted in many channels fluctuating together. The 16 main detector PMTs all saw a similar increase in pedestal over the course of the experiment, with the effect varying from $7-15\%$ from PMT to PMT. Possible sources for this increase include PMT degradation resulting from continuous high current use and mild radiation damage. Since the drift is much slower than the helicity frequency, there was no effect in measured asymmetries from pedestal drifts.

In addition to monitoring pedestals, the detector yields themselves were also studied. Decreases in beam current-normalized detector yields tracked the same trends (though inverse) as shown in Figure 3.15: with discrete jumps occurring when phototube high voltage was changed or other temporary issues with electronics (blown fuses, room heating) were encountered. Differences in gains and the relative rate of drift over time between individual photomultiplier tubes can cause problems when performing asymmetry calculations (See Section 4.1). In order to minimize these issues, a PMT weighting scheme was introduced that would be applied to combinations of phototubes that could later be used for event-level (as opposed to asymmetry) analysis. Tube combinations were generated by applying a weighting factor w_i to each PMT in

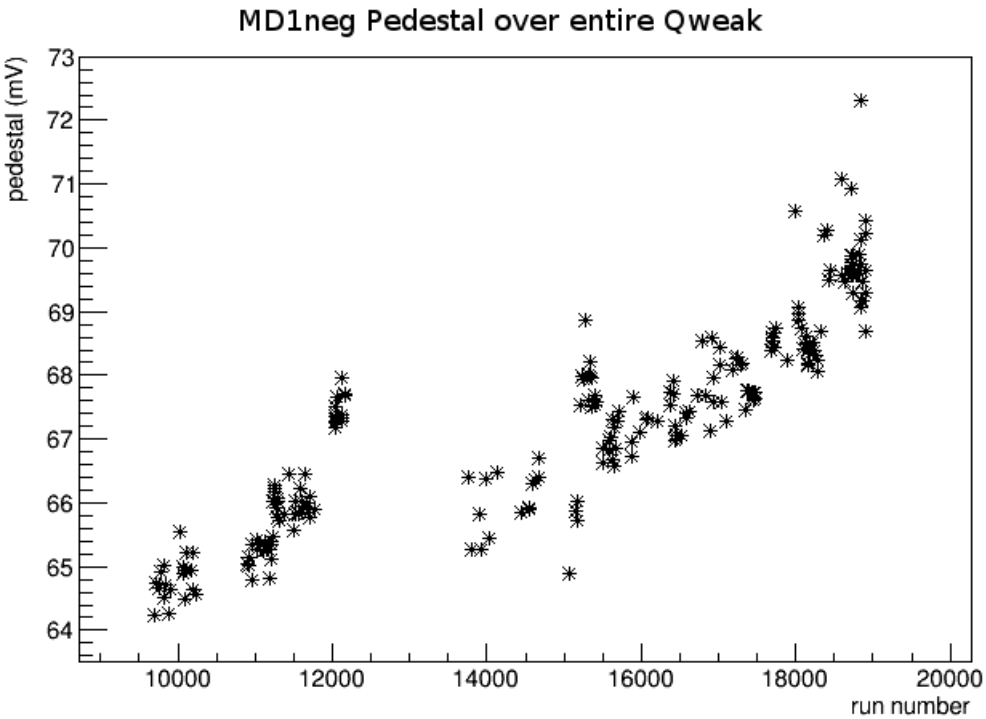

Figure 3.15: Measured pedestal signals versus run number for a typical main detector PMT over the entire Q_{weak} experiment.

the combination:

$$Y_{\text{weighted}} = \frac{\sum_i Y_i w_i}{\sum_i w_i} \tag{3.4}$$

with i running over all PMTs in the combination of interest and

$$w_i = \frac{1}{< Y_i >} \tag{3.5}$$

calculated over a period of roughly constant detector yield. This choice in weights was done in order to account for differences in gains from one PMT to another. The entire Q_{weak} running period was separated into approximately 30 sections during which either the main detector PMT drifts were less than a few percent or a significant change in conditions took place[§]. We confirmed that using these weights addresses differences in gains by calculating the "normalized weighted yield" over time, computing the ratio of each weighted PMT to the sum of all PMTs in the combination:

$$Y^{\text{norm}}_{i,\text{weighted}} = N \times \frac{Y_i/w_i}{\sum_j^N Y_j/w_j} \tag{3.6}$$

where i is a single PMT in a combination of N PMTs. In the case where the weights w_i perfectly account for differences in PMT gains (so that each electron generates the exact same signal, regardless of which PMT is read out), this expression will equate to one. Figure 3.16 shows the level of stability introduced to the yields over time by including these weights. This stability was required for any yield-based analysis that went into determining corrections to the measured asymmetry (see Chapter 4).

The long-term stability issues discussed above were only relevant when performing analysis using detector yields, but had minimal impact on the measured asymmetry. Instabilities, drifts, and noise sources that were relevant at the millisecond-second

[§]Examples include dedicated running time for auxiliary measurements like Aluminum or N $\rightarrow$ Δ backgrounds.

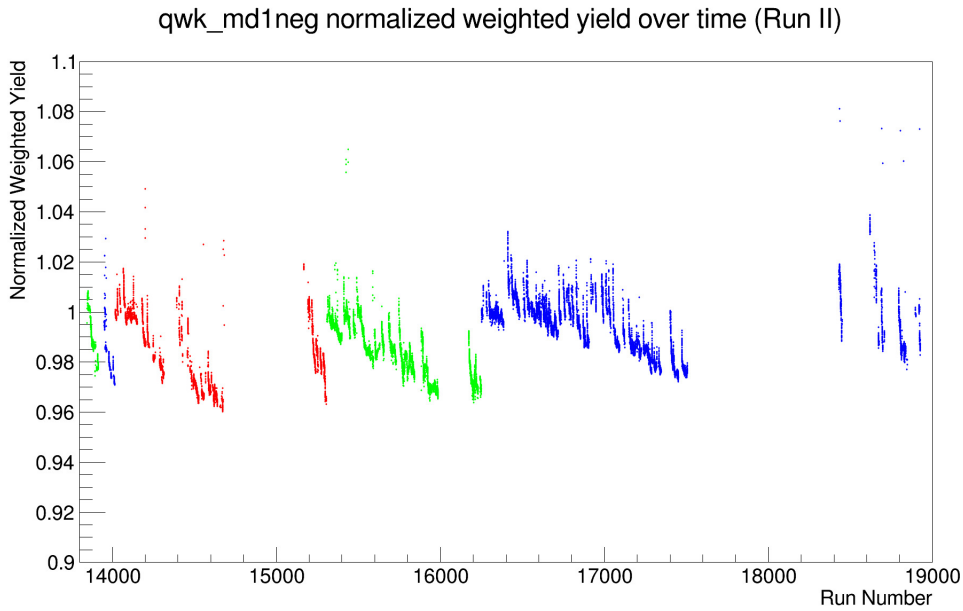

Figure 3.16: Normalized weighted yields for a typical main detector PMT over Run-II. Normalization factors were extracted and introduced into certain PMT combinations in order to minimize the effects from relative drifts between PMTs over time. Colour transitions in the plot correspond to the introduction of a new averaging period to determine the weights in order to bring the value closer to unity.

timescale could have manifested themselves as false asymmetries in the primary measurement if they were helicity correlated. If no correlation to the beam helicity was present then the result was an increase in the RMS width of the asymmetry distribution, resulting in a need for more data to reach the same relative precision. Some of these effects were minimized during data acquisition by the feedback systems mentioned in Section 2.2.1, but these systems were unable to eliminate sporadic events when detector or monitor signals changed suddenly. A discussion of how detector stability cuts addressed these types of events is presented in Section 4.2.

One of the primary reasons for choosing quartz bars for the main detectors was their radiation hardness. One possible explanation of the monotonic decrease in detector yields across all PMTs observed over the whole Q_{weak} data set (see Figure 3.17) is that the radiator material was suffering from radiation damage. Without an unobtrusive method to perform a visual inspection of the bars to search for discolouring, a method

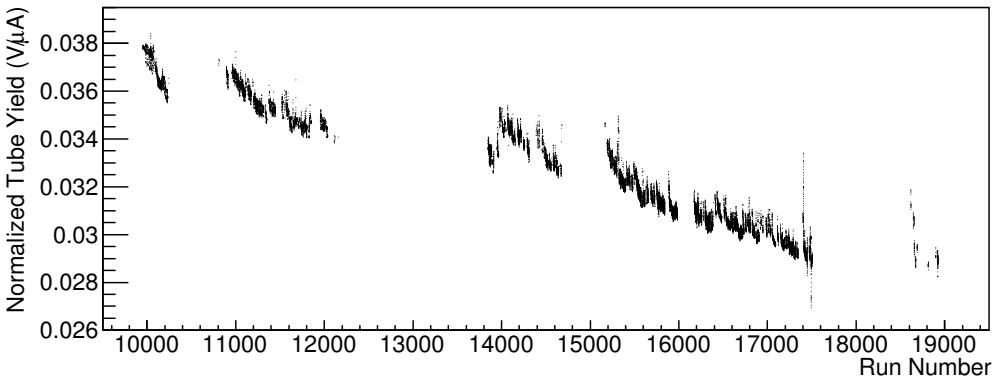

Figure 3.17: Change in measured yield over the entire Q_{weak} experiment for a typical main detector PMT. The slow decrease is attributed to PMT aging.

was developed that used tracking mode data to quantify the change in attenuation of light along the bar over time.

Figure 3.18 shows the ADC spectra for two PMTs plotted against hit position along the length of the bar. Discontinuities at the centre of the bar are the result of light loss across the glue joint, but the slope on either side is a measure of how much the light is attenuated as it passes through the quartz. In the case where significant radiation damage was occurring, the loss of light from events generated far from a PMT would increase over time as the material accumulated more dose (a change in slope in Figure 3.18). Figure 3.19 shows that no significant change in light attenuation across the bar was observed over the course of the experiment for a typical detector. Because of this, we attribute the structure observed in Figure 3.17 to simple aging of the PMT.

3.2.4 Linearity Studies

The nonlinearity of the main detector was studied through a number of tests both during Q_{weak} and after the experiment had completed. These tests included in situ studies using LED's located inside the PMT housings when beam was unavailable, as well as bench tests both before and after the experiment was performed.

A simple 2-LED bench test performed prior to the experiment concluded that the

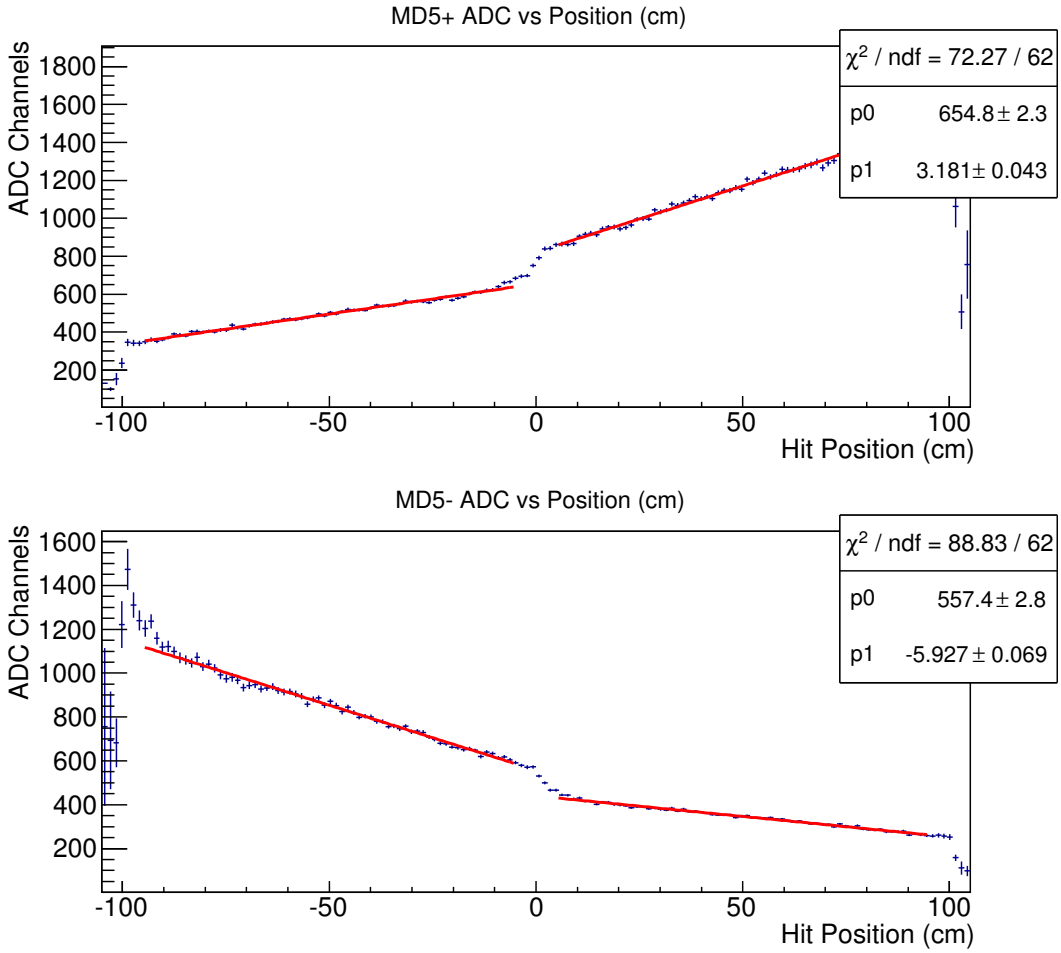

Figure 3.18: Main detector PMT ADC spectra as a function of hit position along the bar. The PMT is on the right-hand side in the top plot and the left in the bottom plot. The slope p1 is a measure of light attenuation along the quartz and discontinuities in the middle are a result of light loss across the glue joint.

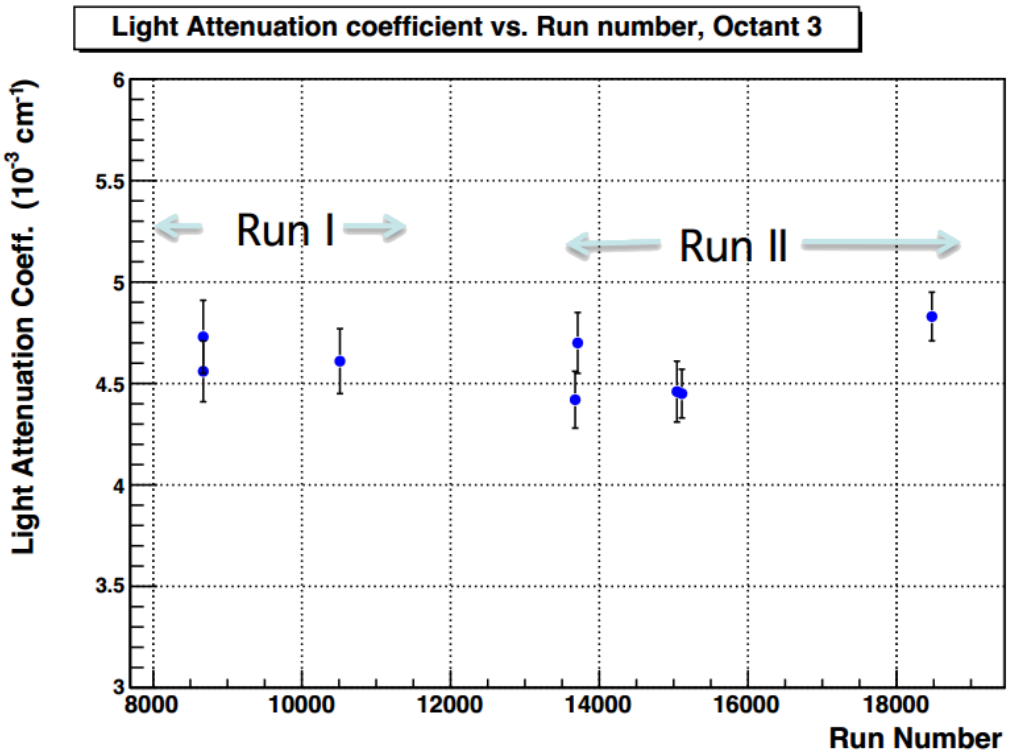

Figure 3.19: Light attenuation coefficient measured during different periods in the experiment. The value is defined as the change in photoelectrons generated at the PMT cathode over different hit positions along the bar, as shown in the slope of Figure 3.18. Averages of slopes taken for each of the four PMT's in octant three (measured using the slopes nearest to the PMT) are presented. A change in coefficient could suggest a decrease in light transmission through the bar caused by radiation damage. The stability of points illustrates the radiation hardness of the synthetic quartz material.

main detector PMT-base combinations were linear at the $10^{-5} - 10^{-4}$ level[5]. This test assumed a model in which a small, fixed-magnitude AC signal was superimposed on a large constant DC signal; in terms of the experimental measurement, this mimics the small parity-violating signal on top of the average signal. During a real experiment however, the system is not as simple as this, and so a more complex 3-LED test was designed after the experiment's conclusion to emulate the real system more closely. In this 3-LED test, a second AC signal was introduced with a frequency of 10 Hz, significantly lower than the helicity flip rate. This system was designed to imitate a signal that drifts slowly (compared to the helicity reversal): an example of such an effect would be gain changes in the photomultiplier tubes due to temperature drifts. In order to maintain confidence in the result, an exact copy of the detector chain (from PMT to analysis by our software) was used.

A measurement of the relative non-linearity x of the PMT was made by comparing the change in the PMT's response to the fast LED when the slow LED was on or off:

$$x = \frac{1}{2}\frac{dV_f/V_f}{dV_m/V_m} \tag{3.7}$$

where dV_f is the amplitude of the PMT's response to the high frequency LED and dV_m is the change in average voltage between the slow LED states. The factor of $1/2$ is a result of expressing the PMT anode current in terms of the LED intensities and is derived in details in [59]. In the 3-LED test, four different light conditions could be met at a given time as shown in Figure 3.20. We define the signal size during these conditions as $V_{i,j}$ where i (j) is the status of the slow (fast) LED, resulting in the four quantities $V_{\text{on,on}}$, $V_{\text{on,off}}$, $V_{\text{off,on}}$, and $V_{\text{off,off}}$. V_f and V_m can be defined in terms of these quantities:

$$
\begin{aligned}
V_f &= \frac{(V_{\text{on,on}} - V_{\text{on,off}}) + (V_{\text{off,on}} - V_{\text{off,off}})}{2} \\
dV_f &= (V_{\text{on,on}} - V_{\text{on,off}}) - (V_{\text{off,on}} - V_{\text{off,off}}) \\
V_m &= \frac{V_{\text{on,on}} + V_{\text{on,off}} + V_{\text{off,on}} + V_{\text{off,off}}}{4} \\
dV_m &= \frac{V_{\text{on,on}} + V_{\text{on,off}} - V_{\text{off,on}} - V_{\text{off,off}}}{2}.
\end{aligned} \tag{3.8}
$$

The nonlinearity x can then be determined by measuring the four signals and using Equations 3.7 and 3.8.

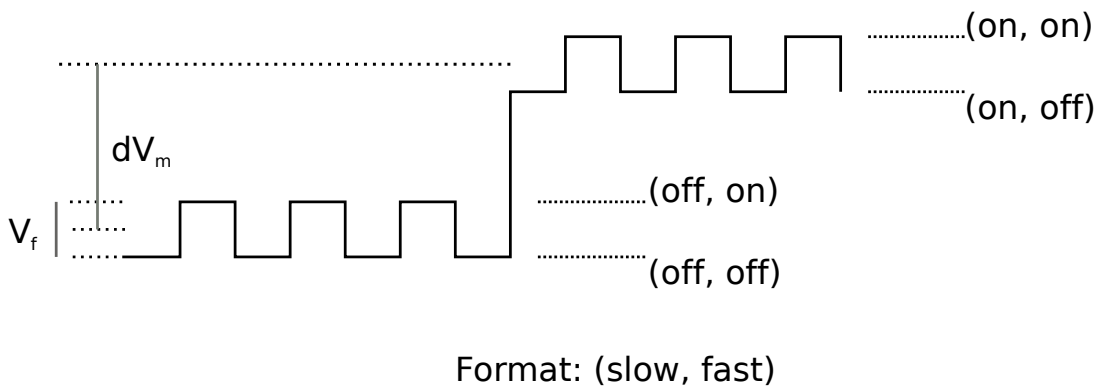

Figure 3.20: Here we see a diagram showing the signal structure of the PMT during the 3-LED test. V_f is defined as the amplitude of the high frequency structure and V_m is the average signal.

.

In addition to measuring the non-linearity itself, we were interested in how it might vary as the PMT voltage was changed. Figure 3.21 shows the measured non-linearity as a function of signal size, for two different PMT high voltage settings. The main detector PMTs were designed to operate at a gain of 2000, roughly corresponding to a PMT bias voltage of 1000 V. Upon the addition of the lead preradiators, gains were dropped by a factor of 10 by lowering the PMT voltage to approximately 800 V. Figure 3.21 shows that a measurable increase in non-linearity is observed in this low gain scheme. This can be attributed to space charge effects being larger for lower PMT bias. For

this single PMT, a non-linearity of $\sim$ 0.6% at 6 V was measured in the 800 V case. The non-linearity of the entire experiment can be estimated by looking at the main detector's sensitivity to beam current during regression (see Section 4.3). During Run-II this quantity varied between ±2% but is still under active study by the collaboration. This nonlinearity was deemed to be sufficiently small as the early designs called for corrections on the order of 1 ppb for non-linearities. Assuming a non-linearity of 2% and an asymmetry of 220 ppb results in a $\sim$ 4 ppb correction.

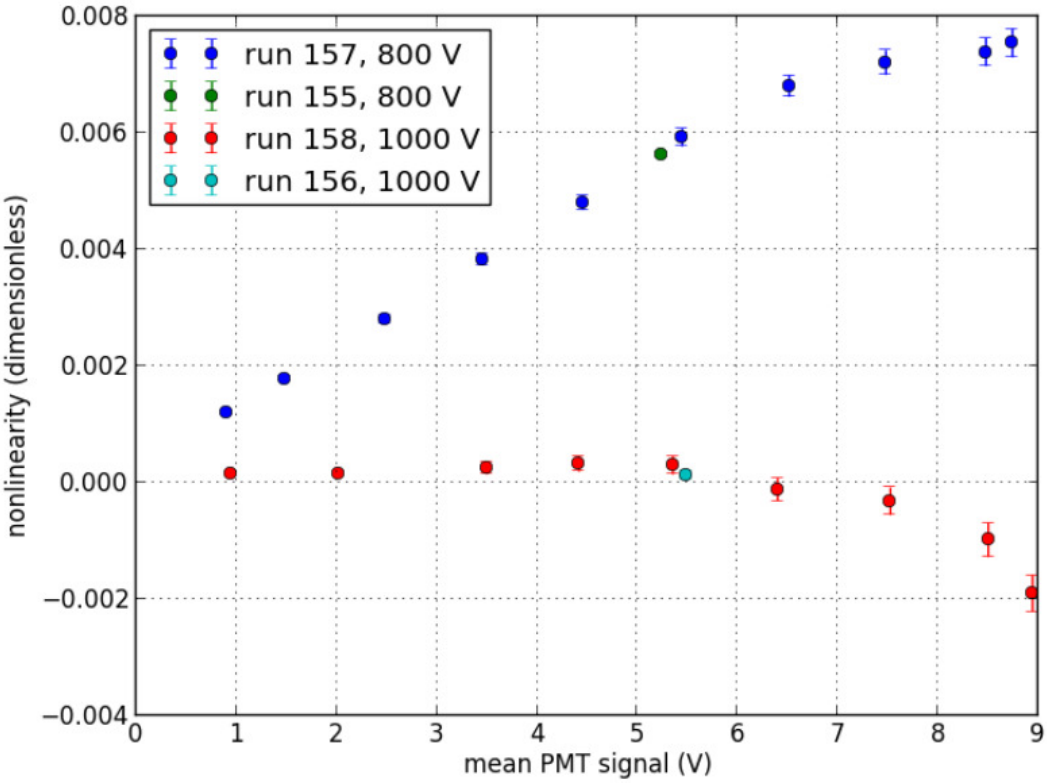

Figure 3.21: Non-linearities measured using a single main detector photomultiplier tube in a test environment after the experiment had concluded. Measurements were taken at different PMT bias voltages, and nonlinearities of $<$ 0.7% were observed. Typically running conditions resulted in signals of 4-7 V from the PMTs.

Chapter 4

Analysis

The goal of the Q_{weak} experiment is to determine the weak charge of the proton Q_W^p by measuring the parity violating asymmetry A_{PV}^{ep} in elastic $\vec{e}p$ scattering. This chapter will describe in detail the analysis that goes into extracting this asymmetry from the measured experimental asymmetry. A review of how to calculate an asymmetry from integrated detector signals will be provided, followed by a discussion on data quality. A number of corrections have to be made to the measured asymmetry to account for shifts resulting from helicity-correlated beam properties (e.g. position and energy) as well as competing physics processes such as inelastic scattering and scattering from the aluminum target windows. Finally, correcting for experimental biases will be reviewed before combining all corrections into an extracted A_{PV}^{ep}. The final equation that will combine all of these corrections is given by:

$$A_{PV}^{ep} = \frac{R_{tot}}{(1 - f_{tot})} \left[< A'_{msr} > - \sum_i f_i A_i \right], \tag{4.1}$$

where R_{tot} contains all multiplicative corrections (experimental biases and radiative correction), A'_{msr} is the measured asymmetry after being corrected for beam polarization, helicity-correlated beam differences, and beamline backgrounds, f_i is the fraction of main detector signal resulting from a background process, and A_i is the asymmetry as-

sociated with that processes (aluminum, inelastic scattering, and neutral particles). f_{tot} is defined as the sum of the fractions f_i, also known as *dilutions factors*. Each of these terms will be discussed in this chapter, with the final result being discussed in Section 4.10. Appendix A.4 provides simple descriptions of the various recurring symbols used throughout this chapter.

The Q_{weak} experiment had a number of time scales over which different pieces of analysis were completed. These periods were defined by the configuration of the accelerator accounting for flips in the sign of the beam's helicity with respect to the electron source. For instance, the insertion of half-wave plates (see Section 2.2) defined the beginning of a new *slug*. Each slug consists of approximately 8 hours of data and there were 184 slugs in Run-II (slugs 137-321, November 2011 - May 2012). Double Wien flips were performed approximately once per month and define *Wien* periods (1-5 in Run-I, 6-10 in Run-II). In addition to these two methods of slow reversal, an additional sign flip was introduced in Run-II as a result of g-2 precession in the accelerator*. Table 4.1 summarizes how the three reversal methods can independently introduce a sign flip to the measured asymmetry.

Slow Reversal	State	Sign Correction
Insertable Half Wave Plate	In	-1
	Out	+1
Double Wien Flip	Left	-1
	Right	+1
g-2 Precession	Yes	-1
	No	+1

Table 4.1: A summary of how slow reversal methods change the expected sign of the measured asymmetry. The expected sign of the asymmetry is determined by the product of the three Sign Correction values for a given configuration.

Averaging over individual runs, slugs, slugpairs, or Wiens can be performed and

*Some data were taken in which electrons made three passes around the accelerator as opposed to one. The machine was configured to provide the same energy as with one-pass beam, but an additional sign flip to the beam polarization was induced.

such results are shown in the remainder of this chapter. A slugpair is defined by the combination of two successive[†] slugs with opposite physics asymmetry. An asymmetry that has taken all of these possible sign flips into account is from now on referred to as a *sign-corrected* asymmetry. This dissertation will include an analysis of only the Run-II data set.

The final measured physics asymmetry is determined by taking a statistics-weighted average of asymmetries calculated with and without an extra sign flip introduced by the aforementioned accelerator elements. Asymmetries labeled with subscripts "in" and "out" were measured during periods in which an extra sign flip was or was not introduced respectively[‡]. In the absence of any offset in the measured asymmetry that does not change with electron polarization, the geometric average of A_{in} and A_{out}, referred to as the *NULL* asymmetry, should be exactly zero. Thus we define the two asymmetry combinations to be used throughout this chapter:

$$A_{\text{NULL}} = \frac{A_{\text{in}} + A_{\text{out}}}{2} \tag{4.2a}$$

$$A_{\text{PHYS}} = \frac{\dfrac{A_{\text{out}}}{(dA_{\text{out}})^2} - \dfrac{A_{\text{in}}}{(dA_{\text{in}})^2}}{\dfrac{1}{(dA_{\text{out}})^2} + \dfrac{1}{(dA_{\text{in}})^2}}, \tag{4.2b}$$

where dA_{in} and dA_{out} are the statistical uncertainties for the measurements A_{in} and A_{out} and are included as weights to account for differences in statistics between the IN and OUT data sets.

In order to eliminate the possibility for bias during the development of analysis techniques, asymmetries for any detector sensitive to the PV asymmetry were *blinded*.

[†]In rare cases, the half-wave plate was not inserted between neighboring runs. In these cases a slugpair is made using the next available slug of opposite flip.

[‡]The IN and OUT terminology comes from the sign flips induced when the half-wave plate was in or out of the laser beam. Over the experiment, these labels were then used to track *all* sign flips, including those from Wien flips and g-2 precession as well.

Blinding was achieved by adding a small, randomly selected and undisclosed offset to every asymmetry at the quartet level, with a different offset used for data from the commissioning period, Run-I, and Run-II so that each data set could be unblinded at a different time. The blinding factor could be any number between -60 and 60 ppb. The blinding factor follows the sign of the expected asymmetry as defined by the status of the IHWP and Double Wien flips and introduces an additional error $dA_{\text{msr, blind}}$ to this analysis after being scaled by the polarization. The magnitude of this error is determined by the following expression:

$$dA_{\text{msr,blind}} = \frac{120 \text{ ppb}}{\sqrt{12} \cdot P}, \tag{4.3}$$

where 120 ppb is the full width of the blinding box and the division by $\sqrt{12}$ accounts for the box being a uniform distribution[60]. Note that the definition of the blinding factor will cause it to be preserved in the calculation of A_{PHYS} but will cancel in A_{NULL}.

4.1 Asymmetry Calculations

Equation 2.2 states that the raw measured asymmetry for a given detector k is defined as:

$$A_k^{\text{raw}} = \frac{(Y_k^{+1} + Y_k^{+2}) - (Y_k^{-1} + Y_k^{-2})}{Y_k^{+1} + Y_k^{+2} + Y_k^{-1} + Y_k^{-2}}, \tag{4.4}$$

where the yields Y^{ij} for the j-th instance of helicity state i in the quartet have already been pedestal subtracted and normalized to the beam current. Detectors were normalized to equally weighted linear combinations of two beam current monitors (BCM1 and BCM2) during Run-I, and to one of the two upgraded monitors (BCM8, see Chapter 2) in Run-II. Combining the results of the sixteen main detector PMT's can be performed in two ways depending on at what point of the calculation the PMT combination is per-

formed. The simplest method for obtaining a single raw asymmetry for a collection of detectors is to use the *average asymmetries* method wherein Equation 4.4 is calculated for each of the N photomultiplier tubes in the detector combination, and then a straight average of the individual PMT asymmetries is performed for every quartet:

$$A_{\text{avg}} = \frac{\sum_{k=1}^{N} A_k^{\text{raw}}}{N}. \tag{4.5}$$

Another possible method of combining multiple PMT asymmetries into a single asymmetry measurement is to sum together detector yields prior to performing the asymmetry calculation as introduced in Section 3.2.3:

$$A_{\text{sum}} = \frac{\left(\frac{\sum_i^N Y_i^+ w_i}{\sum_i^N w_i} - \frac{\sum_i^N Y_i^- w_i}{\sum_i^N w_i} \right)}{\left(\frac{\sum_i^N Y_i^+ w_i}{\sum_i^N w_i} + \frac{\sum_i^N Y_i^- w_i}{\sum_i^N w_i} \right)}, \tag{4.6}$$

where $Y_i^{\pm}$ is the sum of yields for PMT i during positive (negative) helicity states, and the asymmetry combines N PMTs with weights w_i defined in Chapter 3 that account for differences in gain between PMTs. Recall from Section 3.2.3 that the weighting scheme chosen for Q_{weak} uses an average of PMT yields over an user-defined period of stability to determine the weight:

$$w_i = \frac{1}{< Y_i >}. \tag{4.7}$$

This method introduces an additional systematic in the determination of these weight factors, and incorrect weights can introduce geometric biases into the main detector asymmetry results. For example, if PMTs on the beam-left side of the main detector array have a gain factor that is significantly larger than those in the opposite octant (and

if the weights w_i do not properly account for this difference), a magnification of the array's sensitivity to residual horizontal transverse beam polarization (See Section 4.4.1) is accidentally introduced. Alternatively to weighting by a PMT's average yield, one could weight by the RMS width of each PMT's asymmetry distribution. This would have the effect of minimizing the width of the asymmetry distribution for that particular combination, and therefore reduce the amount of data required to reach a given relative precision. Since the transverse asymmetry at Q_{weak} kinematics is on the order of 5 ppm (compared to ~200 ppb for longitudinal polarization)[38], it was deemed more important to minimize our sensitivity to these geometric classes of effects, and thus we weighted by the average PMT yields.

For the purposes of asymmetry analysis, the average asymmetries method of Equation 4.5 was used. This was chosen because it is insensitive to differences in PMT gains and it does not introduce any extra systematic errors through the use of weighting factors. One shortcoming of this method however, is that by definition these combinations do not possess event-level detector yields. Some pieces of analysis will require this level of information, such as the "dithering" method for performing beam corrections (See Section 4.3) and correcting for transverse polarization in the beam (Section 4.4.1). For those applications, the summing yields method of Equation 4.6 was used.

4.2 Data Selection and Quality

The data selection process can be separated into two classes that I will call *prompt* and *post analysis* cuts. Prompt cuts are performed by the analysis engine as each event is processed, whereas post analysis cuts are performed at the 6 minute level[§] by subsystem experts to ensure that only data taken with the correct target with all detectors present is analyzed.

[§]Limits on file sizes resulted in 6 minutes of data to be the most that could be contained within a single file produced by the analysis engine.

Prompt cuts can be further classified into a number of different schemes. The most basic type of event rejection performed corresponded to data for which the data acquisition system reports a hardware error. Single event cuts were also defined for individual channels and included very loose upper and lower limits for a PMT yield to catch instances of readout errors not caught by the hardware error cuts. A basic lower limit for beam current was implemented at 100 μA. By ignoring data that does not meet this current limit we include only data for which the current monitor calibrations are trustworthy. Limits for detectors and beam position monitors were chosen to be very loose when compared to the typical variation of a PMT signal with the intention of catching rare hardware errors not recorded by the DAQ. For the main detector PMT's, an upper limit of 0.05 μA was used, corresponding to a signal of 9 V (compared to the typical signal size of 6-7 V). These cuts resulted in $< 0.1\%$ data loss while the DAQ hardware errors cut out about 1% of the data[40]. In addition to these static limits, a *stability cut* was performed within the analysis engine. A subset of critical channels[¶] were chosen to have their events stored within a 5 second buffer in order to monitor their stability. Figure 4.1 illustrates how these stability cuts were used in order to cut out periods of rapidly changing detector signals. Along with a set of critical beam monitors (including charge monitors and those position monitors used in the calculation of position and angle at the Q_{weak} target) two main detector variables were included in the stability cuts: the summed yields of PMTs in octant 1 (beam left) and octant 7 (beam down). These channels were chosen for their sensitivity to beam excursions and position differences in the horizontal and vertical directions respectively. It is important to note that these cuts were performed in order to catch hardware and data acquisition errors, and were not used to cut out any type of physics background.

[¶]Stability cuts were implemented for any channel without which the final analysis would not be possible.

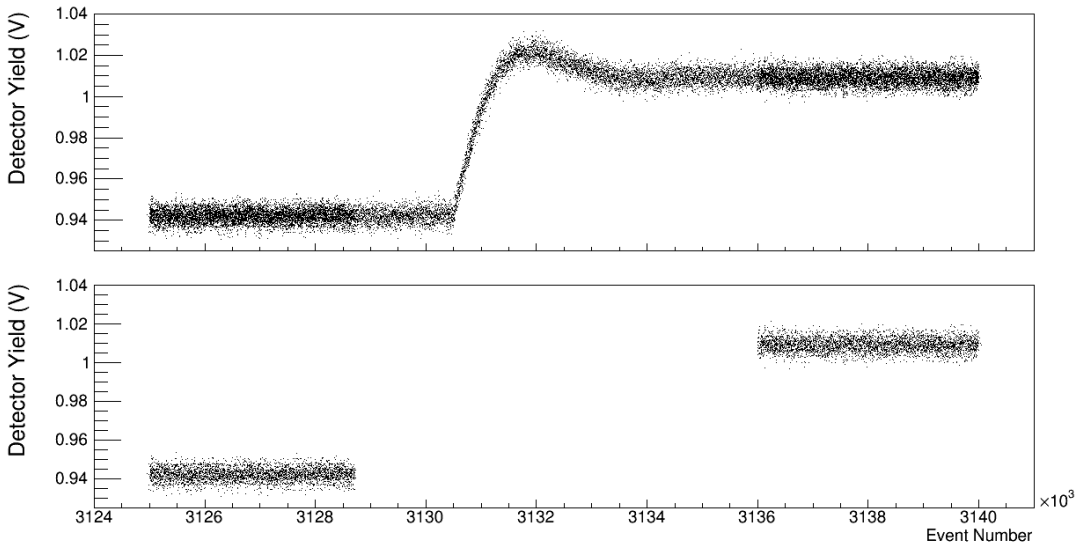

Figure 4.1: An example of a period of data (approximately 7 seconds here) that is removed from the analysis by stability cuts. This structure was the result of an erratic beam modulation cycle (See Section 4.3) during a run on an aluminum target.

4.2.1 Main Detector Asymmetry Widths

The variance of a distribution of quartet-level asymmetries is given by:

$$\sigma^2 = \frac{1}{N}\sum_{i=0}^{N}(A_i - < A >)^2 \tag{4.8}$$

where N asymmetry measurements A_i have been performed and their mean value is $< A >$. For a Gaussian distribution the RMS width is given by σ and is therefore a direct measure of how much the quartet-level asymmetries vary about their mean. Because of this, the RMS width can be used as a metric for the general health of the experiment: an increase in width can indicate whether or not inappropriate data (not corresponding to high current running on the liquid hydrogen target, such as aluminum targets or different kinematics) have leaked into the main data set. Assuming that the

main detector width is dominated by counting statistics, the width can be expressed as:

$$\sigma = \frac{1}{\sqrt{N}} \times \sqrt{1+\alpha^2} \tag{4.9}$$

where N is the number of scattered electrons and α is the resolution of the detector. The resolution is quantified by measuring the detector's photoelectron spectrum (Figure 3.9 and Appendix C) and calculating the ratio of the RMS width to the mean. The average measured resolution for pre-radiated bars was determined to be $\alpha = 51\%$ in this manner. Equation 4.9 can be written to include the factors that go into determining the number of quartets:

$$\sigma = \frac{1}{\sqrt{4.98\frac{\text{MHz}}{\mu\text{A}\cdot\text{bar}} \times 180\mu\text{A} \times \left(\frac{1}{960\text{ Hz}} - 70\mu\text{s}\right) \times 4 \times 8\text{bars}}} \times \sqrt{1+0.51^2} = 212\text{ ppm}, \tag{4.10}$$

where the current-normalized scattered electron rate per bar is the result of simulations documented in [3], 960 Hz is the helicity flip rate, 70 μs is the helicity settling time and the factor of four accounts for the four events per quartet. In Section 2.4 it was presented that the noise contribution to the main detector asymmetry width from target density fluctuations was measured to be 46 ppm. Adding this in quadrature to the result of Equation 4.10 results in an expected asymmetry width of 217 ppm. From the dependence on beam current in Equation 4.10 it is evident that any data taken at beam currents lower than the nominal 180 μA will have larger main detector asymmetry widths. In order to remove this dependence, we look to the current-scaled main detector asymmetry widths when investigating the quality of the data set:

$$\sigma_{\text{scaled}} = \sigma_{\text{raw}} \sqrt{\frac{I}{180}} \tag{4.11}$$

where I is the beam current in units of μA. Figures 4.2 and 4.3 display the raw and regressed scaled main detector widths as a function of time over the five Wien periods

of Run-II. There exist a number of cases where large asymmetry widths resulting from large helicity correlated beam parameter differences were improved by linear regression. Because the main detector asymmetry width was different for alternate targets and kinematics (for example, the width during aluminum running was typically 600 ppm), the absence of any large outliers in the regressed data provides a simple confirmation that no unwanted data has been incorrectly included in the primary hydrogen data set.

4.3 Beam Corrections

This section describes how corrections were performed to account for false asymmetries arising from the beam properties (charge, energy, position, and angle at the target) changing with helicity. Under ideal circumstances the beam position and intensity would be independent of the electron helicity state; however, real helicity-correlated changes in the beam's properties can give rise to unwanted false asymmetries by changing the flux of scattered electrons observed in any given octant. In a simple model, these false asymmetries can be removed by measuring the helicity-correlated differences in the beam parameters, ΔX_i, and the detector sensitivity to these parameters, S_i, using the equation:

$$A_{\text{false}} = \sum_{i=1}^{6} S_i \Delta X_i = \sum_{i=1}^{6} \frac{\partial A_{\text{raw}}}{\partial X_i} \Delta X_i. \tag{4.12}$$

Figure 4.4 displays how the main detector asymmetries vary in the presence of helicity-correlated differences in the beam. In Equation 4.12 the ΔX_i are measured using beam current/position monitors for every quartet. Table 4.2 presents how the Run-II beam differences compared to the design goals outlined in [6]. Errors do not correspond to a simple statistical error, but are calculated using:

$$\text{error}(\Delta X_i) = \frac{\text{resolution}}{\sqrt{N}} \tag{4.13}$$

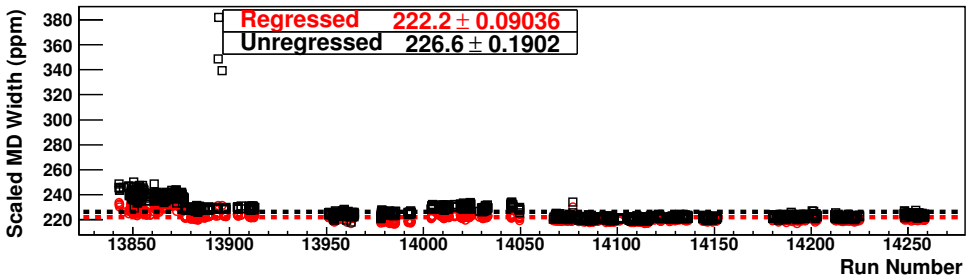

Wien 6

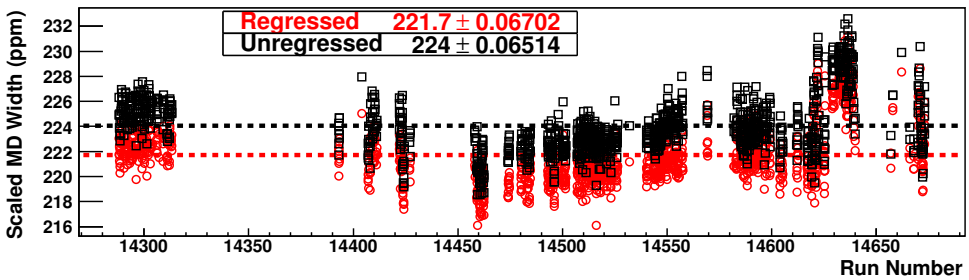

Wien 7

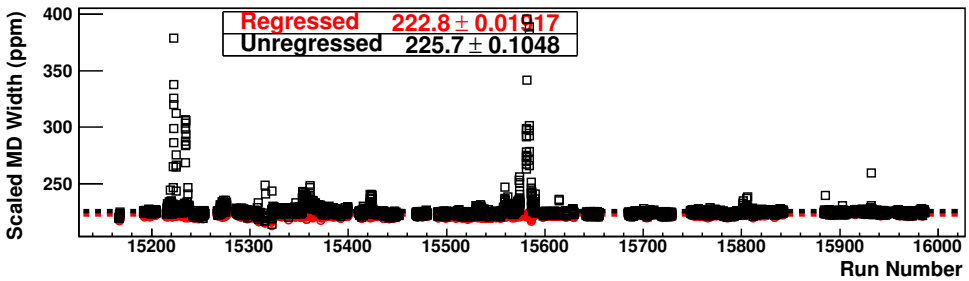

Wien 8

Figure 4.2: Current-scaled main detector asymmetry widths for Wien periods 6, 7 and 8. Regression removes false asymmetries resulting from large helicity-correlated beam differences at the target. Asymmetries here were regressed against variables defined in regression set 10 in Table 4.3.

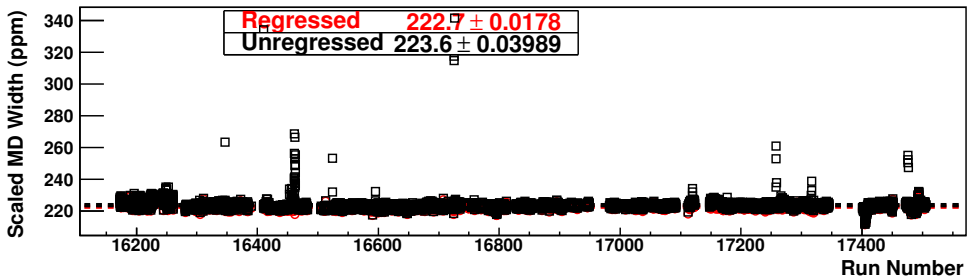

Wien 9

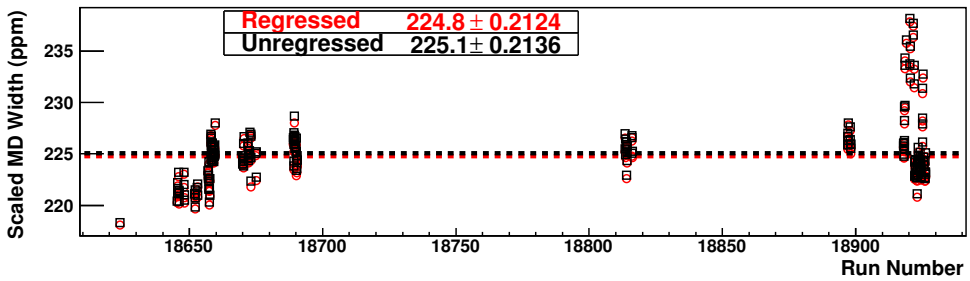

Wien 10

Figure 4.3: Current-scaled main detector asymmetry widths for Wien periods 9 and 10. Regression removes false asymmetries resulting from large helicity-correlated beam differences at the target. Asymmetries here were regressed against variables defined in regression set 10 in Table 4.3.

where N is the number of quartets over Run-II and the resolution for position and angle measurements made using the computed values at the Q_{weak} target were determined in [61] to be 1.72 μm and 0.21 μrad respectively. The energy measurement resolution was determined using the nominal beam dispersion of 4.1 cm/% at its most disperse region[47].

Beam Parameter	Goal	Run-II Average
ΔX (nm)	< 2	-2.11 ± 0.06
ΔY (nm)	< 2	0.6 ± 0.06
$\Delta X'$ (nrad)	< 30	-0.06 ± 0.007
$\Delta Y'$ (nrad)	< 30	-0.05 ± 0.007
ΔE (ppm)	< 1	-0.18 ± 0.00001
A_q (ppm)	< 0.1	0.014 ± 0.001

Table 4.2: Comparing the design goals and observed beam differences measured during Run-II.

Figures showing the slug-level behaviour of these helicity-correlated position, energy, and charge differences are shown in Figures 4.5 through 4.7. The remaining details of the corrections vary between the two methods for determining the slopes S_i: a natural beam jitter-based *linear regression* or a driven beam *dithering* analysis. This dissertation was completed prior to the completion of a dithering analysis technique, so beam corrections will be performed only using the results from natural jitter-based regression. The dithering analysis is intended to provide more accurate determinations of the detector sensitivities, and will hopefully result in a reduced overall systematic error bar.

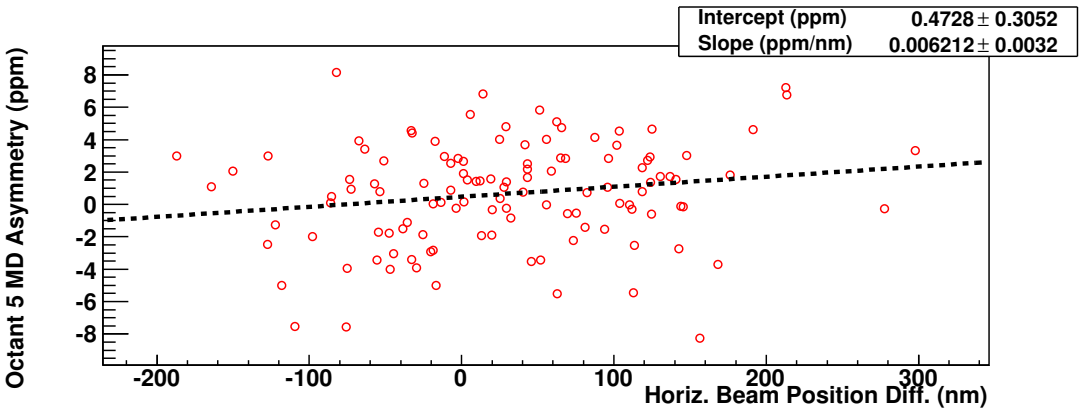

Figure 4.4: Asymmetry measurements from a single main detector octant (octant 5), plotted against the projected helicity-correlated horizontal beam position motion at the target. Each point corresponds to 6 minutes of data and one slug's worth of data is displayed.

4.3.1 Linear Regression

The linear regression analysis for Q_{weak} is performed using a stand alone C++ analysis engine. The regression package was designed to calculate the sensitivities for any given set of detectors (dependent variables) with respect to a set of beam monitor data (independent variables). The beam position, angle, and energy were always included as independent variables, and other variables were added and studied in parallel regression corrections. The dependence of the analysis results on the choice of independent variables will be discussed in Section 4.3.2. The regression is based on performing a multivariable least squares analysis[60] to extract the correlation matrix elements that correspond to the detector sensitivities. These detector-monitor correlations were extracted from each detector's response to natural beam motion during regular data acquisition. Sensitivities were calculated for each 6 minute segment of data using the prescription outlined in [60] and reproduced in Appendix A.2. Corrections to dependent variables using these sensitivities were then made at the quartet level using each quartet's measured helicity correlated beam parameter differences.

Choosing the set of beam monitors against which the calculated asymmetries should

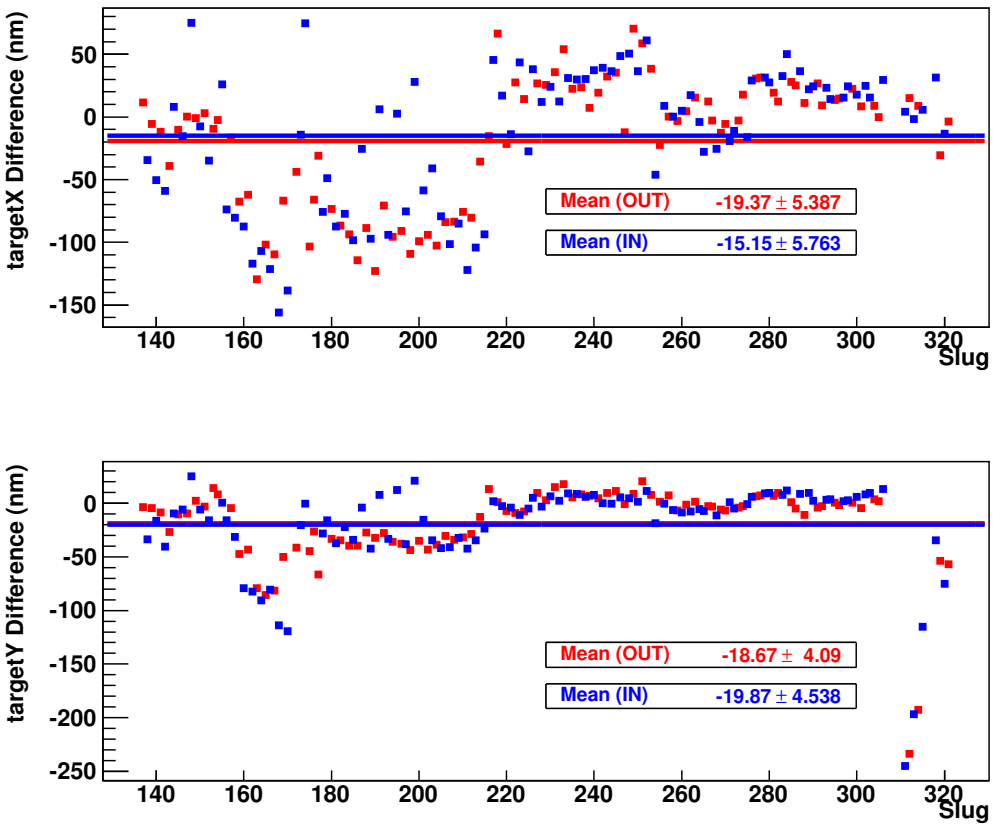

Figure 4.5: Run-II helicity correlated position differences at the target measured using computed beam position variables. IN and OUT labels refer to the status of the insertable half wave plate, which induces a sign flip in the measured asymmetry but ideally has no effect on the beam parameters. Errors in the fits correspond to statistical errors as opposed to actual monitor resolution.

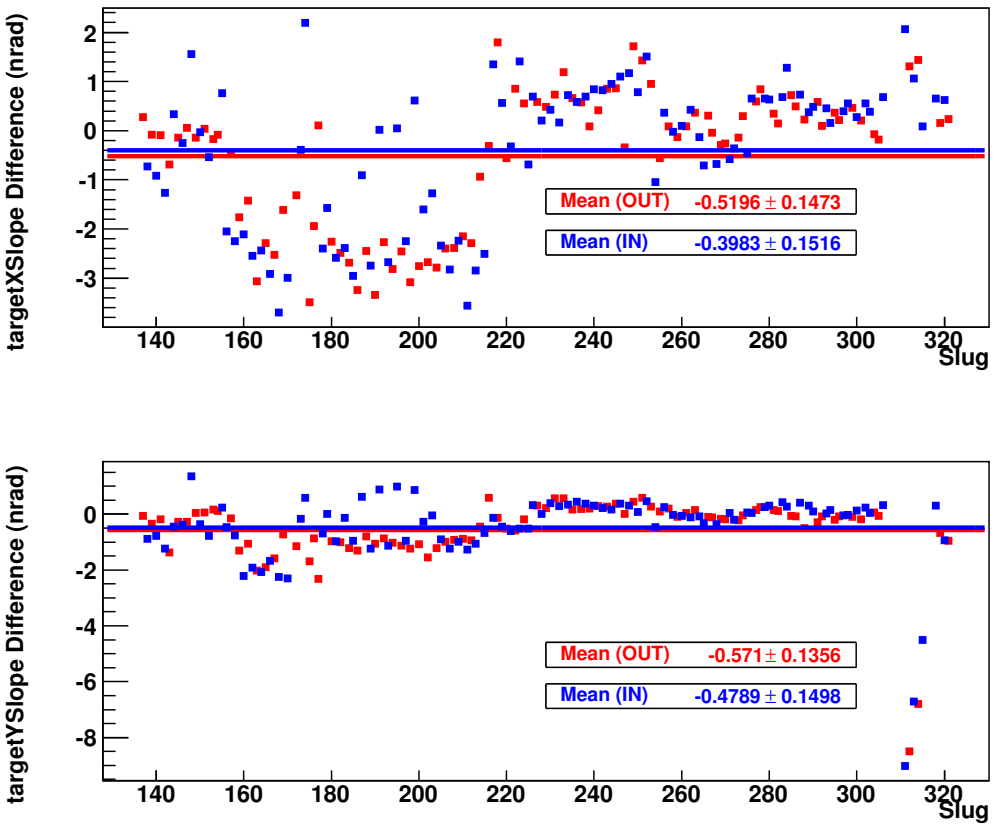

Figure 4.6: Run-II helicity correlated angle differences at the target measured using computed beam angle variables. IN and OUT labels refer to the status of the insertable half wave plate, which induces a sign flip in the measured asymmetry but ideally has no effect on the beam parameters. Errors correspond to statistical errors as opposed to actual monitor resolution.

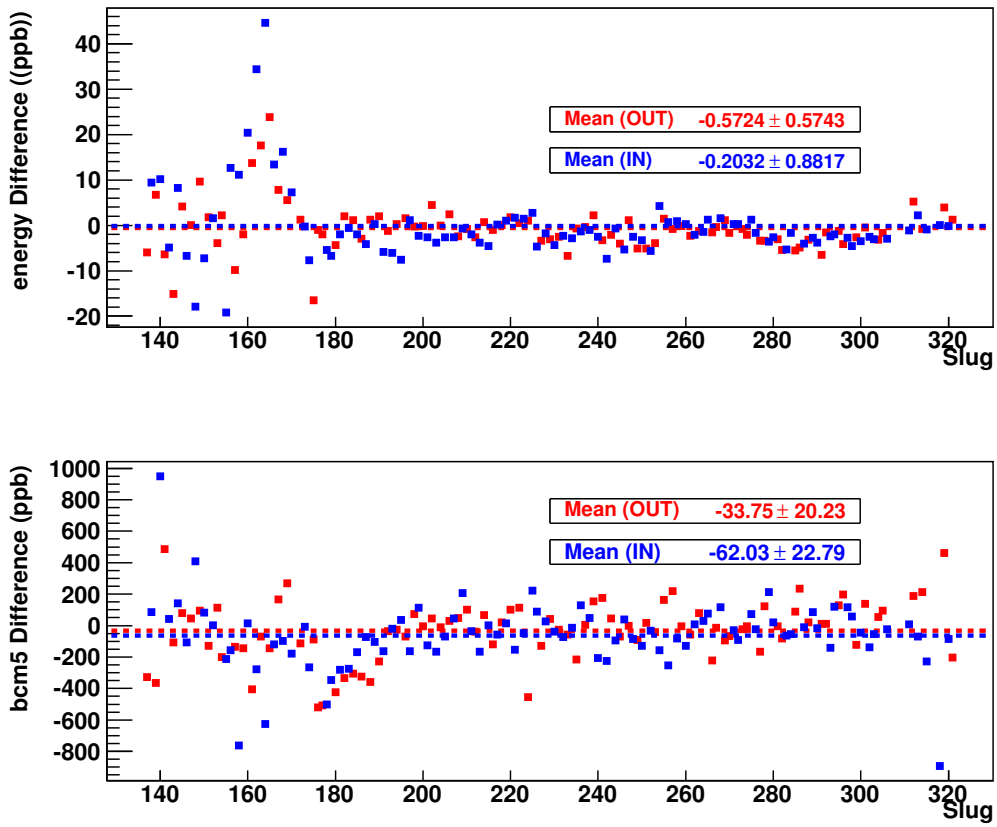

Figure 4.7: Run-II helicity correlated energy differences (measured using the computed energy variable) and charge asymmetries. IN and OUT labels refer to the status of the insertable half wave plate, which induces a sign flip in the measured asymmetry but ideally has no effect on the beam parameters. Errors correspond to statistical errors as opposed to actual monitor resolution.

be regressed must be done carefully, as this choice has the potential to introduce a new systematic error. Finding a set of completely independent monitors that correspond to all helicity-dependent beam parameters was not practical for this analysis, as correlations exist between positions and angles in a given direction, as shown in Figure 4.8. In addition to the correlation between position and angle differences, residual energy dispersion in the beam couples to horizontal position differences (as was discussed in Section 2.2.1), resulting in the two becoming correlated. This correlation could change over time as the amount of residual energy dispersion changed, and so a unique set of slopes that perfectly described the system at all times could not be determined.

In an effort to systematically study the effects of using different independent variables in regression, a number of regression schemes were implemented. Each scheme used the same set of independent variables but would use a different set of monitors to regress against. Table 4.3 displays the details for each scheme, where the "calculated" variables refer to the position and energy variables defined in software and described in Chapter 2. "Standard charge" refers to the beam current variable that the detectors were normalized to, and sets 6-8 use linear combinations of Hall-C BPM's upstream of the target instead of the calculated position and angle at the target.

Past analysis of Q_{weak} data using natural jitter-based regression[3][40][47] were limited to the Run-I data set, during which time BCM5 and BCM6 had noisy receivers and were generally unreliable. The improvements to these receivers introduced in Section 2.2.1 allowed for them to be used with confidence in the analysis of Run-II data. With regression schemes `set 4` and `set 10` now trustworthy, we have a set of independent variables that include a charge measurement other than the variable which the main detectors are normalized against. This is an important improvement in the Run-II analysis, as it was shown[62] that using the same current monitor in normalization and regression introduces a strong bias due to the injection of BCM noise into the main detectors via normalization. A limited set of schemes, marked by asterisks in Table 4.3,

Scheme	Position/Angle	Energy	Charge	Other
Std*	Calc. variables	Calc. energy	-	-
5+1*	Calc. variables	Calc. energy	Standard charge	-
Set 3*	Calc. variables	3c12X	Standard charge	-
Set 4*	Calc. variables	Calc. energy	BCM5	-
Set 5	Calc. variables	3c12X	-	-
Set 6	3h09b/3h04 combos	3c12X	Standard charge	-
Set 7*	3h09b/3h04 combos	3c12X	-	-
Set 8*	3h09/3h04 combos	3c12X	Standard charge	-
Set 9	Calc. variables	Calc. energy	Standard charge	uslumi_sum
Set 10*	Calc. variables	Calc. energy	BCM6	-
Set 11*	Calc. variables	3c12X	-	-
Set 12	Calc. variables + 3h04	3c12X	-	-
Set 13	Calc. variables	3c11X	-	-

Table 4.3: The different regression schemes used throughout the Q_{weak} experiment. Schemes differed according to which independent variables were used. Calculated beam position, angle, and energy variables are described in Chapter 2. The 3h09b/3h04 BPM combinations correspond to an equally-weighted linear combination of the raw signals from those two monitors. The 3c12X energy measurement is simply a measurement of horizontal helicity-correlated position differences at the most dispersive region in the beamline. In schemes where beam current was regressed against, the Standard charge variable corresponds to the same charge monitor that detectors were regressed against. Only schemes marked with an asterisk (*) denote those used in studying scheme dependence in Run-II.

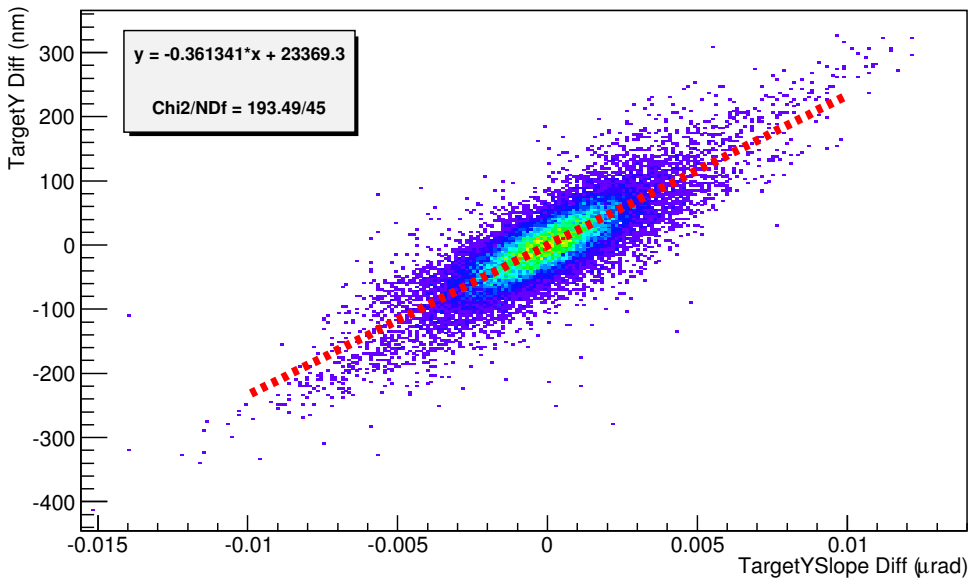

Figure 4.8: Correlations between vertical beam position and angle at the liquid hydrogen target.

was selected to study the effects of choosing one set of independent variables over another. The results of this study will be discussed below.

4.3.2 Regression Scheme Dependence

Regressed asymmetries were determined for the entire Run-II data set using the reduced set of regression schemes marked with asterisks in Table 4.3. These results are summarized in Table 4.4 where both the physics and null asymmetries have been determined at the *slugpairs* level. Recall that a slugpair is defined by combining two $\sim$ 8 hour periods of opposite physics asymmetry sign (as determined by the half-wave plate, Double Wien flips, and g-2 precession). The advantage to using slugpairs is that they provide an initial level of cancellation of false asymmetries that do not flip with the beam helicity. For example, assume that A_{in} and A_{out} both include an offset b that does not change sign

like the physics asymmetry (A_{phys}) does:

$$A_{\text{out}} = A_{\text{phys}} + b \tag{4.14}$$

$$A_{\text{in}} = -A_{\text{phys}} + b. \tag{4.15}$$

Sign-correcting and combining these asymmetries will perfectly cancel out this offset:

$$\frac{A_{\text{out}} - A_{\text{in}}}{2} = \frac{(A_{\text{phys}} + b) - (-A_{\text{phys}} + b)}{2} = A_{\text{phys}}. \tag{4.16}$$

This initial level of cancellation provides a noticeable improvement in the quality of the data and the method of quantifying this improvement will be discussed below.

A few methods for quantifying the quality of a given regression scheme exist, including simply comparing the computed NULL asymmetries (A_{NULL}), defined in Equation 4.2, as that combination of "in" and "out" data that should be consistent with zero. A more quantitative method makes use of the fact that the physics asymmetry should be constant over time; the extent to which a given scheme corrects all data to a single, unchanging asymmetry is extracted by plotting the physics and null asymmetries versus slugpair number and fitting them to constant values. The reduced χ^2 of the physics asymmetries determined from each regression scheme allow for a direct comparison of each fit's success in removing false asymmetries. Since small differences in reduced χ^2 can sometimes be difficult to put into perspective, we also tabulate the corresponding fit probabilities: which quantify how likely it is that the data can be described by the fitted function. Figure 4.9 shows the result of these fits for the corrected asymmetries for the "`on set10`" regression scheme.

Table 4.4 shows that there is little difference between the quality of fits from one scheme to another, with asymmetries regressed with `set 10` fitting a constant value slightly better than other schemes. Past analyses [12] [39] [40] have all relied on "`on`

	Null					Phys			
	Asym(ppb)	Error(ppb)	χ^2/ndf	Prob		Asym(ppb)	Error(ppb)	χ^2/ndf	Prob
off	5.532	7.862	1.543	0.001		-161.243	7.695	1.133	0.187
std	9.150	7.797	1.366	0.013		-160.549	7.633	1.016	0.439
5+1	9.437	7.799	1.383	0.010		-160.614	7.634	1.026	0.413
set 3	9.742	7.800	1.376	0.011		-160.601	7.635	1.029	0.405
set 4	10.349	7.797	1.369	0.013		-160.674	7.632	1.022	0.423
set 7	8.708	7.801	1.362	0.014		-160.244	7.636	1.014	0.444
set 8	9.262	7.800	1.371	0.012		-160.694	7.635	1.027	0.410
set 10	10.090	7.799	1.357	0.015		-160.792	7.634	1.010	0.455
set 11	8.860	7.799	1.377	0.011		-160.915	7.635	1.018	0.434

Table 4.4: Uncorrected blinded physics and null asymmetries for Run-II, for different regression schemes, computed on slugpairs. Entries correspond to plotting the Null and Phys asymmetries versus time (slugpairs) and fitting a constant value to each. The reduced χ^2 and probability that the data represent a single, constant value come from these fits.

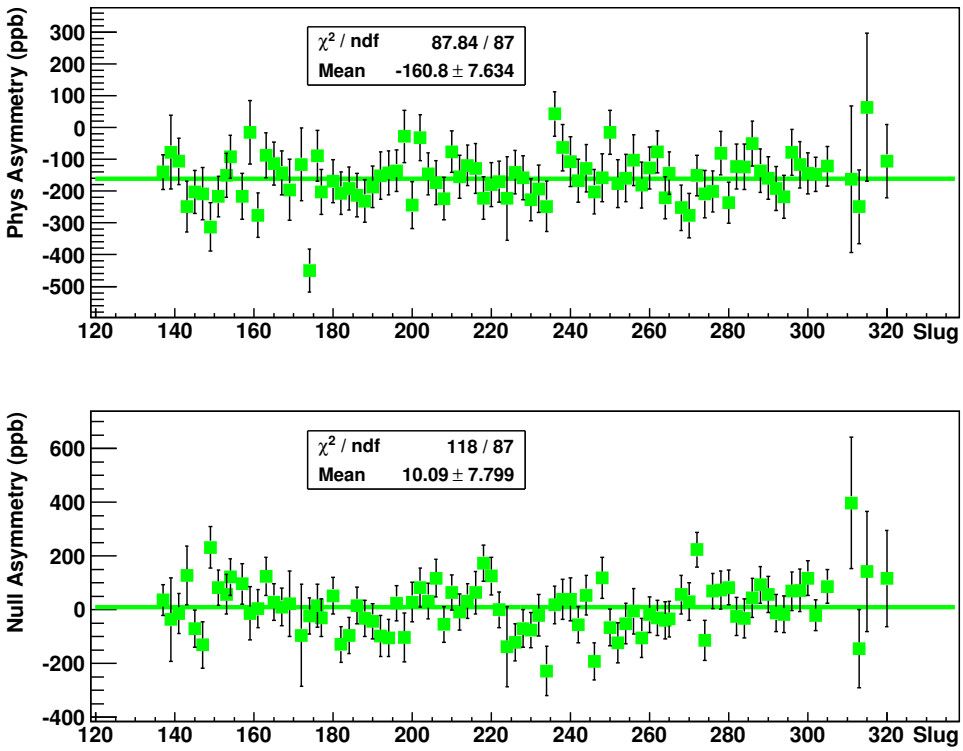

Figure 4.9: `on set10`-regressed main detector null and physics asymmetries plotted versus slugpair number (time) for all of Run-II. Asymmetries have not been corrected for beam polarization or any backgrounds.

5+1" for beam corrections, which used the same current monitor for normalization and regression. It is not surprising that a nearly identical scheme, differing only in an improved choice in charge monitor, would prove to be the most reliable. Figure 4.10 displays, for each slug in Run-II, the corrections made using `on set10`, defined as the difference between regressed and raw results.

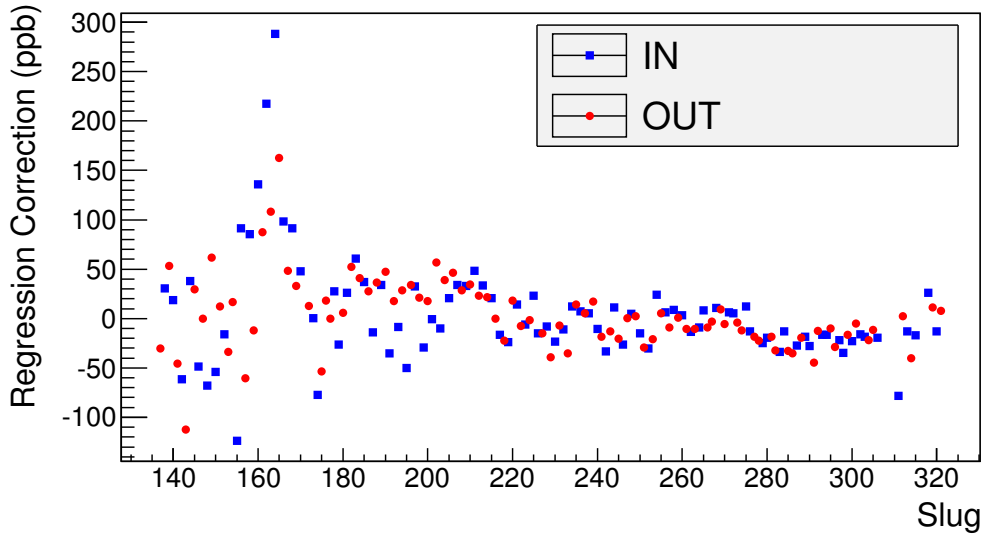

Figure 4.10: The corrections applied to the main detector asymmetry by linear regression during Run-II when using the `on set10` regression scheme. Asymmetries have been sign-corrected.

Comparing the results in Table 4.4 allows for a quantitative estimate of the error introduced by choosing one scheme over another. In the absence of any significant correlation between individual choices and the measured asymmetry (e.g. a difference between results using one energy variable over another) we assign a systematic error equal to the standard deviation of the regressed asymmetries displayed in Table 4.4: $dA_{\text{msr, scheme}} = 0.3$ ppb.

4.4 Polarization

Measured asymmetries need to be corrected for imperfect polarization of the electron beam. As discussed in Section 2.3, Q_{weak} made polarization measurements using two independent measurement techniques. At the time of this analysis, only analysis using data from the Møller polarimeter was in a final state for Run-II, with an in-depth analysis available in [63]. A total of 37 measurements were made throughout Run-II using this method, with typical polarizations of 88% being determined. The average polarization and statistical errors from these measurements are displayed as a function of slug number in Figure 4.11 for the Run-II data set. Variation in beam polarization can be attributed primarily to a decrease in the quantum efficiency of the GaAs photocathode during prolonged high current use. Asymmetry data are corrected for polarization at the slug level, after linear regression and correction for beamline backgrounds (Section 4.6). Each Møller measurement resulted in a $\sim 0.3\%$ statistical error bar, and the net systematic error bar is quoted as 0.84%. Sources of systematic errors for the Møller polarimeter include sensitivity to beam position and angle, target temperature, and magnet performance[63]. Polarization corrections are done separately for the Aluminum and inelastic data sets (Section 4.5).

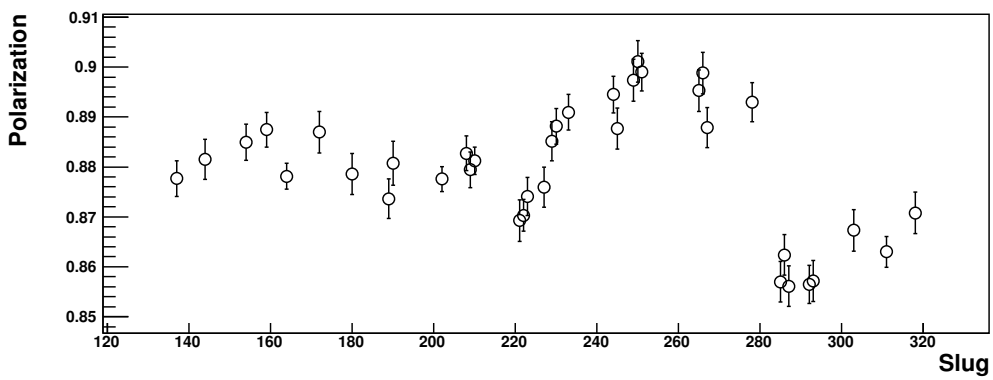

Figure 4.11: Beam polarization measured during Run-II using the Hall-C Møller polarimeter. Error bars correspond only to statistical errors, with systematics discussed in [63] and summarized in Section 4.4.

4.4.1 Transverse Leakage

Imperfect longitudinal electron polarization leads to an additional correction to be applied to the measured physics asymmetry. The parity-conserving asymmetry from elastic $\vec{e}p$ scattering of transversely polarized electrons is ~ -4.8 ppm[38] and is injected into the main measurement through residual transverse beam polarization. The physics interpretation of this asymmetry as well as the methodology developed to correct for it, are available in [38]. The sensitivity to this leakage is a result of broken azimuthal symmetry of the main detector array. The detector geometry was chosen to reduce sensitivity to these types of geometric effects, but ultimately a correction must still be made, even if it is small. The measured transverse asymmetry is given by

$$A^{\text{trans}} = -B_n|P_T|\sin(\phi_e - \phi_s), \tag{4.17}$$

where B_n is the beam normal single spin asymmetry, P_{T} is the fractional transverse polarization, and ϕ_e and ϕ_s are the azimuthal angles of the detector and polarization vectors respectively. Figure 4.12 provides a simple illustration of the geometry.

In a detector system with broken azimuthal symmetry the sine term in Equation4.17 will fail to integrate to zero over the detector acceptance. In order to make a correction to the measured asymmetry, three quantities must then be measured: the transverse asymmetry, the amount of residual transverse polarization, and the extent to which the detector symmetry is broken.

Measurements of the experimental asymmetry with transversely polarized beam were performed by configuring the injector to provide as close as possible to complete transverse polarization to Hall-C. Data were taken during periods of fully transverse and horizontal beam polarization, using standard LH_2 , aluminum, and carbon targets. The QTOR field was tuned to focus $N \rightarrow \Delta$ transition events onto the detector array for an additional measurement as well. A -4.81 ± 0.06 ppm physics asymmetry was

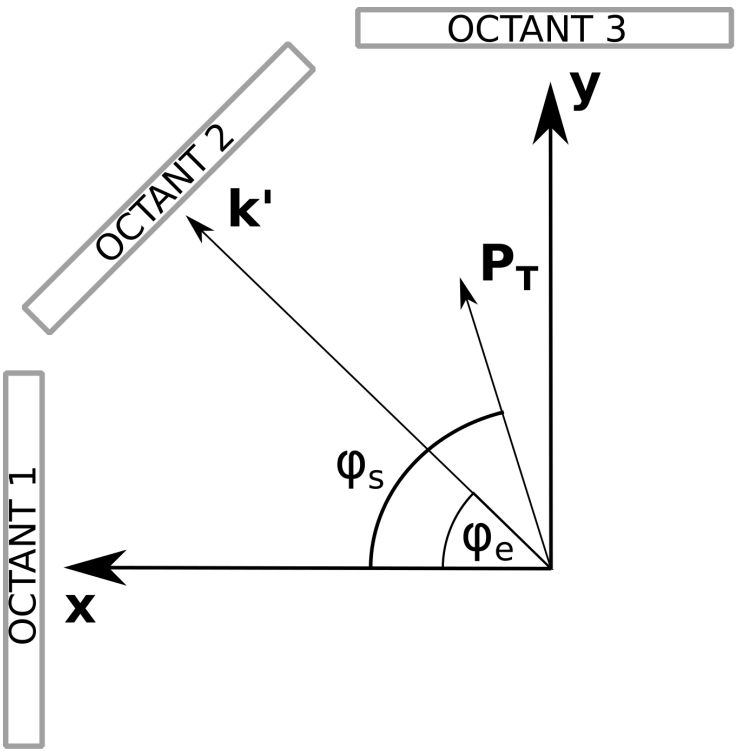

Figure 4.12: A simple diagram illustrating the transversely polarized electron scattering kinematics. This figure looks downstream at the main detector array. The scattered electron momentum is represented here by the vector $\mathbf{k}'$, and $\mathbf{P_T}$ is the direction of transverse polarization. ϕ_e and ϕ_s are the azimuthal angle of the scattering and polarization vectors respectively.

measured for elastic events from the LH_2 target[38].

Determination of the amount of residual transverse polarization in the beam was accomplished by plotting the measured asymmetry versus the average azimuthal angle of the main detector octants, as seen in Figure 4.14, and fitting a function of the form $A = B_n(P_v \cos\phi_e + P_h \sin\phi_e) + C$, where P_v and P_h are the fraction of transverse beam polarization in the vertical and horizontal directions respectively. Figure 4.13 shows how the amounts of vertical and horizontal transverse beam polarization changed throughout the experiment. Quantifying the level of azimuthal symmetry breaking was performed by measuring the asymmetry in the combination of horizontal (vertical) octants during horizontal (vertical) transverse polarization. For a fully symmetric detector array these combinations would be zero. By using these methods of extraction, a final systematic uncertainty of $dA_{\text{trans}} = \pm 0.0016$ ppm was applied to the main asymmetry measurement[38].

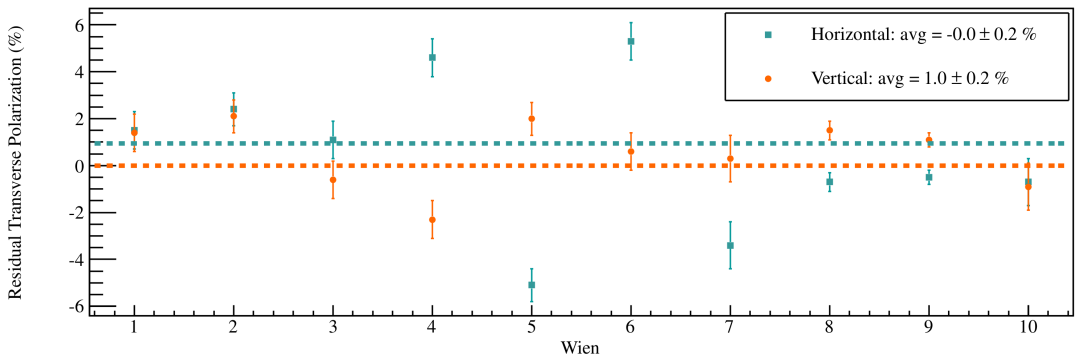

Figure 4.13: Residual transverse polarization over the whole Q_{weak} experiment. For a full analysis, see [38].

4.5 Physics Backgrounds

The measured main detector signals include a number of non-negligible backgrounds that contribute to the asymmetry. For this analysis, we separate background corrections into those resulting from competing physics processes and those originating from

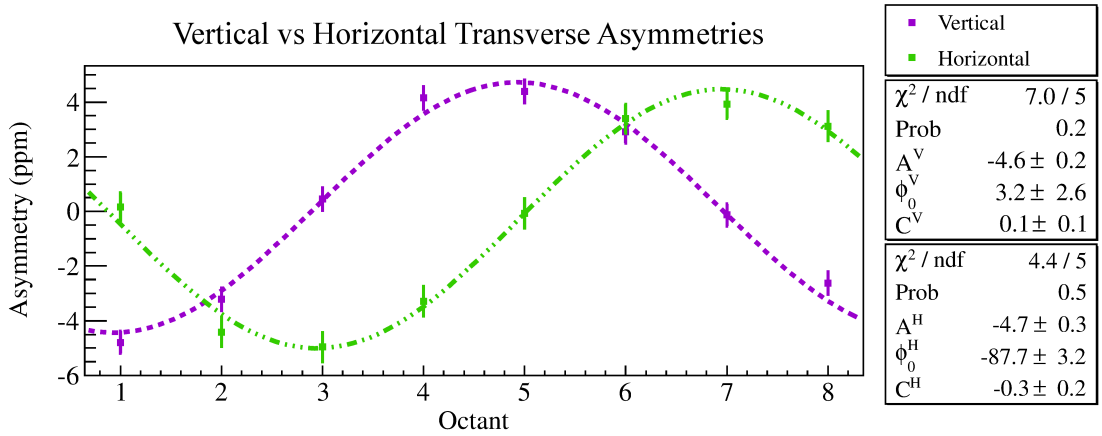

Figure 4.14: Azimuthal dependence of the raw asymmetries during vertical and horizontal transverse beam polarization running. A full analysis of the transverse asymmetry is available in [38].

helicity-correlated effects in the beam, with the former being the focus of this section. Correcting for both effects requires knowledge of the asymmetry associated with the background process as well as what fraction of the primary signal comes from that source; the latter is known as the *dilution factor* f_b and is defined as follows for a given background process:

$$f_b = \frac{Y_b}{Y_b + Y_{\mathrm{ep}}}. \tag{4.18}$$

where the b and ep subscripts correspond to the background and primary elastic signals respectively. Removal of background physics asymmetries from the measured asymmetry is performed by subtracting the false asymmetry from that source:

$$A_{bi}^{\mathrm{false}} = f_b A_b. \tag{4.19}$$

Background physics processes that are corrected for in $\mathrm{Q_{weak}}$ include events scattered from the aluminum target windows, neutral particle interactions in the quartz, and inelastic scattering events. This section will describe the methodology used for determining each of these corrections.

4.5.1 Aluminum

Events corresponding to scattering from the two aluminum target windows result in the largest background correction for Q_{weak} . Because of this, high-precision determinations of both the aluminum asymmetry and dilution factors were required, and so dedicated measurements were performed using a number of solid targets. Although targets of varying thickness and location were occasionally used, the majority of production aluminum data were taken at currents of 20−100 μA on the 4%-radiation length downstream aluminum target[‖].

Determination of the aluminum physics asymmetry was performed in the same manner in which the LH_2 asymmetry was extracted from raw data, including corrections for beam polarization, helicity-correlated beam parameters, backgrounds, and radiative effects within the target cell. At the current state of analysis, the asymmetry was measured to be

$$A_{\mathrm{Al}} = 1.4583 \pm 0.202 \text{ ppm}, \tag{4.20}$$

where the error combines statistical (63 ppb), systematic (172 ppb), and model-dependent (86 ppb) contributions[64].

For this analysis, the initial aluminum dilution measurement of $f_{\mathrm{Al}} = 3.2 \pm 0.2\%$[12] will be used. This value was determined by measuring the main detector yields using an evacuated target cell. The ratio $Y_{\mathrm{empty}}/Y_{\mathrm{full}}$ then gives access to the aluminum dilution factor. Data were taken at a reduced beam current of 1 μA on the empty cell (to address the lack of heat dissipation normally provided by the flowing hydrogen). Data were taken on a 4% radiation length carbon target at both the reduced current and at the nominal 180 μA current for regular LH_2 running in order to provide a normalization of rates from low to high current. For a complete analysis of early aluminum data, see

[‖]The solid targets were positioned along the beamline at locations that corresponded to the upstream and downstream faces of the LH_2 cell.

reference[3].

4.5.2 Neutral Particle Interactions

The *neutral background* correction is applied to account for signals generated in the main detector resulting from the interaction of electrically neutral particles. These events correspond almost entirely to photons generated by primary elastic electrons scraping in the collimator and shield wall edges, but did include a component from neutrons from similar sources. These photons carry a physics asymmetry determined by the scattered electron from which they were produced.

Measurement of the neutral particle interaction dilution factor is achieved by comparing events registered in the main Čerenkov detectors and trigger scintillator systems during event mode running. The only neutral particles that the trigger scintillator material detects are low energy (< 100 keV) X-rays[65]. These events deposit a very small amount of charge into the trigger scintillator PMT and can be removed by cutting on the total deposited charge. We then assume that any event that is seen by the main detectors but not by the trigger scintillator results from a neutral particle. One can imagine events corresponding to charged particles bypassing the trigger scintillator and striking the main detectors through multiple scattering, but results from simulations indicate that this effect should be negligible[3]. Using this method of identifying events in the main detector that do not generate signals in the trigger scintillator, the neutral particle dilution factor was determined to be $f_{\text{neut}} = 0.127 \pm 0.138\%$[66].

Determination of the asymmetry from neutral particles is beyond the scope of this dissertation, but is currently achieved by taking our early measurements of the elastic LH_2 , inelastic, and aluminum asymmetries[12] alongside an estimate for the Møller asymmetry at Q_{weak} kinematics, and combining them based on relative dilution factors obtained through a GEANT4 simulation. Using this technique, the neutral particle asymmetry for Q_{weak} was determined to be[66]:

$$A_{\text{neut}} = -0.238 \pm 0.057 \text{ ppm}. \tag{4.21}$$

4.5.3 Inelastic Scattering

Compared to the background from the aluminum windows, backgrounds resulting from the inelastic scattering of electrons from the proton are very small. This background results from a parity violating asymmetry associated with the $N \rightarrow \Delta$ transition. Figure 4.15 shows the result of a GEANT3 simulation that determined the expected event rates for different scattering processes in the target, including inelastic scattering. The main Q_{weak} measurement was performed at a QTOR current far away from the inelastic peak.

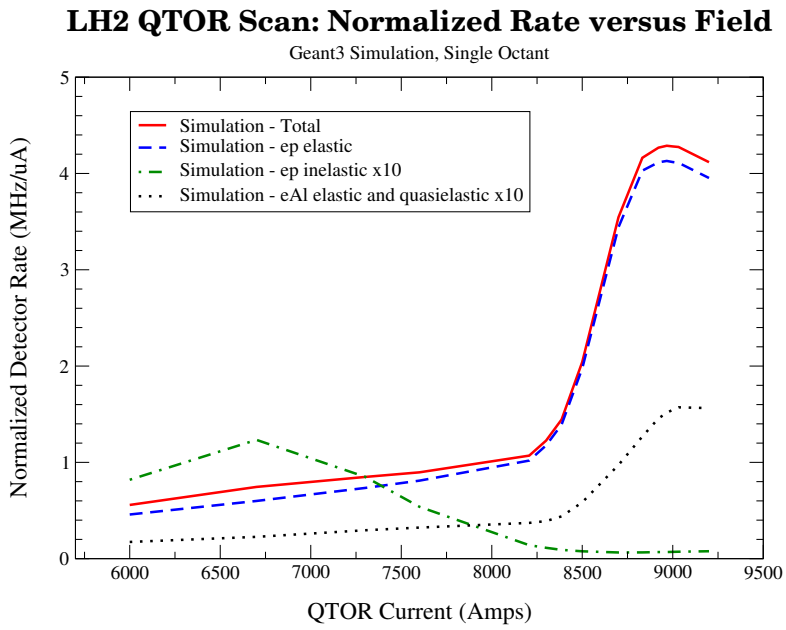

Figure 4.15: Simulated event rates for different scattering processes in the target, plotted versus QTOR magnet current. Data for the main hydrogen measurement were taken at 8921 A, far away from the inelastic peak near 6700 A.

As outlined at the start of this section, a correction requires the determination of both the value of the asymmetry as well as the dilution factor. Without a feasible experimental method for determining the dilution, GEANT3 simulations were carried out

to determine the fraction of inelastic events at the nominal QTOR field strength. Figure 4.16 shows the result of these simulations, which found that the dilution factor, with QTOR set to 8921 A, is $f_{\text{inel}} = 0.0002 \pm 0.000005$ (statistical error only); the maximum fractional rate is observed at QTOR 6700 A and is $f_{\text{inel}} = 0.2757 \pm 0.0036$ (statistical only)[49]. The error bar on f_{inel} is artificially inflated to 100% of the mean value in order to address inconsistencies between the simulated and observed inelastic rates[47]. Measurements of the inelastic asymmetry were performed at this reduced field strength and were subsequently corrected for the usual systematics (helicity correlated beam parameters, polarization, etc) and backgrounds (aluminum, elastic scattering), resulting in an inelastic asymmetry of

$$A_{\text{inel}} = -3.20 \pm 0.97 \text{ ppm}. \tag{4.22}$$

Although the size of this asymmetry and its error are large compared to the main elastic asymmetry ($\sim$ 220 ppb), scaling these by the dilution factor reduces their contribution from the ppm-level to the 0.1 ppb-level, where they result in an insignificant correction to the main Q_{weak} asymmetry.

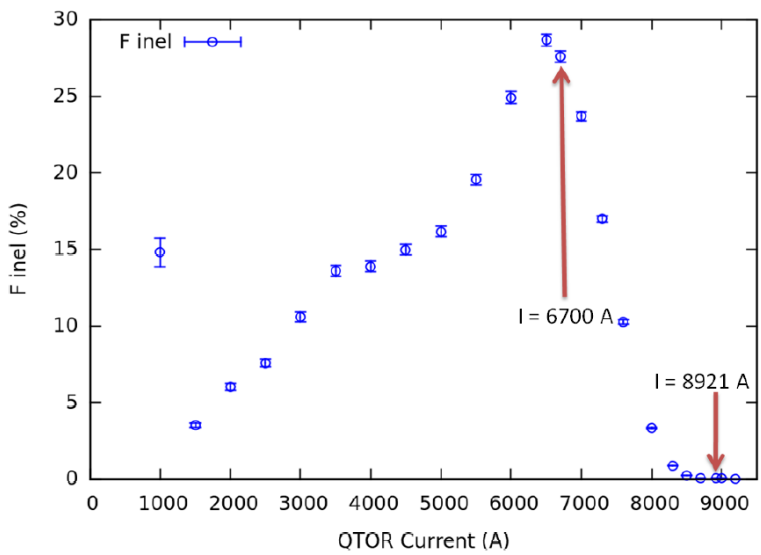

Figure 4.16: Simulated dilution factors for the inelastic scattering background process. Nominal QTOR current for hydrogen running was 8921 A[49].

4.6 Beamline Backgrounds

The upstream luminosity monitors were designed and placed in a location such that they should have measured no significant asymmetry but would be sensitive to changes in scattered beam luminosity as a result of density fluctuations in the target. However, it became clear early in the experiment that the upstream lumis were measuring a large asymmetry on the order of 1-10 ppm (See Figure 4.17). Because the asymmetry was insensitive to the insertion of the half-wave plate, a model was developed that describes this background as resulting from electrons scattering from the beamline as opposed to a competing physics process in the target. The source of this extra signal in the main detectors was traced back, by simulations and systematic studies, to the tungsten plug located in the centre of the primary collimator. Recall from Section 2.5 that the tungsten plug was designed to shield the detectors from events scattered at very forward angles. One current model describing this asymmetry includes a helicity-correlated beam halo interacting with the tungsten plug. A halo can be described as a component of the beam not contained within its primarily Gaussian structure[67]. Since this halo results from effects at the Pockel's cell at the polarized injector(which is after the half wave plate, see Figure 2.4), it must be independent of the half wave plate state.

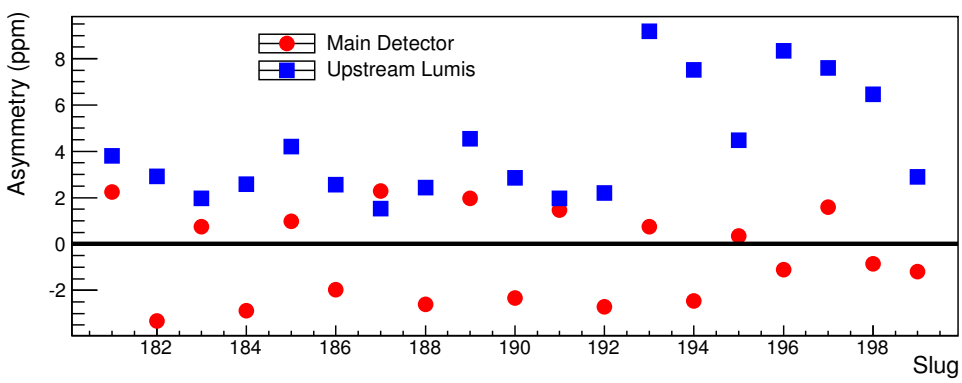

Figure 4.17: Typical upstream luminosity monitor asymmetries in Run-II. Unlike the main detectors, they do not flip with the half-wave plate.

In order to confirm the hypothesis that the tungsten plug was the source of the background, the *Tungsten Shutter* test was performed. By installing 2 inch thick retractable blocks of tungsten on the downstream face of octants 1 and 5 of the primary collimator we were able to block the elastically scattered electrons from reaching those octants. Any signal detected in those two octants while the shutters were in place could then be attributed to backgrounds generated at or downstream of the primary collimator. This would also provide a measurement for how much of the main detector signal could be attributed to this source.

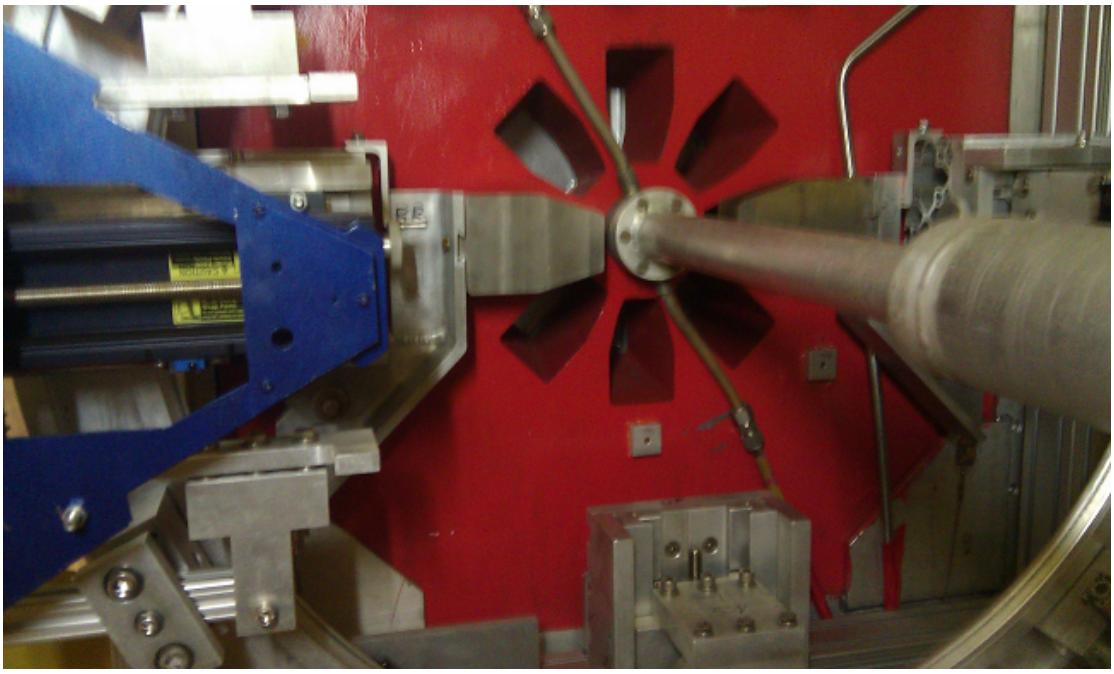

Figure 4.18: Tungsten shutters located in octants 1 and 5 on the downstream face of the primary collimator.

Quantification of the main detector dilution from the beamline background asymmetry is done by defining the *fractional yield*:

$$Y_{\text{frac}} = \frac{(Y_1 + Y_5)/2}{(Y_2 + Y_3 + Y_4 + Y_6 + Y_7 + Y_8)/6}, \tag{4.23}$$

where Y_i is the yield measured using the sum of PMTs in octant i and the octant numbering is defined in Figure 2.3. Recall that octants 1 and 5 are located beam left and

right respectively and correspond to the tungsten shutter octants shown in Figure 4.18. Pedestal data were acquired more frequently during the tungsten shutter tests in an effort to reduce the effects of slowly drifting pedestals on the reduced signals. In an effort to further characterize the nature of this new background with the shutters in place, the beam was intentionally detuned by varying the fields in one of two focusing quadrupole magnets; this resulted in a less focused beam. The defocusing of the beam in this manner was observed to increase the RMS width of the upstream lumi asymmetry distribution and thus alert shift crews to an increase in noise coming from the beamline background. Figure 4.19 displays the correlation between the fractional yield and upstream lumi widths during these detuned beam studies.

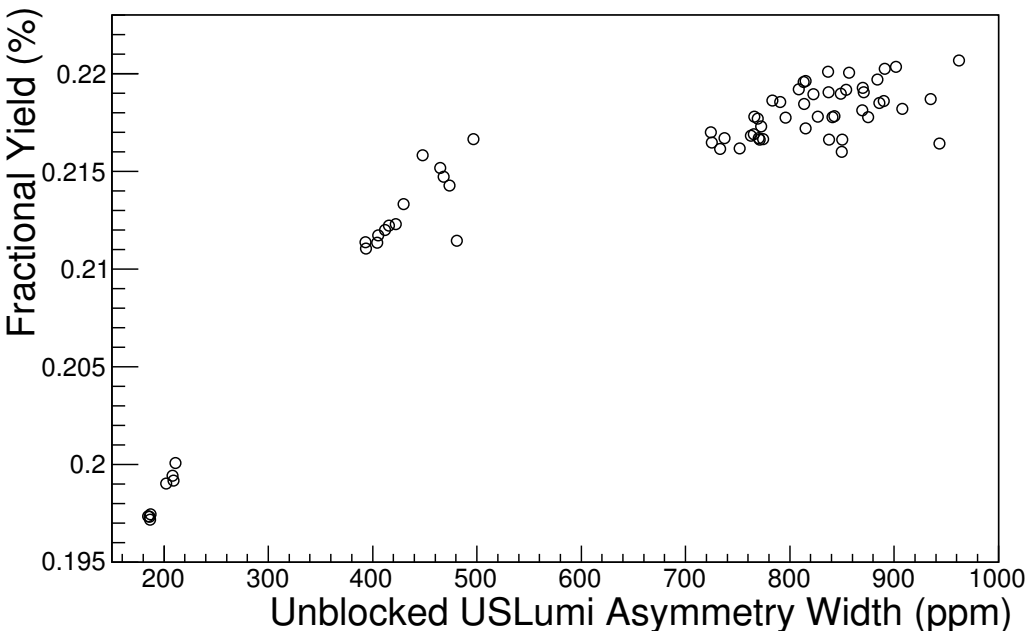

Figure 4.19: A correlation is observed between the fractional yield (Equation 4.23) and the upstream lumi asymmetry width during detuned blocked octant running. Error bars on these quantities are too small to appear at this scale. Different clusters of runs correspond to periods during which the beam was tuned to increase or decrease the upstream luminosity monitor asymmetry widths.

Careful tuning of the beam to minimize the upstream lumi widths was also performed during this test, with a smallest fractional yield of 0.193% being observed. An

average of these "good" and "bad" configurations was used to quantify the dilution factor, along with a 33% relative error bar. This error bar was chosen primarily to allow for the worst-case background to be twice as high as it was in the detuned study[68]. The resulting beamline background dilution factor is then:

$$f_{\mathrm{BB}} = 0.00193 \pm 0.00064. \tag{4.24}$$

During normal production running, significant correlations were observed between the upstream luminosity monitors and the two background detectors located near octant 3 (Figure 2.15) of the main detectors. These correlations (shown in Figure 4.20) give additional confirmation to the hypothesis that a large background asymmetry measured by the upstream lumis was also present as a background in the main detector shield hut.

Correcting for this beamline background asymmetry in the main detectors was performed in the same way as the asymmetries resulting from helicity-correlated beam differences: by measuring the correlation between the main detectors and the luminosity monitors and subtracting the false asymmetry defined by

$$\Delta A_{\mathrm{BB}} = \frac{\partial A^{\mathrm{MD}}}{\partial A^{\mathrm{US}}} < A^{\mathrm{US}} >= C^{\mathrm{MD}}_{\mathrm{US}} < A^{\mathrm{US}} >, \tag{4.25}$$

where $< A^{\mathrm{MD(US)}} >$ is the main detector (upstream luminosity monitor) asymmetry averaged over an entire slug. It is important to note that these correlation factors must be determined from unblocked data and that the blocked-octant data are only useful in determining the dilution factor. Figure 4.21 displays, for Run-II, the slug level correlations between the main detector and upstream lumi asymmetries. Careful studies have been performed[69] that include accounting for the correlation resulting from real physics events in both detectors. The final extracted correlation coefficient for on

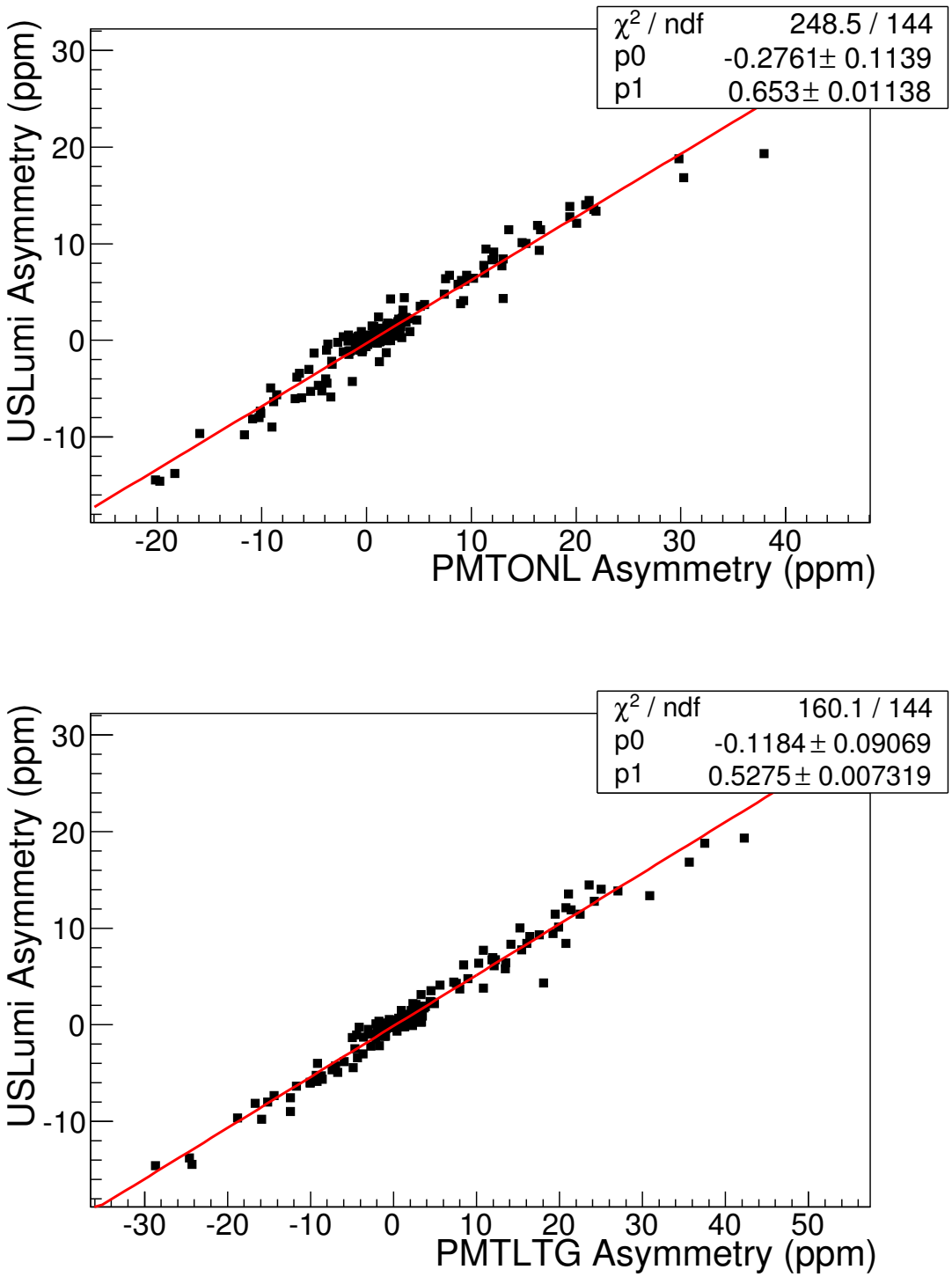

Figure 4.20: Upstream luminosity monitor correlations to background detectors during Run-II. Background detectors were located in the main detector shield hut, placed at lower radius in octant 3 of the main detector. The top plot shows to correlation to the PMTONL background detector, with the bottom showing the correlation to PMTLTG. Descriptions of these monitors are provided in Section 2.6.2.

`set10`-regressed data in Run-II is then:

$$C_{\mathrm{US}}^{\mathrm{MD}} = 5.00 \pm 1.62 \frac{\mathrm{ppb}}{\mathrm{ppm}}. \tag{4.26}$$

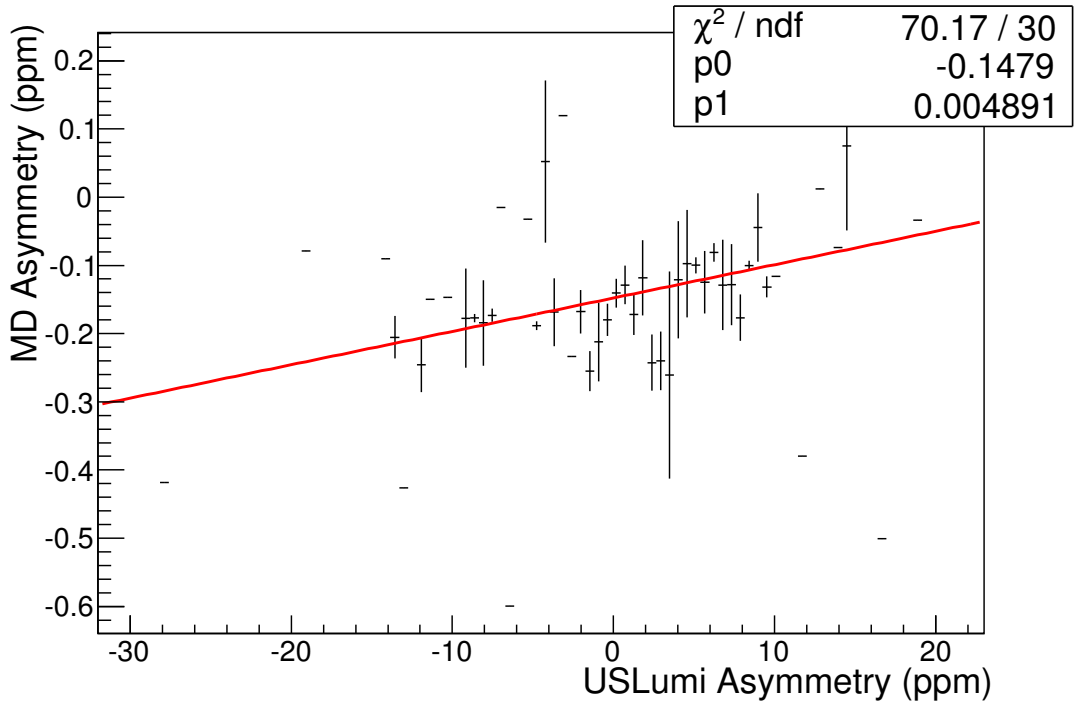

Figure 4.21: A plot showing the correlation between main detector and upstream lumi regressed asymmetries during Run-II. The lumi asymmetry plotted here has not been corrected for the dilution of the beamline background asymmetry by the elastic signal; doing so yields the slope in Equation 4.26.

The correction defined in Equation 4.25 is performed at the slug level to account for changing upstream lumi asymmetries over the course of the experiment. The importance of this correction is made clear when one recalculates the null asymmetry and goodness of fits after accounting for beamline backgrounds. Table 4.5 displays the null and physics asymmetries (`set 10`-regressed) before and after correcting for the beamline background asymmetry as described in this section. It is only after performing this correction that the null asymmetry is consistent with zero. Additionally, the correction noticeably increases the probability that the Run-II asymmetry data are consistent with

a constant value as determined from the horizontal fits in Figure 4.22 (46% to 62%).

	Null Asymmetry			
	A (ppb)	dA (ppb)	χ^2/ndf	Prob.
Before BB	11.3	8.9	1.357	0.015
After BB	1.3	8.9	1.295	0.033
	Physics Asymmetry			
	A (ppb)	dA (ppb)	χ^2/ndf	Prob.
Before BB	-182.6	8.7	1.007	0.455
After BB	-186.9	8.7	0.946	0.623

Table 4.5: Run-II main detector null and physics asymmetries before and after correcting for beamline backgrounds. χ^2/ndf and probability correspond to fitting a constant value through these quantities plotted versus slugpairs. Asymmetries include polarization corrections.

4.7 Radiative Corrections

Electromagnetic radiative effects important for the Q_{weak} experiment are primarily characterized by the emission of a real bremsstrahlung photon or by virtual photon loops. These processes can result in depolarization of the incident electron and changes in the energy and scattering angle of the electron, and thereby have a measurable effect on the measured asymmetry and Q^2. Interactions can take place both internal or external to the field of the scattering nucleus, and in both cases the interaction can occur either before or after the scattering event (see Figure 4.23). A GEANT3 simulation that accounts for these initial or final state radiative effects, along with the discrete energy loss associated with external bremsstrahlung radiation, has been performed[47]. The result of these simulations, updated for Run-II conditions, is the following multiplicative correction to the physics asymmetry[70]:

$$R_{\mathrm{RC}} = 1.0101 \pm 0.0007. \tag{4.27}$$

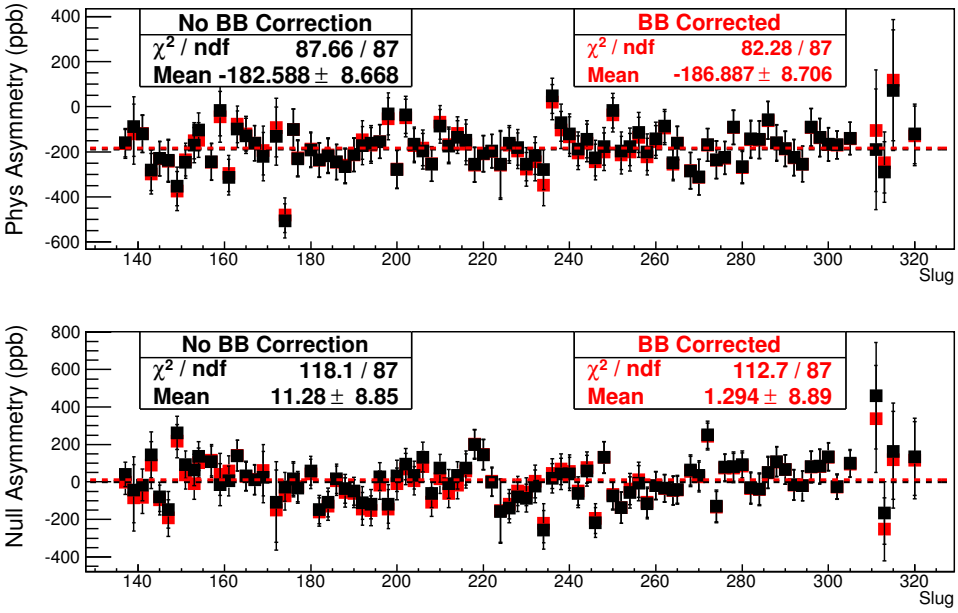

Figure 4.22: A comparison between physics and null asymmetries, calculated at the slugpair level, with and without beamline background corrections. Red points have been corrected for beamline backgrounds and the dashed lines correspond to constant value fits to the data.

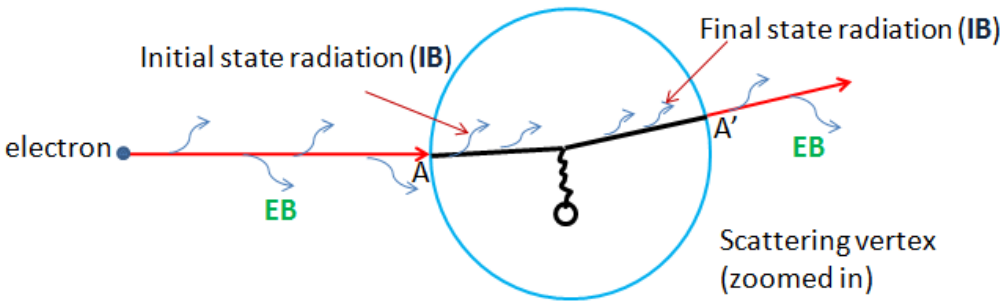

Figure 4.23: A scattering diagram that illustrates the difference between initial and final state radiation used in electromagnetic radiative corrections for Q_{weak} . Discrete energy loss through bremsstrahlung can occur inside or outside of the scattering nucleus.

4.8 Experimental Bias Corrections

This section will discuss corrections for experimental effects that bias the measured asymmetry. Like the radiative corrections discussed in the previous section, these are multiplicative corrections to the measured asymmetry and include a detector light-weighting bias (R_{det}) and corrections resulting from the detector's acceptance (R_{acc}) and extracted momentum transfer (R_{Q^2}). We define the total experimental bias correction as the product of these factors:

$$R_{\text{bias}} = R_{\text{det}} \times R_{\text{acc}} \times R_{Q^2}. \tag{4.28}$$

This section will explain each of these corrections.

The detector bias correction R_{det} accounts for the fact that both the average Q^2 and the efficiency of light collection in the main detector vary across the length of the bar (Figures 3.6 and 3.7). Simulations performed using GEANT4 were performed in which the asymmetry was determined with or without accounting for this light-weighting effect. The size of the correction was determined by computing the ratio of unbiased to biased asymmetries calculated in this manner. This ratio is only correct if the value of $< Q^2 >$ used in the simulation matches the experimentally measured value. A correction to this ratio to account for differences between simulated and measured momentum transfers was applied as δQ^2, using the prescription in [71]. The detector bias correction is then:

$$R_{\text{det}} = \frac{A^{\text{sim}}_{\text{unbiased}}}{A^{\text{sim}}_{\text{biased}}} \times \delta < Q^2 >= 0.987 \pm 0.007 \tag{4.29}$$

The main detectors provide an asymmetry measurement corresponding not to a single value of Q^2 but to a range of momentum transfers. Figure 4.24 presents the range of momentum transfers accepted by the Q_{weak} apparatus. Because the asymmetry and eventual weak charge extractions are quoted at a single value, an additional correction

needs to be performed to account for the acceptance of the experiment. R_{acc} is determined by comparing simulated values for the asymmetry at an average Q^2 and the average asymmetry over the Q^2 range accepted by the apparatus[72]:

$$R_{\text{acc}} = \frac{A_{\text{tree}}(< Q^2 >)}{< A_{\text{tree}}(Q^2) >} = 0.980 \pm 0.01. \tag{4.30}$$

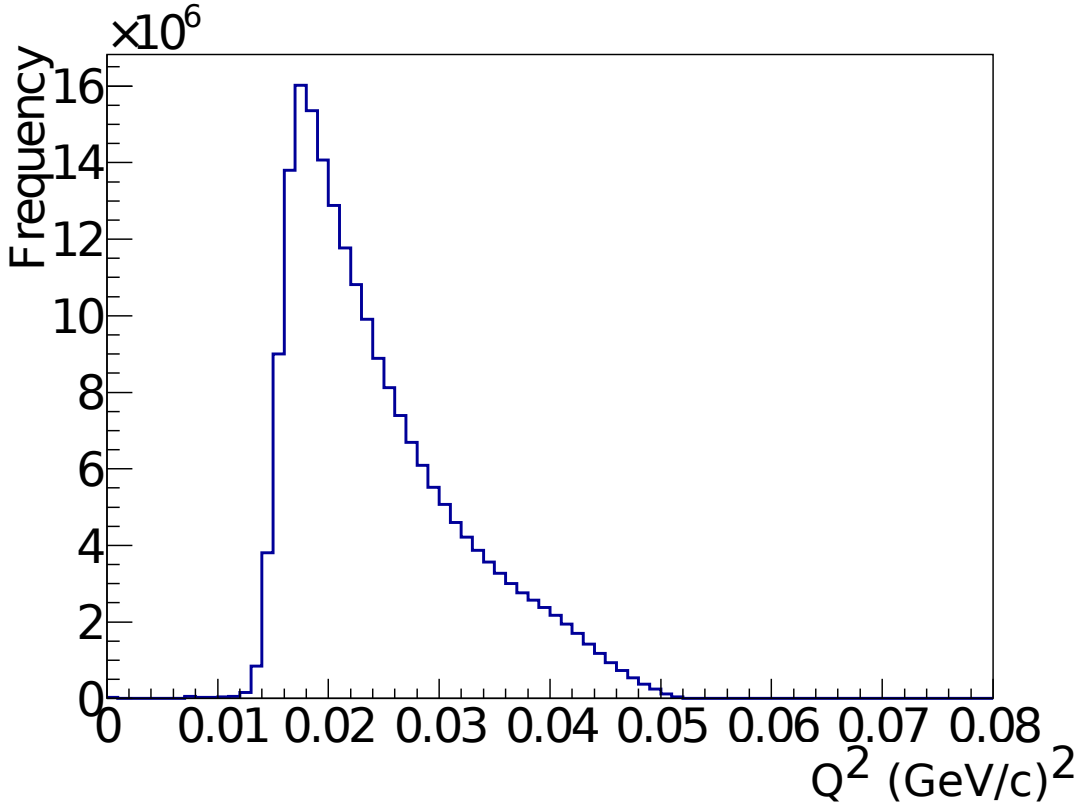

Figure 4.24: The distribution of momentum transfer accepted by the main detectors. The curve comes from a GEANT4 simulation including only hydrogen events.

A final bias correction is performed in order to quote our parity violating asymmetry at a single value of momentum transfer. Alternatively, one could simply provide the asymmetry and Q^2 errors separately and then propagate the latter into the calculation of Q_W^p. Using the same method as was used for the early Q_{weak} result[12][73] and with an updated Q^2 error of $dQ^2/Q^2 = 1.45\%$[74], we assign the following correction:

$$R_{Q^2} = 1.000 \pm 0.018. \tag{4.31}$$

Since all of these corrections are multiplicative, we can then combine them with the radiative correction factor R_{RC} from the previous section to obtain the *total bias correction* R_{tot} as

$$R_{\mathrm{tot}} = R_{\mathrm{RC}} \times R_{\mathrm{det}} \times R_{\mathrm{acc}} \times R_{Q^2} = 0.9770 \pm 0.0317. \tag{4.32}$$

4.9 Kinematics

The effective momentum transfer Q^2 and scattered electron beam energy E_s are both determined from simulations for this dissertation. Both quantities have also been measured, but the final analysis has not yet been completed for the Run-II data set. For $\mathrm{Q_{weak}}$ Run-II, the tree level acceptance-averaged momentum transfer is determined from simulation to be (using a 1.45% error value determined from data[74])[70]:

$$< Q^2 >_{\mathrm{tree}} = 0.02455 \pm 0.0003\ (\mathrm{GeV/c})^2. \tag{4.33}$$

From these same GEANT3 simulations, we determine the effective scattered electron energy by accounting for continuous energy loss via ionization throughout the length of the target using the relation

$$E_s =< E_{\mathrm{beam}} - \frac{dE}{dz} \cdot z >= 1.153 \pm 0.003\ (\mathrm{GeV}) \tag{4.34}$$

where the initial beam energy is given by E_{beam}, $\frac{dE}{dz}$ is the rate of energy loss through the target, and z is the distance traveled through the target by the electron prior to scattering. The energy and momentum transfer can then be used to calculate the effective scattering angle using the following equation[24]:

$$\cos\theta_{\text{eff}} = \frac{1 - \dfrac{< Q^2 >_{\text{tree}}}{2E_s^2}\left(1 + \dfrac{E_s}{M}\right)}{1 - \dfrac{< Q^2 >_{\text{tree}}}{2E_s^2}\dfrac{E_s}{M}}, \tag{4.35}$$

where M is the rest mass of the proton. Using the values from simulation in Equations 4.33 and 4.34, one obtains $\theta_{\text{eff}} = 7.9°$. Both E_s and Q^2 (and θ by extension) will be determined using real data for the final, unblinded Q_{weak} result.

4.10 Parity Violating Asymmetry Result

This section will collect together all of the corrections discussed in this chapter, resulting in a final measured parity violating elastic $\vec{e}p$ scattering asymmetry. Most of the corrections introduced above correspond to physics effects that did not vary over the course of the experiment and so can be applied as a global correction to the entire Run-II data set. However, effects from helicity correlated beam parameters, beam polarization, and beamline background asymmetries vary enough over the experiment to require corrections performed on shorter timescales. We define the Run-II averaged measured asymmetry A'_{msr} by computing the error-weighted average of the following quantity, computed for each slug in Run-II:

$$A'_{\text{msr}} = \frac{A_{\text{msr,slug}} - \Delta A_{\text{BB}}}{P}, \tag{4.36}$$

where $A_{\text{msr,slug}}$ is the regressed main detector asymmetry, P is the fraction of longitudinal beam polarization measured nearest to that slug, and ΔA_{BB} is defined in Equation 4.25.

With this definition in place, we can then define the fully corrected parity violating asymmetry as

$$A_{\text{PV}}^{\text{ep}} = \frac{R_{\text{tot}}}{(1 - f_{\text{tot}})}\left[< A'_{\text{msr}} > - f_{\text{al}}A_{\text{al}} - f_{\text{neut}}A_{\text{neut}} - f_{\text{inel}}A_{\text{inel}}\right], \tag{4.37}$$

where $f_{\text{tot}} = f_{\text{al}} + f_{\text{neut}} + f_{\text{inel}} + f_{\text{BB}}$.

Accounting for the ±60 ppb blinding box is achieved using Equation 4.3 with $P = 0.8805$ as the Run-II averaged beam polarization measured using the Møller polarimeter. Combining all the results discussed in this chapter results in the following $\vec{e}p$ elastic scattering asymmetry:

$$A_{\text{PV}}^{\text{ep}} = -235.6 \pm 8.7\ (\text{Stat}) \pm 9.3\ (\text{Syst.}) \pm 39.3\ (\text{Blind})\ \text{ppb}. \tag{4.38}$$

Unlike previous analysis of Q_{weak} data[12][40][47], decoupling the statistical and systematic error bars requires some non-trivial algebra, and a final method for doing so has not yet been developed for the full, unblinded result. Systematic errors from regression, polarization, and beamline backgrounds are propagated into the measured asymmetry A'_{msr} at the slug level, resulting in a combined statistical and systematic error bar on that quantity. The relative sizes of these corrections, along with the other corrections that are applied once for all the data, are listed in Table 4.6 and are presented graphically in Figure 4.25. The errors assigned for regression and the beamline background corrections underestimate the true uncertainty from these corrections. This is because the correlated point-to-point errors for each correction (at the runlet level for regression and the slug level for beamline backgrounds) have been averaged together as though they were entirely independent. A proper investigation of how to account for these correlated errors is outside the scope of this thesis but will be required for the final unblinded analysis. Table 4.7 and Figure 4.26 display the relative sizes of the uncertainties (or the effective increase in error bar, in the case of the slug-level corrections) that are combined in quadrature to determine the systematic errors on $A_{\text{PV}}^{\text{ep}}$.

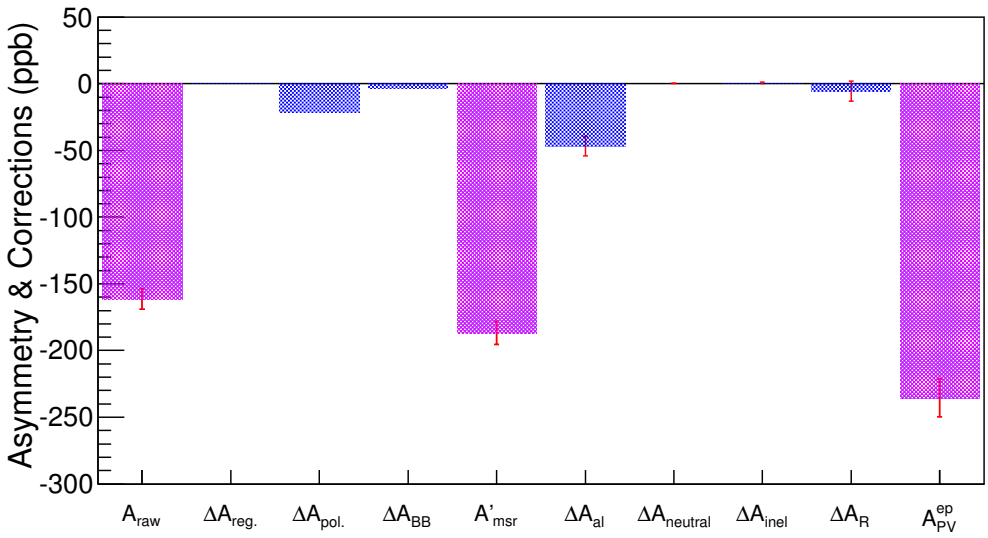

Figure 4.25: The various corrections applied to take A_{raw} to $A^{\text{ep}}_{\text{PV}}$. Effective shifts from slug-level corrections are determined by calculating the asymmetries with or without those corrections. The -3 ppb shift resulting from bias corrections ΔA_R corresponds to the difference in asymmetries determined with or without that multiplicative correction.

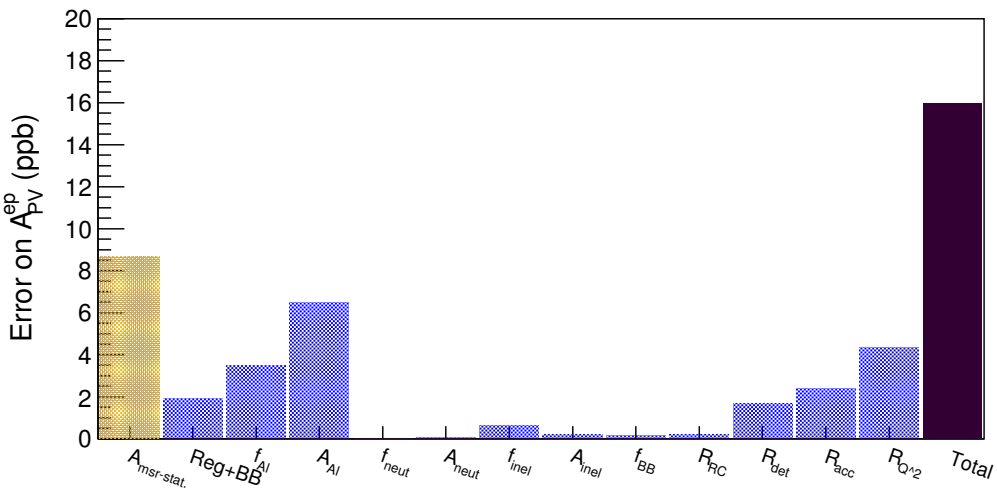

Figure 4.26: Contributions of various corrections to the error on the final parity violating asymmetry. The effective Run-II correction for the slug level regression and beamline background corrections (Reg+BB) was computed as the difference between the raw and corrected asymmetries averaged over the entire data set.

Quantity	Value (ppb)	Error (ppb)
A_{raw}	-161.24	7.69
$< A'_{\mathrm{msr}} >$	-186.89	8.71
Corrections		
Aluminum	-46.67	7.40
Neutral Backgrounds	0.30	0.07
Inelastic Background	0.64	0.65
Experimental Bias	-3.00	5.66
$A_{\mathrm{PV}}^{\mathrm{ep}}$	-235.61	12.77

Table 4.6: Asymmetries and effective additive corrections applied. The regression, beamline background, and polarization corrections were applied at the slug level, with the net effect over the entire Run-II period summarized here. Experimental bias corrections are actually performed multiplicatively, but their effective shift on the asymmetry is presented here for ease of comparison.

Quantity	Contribution to $dA_{\mathrm{PV}}^{\mathrm{ep}}$(ppb)
Statistics	8.74
Regression, BB	1.19
Biases and Rad. Corr.	5.16
A_{al}	6.55
f_{al}	3.45
A_{neut}	0.07
f_{neut}	0.01
A_{inel}	0.20
f_{inel}	0.62
f_{BB}	0.16
Reg scheme dep	0.35
Transverse	1.84
Stat. + Syst.	12.71
Blinding Box	39.3
Total	41.37

Table 4.7: The total contributions to the final error on $A_{\mathrm{PV}}^{\mathrm{ep}}$.

Chapter 5

Results and Conclusions

A 17.5% relative measurement of the parity violating asymmetry from elastic $\vec{e}p$ scattering was determined from a blinded analysis of the $\mathrm{Q_{weak}}$ Run-II data set. This asymmetry result has the smallest statistical and systematic errors determined to date from the $\mathrm{Q_{weak}}$ experiment, and is based on an initial procedure that can be improved as analysis progresses. Some suggestions for future improvement are given at the end of this chapter. This chapter will describe the extraction of the weak charge of the proton Q_W^p using the measured asymmetry. A full discussion of the extraction procedure and its results will be presented.

5.1 Physics Extraction

This section will provide a review of the general Q_W^p extraction method, independent of the $A_{\mathrm{PV}}^{\mathrm{ep}}$ result. Systematic and model-dependent effects will be discussed prior to applying the method to the Run-II blinded result.

5.1.1 Fitting Methodology

Recall Equation 1.81, wherein the parity violating asymmetry is expressed in terms of the various form factors and kinematics quantities defined in Chapter 1:

$$A_{\mathrm{PV}} = -\left(\frac{G_F Q^2}{4\pi\alpha\sqrt{2}}\right)\left[\frac{\epsilon G_E^{\gamma p} G_E^{Zp} + \tau G_M^{\gamma p} G_M^{Zp} - \left(1 - 4\sin^2\theta_W\right)\epsilon' G_M^{\gamma p} G_A^Z}{\epsilon\left(G_E^{\gamma p}\right)^2 + \tau\left(G_M^{\gamma p}\right)^2}\right] \tag{5.1}$$

which describes the theoretical asymmetry in terms of electromagnetic $G_{E,M}^{\gamma p}$ and electroweak $G_{E,M}^{Zp}$ form factors of the proton. For the sake of notational simplicity, one defines the *reduced* asymmetry by dividing out the initial Q^2-dependence and constants $A_0 = -G_F Q^2/(4\pi\alpha\sqrt{2})$:

$$\overline{A_{\mathrm{PV}}} = \frac{A_{\mathrm{PV}}}{A_0} = \frac{\epsilon G_E^{\gamma p} G_E^{Zp} + \tau G_M^{\gamma p} G_M^{Zp} - \left(1 - 4\sin^2\theta_W\right)\epsilon' G_M^{\gamma p} G_A^Z}{\epsilon\left(G_E^{\gamma p}\right)^2 + \tau\left(G_M^{\gamma p}\right)^2}. \tag{5.2}$$

Equation 5.2 can be rewritten in a simple form in terms of Q_W^p, Q^2, and a term that depends on the proton's electromagnetic, axial, and strange form factors[75]:

$$\overline{A_{\mathrm{PV}}} = Q_W^p + Q^2 B(Q^2, \theta). \tag{5.3}$$

where Q_W^p is the weak charge of the proton and $B(Q^2, \theta)$ is the hadronic form factor term introduced in Chapter 1.

It is from this equation that the primary methodology for extracting Q_W^p is derived: namely, performing a fit to the existing PVES data at various momentum transfers in order to determine a functional form for $\overline{A_{\mathrm{PV}}}$ and then by extrapolating to $Q^2 = 0$ GeV/c^2. Asymmetry measurements with $Q^2 \leq 0.1$ GeV/c^2 were taken from the results of the SAMPLE[22], PVA4[23], G0[25], and HAPPEX[24] experiments and fitted using the technique first used in [21]. This data set is provided in Appendix B and was used for the initial low statistics extraction of Q_W^p[12] as well as in the studies explained in this

section. In order to perform the fit, a basis of independent fitting parameters had to be chosen based on certain assumptions as well as what kinds of input were available both from existing data and theoretical calculations. Note first that global fits for the electromagnetic form factors of the proton and neutron exist for varying Q^2 ranges and with different built-in assumptions, whereas no such fits exist for the electroweak form factors. With this in mind, along with the additional goal of wanting to constrain the quark couplings $C_{1u,d}$ in our fit, we write the electromagnetic and electroweak form factors in terms of their individual quark contributions, scaling by the appropriate weak vector couplings $g_V^{u,d,s}$ (Table 1.2):

$$G_E^{\gamma p} = \frac{2}{3}G_E^{up} - \frac{1}{3}G_E^{dp} - \frac{1}{3}G_E^{sp} \tag{5.4a}$$

$$G_E^{\gamma n} = \frac{2}{3}G_E^{un} - \frac{1}{3}G_E^{dn} - \frac{1}{3}G_E^{sn} \tag{5.4b}$$

$$G_E^{Zp} = g_V^u G_E^{up} + g_V^d G_E^{dp} + g_V^s G_E^{sp}, \tag{5.4c}$$

and similarly for the magnetic form factors $G_M^{\gamma p}$, $G_M^{\gamma n}$, and G_M^{Zp}. In an effort to make as few assumptions as possible, we then forgo the traditional assumption of charge symmetry in the nucleon ($G_{Ep}^u = G_{En}^d$) and parameterize the effects of charge symmetry violation below, for the electric form factors and similarly for the magnetic form factors:

$$G_{En}^d = G_{Ep}^u - G_E^{\delta u} \tag{5.5a}$$

$$G_{En}^u = G_{Ep}^d - G_E^{\delta d} \tag{5.5b}$$

$$G_{En}^s = G_{Ep}^s - G_E^{\delta s}. \tag{5.5c}$$

where δ superscripts denote the extent to which charge symmetry is broken.

Using Equations 5.5 and 5.4 allows us to write G_E^{Zp} and G_M^{Zp} in terms of the (known)

electromagnetic form factors (See Section 5.1.2), the C_1's, and a term that contains contributions from strangeness in the nucleon and charge symmetry violation $\xi_V^{(0)}$:

$$G_E^{Zp} = -2(2C_{1u} + C_{1d})G_E^{\gamma p} - 2(C_{1u} + 2C_{1d})G_E^{\gamma n} + \xi_V^{(0)} G_E^s. \tag{5.6}$$

The complete derivation of Equation 5.6 is given in Appendix A.3.

By using this equation (and its magnetic analog, with indentical structure), we can then write the reduced asymmetry in terms of the electromagnetic form factors ($G_{E,M}^{\gamma\{p,n\}}$), the weak vector couplings ($C_{1u,d}$), the weak axial form factor (G_A^Z), and the strange electric and magnetic form factors ($G_{E,M}^s$). The axial form factor has terms for both the proton and neutron, which are independent results of the fit. With the electromagnetic terms well determined, this leaves a minimum of six free parameters.

The strange form factor in Equation 5.6 is parameterized using a simple dipole form, defined as:

$$G_D = \left(\frac{1}{1 + \frac{\Lambda^2}{Q^2}} \right)^2 . \tag{5.7}$$

This parameterization, first used in [76], provides a Q^2 dependence to the form factors that matches experimental observations. A simple, and easily interpretable model defines the strange form factors in terms of the strange radius ρ_s and moment μ_s of the proton[77]:

$$G_E^s = Q^2 \rho_s G_D \tag{5.8a}$$

$$G_M^s = \mu_s G_D, \tag{5.8b}$$

with a mass scale of $\Lambda = 1$ (GeV/c)^2. Sensitivity to the choice in this parameter was studied in the context of the early Q_{weak} result[12] by varying Λ between 0.7 (GeV/c)^2

and 2 (GeV/c)^2. The final weak charge extraction varied by only 1.5% within this range[12], and lower values of Λ are disfavoured by lattice QCD calculations[77].

The axial form factor G_A^Z can be separated into an isoscalar (T=0) and isovector (T=1) piece, where T is the quantum number associated with weak isospin symmetry. The isoscalar axial form factor $G_A^{Z(T=0)}$ vanishes at tree level but is not negligible at the kinematics of Q_{weak} and the other experiments used in the fit. The value and uncertainty on this term are constrained by theoretical calculations in [78], resulting in the fit having only five free parameters, including the isovector piece $G_A^{Z(T=1)}$ of the weak axial form factor*.

With parameterizations in place for the electromagnetic, strange, and axial form factors, the fit can then be performed. Fitting is done using a χ^2 minimization routine with:

$$\chi^2 = \left(\frac{A_{\text{fit}}(G_A^{Zp}, G_A^{Zn}, \rho_s, \mu_s, C_{1u}, C_{1d}) - A_{\text{data}}}{dA_{\text{data}}} \right)^2 . \tag{5.9}$$

The numerical values for the 6 parameters in the fit are determined by solving the simultaneous differential equations:

$$\frac{\partial \chi^2}{\partial V_i} = 0, \tag{5.10}$$

where V_i are the 6 parameters of the fit as defined at the inputs to A_{fit} in Equation 5.9. The following section will address systematic effects related to the electromagnetic form factors $G_{E,M}^{\gamma\{p,n\}}$.

*The decomposition of the axial current in terms of the isovector and isoscalar pieces is available in [79].

5.1.2 Electromagnetic Form Factors

A number of fits have been performed over the last decade to determine the electric and magnetic form factors of both the proton and the neutron with as precise uncertainties as possible[7][17][18][19][76]. Fits vary in their exact dependence on momentum transfer, their treatment of correlations between electric and magnetic form factors, and applications of higher order corrections such as two-photon exchange diagrams. Unfortunately, no fits were specifically optimized for the low momentum transfer of the Q_{weak} experiment, so no single option could be singled out as most appropriate for our kinematics. Choosing one fit over another introduces a possible source of uncertainty to the extent that the various fits differ from one another. Additionally, the errors on the form factors themselves (as provided by the fit authors) need to be propagated through our analysis.

At the time of this analysis, four fits were considered for use in the extraction of Q_W^p: Kelly[17], Friedrich & Walcher[18], Arrington & Sick[7], and a simple dipole form as in Equation 5.7 with a mass term of $\Lambda = 0.71$ (GeV)^2. In order to study the sensitivity of the extracted value for Q_W^p on this choice, the extraction was performed using a hypothetical asymmetry data point at Q_{weak} kinematics that agrees with the standard model (-214.2 ± 0.0030 ppb)[40]. Using the four different electromagnetic form factor fits resulted in a variation of less than 1% in the proton's weak charge as shown in Table 5.1.

	Q_W^p	dQ_W^p
Arrington & Sick	0.0705	0.0023
Kelly	0.0702	0.0023
Dipole	0.0702	0.0023
Friedrich & Walcher	0.068	0.0023

Table 5.1: The proton's weak charge extracted using a theoretical asymmetry at Q_{weak} kinematics and with different electromagnetic form factor fits.

The Friedrich & Walcher fit stands out as being particularly different from the others

(although still agreeing within errors) and the dipole form is poorly motivated with respect to theory. As a result, we move forward by considering both the Kelly and Arrington & Sick fits as legitimate choices. Their electromagnetic form factors are parameterized using a continued fraction expansion:

$$G_{\mathrm{CF}}(Q^2) = \cfrac{1}{1 + \cfrac{b_1 Q^2}{1 + \cfrac{b_2 Q^2}{1 + \cdots}}} \tag{5.11}$$

with parameters given in their Tables I and III[7], and reproduced in Table 5.2.

	b_1	b_2	b_3	b_4	b_5
$G_E^{\gamma p}$	3.478	-0.140	-1.311	1.128	-0.233
$G_M^{\gamma p}/\mu_p$	3.224	-0.313	-0.868	4.278	-1.102
$G_E^{\gamma n}$	0.977	-20.82	22/02	-	-
$G_M^{\gamma n}/\mu_n$	3.297	-0.258	0.001	-	-

Table 5.2: Fit parameters to the continued fraction expansion used by Arrington & Sick in their electromagnetic form factor parameterization[7].

The errors in Table 5.1 underestimate the true uncertainties as they do not include the errors on the form factors themselves as quoted by the individual fit authors.

Electromagnetic form factor errors reported by fit authors were quoted either as uncertainties on the form factors themselves or uncertainties on the fit parameters that describe them as functions of momentum transfer. Instead of a full theoretical propagation of errors through our extraction formalism, a Monte Carlo technique was employed wherein our fit was performed one thousand times, each time with the electromagnetic form factors being shifted within their reported errors in a uniformly correlated manner[†]. Using the same hypothetical data point introduced above as input (alongside the

[†]A random number was sampled from a normal distribution and then used to shift both the electric and magnetic form factors in the same direction.

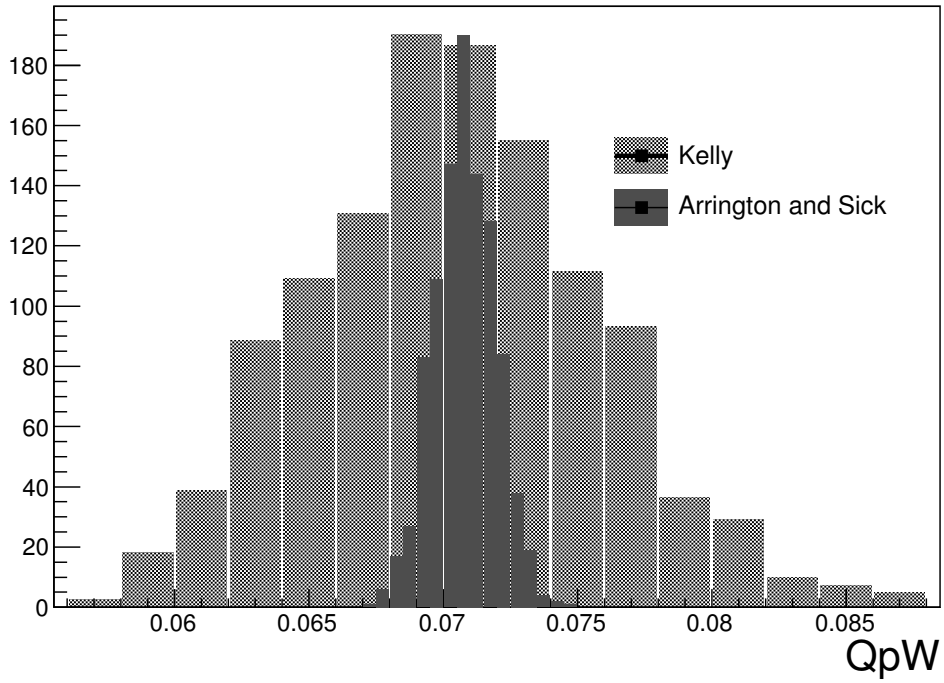

Figure 5.1: Results from a Monte Carlo simulation in which Q_W^p is calculated 1000 times using either Kelly[17] or Arrington & Sick[7] electromagnetic form factors, varied within reported errors. The hashed bars correspond to Kelly (mean = 0.0708, RMS = 0.0052) and the solid bars are Arrington & Sick (mean = 0.0708, RMS = 0.0011).

other points used in the early Q_{weak} result[12]), the distributions in Figure 5.1 were generated.

We interpret the RMS widths of the distributions in Figure 5.1 as reflecting the impact that the fitting errors have on the total extracted value of Q_W^p. Using this model, the Arrington & Sick fit has less of an impact on the extracted weak charge error. The Arrington & Sick fit was designed with low Q^2 experiments in mind, and takes extra care when accounting for correlations between electric and magnetic form factors when compared to the Kelly extraction. For these reasons, we move forward using only the Arrington & Sick fit.

5.2 The Weak Charge of the Proton

Before the fitting routine described in Section 5.1.1 can be performed, an additional correction to all asymmetry inputs must be applied to account for the Q^2- and energy-dependence of the $\square_{\gamma Z}$ diagram shown in Figure 1.9 and discussed in detail in [80] and [30], with recent progresses documented in [31]. These corrections require non-perturbative inputs to account for both short- and long-range physics; the best technique for handling these types of corrections are dispersion relations[31]. At $\mathrm{Q_{weak}}$ kinematics, the correction is calculated to be $\square_{\gamma Z} = -12.59$ ppb, yielding a final asymmetry of $A_{\mathrm{PV}}^{\mathrm{ep}} = -223.0 \pm 41.4$ ppb for Run-II. This result does not currently include errors due to uncertainty in the $\square_{\gamma Z}$ determination, but preliminary studies suggest a < 1 ppb additional error to the asymmetry[81].

The fitting procedure introduced in Section 5.1.1 determines the values for ρ_s, μ_s (Equation 5.8), G_{Ap}^Z, G_{An}^Z, C_{1u}, and C_{1d} that minimize the χ^2 of the fit. The resulting $\overline{A_{\mathrm{PV}}}$ is a function of momentum transfer and scattering angle. The intercept at $Q^2 = 0$ (GeV/c)^2 then gives the weak charge of the proton as is clear in Equation 5.3. Since the fit is still a function of two parameters, it can be difficult to visualize with a single figure. In order to plot the reduced asymmetry versus Q^2 without ignoring the θ-dependence, we rotate each data point into the forward angle limit $\theta = 0°$ using the following relation:

$$A_{\mathrm{PV}}^{\theta=0°} = A_{\mathrm{PV}} - \left[A_{\mathrm{calc}}(Q^2, \theta) - A_{\mathrm{calc}}(Q^2, 0°)\right] \tag{5.12}$$

where A_{calc} corresponds to the asymmetry calculated by substituting that particular experiment's kinematics along with the results of the full fit, into Equation 5.2. Note that this is simply done after the fit is complete in order to plot the reduced asymmetry versus Q^2 with the angular dependence removed. The resulting Q_W^p when including the blinded Run-II asymmetry is determined using Equation 1.76, $Q_W^p = -2(2C_{1u} + C_{1d})$,

and the C_1's determined from the fit:

$$Q_W^p(\text{Run-II Blinded + PVES}) = 0.0717 \pm 0.0094 \tag{5.13}$$

where the fit is displayed in Figure 5.2, and a summary of the inputs and conditions for the fit are available in Appendix B. The six parameters extracted by the fit are:

$$\begin{aligned} G_A^{Zp} &= -0.63 \pm 0.37 \\ G_A^{Zn} &= 0.72 \pm 0.47 \\ \rho_s &= 0.19 \pm 0.11 \text{ GeV}^{-2} \\ \mu_s &= -0.18 \pm 0.15\ \mu_N \\ C_{1u} &= -0.185 \pm 0.007 \\ C_{1d} &= 0.33 \pm 0.01. \end{aligned} \tag{5.14a}$$

Additional constraints on the neutral weak quark couplings are available through results of atomic parity violation experiments (APV). These constraints are incorporated in the fit by adding an extra term to Equation 5.9. Parity violating electron scattering and atomic parity violation experiments provide different constraints on the isovector ($C_{1u} - C_{1d}$) and isoscalar ($C_{1u} + C_{1d}$) combinations of these couplings as was shown in Figure 1.6. The newest analysis[82] of the ^{133}Cs APV experiment[83], combined with the PVES results shown above, results in neutral weak vector couplings of

$$\begin{aligned} C_{1u}(\text{PVES+APV}) &= -0.187 \pm 0.004 \\ C_{1d}(\text{PVES+APV}) &= 0.339 \pm 0.004, \end{aligned} \tag{5.15a}$$

and a new Q_W^p determination of

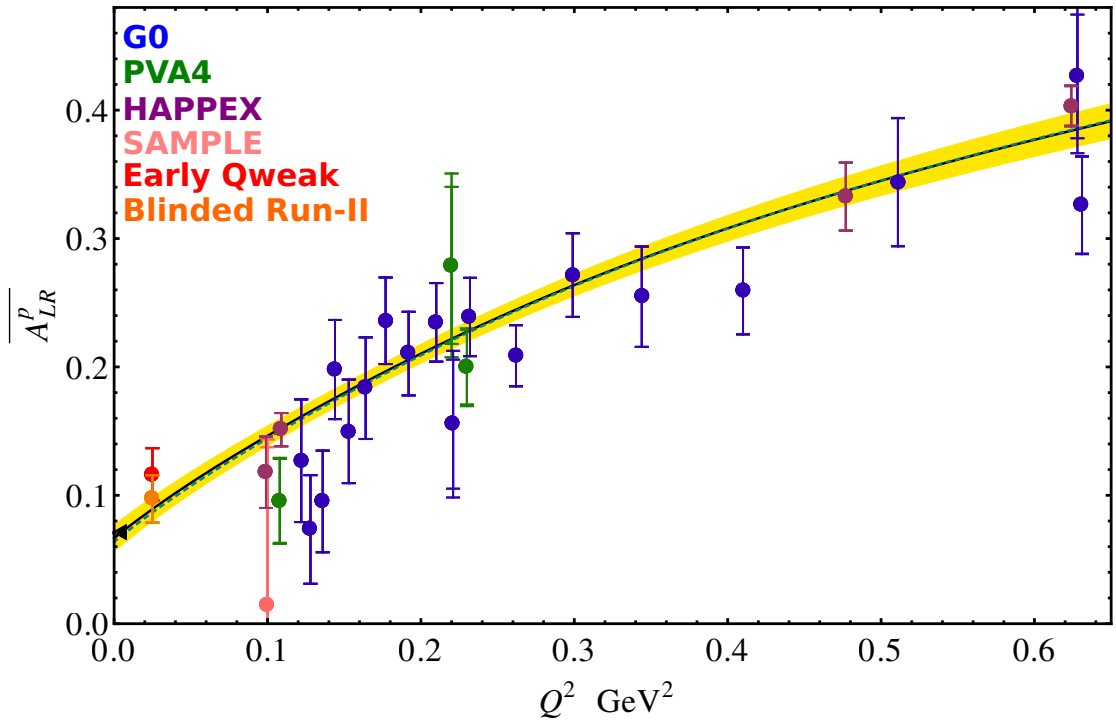

Figure 5.2: The result of a global fit to PVES asymmetries. The black line and yellow band correspond to the mean and uncertainty from the fit including both Q_{weak} points (early result in red and Run-II blinded in orange), and the dashed line shows the result with no Q_{weak} results included. The standard model prediction is shown as the black triangle near the intercept at $Q^2 = 0$.

$$Q^p_W(\text{Run-II Blinded + PVES + APV}) = 0.071 \pm 0.009. \tag{5.16}$$

Similarly, Equation 1.76 provides the weak charge of the neutron in terms of the C_1's, and so we also obtain:

$$Q^n_W(\text{Run-II Blinded + PVES + APV}) = -0.981 \pm 0.009. \tag{5.17}$$

5.3 The Weak Mixing Angle $\sin^2\theta_W$

The standard model formula for the proton's weak charge, including radiative corrections and effects from supersymmetry was provided in Equation 1.87. Ignoring the new physics terms, we can write:

$$Q_W^p(\mathrm{SM}) = [\rho_{\mathrm{NC}} + \Delta_e] \times [1 - 4\sin^2\hat{\theta}_W + \Delta_e'] + \Box_{WW} + \Box_{ZZ} + \Box_{\gamma Z}, \tag{5.18}$$

where an explanation of terms was given alongside Equation 1.87. Calculations of the correction factors are done in [2] and yield the results in Table 5.3.

Correction	Value
Δ_e	−0.00116
Δ_e'	−0.00142
$\Box_{WW}$	0.018317
$\Box_{ZZ}$	0.001926
$\Box\gamma Z$	0.0054
ρ_{NC}	1.00833

Table 5.3: The electroweak radiative corrections defined in [2]. The value for $\Box_{\gamma Z}$ was taken from [31]. Uncertainties are not provided here but have negligible effect when propagated through Equation 5.18.

Using Equations 5.18 and 5.16 and the corrections in Table 5.3, one calculates the weak mixing angle as:

$$\sin^2\theta_W = \frac{1}{4}\left[1 + \Delta_e' - \frac{Q_W^p - \Box_{WW} - \Box_{ZZ} - \Box_{\gamma Z}}{\rho_{\mathrm{NC}} + \Delta_e}\right] = 0.238 \pm 0.002. \tag{5.19}$$

where the error corresponds simply to the difference between weak mixing angles computed using Q_W^p or $Q_W^p + dQ_W^p$:

$$d\sin^2\theta_W = \sin^2\theta_W(Q_W^p) - \sin^2\theta_W(Q_W^p + dQ_W^p). \tag{5.20}$$

This result is in good agreement with the theoretical prediction using the standard model: $\sin^2\theta_W(\overline{MS}) = 0.23807 \pm 0.0002$[2][‡]. It is important to note however, that the value of the weak mixing angle determined above uses a blinded asymmetry and is subject to change upon the unblinding of the data. An updated version of the running plot shown in Figure 1.2 is shown in Figure 5.4.

5.4 Conclusions and Future Work

An initial, blinded analysis of the Q_{weak} experiment's Run-II data set has been performed. The parity violating asymmetry from elastic $\vec{e}p$ scattering at $Q^2 = 0.02455 \pm 0.0006$ (GeV/c)^2, accounting for $\square_{\gamma Z}$ corrections, was determined to be

$$A_{\mathrm{PV}}^{\mathrm{ep}} = -223.0 \pm 8.7\ (\mathrm{stat.}) \pm 9.3\ (\mathrm{syst.}) \pm 39.3\ (\mathrm{blind})\ \mathrm{ppb}. \tag{5.21}$$

From this result, the weak charge of the proton Q_W^p and the weak mixing angle $\sin^2\theta_W$ were extracted:

$$\begin{aligned} Q_W^p &= 0.071 \pm 0.009 \\ \sin^2\theta_W &= 0.238 \pm 0.002. \end{aligned} \tag{5.22}$$

Even with the blinding errors, the Run-II results presented in this dissertation have provided improved constraints on a number of standard model parameters including the weak mixing angle $\sin^2\theta_W$ and the neutral weak vector couplings. In an effort to explore the full impact of the Run-II analysis on the final Q_{weak} result, we can ignore the contribution to the error bar resulting from the blinding and look at how the errors

[‡]The $\overline{MS}$ notation refers to the modified minimal subtraction scheme: a renormalization scheme in quantum field theory which absorbs infinities that arise when performing perturbative calculations beyond tree level[84].

on the results change. Figure 5.5 displays the relative size of the error on the reduced asymmetry when the blinding error is removed, and Figure 5.6 shows similarly for the isoscalar and isovector combinations of the neutral weak vector couplings. Chapter 1 introduced the following equation for quantifying the impact of a weak charge measurement in terms of the mass scale of new physics it is sensitive to:

$$\frac{\Lambda}{g} \sim \frac{1}{\sqrt{2\sqrt{2}G_F}} \cdot \frac{1}{\sqrt{\delta Q_W^p(\mathrm{Exp})}}. \tag{5.23}$$

Ignoring the blinding error reduces the error on the proton's weak charge from $\delta Q_W^p = 0.0093$ to $\delta Q_W^p = 0.0056$ (including constraints from APV on the C_1's.). With this unblinded Run-II error, agreement with the standard model rules out any new physics at or below a 1.6 TeV mass scale at the 95% confidence level with $g = 1$. In the high-energy physics models where $g = 4\pi$ discussed in Chapter 1, new physics with compositeness scales at or below ~ 21 TeV are excluded.

The most significant improvement to the Run-II results presented in this Chapter will come from the unblinding of the data. Beyond that, a number of methods to reduce systematic errors are currently being studied, including improvements to aluminum analysis and the methods for determining kinematics from real data as opposed to simulations. The use of real data for determining the kinematics of the experiment will also provide improved results when compared to the simulated values presented in Section 4.9.

Correcting for beamline backgrounds and polarization in the published Q_{weak} commissioning data was done using a single correction[12]. The blinded Run-I analysis improved on this by correcting for polarization based on two polarization measurements. This dissertation was the first of its kind in that both polarization and beamline backgrounds were corrected at the slug level, using 63 separate polarization measurements in order to track the changing beam polarization over time. Improvements to both

the error on the polarization measurements as well as the method by which that error is propagated into the final asymmetry are expected to be available for the final Q_{weak} result.

With respect to the extraction of Q_W^p from the elastic asymmetry, there are a number of ongoing studies aiming to reduce the model dependence of the fitting routine described in Section 5.1.1. These include removing the deuterium and helium data points from the fit, resulting in the removal of the neutron's electromagnetic and weak axial form factors. With these removed, the more recent determination of the the electromagnetic form factors of the proton, optimized at low Q^2[19] could be used.

The final, unblinded Q_{weak} result will combine data from the commissioning period, Run-I, and Run-II. It will provide the most precise determination of the proton's weak charge, and will provide highly anticipated constraints on a number of parameters including the weak mixing angle and neutral weak vector couplings of the up and down quarks. Future parity violation experiments will benefit greatly from advances in technology as well as analysis methodology as results of the Q_{weak} experiment.

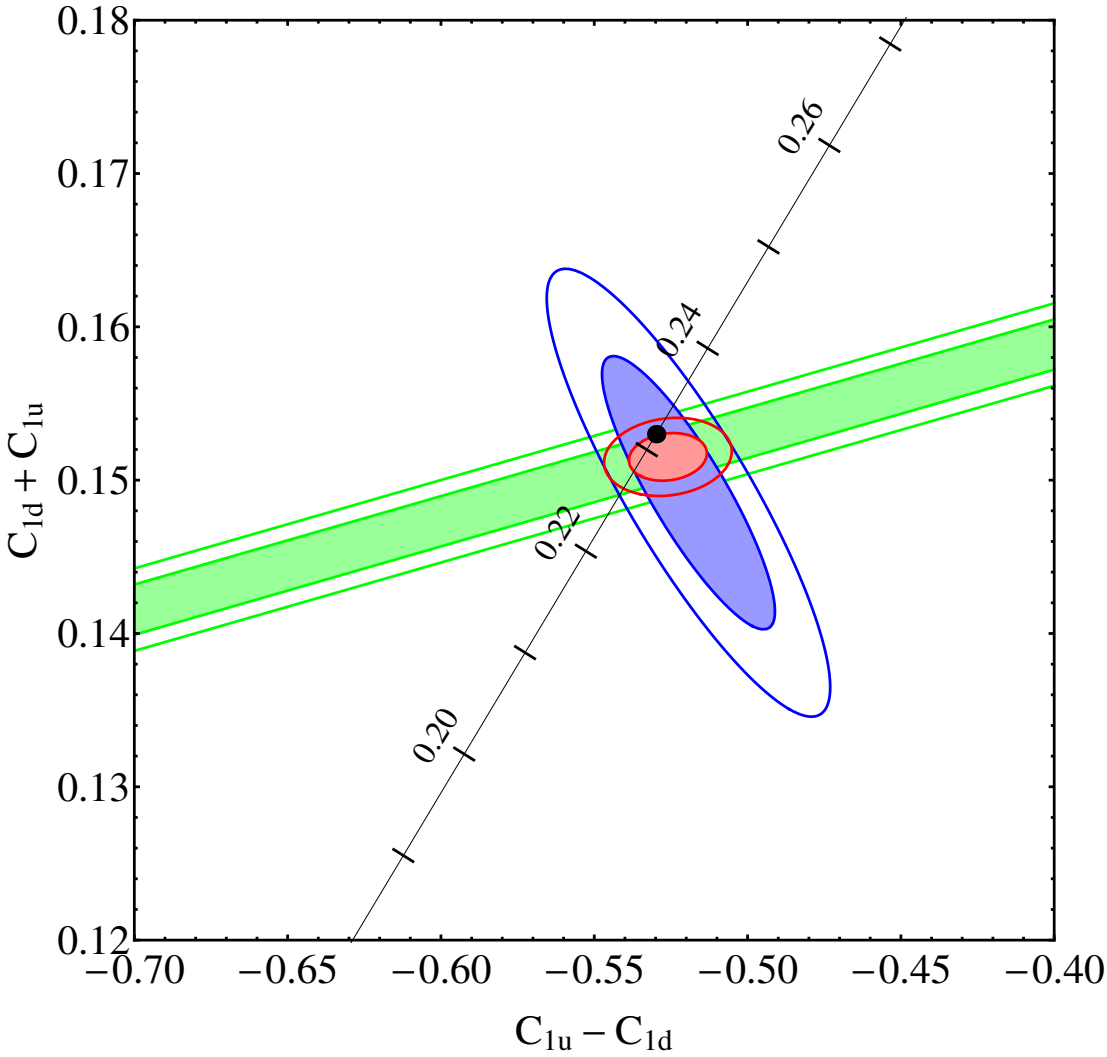

Figure 5.3: An updated version of Figure 1.6 that displays the constraints on the isoscalar and isovector combinations of the neutral weak quark couplings determined using APV and PVES data. The green band corresponds to constraints from atomic parity violation, the red and blue ellipses are from PVES data with and without any Q_{weak} data respectively.

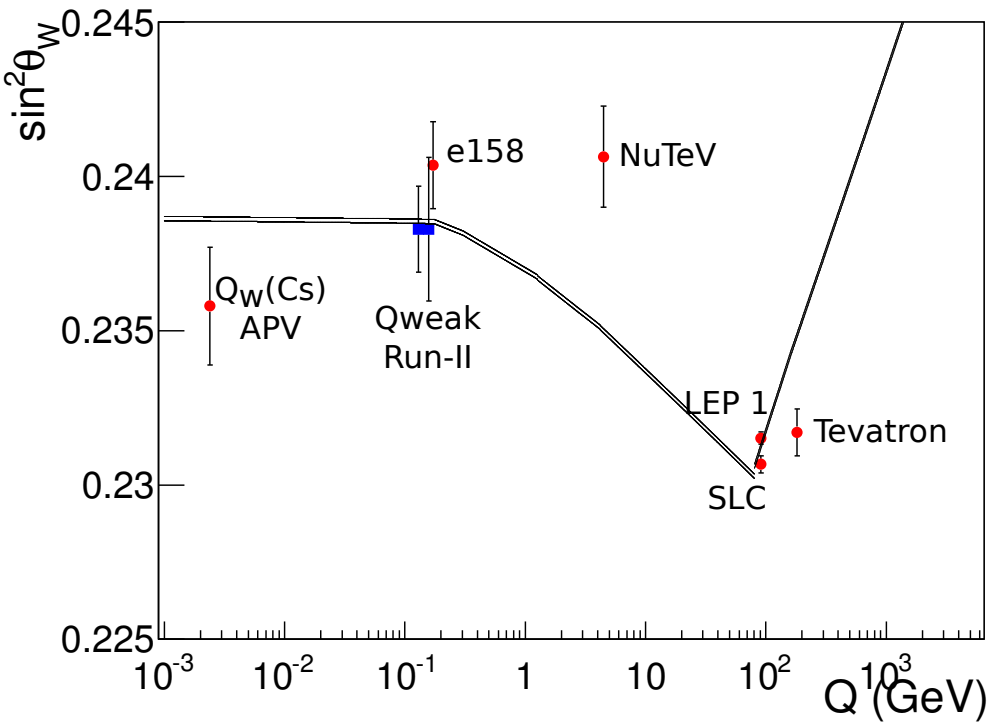

Figure 5.4: An updated version of the running of the weak mixing angle with momentum transfer. The Tevatron point has been artificially displaced on the horizontal axis from the Z-pole in order to be more visible. The weak mixing angle determined from the blinded Run-II data set is shown both with and without errors from blinding, with the unblinded error point displaced to the left. The black lines correspond to theoretical lower and upper limits determined in [2].

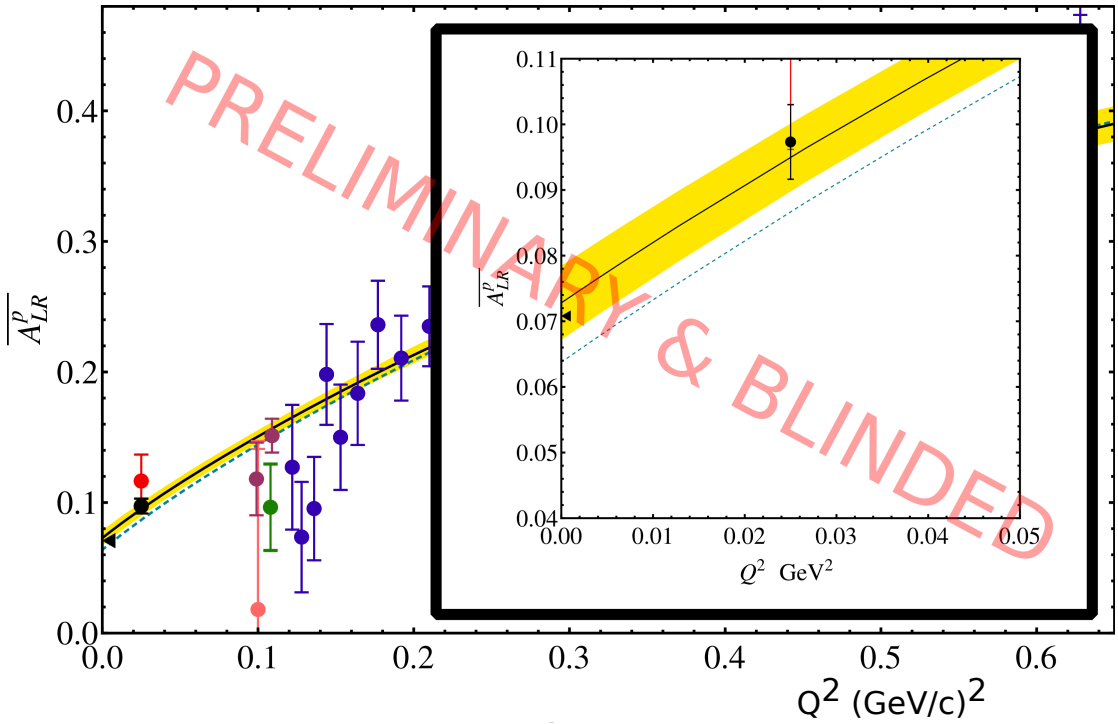

Figure 5.5: Reduced asymmetry plot with the blinding error has been removed from the Run-II point presented in this dissertation. The blinding offset leaves the mean value of the proton's weak charge uninterpretable, but the size of the error bar reflects the unblinded Run-II precision. The insert provides a zoomed in view of the Run-II point without a blinding error, and the other curves are defined in the caption of Figure 5.2

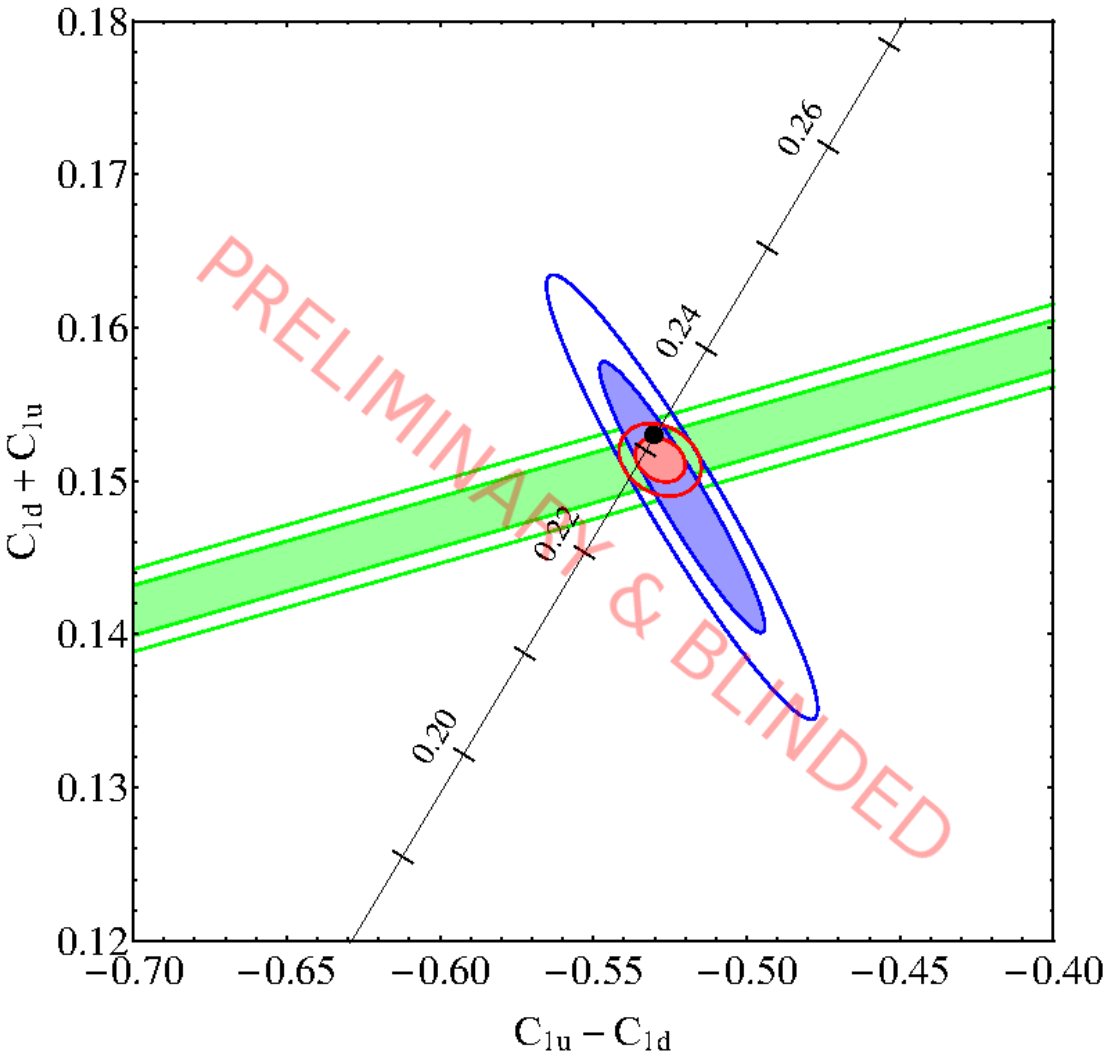

Figure 5.6: The neutral weak quark coupling constraints after removing the Run-II blinding error. The centre of the small red ellipse is subject to shift after unblinding but the size will remain the same.

Bibliography

[1] Fermilab. Inquiring minds. url=https://www.fnal.gov/pub/inquiring/matter/madeof/index.html. Accessed March 2015.

[2] Jens Erler, Andriy Kurylov, and Michael J. Ramsey-Musolf. Weak charge of the proton and new physics. *Phys. Rev. D*, 68:016006, Jul 2003.

[3] Katherine Myers. *The First Determination of the Proton's Weak Charge Through Parity-Violating Asymmetry Measurements in Elastic e + p and e + Al Scattering*. PhD thesis, The George Washington University, May 2012.

[4] T. Allison, M. Anderson, D. Androic, et al. The Qweak Experimental Apparatus. *Nuclear Instruments and Methods in Physics Research Section A: Accelerators, Spectrometers, Detectors and Associated Equipment*, 781(0):105 – 133, 2015.

[5] Peiqing Wang. *A Measurement of the Proton's Weak Charge Using an Integration Čerenkov Detector System*. PhD thesis, University of Manitoba, 2011.

[6] D. et al. Armstrong. Qweak jeopardy proposal: E05-008. Qweak Document Database (Document 190-v1), 2004.

[7] John Arrington and Ingo Sick. Precise determination of low-q nucleon electromagnetic form factors and their impact on parity-violating e-p elastic scattering. *Phys. Rev. C*, 76:035201, Sep 2007.

[8] K.A. Olive et al. Review of Particle Physics. *Chin.Phys.*, C38:090001, 2014.

[9] S. Chatrchyan, V. Khachatryan, A. M. Sirunyan, et al. Observation of a new boson at a mass of 125 GeV with the CMS experiment at the LHC. *Physics Letters B*, 716(1):30 – 61, 2012.

[10] G. Aad, B. Abbott, J. Abdallah, et al. Combined measurement of the higgs boson mass in pp collisions at $\sqrt{s} = 7$ and 8 tev with the atlas and cms experiments. *Phys. Rev. Lett.*, 114:191803, May 2015.

[11] F. Mandl and G Shaw. *Quantum Field Theory: Second Edition*. John Wiley & Sons, Ltd., New York, 2010.

[12] D. Androic, D. S. Armstrong, A. Asaturyan, et al. First determination of the weak charge of the proton. *Phys. Rev. Lett.*, 111:141803, Oct 2013.

[13] F. Halzen and A. D. Martin. *Quarks and Leptons: An Introductory Course in Modern Particle Physics*. John Wiley & Sons, Ltd., New York, 1984.

[14] E. Noether. Invariante variationsprobleme. *Nachrichten von der Königl. Gesellschaft der Wissenschaften zu Göttingen, Mathematisch-Physikalische Klasse*, 1918.

[15] Robert G. Sachs. Nucleon electromagnetic form factors at high momentum transfer. *Phys. Rev. Lett.*, 12:231–233, Mar 1964.

[16] M.J. Musolf, T.W. Donnelly, J. Dubach, S.J. Pollock, S. Kowalski, et al. Intermediate-energy semileptonic probes of the hadronic neutral current. *Phys.Rept.*, 239:1–178, 1994.

[17] J. Kelly. Simple parametrization of nucleon form factors. *Phys. Rev. C*, 70:068202, Dec 2004.

[18] J. Friedrich and Th. Walcher. A coherent interpretation of the form factors of the nucleon in terms of a pion cloud and constituent quarks. *The European Physical Journal A - Hadrons and Nuclei*, 17(4):607–623, 2003.

[19] Siddharth Venkat, John Arrington, Gerald Miller, and Xiaohui Zhan. Realistic transverse images of the proton charge and magnetization densities. *Phys. Rev. C*, 83:015203, Jan 2011.

[20] Douglas H. Beck and Barry R. Holstein. Nucleon structure and parity-violating electron scattering. *International Journal of Modern Physics E*, 10(01):1–41, 2001.

[21] R. Young, R. Carlini, A. Thomas, and J. Roche. Testing the standard model by precision measurement of the weak charges of quarks. *Phys. Rev. Lett.*, 99:122003, Sep 2007.

[22] E. J. Beise, M. L. Pitt, and D. T. Spayde. The SAMPLE experiment and weak nucleon structure. *Progress in Particle and Nuclear Physics*, 54(1):289 – 350, 2005.

[23] F. Maas, P. Achenbach, K. Aulenbacher, et al. Measurement of strange-quark contributions to the nucleon's form factors at $Q^2 = 0.230\,(\mathrm{GeV}/c)^2$. *Phys. Rev. Lett.*, 93:022002, Jul 2004.

[24] K. Aniol, D. Armstrong, T. Averett, et al. Parity-violating electroweak asymmetry in $\vec{e}p$ scattering. *Phys. Rev. C*, 69:065501, Jun 2004.

[25] D. Androic, D. Armstrong, J. Arvieux, et al. Strange Quark Contributions to Parity-Violating Asymmetries in the Backward Angle G0 Electron Scattering Experiment. *Phys. Rev. Lett.*, 104:012001, Jan 2010.

[26] P. L. Anthony, R. G. Arnold, C. Arroyo, K. Bega, et al. Precision Measurement of the Weak Mixing Angle in Moller Scattering. *Phys. Rev. Lett.*, 95:081601, Aug 2005.

[27] Juliette Mammei. The MOLLER Experiment. *Nuovo Cim.*, C035N04:203–208, 2012.

[28] Jens Erler, Charles J. Horowitz, Sonny Mantry, and Paul A. Souder. Weak polarized electron scattering. *Annual Review of Nuclear and Particle Science*, 64(1):269–298, 2014.

[29] Estia J. Eichten, Kenneth D. Lane, and Michael E. Peskin. New tests for quark and lepton substructure. *Phys. Rev. Lett.*, 50:811–814, Mar 1983.

[30] N.L. Hall, P.G. Blunden, W. Melnitchouk, A.W. Thomas, and R.D. Young. Constrained γZ correction to parity-violating electron scattering. *AIP Conf.Proc.*, 1563:94–97, 2013.

[31] N.L. Hall, P.G. Blunden, W. Melnitchouk, A.W. Thomas, and R.D. Young. Quark-hadron duality constraints on γZ box corrections to parity-violating elastic scattering. *arXiv*, 1504.03973, 2015.

[32] C.W. Leemann, D.R. Douglas, and G.A. Krafft. The Continuous Electron Beam Accelerator Facility: CEBAF at the Jefferson Laboratory. *Ann.Rev.Nucl.Part.Sci.*, 51:413–450, 2001.

[33] Y.C. Chao, M. Drury, C. Hovater, A. Hutton, G.A. Krafft, et al. CEBAF accelerator achievements. *J.Phys.Conf.Ser.*, 299:012015, 2011.

[34] W. Barry. A general analysis of thin wire pickups for high frequency beam position monitors. *Nuclear Instruments and Methods in Physics Research Section A: Accelerators, Spectrometers, Detectors and Associated Equipment*, 301(3):407 – 416, 1991.

[35] R. Dickson and V. A. Lebedev. Fast digital feedback system for energy and beam position stabilization. IEEE Particle Accelerator Conference (PAC 99), 1999.

[36] C. Yan, R. Carlini, and D. Neuffer. Beam energy measurement using the Hall C beamline. *Conf.Proc.*, C930517:2136–2138, 1993.

[37] C. Yan and R. Carlini. Hall C beamline instrumentation. CEBAF Summer Workshop, 1992.

[38] D. Buddhini P. Waidyawansa. *A 3% Measurement of the Beam Normal Single Spin Asymmetry in Forward Angle Elastic Electron-Proton Scattering using the Qweak Setup*. PhD thesis, Ohio University, 2013.

[39] R. Subedi. Summary report on the BCMs for qweak. Qweak Document Database (Document 1777-v1), 2013.

[40] Rakitha Beminiwatha. *A Measurement of the Weak Charge of the Proton through Parity Violating Electron Scattering using the Qweak Apparatus: A 21% Result*. PhD thesis, Ohio University, 2013.

[41] Joshua Hoskins. *Determination of the Proton's Weak Charge via Parity Violating Electron Scattering*. PhD thesis, College of William and Mary, 2015.

[42] M. Hauger, A. Honegger, J. Jourdan, G. Kubon, T. Petitjean, et al. A High precision polarimeter. *Nucl.Instrum.Meth.*, A462:382–392, 2001.

[43] D. Gaskell, D.G. Meekins, and C. Yan. New methods for precision Moeller polarimetry. *Eur.Phys.J.*, A32:561–564, 2007.

[44] D.S. Armstrong, A. Asaturyan, T. Averett, J. Benesch, J. Birchall, et al. The Qweak Experiment: A Search for New Physics at the TeV Scale via a Measurement of the Proton's Weak Charge. Proposed to the JLab PAC, 2007. *arXiv*, 1202.1255, 2012.

[45] A. Narayan, D. Dutta, V. Tvaskis, and J.W. Martin. A diamond micro-strip electron detector for Compton polarimetry. *Nuovo Cim.*, C035N04:134–136, 2012.

[46] G.R. Smith. The Q(weak) target performance. *Nuovo Cim.*, C035N04:159–163, 2012.

[47] Adesh Subedi. *Determination of the weak charge of the proton through parity violating asymmetry measurements in the elastic e+p scattering*. PhD thesis, Mississippi State University, 2014.

[48] Juliette Mammei. *Parity-Violating Elastic Electron Nucleon Scattering: Measurement of the Strange Quark Content of the Nucleon and Towards a Measurement of the Weak Charge of the Proton*. PhD thesis, Virginia Polytechnic Institute and State University, April 2010.

[49] John Leacock. *Measuring the Weak Charge of the Proton and the Hadronic Parity Violation of the $N \to \Delta$ Transition*. PhD thesis, Virginia Polytechnic Institute and State University, 2012.

[50] John P. Leckey. *The First Direct Measurement of the Weak Charge of the Proton*. PhD thesis, College of William and Mary, 2012.

[51] Jie Pan. *Towards a Precision Measurement of Parity-Violating e-p Elastic Scattering at Low Momentum Transfer*. PhD thesis, University of Manitoba, 2012.

[52] Dietrich Müller. Electron showers of high primary energy in lead. *Phys. Rev. D*, 5:2677–2683, Jun 1972.

[53] D. Mack. PMT selection and prototype voltage dividers for the Qweak cerenkov detector. Qweak Document Database (Document 221-v1), 2005.

[54] M. Anderson. Results from the 1st and 2nd prototype low gain base for the Qweak experiment. Qweak Document Database (Document 604-v1), 2006.

[55] M. Gericke. Diode mode saturation and linearity tests of the QWeak main Čerenkov detector PMTs. Qweak Document Database (Document 534-v1), 2006.

[56] S. MacEwan. Gain tests for current mode PMT bases. Qweak Document Database (Document 1154-v2), 2010.

[57] S. MacEwan. Main detector pe/event during QTOR scan. https://qweak.jlab.org/elog/Detector/42, 2011.

[58] W. R. Leo. *Techniques for Nuclear and Particle Physics Experiments*. Springer-Verlag, Berlin, 1987.

[59] R. Mahurin. Linearity measurements in the main detectors. Qweak Document Database (Document 1696-v2), 2012.

[60] Ph. R. Bevington. *Data reduction and error analysis for the physical sciences*. McGraw-Hill, New-York, 1969.

[61] B. Waidyawansa. Error on target bpm position and angle calculations. https://qweak.jlab.org/elog/Analysis+&+Simulation/788, 2012.

[62] D. Mack. The apparent nonlinearity in Run I is dominated by BCM noise: A simulation. https://qweak.jlab.org/elog/Analysis+&+Simulation/1216, 2014.

[63] J. Magee. Moller polarimeter analysis: Qweak Run 2. Qweak Document Database (Document 1955-v3), 2014.

[64] K. Myers. Aluminum asymmetry analysis. Qweak Document Database (Document 2142-v2), 2015.

[65] Saint-Gobain Crystals. Premium plastic scintillators (data sheet). url=http://www.crystals.saint-gobain.com/. Accessed May 2015.

[66] M. McHugh. Run 2 neutral background analysis. Qweak Document Database (Document 2144-v1), 2015.

[67] A. Freyberger Y. Roblin. Studies of beam halo formation in the 12 GeV CEBAF design. JLAB-TN-06-048, 2006.

[68] D. Mack. Wien0 beamline background dilution central value and uncertainty. https://qweak.jlab.org/elog/Analysis+&+Simulation/784, 2012.

[69] E. Kargiantoulakis. Progress towards the beamline backgrounds correction, connections to beam asymmetries. https://qweak.jlab.org/elog/Analysis+&+Simulation/2115, 2015.

[70] A. Subedi. GEANT3 based run 2 RRC simulation results. https://qweak.jlab.org/elog/Analysis+&+Simulation/71449, 2015.

[71] V. Gray and W. Deconinck. Light-yield weighting effects on asymmetry. https://qweak.jlab.org/elog/Analysis+&+Simulation/765, 2012.

[72] M. Pitt. Effective kinematics and acceptance correction for official Wien 0 hydrogen result. https://qweak.jlab.org/elog/Analysis+&+Simulation/794, 2012.

[73] K. Paschke. Propagating Q2 error: Wien 0. https://qweak.jlab.org/elog/Analysis+&+Simulation/906, 2013.

[74] D. Armstrong. Tracking/kinematics update March 2015. Qweak Document Database (Document 2157-v1), 2015.

[75] Jens Erler and Michael J. Ramsey-Musolf. Weak mixing angle at low energies. *Phys. Rev. D*, 72:073003, Oct 2005.

[76] S. Galster, H. Klein, J. Moritz, K. H. Schmidt, D. Wegener, and J. Bleckwenn. Elastic electron-deuteron scattering and the electric neutron form factor at four-momentum transfers 5 $\mathrm{fm}^2 < \mathrm{q2} < 14\ \mathrm{fm}^2$. *Nuclear Physics B*, 32(1):221 – 237, 1971.

[77] Takumi Doi, Mridupawan Deka, Shao-Jing Dong, et al. Nucleon strangeness form factors from $N_f = 2 + 1$ clover fermion lattice QCD. *Phys. Rev. D*, 80:094503, Nov 2009.

[78] Shi-Lin Zhu, S. Puglia, B. Holstein, and M. Ramsey-Musolf. Nucleon anapole moment and parity-violating ep scattering. *Phys. Rev. D*, 62:033008, Jul 2000.

[79] R. González-Jiménez, J. A. Caballero, and W. T. Donnelly. Using electron scattering to constrain the axial-vector form factor. *arXiv*, 1501.03937, 2015.

[80] Mikhail Gorchtein, C.J. Horowitz, and Michael J. Ramsey-Musolf. Model-dependence of the γZ dispersion correction to the parity-violating asymmetry in elastic ep scattering. *Phys.Rev.*, C84:015502, 2011.

[81] R. Young. Private communication., 2014.

[82] V. A. Dzuba, J. C. Berengut, V. V. Flambaum, and B. Roberts. Revisiting parity nonconservation in cesium. *Phys. Rev. Lett.*, 109:203003, Nov 2012.

[83] C. S. Wood, S. C. Bennett, D. Cho, B. P. Masterson, J. L. Roberts, C. E. Tanner, and C. E. Wieman. Measurement of parity nonconservation and an anapole moment in cesium. *Science*, 275(5307):1759–1763, 1997.

[84] G. 't Hooft. Dimensional regularization and the renormalization group. *Nuclear Physics B*, 61(0):455 – 468, 1973.

Appendix A

Derivations and Expressions

A.1 Final Asymmetry Errors and Corrections

This section defines the partial errors for the parity violating asymmetry from the various different corrections applied.

$$
\begin{aligned}
dA^{\mathrm{ep}}_{\mathrm{PV}}|_{A'_{\mathrm{msr}}} &= \frac{R_{\mathrm{tot}}}{(1-f_{\mathrm{tot}})} \times dA'_{\mathrm{msr}} \\
dA^{\mathrm{ep}}_{\mathrm{PV}}|_{R_{\mathrm{tot}}} &= \frac{1}{(1-f_{\mathrm{tot}})}\left[A'_{\mathrm{msr}} - \sum_i f_i A_i\right] \times dR_{\mathrm{tot}} \\
dA^{\mathrm{ep}}_{\mathrm{PV}}|_{A_i} &= \frac{R_{\mathrm{tot}}}{(1-f_{\mathrm{tot}})} \times f_i \times dA_i \\
dA^{\mathrm{ep}}_{\mathrm{PV}}|_{f_i} &= \frac{R_{\mathrm{tot}}}{(1-f_{\mathrm{tot}})^2}\left[A'_{\mathrm{msr}} - \left(\sum_i f_i A_i\right) - A_i(1-f_i)\right] \times df_i \\
dA^{\mathrm{ep}}_{\mathrm{PV}}|_{f_{\mathrm{BB}}} &= \frac{R_{\mathrm{tot}}}{(1-f_{\mathrm{tot}})^2}\left[A'_{\mathrm{msr}} - \sum_i f_i A_i\right] \times df_{\mathrm{BB}}
\end{aligned}
$$

In the case of the experimental bias correction, an *effective additive* correction can be determined that represents the size of a correction that is equivalent to the effect that

the multiplicative correction had. For this dissertation, this quantity is defined as:

$$\Delta A_R = A_{\mathrm{PV}}^{\mathrm{ep}} - \left[< A'_{\mathrm{msr}} > - \sum_i f_i A_i \right],$$

where we recall the definition of A'_{msr} as

$$A'_{\mathrm{msr}} = \frac{A_{\mathrm{msr,slug}} - \Delta A_{\mathrm{BB}}}{P}.$$

A.2 Linear Regression

This section will collect the methods for determining regression coefficients described in [60] and cast them into terms appropriate for $\mathrm{Q_{weak}}$ analysis. Note that the notation used in these derivations is specific to this section.

Begin with an equation describing the measured asymmetry ξ in terms of a main physics asymmetry A and false asymmetries introduced by helicity-correlated beam differences:

$$\xi = A + \sum_j^n S_j \Delta X_j \tag{A.1}$$

where there are n independent variables. S_j is the detector's sensitivity to variable j and ΔX_j is the helicity-correlated difference measured for variable j. Performing N independent measurements of ξ allows us to write a solution for A as:

$$A = \frac{1}{N} \left[\sum_i^N \xi_i - \sum_j^n S_j \Delta X_j \right]. \tag{A.2}$$

The χ^2 function to be minimized can then be written as:

$$\chi^2 = \frac{1}{\sigma_\xi^2} \sum_i^N \left[(\xi_i - \bar{\xi}) - \sum_j^n S_j (\Delta X_{ji} - \overline{\Delta X_j}) \right]^2 \tag{A.3}$$

where $\bar{\xi}$ and $\overline{\Delta X_j}$ are the average measured asymmetry and beam property differences respectively. Minimizing this function will result in n simultaneous equations for slopes S_k:

$$\sum_i^N (\xi_i - \bar{\xi})(\Delta X_{ki} - \overline{\Delta X_k}) = \sum_j^n \left[S_j \sum_i^N (\Delta X_{ji} - \overline{\Delta X_j})(\Delta X_{ki} - \overline{\Delta X_k}) \right], \quad k = 1..n \tag{A.4}$$

We can now proceed by adopting Bevington's[60] notation for defining the linear correlation coefficients between the j-th independent variable and the measured asymmetry ξ as:

$$r_{j\xi} \equiv \frac{s_{j\xi}^2}{s_j s_\xi} \qquad \text{where:} \tag{A.5}$$

$$s_{j\xi}^2 \equiv \frac{1}{N-1} \sum_i^N \left[(\Delta X_{ij} - \overline{\Delta X_j})(\xi_i - \bar{\xi}) \right] \tag{A.6}$$

$$s_\xi^2 \equiv \frac{1}{N-1} \sum_i^N (\xi_i - \bar{\xi})^2 \tag{A.7}$$

$$s_j^2 \equiv \frac{1}{N-1} \sum_i^N (\Delta X_{ij} - \overline{\Delta_j})^2 \tag{A.8}$$

We similarly define the linear correlation coefficients between two independent variables by replacing instances of ξ with a second independent variable.

Equation A.4 can then be written as n simultaneous equations of the form:

$$r_{1\xi} = b_1 r_{11} + b_2 r_{21} + \ldots + b_n r_{n1} \tag{A.9}$$

$$r_{1\xi} = b_1 r_{11} + b_2 r_{21} + \ldots + b_n r_{n1} \tag{A.10}$$

$$\vdots \tag{A.11}$$

$$r_{1\xi} = b_1 r_{11} + b_2 r_{21} + \ldots + b_n r_{n1} \tag{A.12}$$

where the coefficients b_j are related to the desired slopes S_j by:

$$b_j = S_j \frac{s_j}{s_\xi}. \tag{A.13}$$

Inversion of the matrix **r** results in a matrix with elements r_{jk}^{-1} which then allows for the correlation slopes to be extracted as:

$$S_j = \frac{s_\xi}{s_j} \sum_k^n \left(r_{k\xi} r_{jk}^{-1} \right). \tag{A.14}$$

This formalism is what is programmed into the stand alone regression engine.

A.3 Electroweak Form Factors

This section provides the derivation of the following equation relating the electroweak form factor of the proton to the electric form factors and weak charges of the nucleon:

$$G_E^{Zp} = Q_W^p G_E^{\gamma p} - Q_W^n G_E^{\gamma n} - \left[G_E^{sp} - \frac{1}{3}\Delta \right] \tag{A.15}$$

Begin by writing out the electroweak form factor of the proton and the electric form factors of the proton and neutron in terms of their constituent quarks, scaled by the appropriate couplings:

$$G_E^{\gamma p} = \frac{2}{3}G_E^{up} - \frac{1}{3}G_E^{dp} - \frac{1}{3}G_E^{sp} \tag{A.16a}$$

$$G_E^{\gamma n} = \frac{2}{3}G_E^{un} - \frac{1}{3}G_E^{dn} - \frac{1}{3}G_E^{sn} \tag{A.16b}$$

$$G_E^{Zp} = g_V^u G_E^{up} + g_V^d G_E^{dp} + g_V^s G_E^{sp}, \tag{A.16c}$$

where $g_v^u = (1 - \frac{8}{3}\sin^2\theta_W)$ and $g_v^{d,s} = (-1 + \frac{4}{3}\sin^2\theta_W)$ are the weak vector couplings of the quarks presented in Table 1.2.

We parameterize effects from charge symmetry breaking ($G_E^{up} \neq G_E^{dn}$) by writing:

$$G_E^{dn} = G_E^{up} - G_E^{\delta u} \tag{A.17a}$$

$$G_E^{un} = G_E^{dp} - G_E^{\delta d} \tag{A.17b}$$

$$G_E^{sn} = G_E^{sp} - G_E^{\delta s}. \tag{A.17c}$$

Substituting Equation A.17 into Equation A.16b gives:

$$G_E^{\gamma n} = \frac{2}{3}G_E^{dp} - \frac{1}{3}G_E^{up} - \frac{1}{3}G_E^{sp} - \frac{2}{3}G_E^{\delta d} + \frac{1}{3}G_E^{\delta u} + \frac{1}{3}G_E^{\delta s}. \tag{A.18}$$

We then compute the following linear combinations of the electric form factors of the proton and neutron:

$$2G_E^{\gamma p} + G_E^{\gamma n} = G_E^{up} - G_E^{sp} + \frac{1}{3}\left(G_E^{\delta u} + G_E^{\delta s} - 2G_E^{\delta d}\right) \tag{A.19a}$$

$$G_E^{\gamma p} + 2G_E^{\gamma n} = G_E^{dp} - G_E^{sp} + \frac{2}{3}\left(G_E^{\delta u} + G_E^{\delta s} - 2G_E^{\delta d}\right). \tag{A.19b}$$

Equations A.19 can be rearranged to give the electric form factors of the up and down quarks in the proton:

$$G_E^{up} = 2G_E^{\gamma p} + G_E^{\gamma n} + G_E^{sp} - \frac{1}{3}\left(G_E^{\delta u} + G_E^{\delta s} - 2G_E^{\delta d}\right) \tag{A.20a}$$

$$G_E^{dp} = G_E^{\gamma p} + 2G_E^{\gamma n} + G_E^{sp} - \frac{2}{3}\left(G_E^{\delta u} + G_E^{\delta s} - 2G_E^{\delta d}\right). \tag{A.20b}$$

We can then substitute Equation A.20 into Equation A.16c to obtain:

$$G_E^{Zp} = \left(2g_v^u + g_v^d\right)G_E^{\gamma p} + \left(g_v^u + 2g_v^d\right)G_E^{\gamma n} + \left(g_v^u + g_v^d + g_v^s\right)G_E^{sp} - \frac{1}{3}\left(g_v^u - 2g_v^d\right)\Delta \tag{A.21}$$

where $\Delta = G_E^{\delta u} + G_E^{\delta s} - 2G_E^{\delta d}$ contains the charge symmetry breaking terms. Substituting in the weak vector couplings of the quarks then gives:

$$G_E^{Zp} = \left(1 - 4\sin^2\theta_W\right)G_E^{\gamma p} + (-1)\,G_E^{\gamma n} + (-1)\left[G_E^{sp} - \frac{1}{3}\Delta\right] \tag{A.22a}$$

$$G_E^{Zp} = Q_W^p G_E^{\gamma p} - Q_W^n G_E^{\gamma n} - \left[G_E^{sp} - \frac{1}{3}\Delta\right]. \tag{A.22b}$$

This entire derivation can be performed identically for the magnetic form factors. The ξ factor presented in the text combines effects from strangeness in the nucleon and charge symmetry breaking.

A.4 Asymmetry Symbol Definitions

The following pages provide descriptions for the many symbols used throughout the asymmetry analysis of Chapter 4. Asymmetries are assumed to correspond to the full main detector array unless otherwise indicated.

$A'_{\mathbf{msr}}$ A symbol used to collect corrections done at the slug level. Corrects the regressed asymmetry for beamline backgrounds and polariazation.

$A^{\mathbf{MD}}$ An asymmetry measured using the main detector array.

$A^{\mathbf{US}}$ An asymmetry measured using the upstream luminosity monitors.

$A^{\mathbf{ep}}_{\mathbf{PV}}$ The main asymmetry result: the parity-violating asymmetry from elastic electron-proton scattering.

$A^{\mathbf{raw}}_{k}$ The raw asymmetry measured using detector k.

$A^{\mathbf{trans}}$ The asymmetry associated with residual transverse polarization in the electron beam.

$A_{\mathbf{NULL}}$ A combination of A_{in} and A_{out} that should ideally equal zero.

$A_{\mathbf{PHYS}}$ A combination of A_{in} and A_{out} that gives the main measured asymmetry.

$A_{\mathbf{al}}$ The asymmetry associated with events scattered from aluminum target windows.

$A_{\mathbf{avg}}$ An asymmetry assigned to a combination of PMT's. Calculated by first determining the asymmetries measured using the individual PMT's and then combining those together with equal weights.

$A_{\mathbf{false}}$ A false asymmetry caused when the beam's position, angle, or energy vary with helicity.

$A_{\mathbf{inel}}$ The asymmetry associated with inelastic scattering events.

$A_{\mathbf{in}}$ An asymmetry measured during conditions where a sign flip is expected from half-wave plate insertion, double wien flips, or g-2 precession.

$A_{\mathbf{msr}}$ A regressed main detector asymmetry.

$A_{\mathbf{neut}}$ The asymmetry associated with neutral current events that generate light in the main detectors.

$A_{\mathbf{out}}$ An asymmetry measured during conditions where no additional sign flip is expected from half-wave plate insertion, double wien flips, or g-2 precession.

$A_{\mathbf{sum}}$ An asymmetry assigned to a combination of PMT's. Calculated by first combining the yields from individual PMT's and then calculating an asymmetry using those combined yields.

B_n The beam normal single spin asymmetry. Used in transverse asymmetry analysis.

$C_{\mathbf{US}}^{\mathbf{MD}}$ The correlation (slope) between the asymmetries measured using the main detectors and the upstream luminosity monitors. Used in correcting for beamline backgrounds.

P The linear polarization of the electron beam.

P_T The transverse polarization of the electron beam.

Q^2 The momentum transfer (squared) of the electron proton scattering event.

$R_{\mathbf{RC}}$ A multiplicative factor that performs radiative corrections on the measured asymmetry.

$R_{\mathbf{acc}}$ A correction that accounts for the range of Q^2 accepted by the apparatus.

$R_{\mathbf{det}}$ A correction that accounts for the convolution of Q^2 and light collection varying over the face of the quartz bars.

$R_{\mathbf{tot}}$ The product of the four above R terms.

R_{Q^2} A correction that propagates uncertainty in Q^2 into the measured asymmetry $A_{\mathrm{PV}}^{\mathrm{ep}}$.

S_i A PMT's sensitivity to helicity-correlated changes in variable i.

$Y^{+1}(Y^{-2})$ The PMT yield measured during the first (second) period of positive (negative) beam helicity.

$Y_{\mathbf{frac}}$ The yield measured using main detector bars where the primary collimator in that octant has been blocked. Used in the determined of f_{BB}.

$\Delta A_{\mathbf{BB}}$ A false asymmetry caused by beamline backgrounds.

ΔX_i Helicity correlated beam differences in variable i (position, angle, energy).

ϕ_e The azimuthal angle of a given main detector bar.

ϕ_s The polarization vector angle of a scattered electron.

$dA_{\mathbf{msr,blind}}$ An error assigned to the measured asymmetry that accounts for the unknown additive blinding factor.

$dA_{\mathbf{msr,scheme}}$ An error assigned to the measured asymmetry to account for differences resulting from our choice in which variables to use during linear regression.

$f_{\mathbf{BB}}$ The fraction of a detector's signal resulting from beamline backgrounds.

$f_{\mathbf{al}}$ The fraction of a detector's signal resulting from scattering from the aluminum windows.

$f_{\mathbf{inel}}$ The fraction of a detector's signal resulting from inelastic scattering.

$f_{\mathbf{neut}}$ The fraction of a detector's signal resulting from electrically neutral particles.

$f_{\mathbf{tot}}$ The sum of the above fractions, or *dilution factors*.

w_i The weight used in order to combine yields from various PMT's into a single combined yield. Used in the calculation of A_{sum}.

Appendix B

Fitting Details

This appendix will serve as a record of the input conditions and results of the fitting routine used to extract $Q_W^p$from $A_{\mathrm{PV}}^{\mathrm{ep}}$. The inputs are:

- **Included data**: what data points were used in the fit. Table B.1 provides a reference for which experimental result corresponds to each index.
- **Strangeness order**: higher order expansions of strangeness are available in the code but were not used in this analysis.
- **Zhu Isoscalar, Isovector**: whether or not the theoretical constraints on the isoscalar and/or isovector axial form factors were used in performing the fit.
- **APV Setting**: whether or not APV data were used to constrain the neutral weak quark couplings C_{1u} and C_{1d}.
- **EMFF Fits**: which electromagnetic form factor parameterization was used (Kelly, Arrington & Sick, Friedrich & Walcher, or a simple dipole form).
- **Q-weak hypothetical measurement**: the new asymmetry and error introduced into the fit.

Outputs include the total and reduced chi-squared of the fit, the 6 fit results, and the weak charges of the proton and neutron computed using the C_1's from the fit. The full correlation matrix is provided following the fit outputs, where entry (i,j) corresponds to the correlation between variable i and j, ordered as they appear in the fit output.

Run-II Result with Blinding Error and No APV Constraints

Included data:{1, 2, 3, 4, 5, 6, 7, 8, 9, 10, 11, 12, 13, 14, 15, 16, 17, 18, 19, 20, 21, 22, 23, 24, 27, 28, 29, 30, 31, 32, 33, 34, 35}

Strangeness order = 1

Zhu Isoscalar = True

Zhu Isovector = False

APV Setting = None

EMFF Fits = AS

Q–weak hypothetical measurement = -0.22302 ± 0.04137

Total chi^2 = 37.42

chi^2/dof = 1.24733

GApEFF = -0.629625 ± 0.370084

GAnEFF = 0.723068 ± 0.471384

\[Rho]Es = 0.190108 ± 0.112647 [GeV^−2]

\[Mu]s = -0.177451 ± 0.147484 [\[Mu]N]

C1u = -0.185048 ± 0.0069014

C1d = 0.334228 ± 0.0119354

Q–weak–p = 0.0717357 ± 0.00935258

Q–weak–n = -0.966815 ± 0.0350053

$$\begin{pmatrix} 1. & -0.283521 & 0.57108 & -0.56026 & -0.273622 & 0.212796 \\ -0.283521 & 1. & -0.0713239 & -0.031093 & 0.385506 & -0.376701 \\ 0.57108 & -0.0713239 & 1. & -0.871326 & 0.0111074 & -0.152767 \\ -0.56026 & -0.031093 & -0.871326 & 1. & -0.368424 & 0.433494 \\ -0.273622 & 0.385506 & 0.0111074 & -0.368424 & 1. & -0.944214 \\ 0.21279 & 6-0.376701 & -0.152767 & 0.433494 & -0.944214 & 1. \end{pmatrix}$$

Run-II Result without Blinding Error and No APV Constraints

```
Included data:{1, 2, 3, 4, 5, 6, 7, 8, 9, 10, 11, 12, 13,
    14, 15, 16, 17, 18, 19, 20, 21, 22, 23, 24, 27, 28,
   29, 30, 31, 32, 33, 34, 35}
Strangeness order = 1
Zhu Isoscalar = True
Zhu Isovector = False
APV Setting = None
EMFF Fits = AS
Q-weak hypothetical measurement = -0.22302 ± 0.0127

Total chi^2 = 36.4598
chi^2/dof = 1.25724
GApEFF = -0.620518 ± 0.364581
GAnEFF = 0.713828 ± 0.466947
\[Rho]Es = 0.193879 ± 0.109526 [GeV^-2]
\[Mu]s = -0.177022 ± 0.147454 [\[Mu]N]
C1u = -0.185481 ± 0.00620159
C1d = 0.334561 ± 0.0117062

Q-weak-p = 0.0728037 ± 0.00564472
Q-weak-n = -0.967282 ± 0.0348536
```

$$\begin{pmatrix} 1. & -0.265887 & 0.553739 & -0.572761 & -0.2222 & 0.18467 \\ -0.265887 & 1. & -0.0398371 & -0.0285117 & 0.364974 & -0.359717 \\ 0.553739 & -0.0398371 & 1. & -0.902195 & 0.134426 & -0.209828 \\ -0.572761 & -0.0285117 & -0.9021951. & -0.401376 & 0.438186 & \\ -0.2222 & 0.364974 & 0.134426 & -0.401376 & 1. & -0.975458 \\ 0.18467 & -0.359717 & -0.209828 & 0.438186 & -0.975458 & 1. \end{pmatrix}$$

Run-II Result with Blinding Error and APV Constraints

Included data:{1, 2, 3, 4, 5, 6, 7, 8, 9, 10, 11, 12, 13, 14, 15, 16, 17, 18, 19, 20, 21, 22, 23, 24, 27, 28, 29, 30, 31, 32, 33, 34, 35}

Strangeness order = 1

Zhu Isoscalar = True

Zhu Isovector = False

APV Setting = APVetc

EMFF Fits = AS

Q–weak hypothetical measurement = -0.22302 ± 0.04137

Total chi^2 = 37.5831

chi^2/dof = 1.17447

GApEFF = -0.610022 ± 0.366886

GAnEFF =0.661159 ± 0.445759

\[Rho]Es = 0.177893 ± 0.10851 [GeV^−2]

\[Mu]s = -0.150947 ± 0.132077 [\[Mu]N]

C1u = -0.187231 ± 0.00428899

C1d = 0.338748 ± 0.00414376

Q–weak–p = 0.0714293 ± 0.00932176

Q–weak–n = -0.980529 ± 0.00849698

$$\begin{pmatrix} 1. & -0.283521 & 0.57108 & -0.56026 & -0.273622 & 0.212796 \\ -0.283521 & 1. & -0.0713239 & -0.031093 & 0.385506 & -0.376701 \\ 0.57108 & -0.0713239 & 1. & -0.871326 & 0.0111074 & -0.152767 \\ -0.56026 & -0.031093 & -0.871326 & 1. & -0.368424 & 0.433494 \\ -0.273622 & 0.385506 & 0.0111074 & -0.368424 & 1. & -0.944214 \\ 0.212796 & -0.376701 & -0.152767 & 0.433494 & -0.944214 & 1. \end{pmatrix}$$

Run-II Result with No Blinding Error and APV Constraints

```
Included data:{1, 2, 3, 4, 5, 6, 7, 8, 9, 10, 11, 12, 13,
    14, 15, 16, 17, 18, 19, 20, 21, 22, 23, 24, 27, 28,
   29, 30, 31, 32, 33, 34, 35}
Strangeness order = 1
Zhu Isoscalar = True
Zhu Isovector = False
APV Setting = APVetc
EMFF Fits = AS
Q-weak hypothetical measurement = -0.22302 ± 0.0127

Total chi^2 = 37.7021
chi^2/dof = 1.17819
GApEFF = -0.586738 ± 0.360627
GAnEFF = 0.635463 ± 0.439494
\[Rho]Es = 0.186533 ± 0.10558 [GeV^-2]
\[Mu]s = -0.148591 ± 0.1319 [\[Mu]N]
C1u = -0.188402 ± 0.00262455
C1d = 0.339788 ± 0.00284452

Q-weak-p = 0.0740317 ± 0.00547781
Q-weak-n = -0.982347 ± 0.00666652
```

$$\begin{pmatrix} 1. & -0.233409 & 0.61946 & -0.71954 & -0.219227 & 0.188421 \\ -0.233409 & 1. & -0.14136 & 0.14504 & 0.14966 & -0.143249 \\ 0.61946 & -0.14136 & 1. & -0.909205 & -0.252473 & 0.192178 \\ -0.71954 & 0.14504 & -0.909205 & 1. & 0.00869337 & 0.0210683 \\ -0.219227 & 0.149663 & -0.252473 & 0.00869337 & 1. & -0.942417 \\ 0.188421 & -0.143249 & 0.192178 & 0.0210683 & -0.942417 & 1. \end{pmatrix}$$

Index	Experiment	Target	Q^2	θ	A	dA(stat)	dA(syst)	dA(corr)
1	SAMPLE	Proton	0.1	144	-5.5967	0.67	0.88	0
2	SAMPLE	Deuteron	0.091	144	-7.77	0.73	0.72	0
3	SAMPLE	Deuteron	0.038	144	-3.51	0.57	0.58	0
4	PVA4	Proton	0.23	35.3101	-5.3652	0.54	0.2602	0
5	PVA4	Proton	0.108	35.3728	-1.3262	0.29	0.13	0
6	HAPPEX	Proton	0.477	12.3	-14.9089	0.98	0.5611	0
7	HAPPEX	Helium4	0.091	5.7	-6.72	0.84	0.21	0
8	HAPPEX	Proton	0.099	6	-1.0774	0.24	0.0602	0
9	G0	Proton	0.122	6.67838	-1.4352	0.44	0.2201	0.18
10	G0	Proton	0.128	6.84451	-0.8922	0.41	0.2001	0.17
11	G0	Proton	0.136	7.06051	-1.2184	0.42	0.1702	0.17
12	G0	Proton	0.144	7.27073	-2.6246	0.43	0.1802	0.18
13	G0	Proton	0.153	7.50091	-2.1305	0.43	0.2802	0.21
14	G0	Proton	0.164	7.77401	-2.7857	0.43	0.3202	0.23
15	G0	Proton	0.177	8.08628	-3.8503	0.43	0.2503	0.2
16	G0	Proton	0.192	8.43405	-3.7445	0.48	0.2204	0.19
17	G0	Proton	0.21	8.8358	-4.5681	0.47	0.2604	0.21
18	G0	Proton	0.232	9.30682	-5.1511	0.51	0.3004	0.23
19	G0	Proton	0.262	9.91905	-5.1329	0.52	0.1116	0.17
20	G0	Proton	0.299	10.6346	-7.5848	0.6	0.5305	0.35
21	G0	Proton	0.344	11.4574	-8.2578	0.68	0.8504	0.52
22	G0	Proton	0.41	12.5907	-10.1022	0.67	0.8906	0.55
23	G0	Proton	0.511	14.2004	-16.6618	0.89	1.4805	1.5
24	G0	Proton	0.631	15.9769	-19.82	1.11	1.2808	1.31
25	G0	Proton	0.788	18.1552	-30.717	1.86	2.5605	2.59
26	G0	Proton	0.997	20.8999	-37.9441	7.24	9.0001	0.52
27	HAPPEX	Proton	0.109	6	-1.513	0.12	0.0404	0
28	HAPPEX	Helium4	0.077	6	-6.4	0.23	0.12	0
29	PVA4	Proton	0.22	144.5	-17.1933	0.82	0.89	0
30	G0	Proton	0.221	110	-11.2094	0.86	0.27	0.43
31	G0	Deuteron	0.221	110	-16.93	0.81	0.41	0.21
32	G0	Proton	0.628	110	-45.8217	2.4	0.8004	1
33	G0	Deuteron	0.628	110	-55.5	3.3	2	0.7
34	HAPPEX	Proton	0.624	13.7	-23.6734	0.78	0.3624	0
35	QWEAK	Proton	0.025	7.9	-0.2662	0.0456	0	0

Table B.1: Asymmetry data used in the fit that extracts $Q_W^p$from $A_{\mathrm{PV}}^{\mathrm{ep}}$. The column labeled as dA(corr) corresponds to a correlated systematic error that was used in the G0 experiment[25] that accounts for errors common within their results. Asymmetries are given in parts-per-million, momentum transfer in (GeV/c)^2, and θ in degrees.

Appendix C

Main Detector Calibrations

This appendix contains the results of data acquired to determine the calibration factors required to convert raw ADC readings into photoelectron counts in the main detectors. This study was performed by pulsing a dimly lit LED in front of a single main detector photomultiplier tube and triggering the event mode data acquisition on that PMT. The resulting spectra had their pedestals removed and were fit to a Poisson distribution in post analysis. The height and width of these fitted distributions were then used to extract the "ADC_channel per photoelectron" factors as well as the average number of photoelectrons generated per event during the study.

Entries in Table C.2 marked with an asterisk do not correspond to values extracted by this method. Errors during the study resulted in no calibration factors being extracted for two photomultiplier tubes. For these PMTs, changes between the other PMTs' 2011 and 2012 numbers were averaged and then applied to estimate how much the unmeasured PMTs changed.

The figures following the tables show the main detector PMT photoelectron spectra measured using commissioning data and the calibration factors in Table C.1.

Run	PMT	χ^2/ndf	ch/pe	pe/event
11913	md1p_adc	0.98	18.3953	57.3127
11915	md2p_adc	1.04	15.591	119.097
11916	md3p_adc	2.10	11.3726	8.00301
11917	md3p_adc	0.97	12.7543	190.602
11919	md4p_adc	1.15	15.9229	70.2137
11920	md4p_adc	1.00	16.257	68.2392
11930	md5p_adc	1.01	17.2898	150.876
11931	md5p_adc	0.99	17.0559	152.883
11924	md6p_adc	1.01	18.3154	91.5397
11926	md7p_adc	1.07	16.2473	128.003
11928	md8p_adc	1.11	8.74444	119.585
11932	md8m_adc	2.55	11.9063	5.2653
11933	md8m_adc	1.00	12.6983	125.599
11934	md8m_adc	1.02	12.6713	126.031
11936	md7m_adc	1.03	14.2582	129.131
11939	md6m_adc	1.01	12.5637	145.34
11940	md5m_adc	2.44	9.33307	7.26561
11941	md5m_adc	0.96	10.5552	179.069
11943	md4m_adc	0.96	20.3867	121.419
11944	md3m_adc	2.74	10.2273	9.56381
11945	md3m_adc	1.08	11.8188	171.763
11947	md2m_adc	0.99	11.0545	180.418
11949	md1m_adc	1.05	11.1168	169.321
11950	md1m_adc	1.04	10.9097	73.6283

Table C.1: Main detector pulsed LED calibrations for May 5th, 2011.

Run	PMT	χ^2/ndf	ch/pe	pe/event
17516	md1p_adc	1.25	14.5036	16.2073
17517	md2p_adc	1.51	10.3987	14.4741
17518	md3p_adc	1.37	10.7713	13.2447
17519	md4p_adc	1.34	8.40773	17.9573
17520	md5p_adc	1.37	12.2063	16.6702
17521	md6p_adc	1.46	13.8143	11.4456
17522	md7p_adc	1.69	12.8763	12.1889
**	md8p_adc		7.06338	
17533	md8m_adc	2.22	9.96058	8.1301
17532	md7m_adc	3.09	10.3165	8.49034
17531	md6m_adc	2.24	9.56359	8.92834
17530	md5m_adc	0.92	6.78144	9.29147
17529	md4m_adc	2.47	14.9249	4.78996
17527	md3m_adc	5.37	9.28805	8.27128
17526	md2m_adc	1.93	8.79834	8.63031
**	md1m_adc		8.81238	

Table C.2: Main detector pulsed LED calibrations for April 4th, 2012.

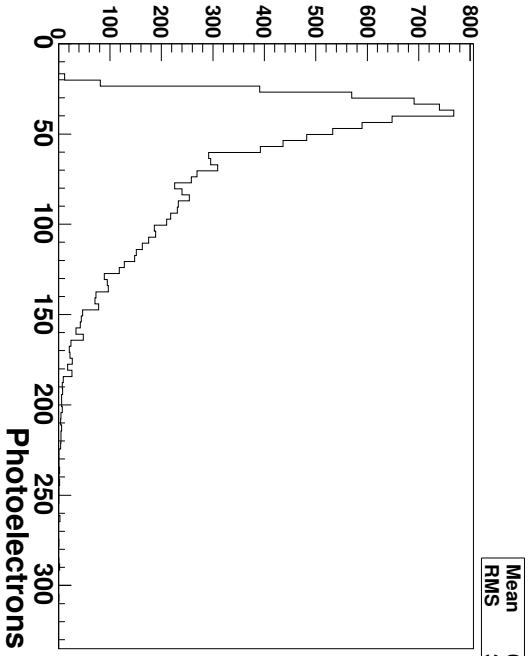

md1m

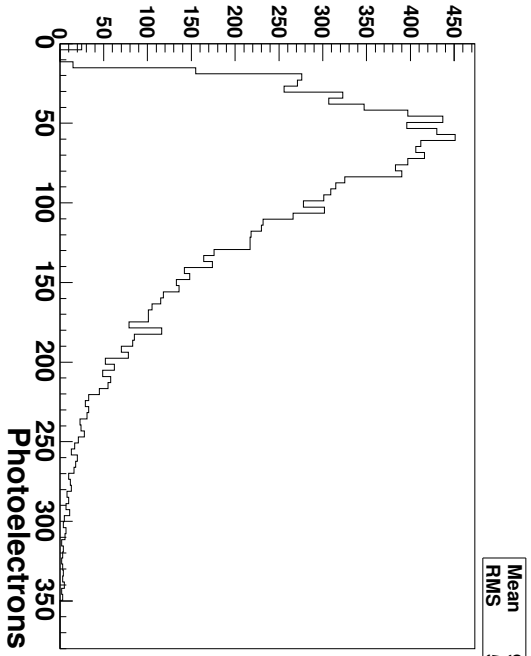

md2m

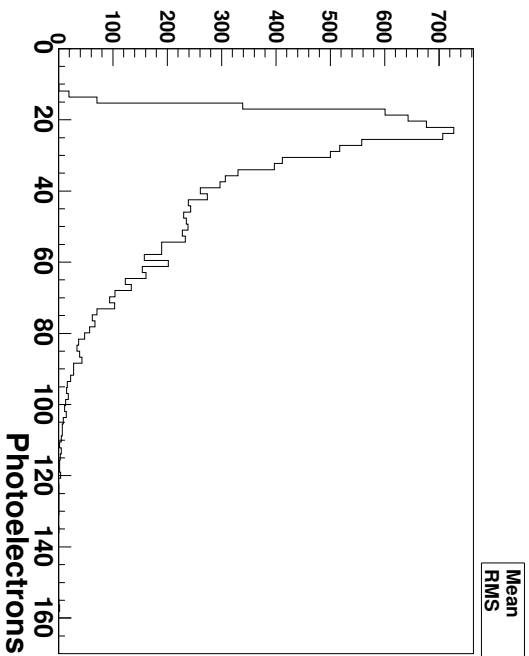

md1p

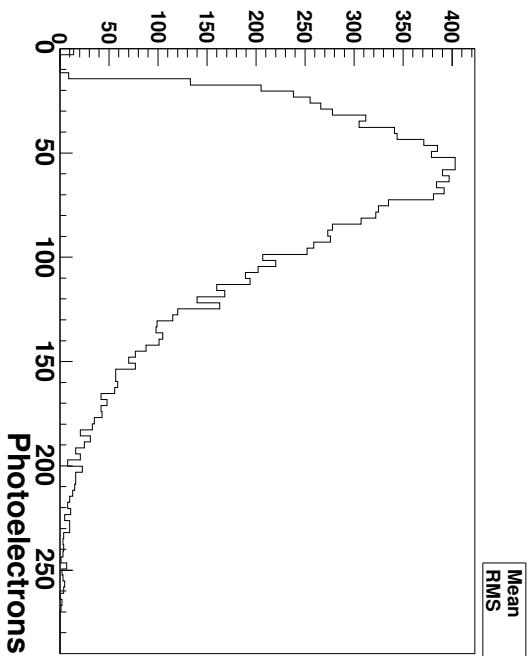

md2p

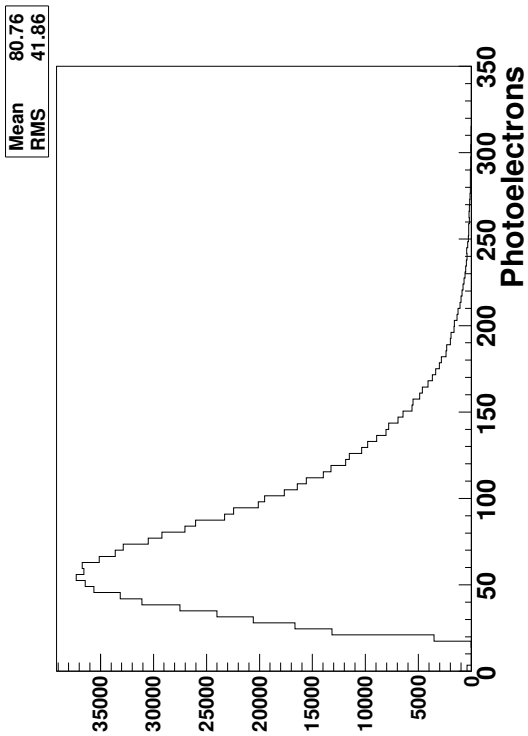

md3p

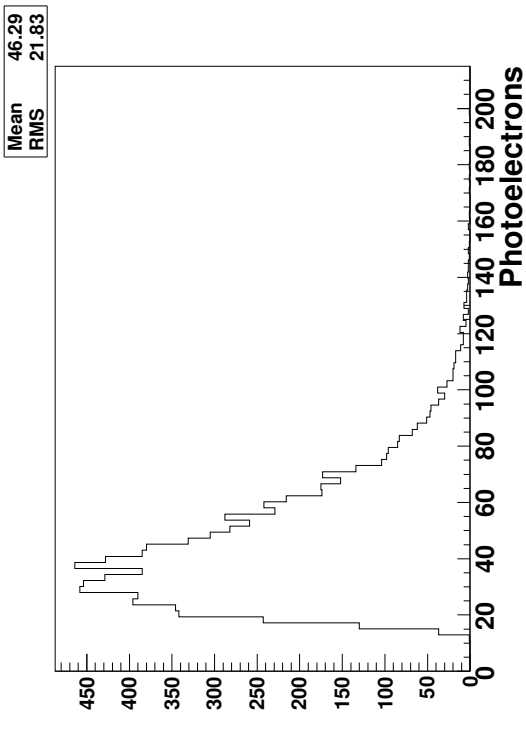

md4p

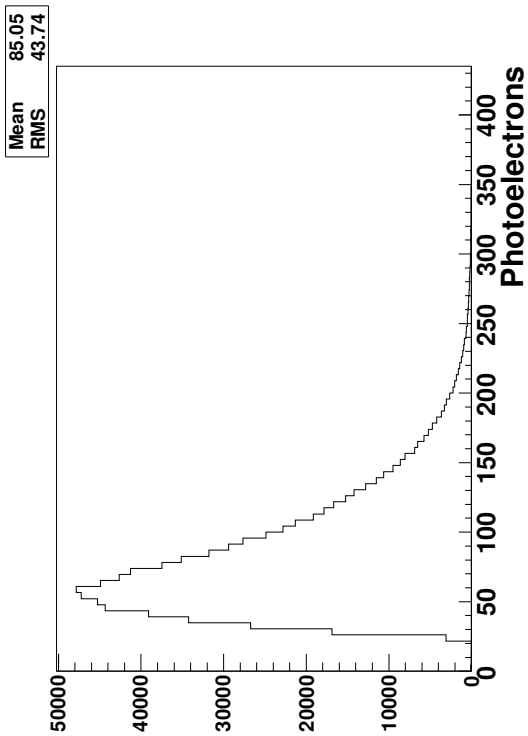

md3m

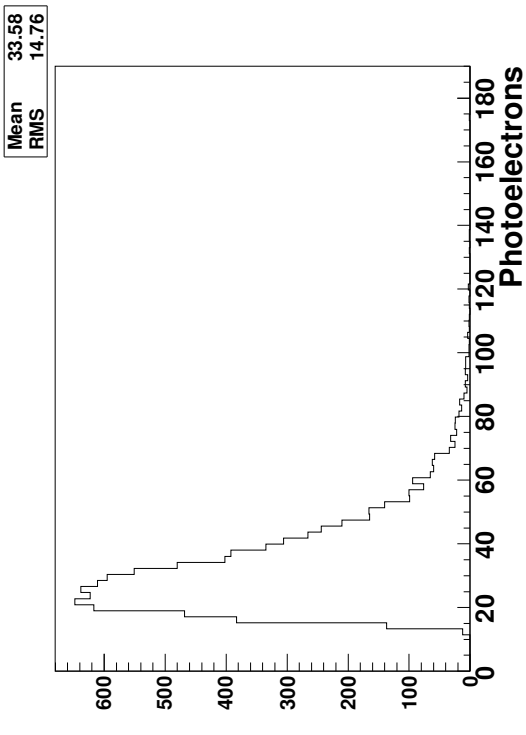

md4m

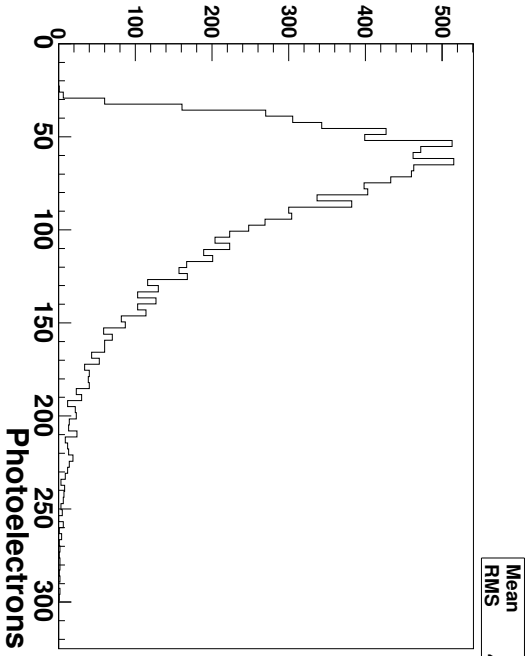

md5m

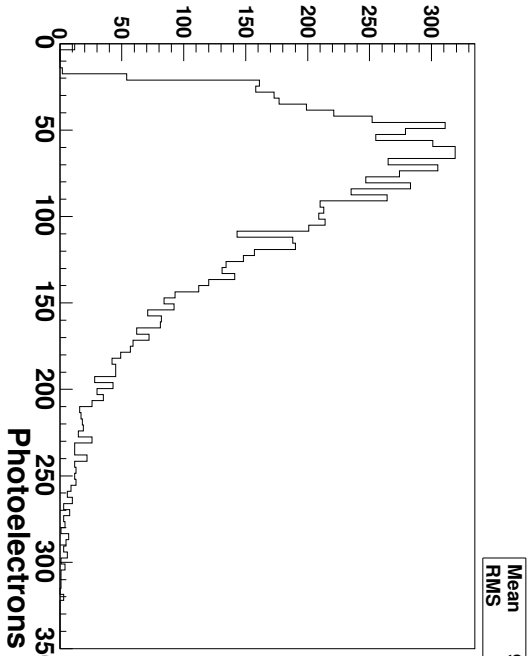

md6m

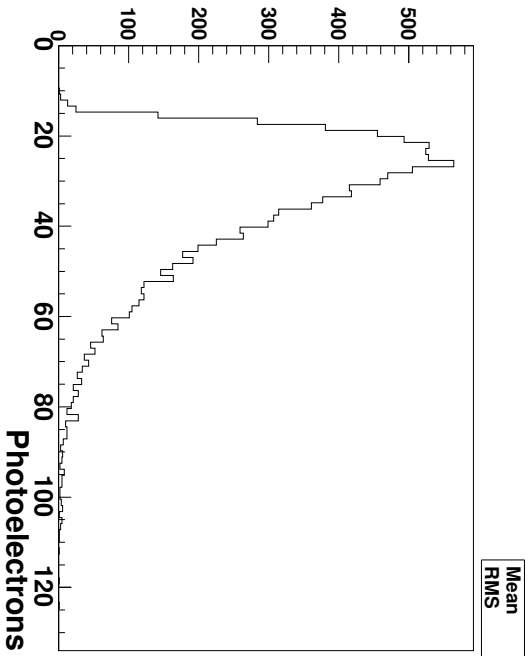

md5p

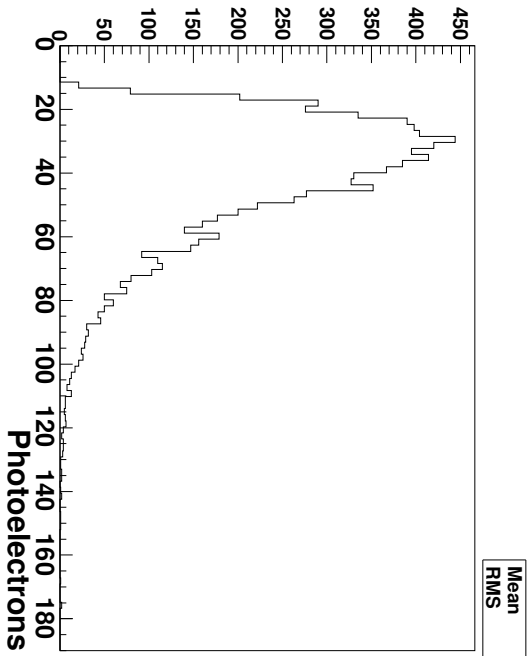

md6p

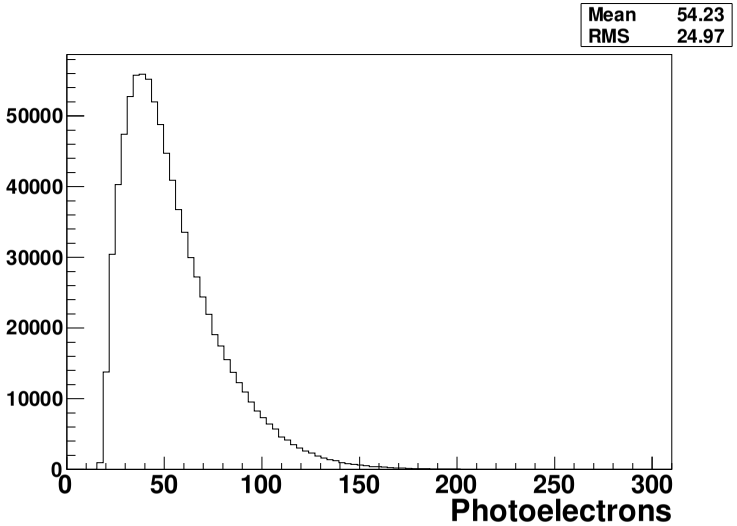

md7m

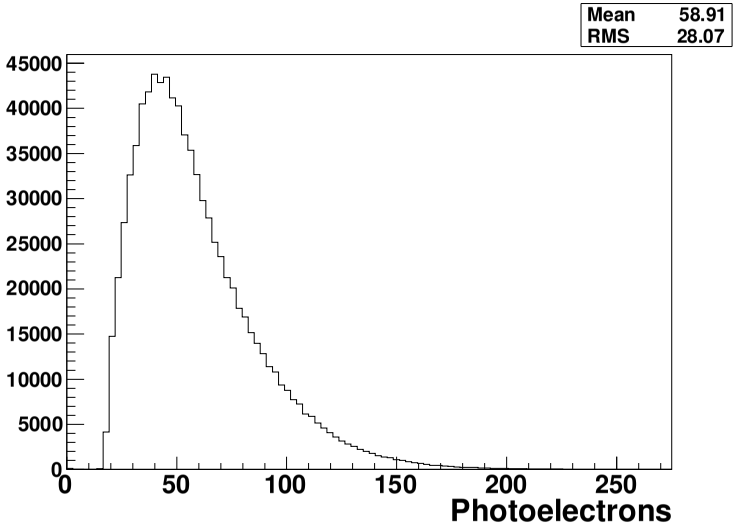

md7p

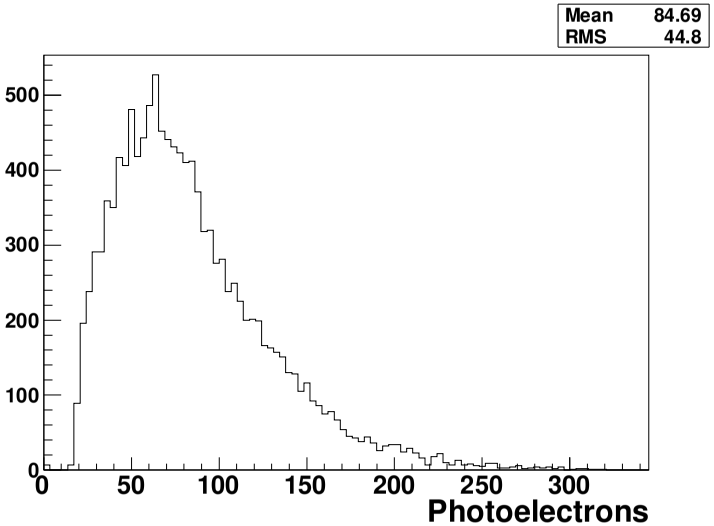

md8m

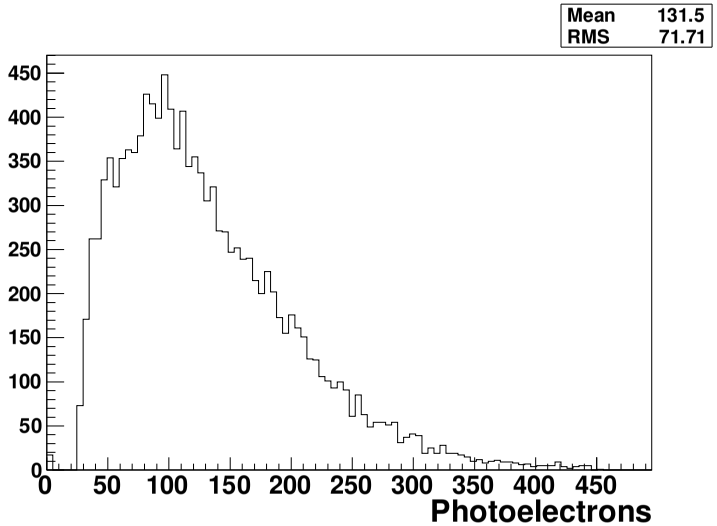

md8p

Appendix D

Photomultiplier Gain Data

Tables and figures here are reproduced from [56] that detail the gain curve measurements for the Q_{weak} low gain photomultiplier tube bases. A complete mapping of bases to PMT's was unable to be compiled due to clerical errors: Table D.1 contains which base locations could be confimed. Table D.2 contains the gain measured for each low gain base as a function of bias voltage, plotted in the figures that follow.

PMT	Tube Serial Number
1-	109
1+	108
2-	123
2+	119
3-	112
3+	113
4-	111
4+	117
5-	115
5+	-
6-	-
6+	-
7-	-
7+	106
8-	104
8+	103
9-	-
9+	100

Table D.1: Tube to base mapping for low gain bases for Run-II.

Base (#) / Bias (V)	1300	1250	1200	1150	1100	1050	1000	950	900	850	800
101	7061.8	4678.7	3052.2	1940.4	1206.1	717.77	409.48	221.21	111.92	52.54	21.6
102	7021.8	4526.6	2943.4	1882.6	1171.3	700.33	399.8	217.84	110.45	52.18	21.64
103	7023.6	4562.3	2936.1	1855	1153.2	689.63	387.18	209	106.3	49.44	20.2
104	7347.4	4734.7	3072.3	1958.6	1215	726.02	407.74	224.75	113.97	53.8	22
105	6598.7	4262.5	2754.2	1752.8	1083.7	645.87	364.23	198.32	100.7	46.66	18.74
106	7220.8	4646.6	2982.5	1895.3	1178.1	702.38	400.38	218.13	111.68	52.66	21.83
107	6198.9	3955.3	2557.5	1624.9	999.62	596.09	338.85	184.17	94.08	44.35	18.27
108	6696.2	4269.3	2770.7	1757.5	1081.1	645.5	370.07	199.73	101.7	48.26	20.12
109	6405.6	4041.8	2630.2	1672.6	1039.3	626.14	358.62	196.79	101.11	48.03	19.95
110	6129.4	3873.2	2491.4	1571.9	973.34	580.63	332.24	180.42	91.97	43.46	17.84
111	6044.8	3753.2	2453.1	1570.7	969.25	578.67	329.23	177.96	90.83	43.32	17.78
112	5971.7	3768.4	2415.7	1539.5	951.32	566.75	322.41	175.1	88.97	41.79	17.12
113	5674.7	3682.7	2387.2	1528.5	935.25	556.19	316.98	172.37	87.75	40.97	16.59
114	40975	31408	23685	17246	12135	8042.6	5074.1	2948.8	1603.4	806.27	387.35
115	6506.5	4098.9	2666.2	1691.3	1054.6	631.1	359.23	196.29	100.15	46.9	19.49
116	40565	30627	22962	16696	11618	7714.5	4824	2831.3	1518.9	756.2	358.34
117	5977	3705.3	2406.6	1531.4	951.29	562.59	320.52	174.31	88.62	41.38	16.81
118	7921.7	5029.6	3375.8	2045.1	1262.3	744.48	422.5	228.62	116.47	54.31	22.22
119	7641.7	4877.1	3158.7	1987.4	1222.3	728.47	409.78	221.05	111.53	52.1	21.01
120	7439.4	4716.9	3037.1	1930.8	1194.2	703.95	398.52	216.52	109.33	51.44	20.84
121	7310	4653.1	2973.3	1901.5	1173.7	697.71	398.01	216.67	110.6	52.29	21.47
122	7405.8	4638.4	4694.2	1892	1173.8	701.91	398.3	216.9	110.46	51.85	21.35
123	7768.9	4928.5	3193.5	2033	1259.8	749.33	427.62	230.22	117.28	55.44	23.19
124	7428	4610.6	2968.9	1900.3	1193.4	710.94	407.45	223.64	113.96	53.81	22.55

Table D.2: Gain measurements for all low gain bases, varying with bias voltages between 800 V and 1300 V in 50 V steps.

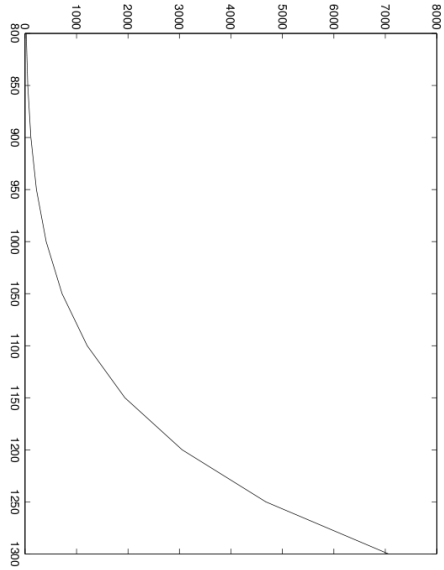

#101

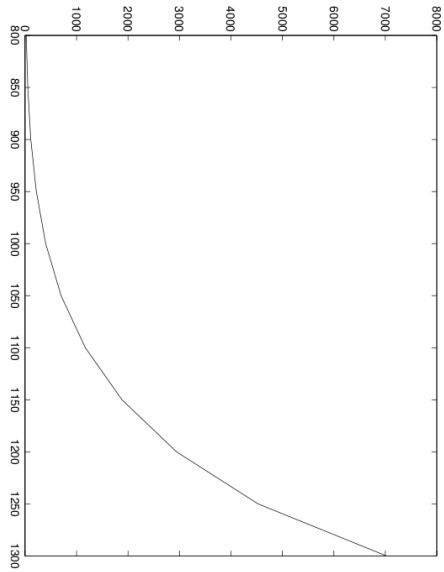

#102

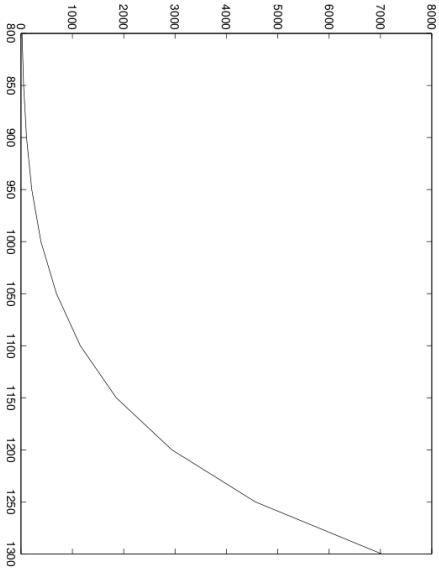

#103

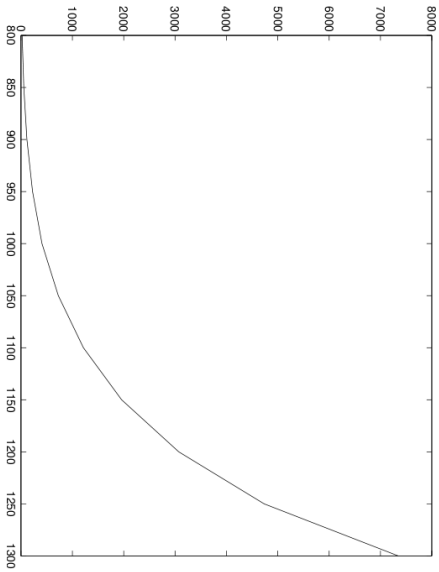

#104

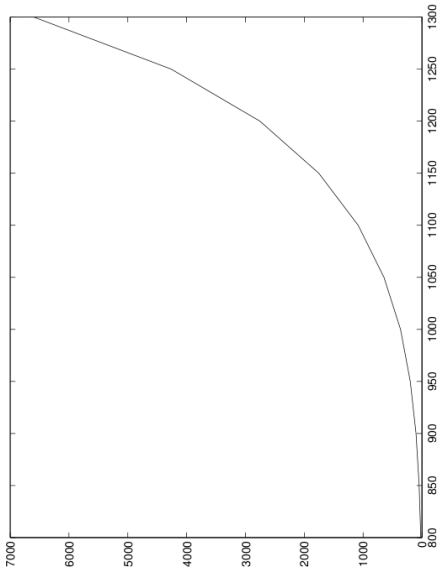

#105

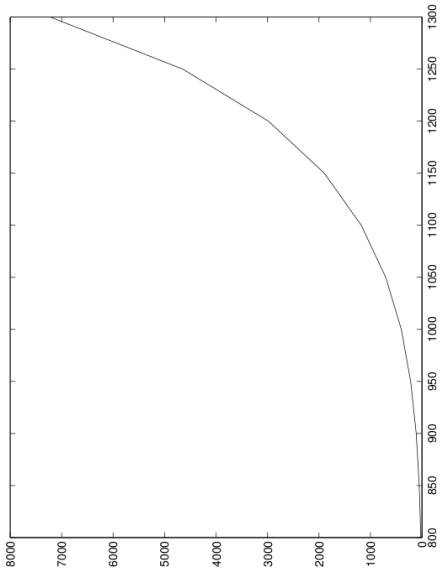

#106

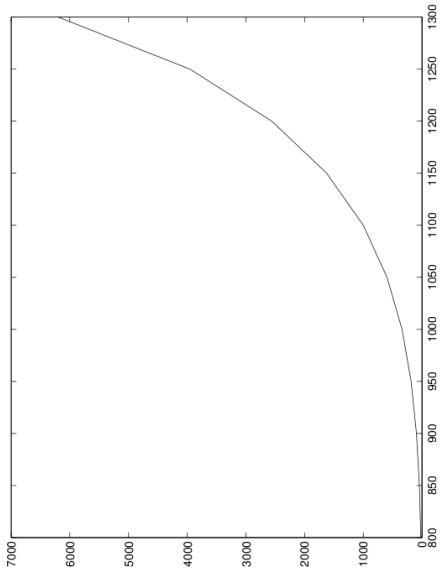

#107

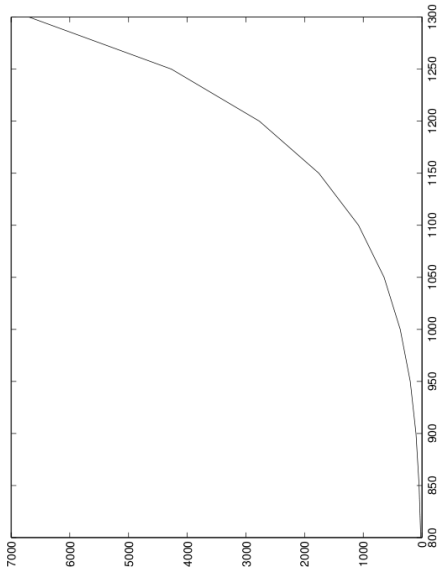

#108

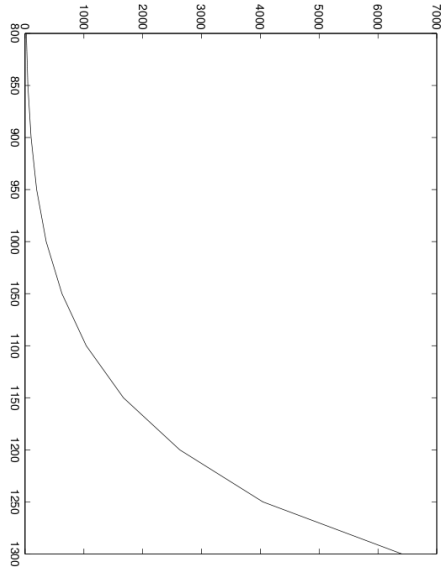

#109

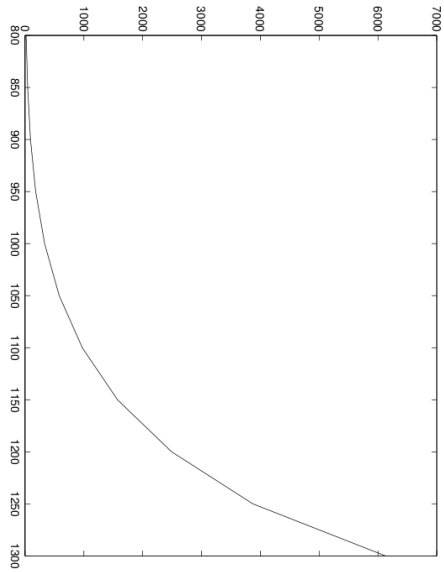

#110

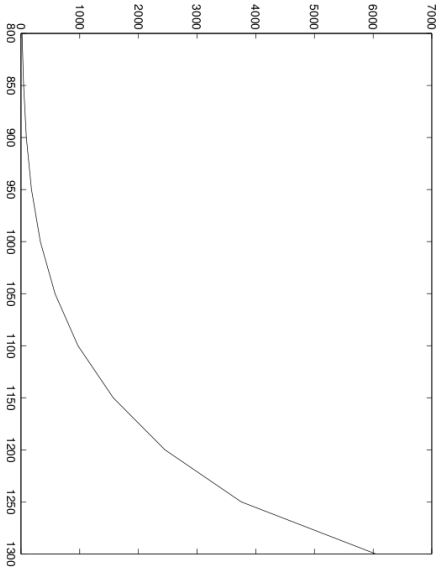

#111

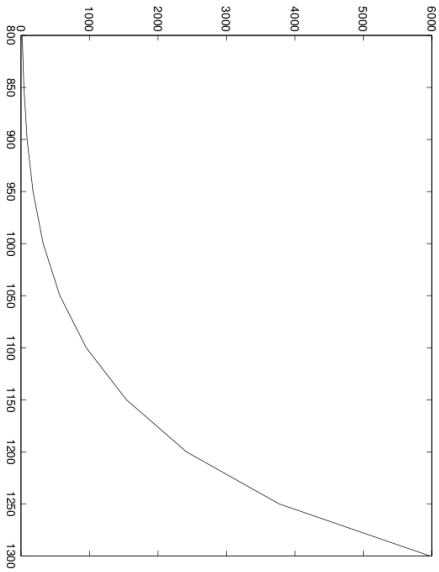

#112

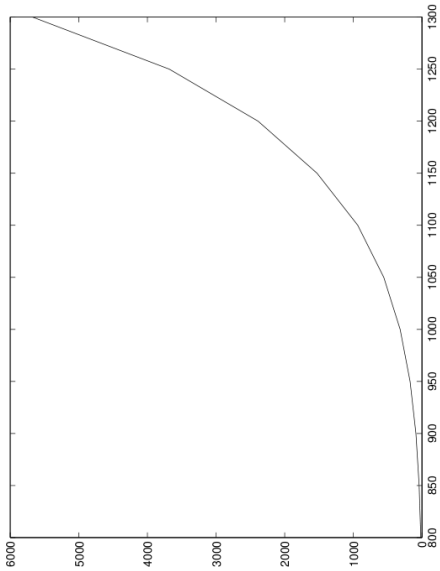

#113

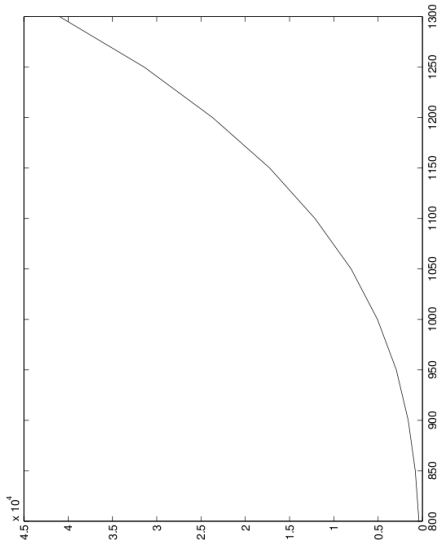

#114

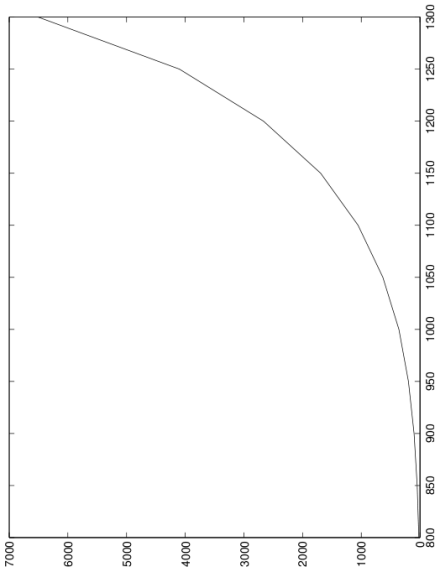

#115

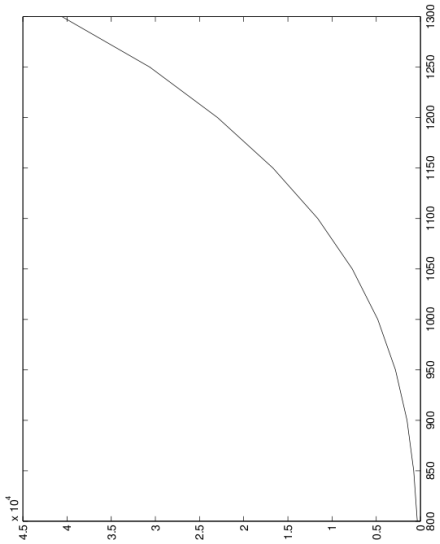

#116

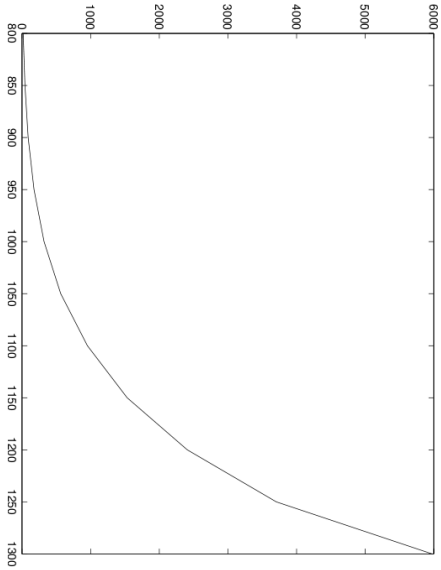

#117

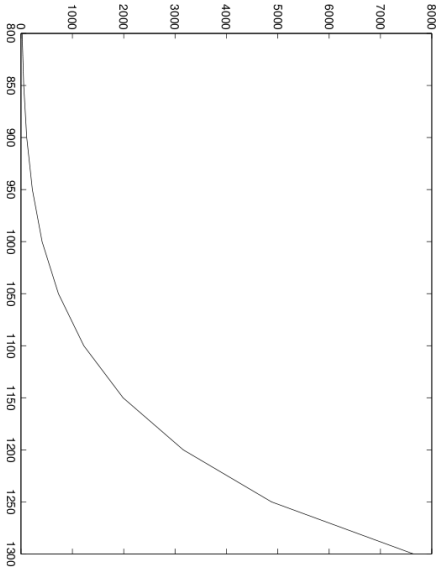

#119

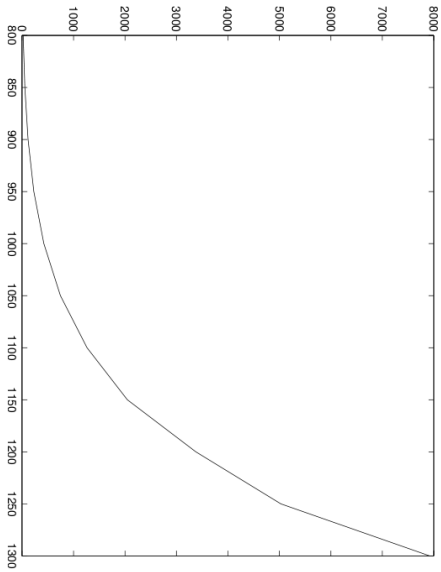

#118

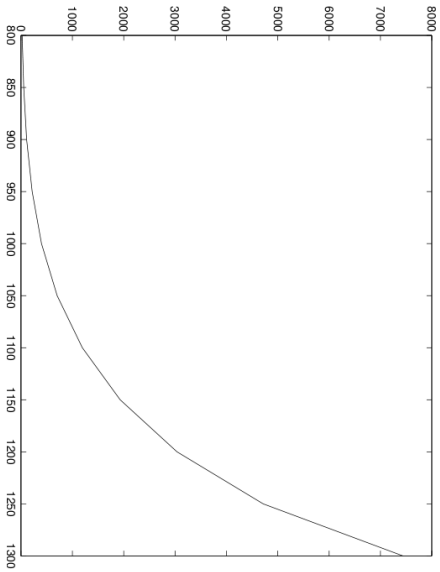

#120

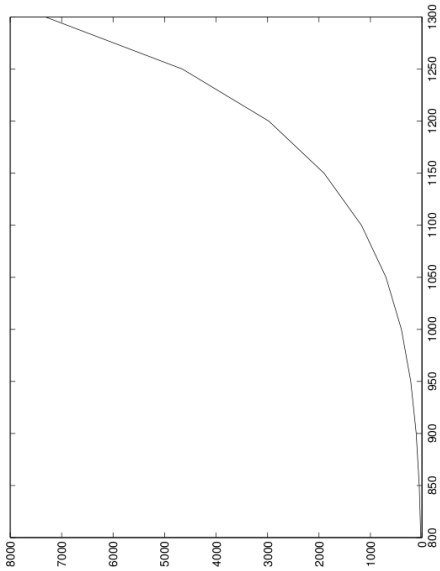

#121

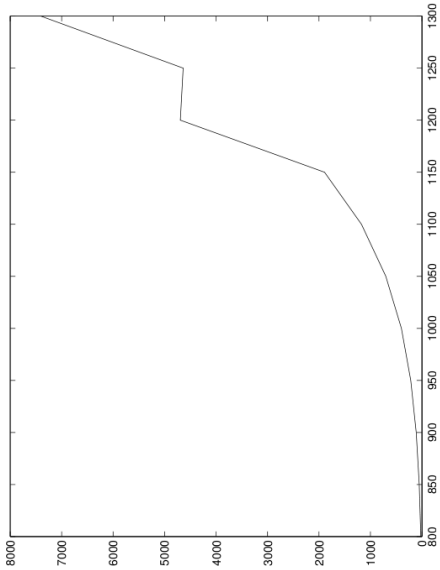

#122

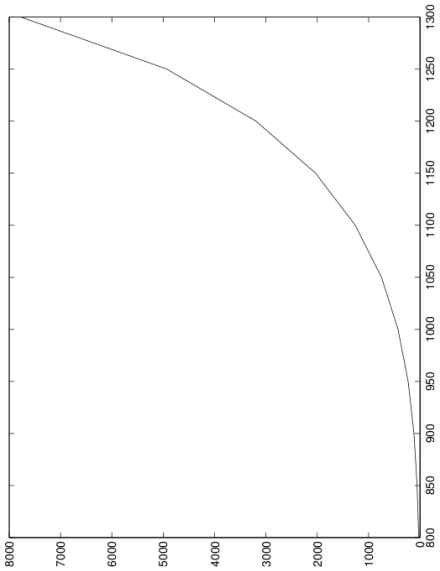

#123

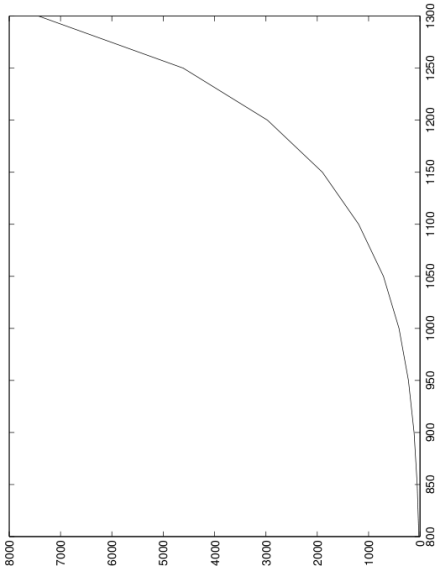

#124

Appendix E

Main Detector Survey Result

The following pages contain the results of the last survery done on the quartz detectors (including the spare background detector MD9).

Jefferson Lab Alignment Group

Data Transmittal

TO: D.Mack, D. Gaskell, D.Wood, M. Dalton		**DATE:** 25 Oct 2012
FROM: Kelly Tremblay	**Checked:**	**# :** C1482

DETAILS: data: step2b\hallc\qweak\120530a

The Quartz Bar Detectors in Hall C were surveyed post run on June 30th, 2012. The table shown on the following page contains the as-found coordinates in both the Qtor magnet system and the local Quartz Bar system as defined in Dave Mack's alignment system (see sketch on final page). Additionally the movements in the local system are shown.

The first group of coordinates are the as-found locations of the bars in the Qtor coordinate system, with the origin at the center of the Qtor magnet. The axis are: Z+ following the beam, X+ transverse in the horizontal direction and Y+ vertically up. Units are meters.

The second group of coordinates describes the as-found locations in the local system for each individual detector. Z+ is in the beam direction with origin at the downstream edge of the bar (570.625 cm downstream of Qtor center, 341 cm radially from beam centerline), X is radially outward from the beamline, and Y follows the downstream top edge of the bar at the appropriate angle.

The column labeled "Ri Component", is the amount that the bars need to be radial displaced in the local quartz X direction. The Ri amount is based upon the amount of Z movement from the ideal Z location and based upon the formula Ri=tan(22.24°)*(Zi-570.625cm) + 341cm. The formula corrects the radial (local X coordinate) position of the bars to catch the beam envelope, as described by D. Mack. Units are centimeters.

The final group of coordinates labeled "Movements", are the calculated amounts the detectors need to move in the local system. The X radial column is the amount the detectors would have to move out after applying the correction amount in the Ri column. A + value indicates the detector needs to move away from the beam centerline. The Y column indicates how much the detector needs to move along the local Y axis. A +Y value would mean the detector moves in positively along the Y axis. A + Z value indicates the detector needs to move downstream from the ideal local value (570.625cm from Qtor center). Units are centimeters.

On the third page, the position of Detector #9 relative to the Qtor coordinate system is shown. There is no ideal location for this 9th detector. The data has a table of coordinates, and rotation values associated with this detector.

	Qtor Coord System				Local Quartz Bar Coords				Movements (cm)		
Detector Side	Z (M)	X (M)	Y (M)	phi angle (deg)	Local X (cm)	Local Y (cm)	Local Z (cm)	Ri component	X Radial (cm)	Y(cm)	Z(cm)
MD1+	5.7757	3.4380	1.2532	0.00	343.80	125.32	577.57	343.84	0.04	0.41	6.94
MD1-	5.7725	3.4364	-1.2614		343.64	-126.14	577.25	343.71	0.07	0.41	6.63
MD2+	5.7796	1.5414	3.3185	45	343.65	125.66	577.96	344.00	0.35	0.07	7.34
MD2-	5.7687	3.3171	1.5381		343.31	-125.80	576.87	343.55	0.24	0.07	6.25
MD3+	5.7734	-1.2575	3.4331	90	343.31	125.75	577.34	343.74	0.44	-0.02	6.71
MD3-	5.7808	1.2571	3.4362		343.62	-125.71	578.08	344.05	0.43	-0.02	7.46
MD4+	5.7846	-3.3266	1.5376	135	343.95	126.50	578.46	344.20	0.25	-0.77	7.84
MD4-	5.7770	-1.5454	3.3125		343.50	-124.95	577.70	343.89	0.39	-0.78	7.07
MD5+	5.7817	-3.4395	-1.2609	180	343.95	126.09	578.17	344.09	0.14	-0.36	7.55
MD5-	5.7831	-3.4418	1.2537		344.18	-125.37	578.31	344.14	-0.04	-0.36	7.69
MD6+	5.7843	-1.5345	-3.3341	225	344.26	127.25	578.43	344.19	-0.07	-1.52	7.80
MD6-	5.7880	-3.3150	-1.5585		344.61	-124.21	578.80	344.34	-0.27	-1.52	8.18
MD7+	5.7877	1.2597	-3.4455	270	344.55	125.97	578.77	344.33	-0.22	-0.24	8.14
MD7-	5.7826	-1.2549	-3.4434		344.34	-125.49	578.26	344.12	-0.22	-0.24	7.64
MD8+	5.7769	3.3105	-1.5540	315	343.97	124.20	577.69	343.89	-0.08	1.53	7.07
MD8-	5.7777	1.5344	-3.3341		344.25	-127.26	577.77	343.92	-0.33	1.53	7.14

The 9th detector is shown below with coordinates based on the Qtor coordinate system referenced above. The units are meters, with angular units in decimal degrees. The horizontal angle formed between the line from the Qtor origin to the detector origin point that is made with the detector plane is 61.9645º. The face of the detector is yawed -1.0546 from the X axis and pitched 0.2074. The Det.Origin is the origin point of the detector and the pt_proj is a point projected perpendicular downstream from the Det.Origin.

Detector 9			
Plane Corner Points			
PT_2	7.3765	-3.7730	-0.2229
PT_3	7.3750	-3.6900	-0.2241
PT_14	7.3803	-3.7756	-1.2293
PT_15	7.3786	-3.6907	-1.2286
detector Points			
Det.Origin	7.3786	-3.7784	-0.7286
pt_proj	7.8785	-3.7688	-0.7268
Survey Targets			
TB_A	7.4104	-3.5270	-1.2321
TB_B	7.4159	-3.8483	-1.2300
TB_C	7.4122	-3.8474	-0.2236
TB_D	7.4059	-3.5255	-0.2282

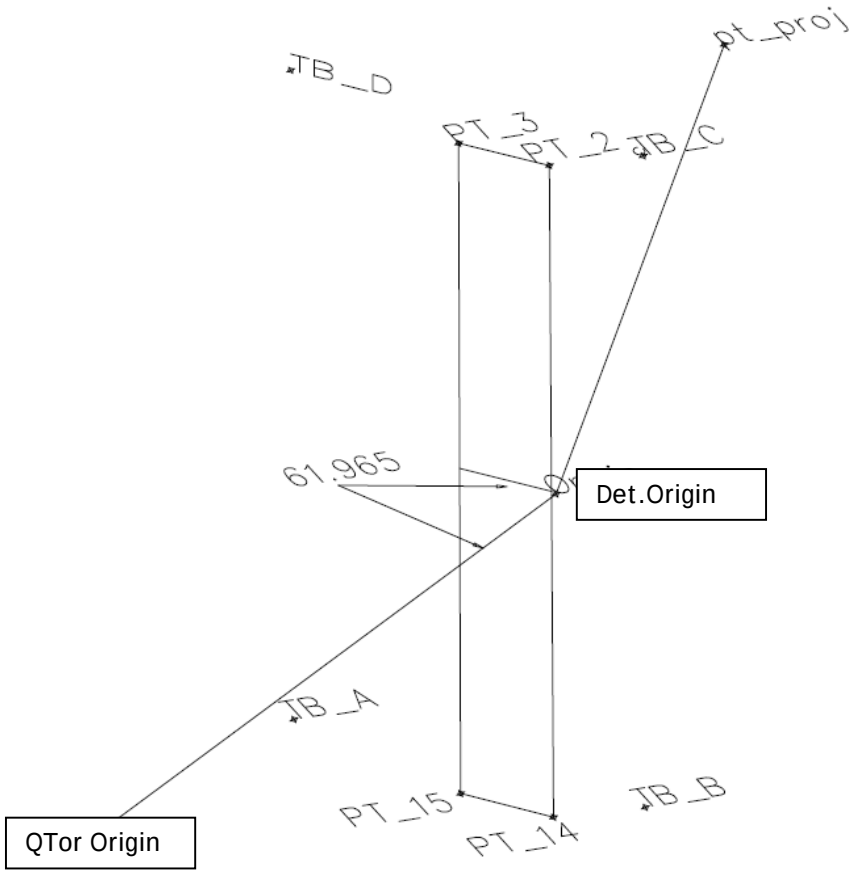

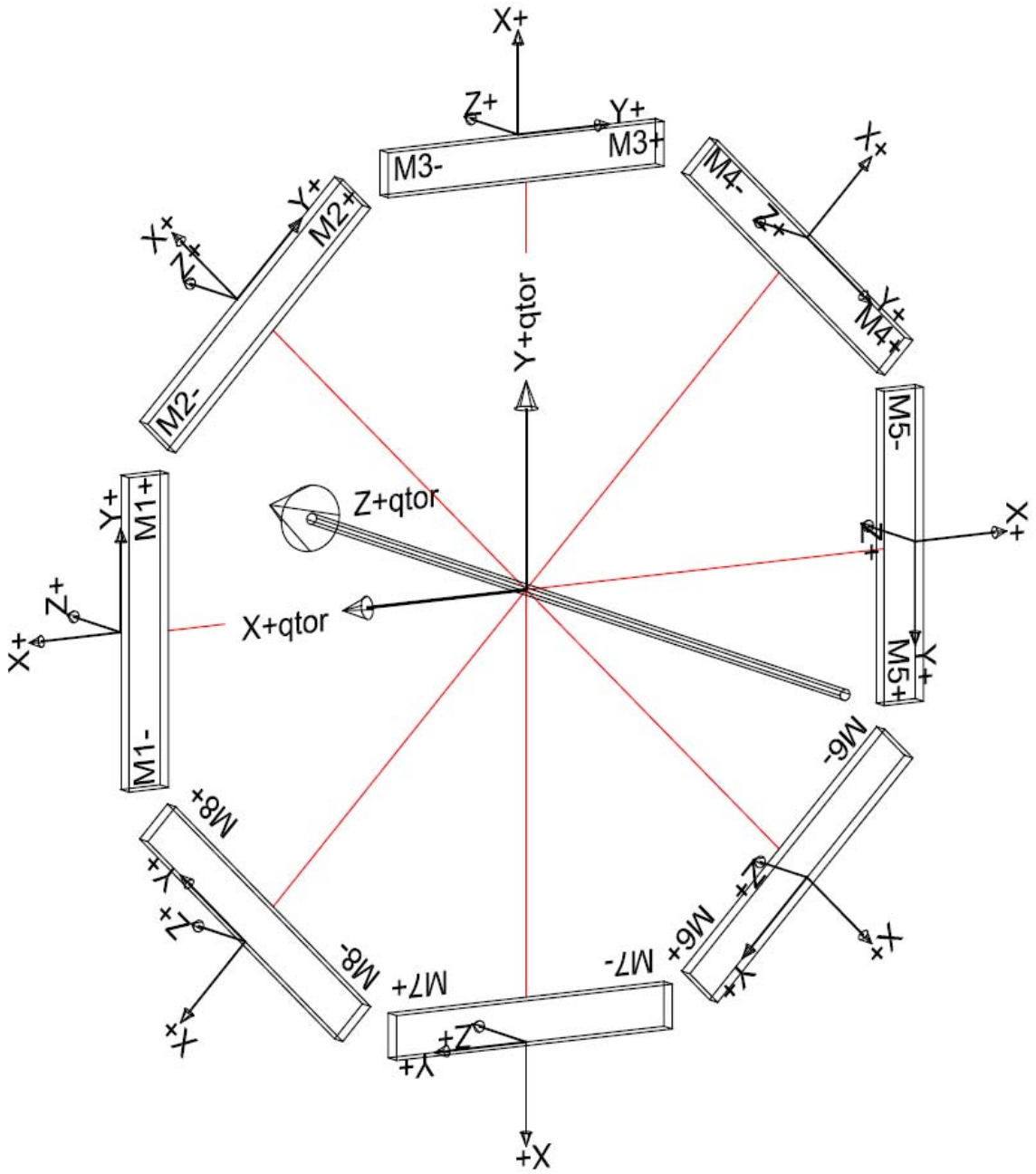

	Qtor Coord System					Local Quartz Bar Coords						
Detector Side	**Z (M)**	**X (M)**	**Y (M)**	**phi angle (deg)**		**Local X (cm)**	**Local Y (cm)**	**Local Z (cm)**		**Ri component**		
MD1+	5.7757	3.4380	1.2532	0.00		343.80	125.32	577.57		343.84		

MD1-	5.7725	3.4364	-1.2614			343.64	-126.14	577.25		343.71		
MD2+	5.7796	1.5414	3.3185	45		343.65	125.66	577.96		344.00		
MD2-	5.7687	3.3171	1.5381			343.31	-125.80	576.87		343.55		
MD3+	5.7734	-1.2575	3.4331	90		343.31	125.75	577.34		343.74		
MD3-	5.7808	1.2571	3.4362			343.62	-125.71	578.08		344.05		
MD4+	5.7846	-3.3266	1.5376	135		343.95	126.50	578.46		344.20		
MD4-	5.7770	-1.5454	3.3125			343.50	-124.95	577.70		343.89		
MD5+	5.7817	-3.4395	-1.2609	180		343.95	126.09	578.17		344.09		
MD5-	5.7831	-3.4418	1.2537			344.18	-125.37	578.31		344.14		
MD6+	5.7843	-1.5345	-3.3341	225		344.26	127.25	578.43		344.19		
MD6-	5.7880	-3.3150	-1.5585			344.61	-124.21	578.80		344.34		
MD7+	5.7877	1.2597	-3.4455	270		344.55	125.97	578.77		344.33		
MD7-	5.7826	-1.2549	-3.4434			344.34	-125.49	578.26		344.12		
MD8+	5.7769	3.3105	-1.5540	315		343.97	124.20	577.69		343.89		
MD8-	5.7777	1.5344	-3.3341			344.25	-127.26	577.77		343.92		